Elastic anisotropy of layered or cracked media: Alternative parameterisation

by

© Filip Piotr Adamus

A Dissertation submitted to the School of Graduate Studies

in partial fulfillment of the requirements for the degree of

Doctor of Philosophy

Department of Earth Sciences

Memorial University of Newfoundland

June 2021

St. John's, Newfoundland and Labrador, Canada

Abstract

This thesis consists of six research papers. Each of them attempts to contribute to the field of elastic anisotropy. We investigate layered or cracked materials in the context of micromechanics and seismology. In the document, we discuss three following topics.

In the first part, we study the overall (effective) elastic properties of a medium that is long-wave equivalent to thin and parallel layers. To obtain the effective elasticity, we use the Backus average. Initially, we consider a typical scenario of isotropic layers that result in a transversely isotropic medium. We propose an alternative parameter that describes the anisotropy of such an effective material. We use it to indicate the presence of fluid within thin layers. Further, we discuss a crucial mathematical approximation of the Backus average and examine a particular case in which the approximation is inaccurate. This time, we allow the layers to exhibit lower symmetry than the isotropic one.

In the second part, we consider an orthotropic symmetry, which is a good analogy to a cracked material. Instead of discussing the medium's microstructure, we focus on the effective properties only. Specifically, we investigate the relations among orthotropic stiffnesses in the context of primary-wave phase velocity. We introduce the so-called cumulative moduli to describe the dependence of quasi P-wave velocity on each elasticity parameter. Such a parameterisation is useful for the velocity approximation.

In the last part, we analyse cracked media in the context of both micromechanics and seismology. We propose an alternative way of obtaining effective elastic properties of a material with many parallel cracks. We represent a set of cracks by a thin layer embedded in a background medium, using Backus average; hence, we generalise the linear-slip method. Finally, we study the influence of cracks on the azimuthal variations of amplitude. We present patterns consisting of a series of azimuthal shapes that change with increasing concentration of inhomogeneities.

Acknowledgements

I wish to thank my supervisor Michael A. Slawinski for his guidance, discussions, and encouragement. He taught me to appreciate theoretical physics and to perceive geophysical problems from a broader scientific context.

Thanks to Tomasz Danek, who revealed to me the usefulness of the numerical approach. I express my gratitude to Heloise Lynn, who inspired me to direct my work towards practical applications. I thank Theodore Stanoev for his scientific and linguistic support.

Also, I wish to acknowledge comments and consultations with Andrej Bóna, Len Bos, Yuriy Ivanov, Mark Kachanov, Mikhail Kotchetov, Alison Malcolm, Andrey Melnikov, Igor Ravve, Benjamin Roure, Robert Sarracino, Md Abu Sayed, Alexey Stovas, graphical support of Elena Patarini, and the proofreading of David Dalton. I thank my thesis examiners Len Bos, Zvi Koren, and Mikhail Kotchetov for their insightful remarks.

I also acknowledge the financial support provided by the Memorial University of Newfoundland in the form of research and teaching assistantships and by The Geomechanics Project supported by Husky Energy and NSERC grants.

Last but not least, I want to thank my family. I am grateful to my parents, who encouraged me to follow the path of science. Thanks to my godfather, who interested me in geophysics. Also, I wish to thank my daughter for her patience and my wife for her continuous support.

Authorship Statement

This document is written in a manuscript format. The doctoral thesis itself is composed of six single-authored research papers. In the appendix, we include—for the convenience of the reader—a co-authored paper referenced therein.

Table of Contents

List of Figures

List of Tables

List of Symbols

Mathematical Relations and Operations

$=$	equality
$\approx$	approximation
$\equiv$	equivalence
$:=$	"defines/denotes"
$=:$	"is defined/denoted by"
$\nabla\cdot$	divergence
$\nabla\times$	curl
∂	partial derivative
$\partial_y x$	partial derivative of x with respect to y
$\overline{x}$	average of x
δ_{ij}	Kronecker's delta
$\to$	"tends to"
$\in$	"belongs to a set"
$\mathbb{R}$	real numbers

Physical quantities

Greek letters

α	constant or P-wave velocity or aspect ratio
β	constant or S-wave velocity
γ	Thomsen parameter
Δ	difference between elasticity parameters
δ	Thomsen parameter
ϵ	Thomsen parameter
ε_{ij}	strain tensor or “eigentensor”
θ	polar or incicence phase angle
λ	Lamé parameter or “cumulative module”
λ_i	Lamé parameter of i-th layer or “eigenvalue”
μ	Lamé parameter or “cumulative module”
μ_i	Lamé parameter of i-th layer
ν	Poisson’s ratio
ρ	mass density
σ_{ij}	stress tensor
υ	“cumulative module”
ϕ	azimuthal phase angle or volume fraction
ϕ_f	volume fraction occupied by cracks
φ	alternative anisotropy parameter
χ	dimensionless constant that relates background and fracture stiffnesses
ψ	azimuthal phase angle

Roman letters

$c_{ijk\ell}$	elasticity tensor components
C_{ij}	elasticity-matrix entries, known as the elasticity parameters or the stiffnesses
$C_{ij}^{\overline{\mathrm{TI}}}$	elasticity parameters of equivalent transversely-isotropic matrix
e	crack density parameter
err	relative error
g	combination of elasticity parameters which values vary from layer to layer
h_f	relative thickness of a set of parallel fractures folded into a single layer
K	incompressibility
k	scaling factor
$\boldsymbol{n}$	normal vector
p_{ij}	proportions between elasticity parameters
q	approximation of "squared-velocity difference" s^2 (see below)
R_{pp}	PP-wave reflection coefficient
ΔR_{pp}	difference between reflection coefficients computed for $0°$ and $90°$ azimuths
$\Delta R_{pp\psi}$	difference between reflection coefficients computed for other azimuths
RSD	relative standard deviation
s^2	squared-velocity difference between P-wave propagating in x_3x_1 and x_3x_2-plane
$\boldsymbol{S}$	compliance tensor
t	weak-anisotropy approximation of "squared-velocity difference" s^2
u_i	displacement vector components
V_P	P-wave velocity (alternatively denoted as V or α)
x_i	coordinate axis
x_ix_j	coordinate plane
$\boldsymbol{Z}$	"excess compliance tensor" or "fracture system compliance tensor"

Chapter 1

Introduction

In accordance with the title, the study of this thesis is embedded in the field of elastic anisotropy. We use the elasticity theory to investigate the directionally-dependent behaviour of layered or cracked media. To facilitate the analysis, we propose alternative parameterisations of the materials' properties. Hence, the title mentions the field of study, the overall scope of investigations, and its method. However, the particular objectives of the research remain unindicated. They vary from chapter to chapter; encompassing them in a single sentence seems to be an unnecessary generalisation. Before we consider the thesis's specific goals, let us discuss the research from a broader scientific context. We pay attention to the basic concepts of the theories or tools employed in the document. Also, we try to indicate the scientific disciplines that are relevant to our investigations. Finally, we focus on each chapter's particular contribution to the quantitative description of mechanical phenomena.

1.1 Scientific context

Continuum mechanics is, using the terminology of Bunge (1967), the *scientific physical theory* that we base our studies on. Due to the absolute space assumption, continuum mechanics belongs to the classical, nonrelativistic physics (Slawinski, 2020a). The primitive concept of the theory states that the body is continuous, where the molecular structure of matter is disregarded (e.g., Malvern, 1969). Hence, in contrast to quantum mechanics, continuum mechanics does not attempt to investigate the nanostructure of the bodies (Slawinski, 2020b). The concept of a continuous medium, also called a continuum, allows us to study materials' deformations. The study of deformable bodies is the essence of continuum mechanics that distinguishes it from particle mechanics, which describes the rigid-body motion. Postulates on material properties inferred from continuum mechanics are close to everyday experience due to the focus on the macroscopic phenomena (Slawinski, 2020b). Therefore, various scientific disciplines such as theoretical seismology or engineering sciences originate from the concept of a continuum.

All branches of classical continuum mechanics (Maugin, 2017) obey its fundamental laws such as the conservation of mass, the balance of linear momentum, and the balance of angular momentum (Coleman and Noll, 1963). However, not every branch describes the deformation of the body in the same way. Different constitutive equations are defining the response to stresses of particular materials (e.g., Mase, 1970). In the thesis, we focus on the elastic continuum only. An elastic continuum is defined by Hooke's law stating that forces are linearly related to small deformations. Specifically, the above-mentioned law can be formulated as,

$$\sigma_{ij} = \sum_{k=1}^{3}\sum_{\ell=1}^{3} c_{ijk\ell}\varepsilon_{k\ell}\,, \qquad i,\, j \in \{1,\, 2,\, 3\}\,, \tag{1.1}$$

where $c_{ijk\ell}$ are the components of a fourth-rank elasticity tensor linearly relating each stress tensor component, σ_{ij} , to all strain tensor components, $\varepsilon_{k\ell}$. The elasticity tensor describes the properties of a continuum, whereas stress and strain tensors from equations (1.1) account for a system of surface forces and deformations, respectively.* Hence, the thesis's research is based on continuum mechanics, and more specifically, on the theory of linear elasticity.

Within the linear elasticity theory, the so-called Hookean solids, expressed by a fourth-rank elasticity tensor, can be a good mathematical analogy to rocks, metals, and other materials that undertake small deformations. The elasticity tensor possesses index symmetries, $c_{ijk\ell} = c_{jik\ell}$, $c_{ijk\ell} = c_{ij\ell k}$, and $c_{ijk\ell} = c_{k\ell ij}$, that result from the basic assumptions of the theory. The first symmetry comes from the balance of angular momentum, the second from the assumption of infinitesimal displacements, and the third from the existence of the strain-energy function. Therefore, a general Hookean solid viewed in a three-dimensional space has only twenty-one, instead of eighty-one, independent components. A symmetric 6×6 matrix can conveniently represent such a tensor in the so-called Voigt's notation. In this notation, Hooke's law can be stated as

$$\begin{bmatrix} \sigma_{11} \\ \sigma_{22} \\ \sigma_{33} \\ \sigma_{23} \\ \sigma_{13} \\ \sigma_{12} \end{bmatrix} = \begin{bmatrix} C_{11} & C_{12} & C_{13} & C_{14} & C_{15} & C_{16} \\ C_{12} & C_{22} & C_{23} & C_{24} & C_{25} & C_{26} \\ C_{13} & C_{23} & C_{33} & C_{34} & C_{35} & C_{36} \\ C_{14} & C_{24} & C_{34} & C_{44} & C_{45} & C_{46} \\ C_{15} & C_{25} & C_{35} & C_{45} & C_{55} & C_{56} \\ C_{16} & C_{26} & C_{36} & C_{46} & C_{56} & C_{66} \end{bmatrix} \begin{bmatrix} \varepsilon_{11} \\ \varepsilon_{22} \\ \varepsilon_{33} \\ 2\varepsilon_{23} \\ 2\varepsilon_{13} \\ 2\varepsilon_{12} \end{bmatrix} , \tag{1.2}$$

where symmetric stress and strain tensors are viewed as 6×1 column vectors, with a factor 2 applied to ε_{12} , ε_{13} , and ε_{23} strain components. Alternatively, the so-called elasticity

*Readers who look for further details on the stress tensor may refer to Slawinski (2020a, Chapter 2.3). Physical meaning of a strain tensor is elaborated in Slawinski (2020a, Chapter 1.4).

matrix can be expressed in Kelvin's notation. In such a case, Hooke's law can be written as

$$\begin{bmatrix} \sigma_{11} \\ \sigma_{22} \\ \sigma_{33} \\ \sqrt{2}\sigma_{23} \\ \sqrt{2}\sigma_{13} \\ \sqrt{2}\sigma_{12} \end{bmatrix} = \begin{bmatrix} C_{11} & C_{12} & C_{13} & \sqrt{2}C_{14} & \sqrt{2}C_{15} & \sqrt{2}C_{16} \\ C_{12} & C_{22} & C_{23} & \sqrt{2}C_{24} & \sqrt{2}C_{25} & \sqrt{2}C_{26} \\ C_{13} & C_{23} & C_{33} & \sqrt{2}C_{34} & \sqrt{2}C_{35} & \sqrt{2}C_{36} \\ \sqrt{2}C_{14} & \sqrt{2}C_{24} & \sqrt{2}C_{34} & 2C_{44} & 2C_{45} & 2C_{46} \\ \sqrt{2}C_{15} & \sqrt{2}C_{25} & \sqrt{2}C_{35} & 2C_{45} & 2C_{55} & 2C_{56} \\ \sqrt{2}C_{16} & \sqrt{2}C_{26} & \sqrt{2}C_{36} & 2C_{46} & 2C_{56} & 2C_{66} \end{bmatrix} \begin{bmatrix} \varepsilon_{11} \\ \varepsilon_{22} \\ \varepsilon_{33} \\ \sqrt{2}\varepsilon_{23} \\ \sqrt{2}\varepsilon_{13} \\ \sqrt{2}\varepsilon_{12} \end{bmatrix}, \tag{1.3}$$

where stress and stain vectors are relative to the same basis. Since Voigt's notation provides a more elegant and simple form of the elasticity matrix, we decide to use this notation in the thesis (with an exception in Appendix A). Nevertheless, the same basis of the stress and strain vectors makes Kelvin's notation convenient for an advanced study of symmetry groups or distances in the space of the elasticity tensors (Slawinski, 2020a).[†]

The description of a Hookean solid represented by an elasticity matrix from equation (1.2) still involves a large number of components; thus, it seems to be complicated. Such a mathematical representation can be a good analogy to solids having a different elastic response in every measured direction. In other words, the elasticity matrix from equation (1.2) is a good description of a completely anisotropic body. However, in practice, many materials subjected to loads present identical or very similar elastic properties in particular directions. Further, some media deform identically, no matter the direction of the load applied; hence, their behaviour is isotropic. A *scientific physical theory* needs to be capable of matching empirical data (Bunge, 1967). To better describe the real phenomena, in general, and directional dependence of material properties, in particular, we use the concept of the material

[†]Equation (1.3), expressed in Kelvin's notation, is invariant under orthogonal transformations; this is not true of equation (1.2), expressed in Voigt's notation. In other words, equation (1.3) is a tensor equation; equation (1.2) is a linear stress-strain equation valid in a fixed coordinate system. Properties of equation (1.2), however, are sufficient to pursue our studies.

symmetries of Hookean solids. A Hookean symmetry is the invariance of the form (matrix or components) of the elasticity tensor under the transformation of the coordinate system. We distinguish eight classes of material symmetry (Cowin and Mehrabadi, 1987) defined in terms of their symmetry groups, which are the set of all orthogonal transformations to which the elastic properties of a given continuum are invariant. There are two extreme cases of material symmetries. The first case is the generally anisotropic symmetry (GA), whose group contains only two orthogonal transformations: the identity and the point symmetry. These two transformations are contained, as a subgroup, in the symmetry groups of all classes. The GA symmetry is exhibited by twenty-one independent elasticity parameters, as shown by the elasticity matrix from equation (1.2). The other extreme case is the isotropic symmetry (iso) represented by the following matrix,

$$\boldsymbol{C}^{\mathrm{iso}} = \begin{bmatrix} C_{11} & C_{11}-2C_{44} & C_{11}-2C_{44} & 0 & 0 & 0 \\ C_{11}-2C_{44} & C_{11} & C_{11}-2C_{44} & 0 & 0 & 0 \\ C_{11}-2C_{44} & C_{11}-2C_{44} & C_{11} & 0 & 0 & 0 \\ 0 & 0 & 0 & C_{44} & 0 & 0 \\ 0 & 0 & 0 & 0 & C_{44} & 0 \\ 0 & 0 & 0 & 0 & 0 & C_{44} \end{bmatrix}, \tag{1.4}$$

having only two independent coefficients. The symmetry group of an isotropic continuum contains all orthogonal transformations. Hence it contains, as its subgroups, the symmetry groups of other seven classes. These classes are: generally anisotropic, monoclinic, orthotropic (ort), tetragonal, trigonal, transversely isotropic (TI), and cubic. The subgroup relation among symmetry classes is presented in Figure 1.1. In the next chapters, we discuss particular symmetries in more details.‡

‡Readers interested in the orthogonal transformations needed to obtain elasticity tensors of particular symmetries may refer to Slawinski (2020a, Chapter 5) or Slawinski (2020b, Chapter 3).

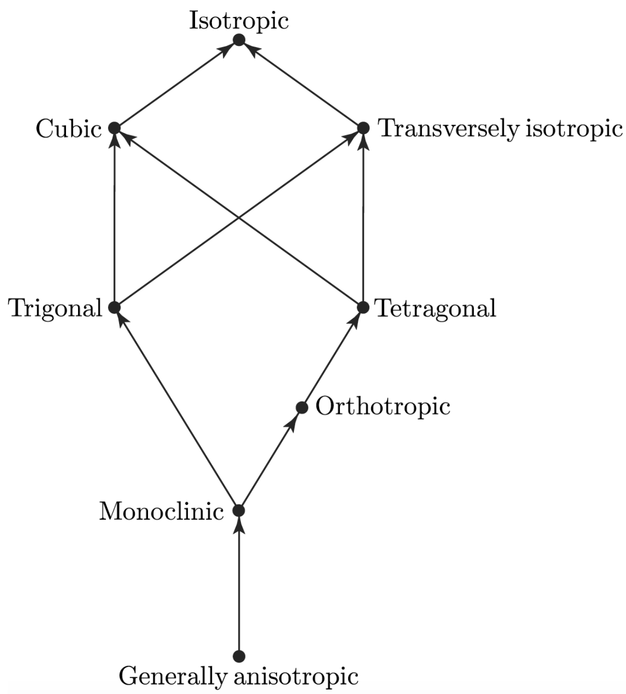

Figure 1.1: Relations among symmetry classes of an elasticity tensor (figure taken from Slawinski (2020a))

In this document, we investigate the anisotropic behaviour of layered or cracked materials. We define a layered medium as an inhomogeneous structure consisting of parallel constituents of individual thicknesses and stiffnesses. On the other hand, we refer to a cracked material if the inhomogeneities are flat, having any orientation. Notice that a special case of a material with parallel cracks can be viewed as a layered medium, where some constituents have infinitesimal thicknesses. Various Hookean symmetries can describe the directional dependence of the aforementioned materials' properties. In general, the medium's anisotropy can be caused by intrinsic properties of the material, for instance, specific crystal orientations in the rock. However, in the case of layered or cracked media, we cope with the anisotropy induced by individual inhomogeneities that are not necessarily intrinsically anisotropic.

To a large extent, the material description depends on the scale at which we regard it. For instance, if we examine a layered medium from a micro or mesoscale, we consider each constituent's properties. However, from a macro perspective of long-wave propagation—if layers are sufficiently thin—the medium can be regarded as a homogeneous one. Specifically, as discussed by Bruggeman (1937) or Postma (1955), thin isotropic layers can be viewed as a transversely-isotropic medium. To quantitatively homogenise the layered material, we can use the average proposed by Backus (1962). If layers are not isotropic but exhibit intrinsic anisotropy, the Backus average can be extended to matrix formalism as shown by Helbig and Schoenberg (1987). Other techniques are used to homogenise a cracked medium. Schoenberg (1980) has described a crack interface as the linear-slip across which the traction vector is continuous, but the displacement is not. This idea was further developed by Schoenberg and Douma (1988) and Schoenberg and Sayers (1995), where a useful homogenisation pattern was proposed. Other, similar, or equivalent techniques were summarised by Kachanov (1992). All the aforementioned methods regarding material at a macroscale as a homogeneous one belong to the scientific discipline of micromechanics. Paraphrasing Kachanov and Sevostianov (2018),

> micromechanics relates the inhomogeneous material to its overall properties that are homogeneous at a macroscale.

Notice that microscale inhomogeneities embedded in the material must be large enough to disregard the molecular structure so that the assumption of continuum remains relevant. The concept of a homogenised, or so-called, effective medium dates back to the nineteenth century and goes well beyond the elasticity theory. Almost two-hundred years ago, effective magnetic properties were studied by Poisson (1824). The effective conductivity was investigated by Mossotti (1836) and Clausius (1879). More than a hundred years ago, the effective properties in the context of fluid mechanics were considered by Einstein (1906).

The idea of homogenisation of elastic media probably dates back to the aforementioned work of Bruggeman (1937).

As we have discussed, the elastic anisotropy of layered or cracked media can be induced by the parallel constituents or the inhomogeneities embedded in the background, respectively. In the first part of the thesis (Chapters 2–3), we focus on the micro-macro properties of the layered media. The investigation is relevant for the scientific disciplines of micromechanics, seismology, exploration geophysics, or engineering sciences. In the second part (Chapters 4–5), we disregard the microstructure and assume the orthotropic symmetry that is a good analogy for a cracked medium (e.g., Schoenberg and Helbig, 1997). This way, we can focus on the macroscale elastic response in the context of seismology. The last part (Chapters 6–7) treats on micro-macro properties of cracked media. The investigation from this third part can be placed in the area of both micromechanics and seismology.

To sum up, we have indicated continuum mechanics and linear elasticity, in particular, to be the theory that underlies our studies. Then, we have discussed the material symmetries that can describe the anisotropic behaviour of deformable bodies. To consider elastic anisotropy of layered or cracked media, we need to be aware of whether we investigate the properties of individual inhomogeneities at the microscale or the effective properties of the homogenised medium at the macroscale. Our investigation focuses on the micro-macro relation that is pertinent to various scientific disciplines and on macro description to approach the seismological objectives. Table 1.1 indicates the theory employed, the scope of the investigation, and the disciplines that are relevant to our studies at each step of the document's main body.

Table 1.1: Thesis content in the context of the theory employed, material symmetry being studied, the medium of interest, the scale of investigation, and the scientific discipline relevancy

chapter	theory	symmetry	medium	scale	discipline
2	l. elast.	iso, TI	layered	micro-macro	various discipl.
3	l. elast.	all except GA	layered	micro-macro	various discipl.
4–5	l. elast.	ort	cracked	macro	seismology
6	l. elast.	any	cracked	micro-macro	micromechanics
7	l. elast.	iso, TI, ort	cracked	micro-macro	seismology

1.2 Thesis outline

This thesis is written in a manuscript format as a collection of six research papers. Each chapter of the document's main body can stand on its own since it corresponds to an independent publication. The research papers collected herein do not differ (excluding the formatting) from their original, published forms. However, due to the notation inconsistency or possible minor adjustments, the last sections of some chapters contain the post-publication comments and explanations. Despite different particular objectives, the research papers are closely related to each other. They share the same theoretical concepts to investigate layered or cracked media, where numerical studies always supplement the theory.

In Chapter 2, we consider a typical situation of a layer-induced anisotropy. Specifically, we replace thin isotropic layers with a transversely-isotropic effective medium, using Backus (1962) average. We try to approach the following inverse problem in the context of possible fluid detection. Having the elastic information at the macroscale, we want to infer the variations of stiffnesses in layers. The elasticity parameters, C_{11} and C_{44} , can be expressed in terms of Lamé coefficients λ and μ . According to Gassmann (1951), the fluctuation of fluid content affects only λ , but not μ . To infer the variations of Lamé coefficients, we use anisotropic parameters shown by Thomsen (1986). Also, we introduce a new anisotropic parameter that is more sensitive to λ fluctuations. Upon numerical analysis, we propose a method of indicating substantial variations of λ—viewed as possible changes of fluid content—by checking the particular values of the aforementioned anisotropy parameters obtained for effective media. As discussed in detail in Appendix A, in general, the fluctuations of λ are proportional to the anisotropy strength; hence, the aforementioned fluid detection approach is reasonable. However, one must be aware of a rare case of constant rigidity in isotropic layers, where varying λ do not cause the effective anisotropy.

In Chapter 3, we investigate the accuracy of the Backus (1962) average as the homogenisation tool. We discuss a crucial approximation used in the average and examine a particular case in which this approximation is mathematically incorrect. We check if such inaccuracy is likely to occur in practice and if it influences the elastic wave propagation.

In Chapter 4, we do not consider the microstructure explicitly, but we focus on the effective properties of the cracked medium in the context of seismology. Particularly, we analyse the contributions of elasticity parameters to the quasi P-wave phase velocity propagating in an orthotropic medium. We concentrate on the squared-velocity difference resulted from the propagation in two mutually perpendicular symmetry planes. Such a difference may arise from the presence of cracks being parallel to one or both of the planes.

In Chapter 5, we again investigate the elastic description of quasi P-wave propagating in orthotropic media. Our studies are not limited to the propagation along symmetry planes, but any polar and azimuthal phase angle is considered. We divide nine orthotropic elasticity parameters into three groups and analyse the relationship among stiffnesses in each group. To describe the dependencies, we introduce the so-called cumulative moduli. Each module is responsible for the relations of a distinct group of three parameters. By introducing such a representation, in certain cases, we can approximate the quasi P-wave velocity for any polar and azimuthal phase angle, knowing less than required nine stiffnesses.

In Chapter 6, we propose an alternative way of obtaining the effective elastic properties of a heavily cracked medium. In contrast to the classical models, we represent cracks by a thin layer embedded in the background material. In other words, we follow the Schoenberg and Douma (1988) matrix formalism for the Backus average, but we relax the assumptions of infinite weakness and marginal thickness of a layer so that it does not correspond to the linear-slip plane.

In the last paper (Chapter 7), we examine the influence of cracks on the azimuthal variations of amplitude. We assume a single set of vertical cracks aligned along horizontal axis. To consider the amplitudes, we focus on a Vavryčuk and Pšenčík (1998) approximation of the PP-wave reflection coefficient. We construct graphic patterns of two-dimensional amplitude variations with azimuth. The patterns consist of a series of shapes that change with the increasing crack concentration. The proposed schemes differ depending on the incidence angle and the background saturation. Some shapes turn out to be more characteristic of gas-bearing rocks.

In each chapter, we introduce the non-conventional parameterisation that allows us to reach the above-mentioned objectives mentioned above. Anisotropy parameter, φ, is useful for the fluid indication in layered media. The coefficient g can describe a particular, problematic case of the Backus (1962) average. We have introduced parameter s^2 to define the squared-velocity difference of quasi P-wave phase velocity. Cumulative moduli ν, λ, and μ facilitate the elastic description of the aforementioned quasi P-wave propagating in orthotropic media. Quantification of heavily cracked elastic material is possible due to the introduction of coefficients h_f and k. Lastly, the parameter ΔR_{pp} helps to analyse the azimuthally dependent reflection coefficient.

This thesis is dedicated to the theoreticians and practitioners who consider layered or cracked media in the context of micromechanics and seismology. Specifically, in the document, we focus on the elastic anisotropy induced by the inhomogeneities, the homogenisation techniques, fluid detection, inverse problems, P-wave elastic description, and seismic azimuthal anisotropy. We believe that the thesis can be exceptionally beneficial for those readers who view layered or cracked materials from both micro and macro perspectives.

Chapter 2

On possible fluid detection in equivalent transversely isotropic media*

Abstract

We consider a transversely isotropic (TI) medium that is long-wave equivalent to a stack of thin, parallel, isotropic layers and is obtained using the Backus average. In such media, we analyse the relations among anisotropy parameters; Thomsen parameters, ϵ and δ, and a new parameter φ. We discuss the last parameter and show its essential properties; it is equal to zero in the case of isotropy of equivalent medium and/or constant Lamé coefficient λ in layers. The second property occurs to make φ sensitive to variations of λ in thin-bedded sequences. According to Gassmann, in isotropic media the variation of fluid content affects only the Lamé coefficient λ, not μ; thus, the sensitivity to changes of λ is an essential property in the context of possible detection of fluids. We show algebraically and

*This chapter consists of the original research paper and the post-publication comments. Herein, we invoke the following paper: Adamus, F. P. (2019). "On possible fluid detection in equivalent transversely isotropic media". *Geophysical Prospecting*, 67(9), 2319–2331.

numerically that φ is more sensitive to these variations than ϵ or δ. Nevertheless, each of these parameters is dependent on the changes of μ; to understand this influence, we exhibit comprehensive tables that illustrate the behaviour of anisotropy parameters with respect to specific variations of λ and μ. The changes of μ in layers can be presented by the Thomsen parameter γ that depends on them solely. Hence, knowing the values of elasticity coefficients of equivalent TI medium, we may compute φ and γ, and based on the aforementioned tables, we predict the expected variation of λ; in this way, we propose a new method of possible fluid detection. Also, we show that the prior approach of possible detection of fluids, proposed by Berryman et al., may be unreliable in specific cases. To establish our results we use the Monte Carlo (MC) method; for the range and chosen variations of Lamé coefficients λ and μ—relevant to sandstones—we generate these coefficients in thin layers and, after the averaging process, we obtain an equivalent TI medium. We repeat that process numerous times to get many equivalent TI media, and—for each of them—we compute their anisotropy parameters. We illustrate φ, ϵ, and δ in the form of cross-plots that are relevant to the chosen variations of λ and μ. Additionally, we present a table with the computed ranges of anisotropy parameters that correspond to different variations of Lamé coefficients.

Keywords: Anisotropy, Numerical study, Parameter estimation.

2.1 Introduction

We consider a transversely-isotropic (TI) medium equivalent to parallel isotropic layers, obtained using the Backus average. In such a medium, we define a new anisotropy parameter, φ. We show that φ is sensitive to variations of Lamé coefficient λ in layers. Based on Gassmann's theory, we treat these variations as possible changes in fluid content. We propose a simple pattern in which the relations between φ and Thomsen parameter γ indicate specific fluctuations of λ. This approach might be useful for fluid detection in equivalent TI media.

Thin, parallel layers may be regarded as the long-wave equivalent medium. Such representation has been considered by various authors. Let us mention only a few of them: Postma (1955), Backus (1962), Schoenberg and Muir (1989), Berryman et al. (1999), Kumar (2013), or Bos et al. (2017). Postma (1955) pointed out that an inhomogeneous medium consisting of fine, isotropic layers can be treated as a homogeneous, transversely isotropic (TI) medium. Nonetheless, he examined only the case of a periodic system of two horizontal layers. Subsequently, Backus (1962) generalised Postma's (1955) work. He did not assume the condition of periodicity and presented a fundamental averaging formula of the TI medium, long-wave equivalent to isotropic or TI layers of various thicknesses. Schoenberg and Muir (1989) showed a method of calculating the elasticity coefficients for the media equivalent to layers exhibiting lower symmetries than the TI symmetry. Kumar (2013) and Bos et al. (2017) presented analytical solutions of Schoenberg and Muir (1989) approach for layers with anisotropies up to monoclinic and up to generally anisotropic, respectively. Herein, we only examine equivalent TI media obtained upon Backus averaging of isotropic layers.

Long-wave equivalent medium is widely used in exploration geophysics, particularly in well-logging. The well-log frequency is significantly higher than the seismic frequency. The Backus averaging allows us to adjust both frequency ranges so that we can establish a reasonable relationship between seismic and reservoir properties (Kumar, 2013). Apart from the above application, an equivalent medium can be considered in the context of possible detection of fluids. Berryman et al. (1999) suggested that the Thomsen (1986) anisotropy parameters computed for equivalent TI media can be indicative of changing fluid content in layers. Explicitly, the authors claim that the negative value of ϵ or the small positive value of ϵ and δ may be viewed as such indicators. Their method is based on the fact that, as stated by Gassmann (1951), the variation of fluid content affects only the Lamé coefficient λ, not μ. Thus, the authors treat the changes of λ in layers as potential fluid variations. The elasticity coefficients for equivalent TI media directly depend on μ and λ. Therefore, the Thomsen parameters computed for such media reflect the changes in the Lamé coefficients.

The goal of this paper is to pursue the work of Berryman et al. (1999) and to propose a new, more efficient approach of detecting changes of λ in layers, based on sole, equivalent TI media information. We introduce a new anisotropy parameter, φ, for which specific ranges, along with its relation with Thomsen parameter, γ, indicate the large variation of λ. In our approach, similarly to Berryman et al. (1999), we assume thin, isotropic layering; thus, our method is not valid for layers that exhibit lower symmetries.

To isolate specific fluctuations of λ and to show that φ might be more efficient than ϵ or δ in the context of detecting these variations, where strong fluctuations of λ are treated as a possible fluid indicator, we perform the following procedure. We execute Monte Carlo (MC) simulations for six different variations of Lamé coefficients in layers. MC is a well-known method that relies on repeated and random sampling to obtain numerical results. Specifically, for a stack of layers, a random, uniformly distributed set of μ and λ is chosen from the given Lamé coefficients range. We restrict the choice of that set by the given range of relative standard deviations of λ and μ; thus, we define the changes of Lamé coefficients in layers. Such a restriction has not been introduced in the previous works on fluid detection in equivalent media. The simulation is repeated s times and, upon Backus averaging, we obtain s different equivalent TI media. For each medium, anisotropy parameters φ, ϵ, and δ are calculated. Then, we analyse cross-plots of φ versus ϵ and δ versus ϵ. We compare the cross-plots for different changes of λ and μ in layers, which allows us to better investigate the relations of the anisotropy parameters in the context of possible detection of fluids.

2.2 Background

2.2.1 Backus averaging

As shown by Backus (1962), a medium that consists of parallel isotropic layers, whose individual thicknesses are much smaller than the wavelength, can be regarded as a single, homogeneous, TI medium. The elasticity coefficients of such a medium are

$$C_{11}^{\overline{\rm TI}} = \overline{\left(\frac{\lambda}{\lambda+2\mu}\right)}^2\,\overline{\left(\frac{1}{\lambda+2\mu}\right)}^{-1} + \overline{\left(\frac{4(\lambda+\mu)\mu}{\lambda+2\mu}\right)}\,, \tag{2.1}$$

$$C_{12}^{\overline{\rm TI}} = \overline{\left(\frac{\lambda}{\lambda+2\mu}\right)}^2\,\overline{\left(\frac{1}{\lambda+2\mu}\right)}^{-1} + \overline{\left(\frac{2\lambda\mu}{\lambda+2\mu}\right)}\,, \tag{2.2}$$

$$C_{13}^{\overline{\rm TI}} = \overline{\left(\frac{\lambda}{\lambda+2\mu}\right)}\,\overline{\left(\frac{1}{\lambda+2\mu}\right)}^{-1}\,, \tag{2.3}$$

$$C_{33}^{\overline{\rm TI}} = \overline{\left(\frac{1}{\lambda+2\mu}\right)}^{-1}\,, \tag{2.4}$$

$$C_{44}^{\overline{\rm TI}} = \overline{\left(\frac{1}{\mu}\right)}^{-1}\,, \tag{2.5}$$

$$C_{66}^{\overline{\rm TI}} = \overline{\mu}\,, \tag{2.6}$$

where $\lambda := C_{33} - 2C_{44}$ and $\mu := C_{44}$ are the Lamé coefficients for each isotropic layer. The overbar in the expressions above denotes the weighted average. The layer thickness weights the average, herein, all layers have the same thickness; therefore, we use an arithmetic average. An equivalent TI medium, whose rotation symmetry axis is parallel to the x_3-axis, is

$$C^{\overline{\mathrm{TI}}} = \begin{bmatrix} C_{11}^{\overline{\mathrm{TI}}} & C_{12}^{\overline{\mathrm{TI}}} & C_{13}^{\overline{\mathrm{TI}}} & 0 & 0 & 0 \\ C_{12}^{\overline{\mathrm{TI}}} & C_{11}^{\overline{\mathrm{TI}}} & C_{13}^{\overline{\mathrm{TI}}} & 0 & 0 & 0 \\ C_{13}^{\overline{\mathrm{TI}}} & C_{13}^{\overline{\mathrm{TI}}} & C_{33}^{\overline{\mathrm{TI}}} & 0 & 0 & 0 \\ 0 & 0 & 0 & C_{44}^{\overline{\mathrm{TI}}} & 0 & 0 \\ 0 & 0 & 0 & 0 & C_{44}^{\overline{\mathrm{TI}}} & 0 \\ 0 & 0 & 0 & 0 & 0 & C_{66}^{\overline{\mathrm{TI}}} \end{bmatrix}, \tag{2.7}$$

where $C_{12}^{\overline{\mathrm{TI}}} = C_{11}^{\overline{\mathrm{TI}}} - 2C_{66}^{\overline{\mathrm{TI}}}$. Consequently, expressions (2.1)–(2.6) consist of five independent coefficients. Throughout the paper, for simplicity, we use Voigt's notation, as opposed to Kelvin's notation.

2.2.2 Stability conditions

The stability conditions state the allowable relations among the elasticity coefficients. These conditions constitute the fact that it is necessary to expend energy to deform a material (e.g., Slawinski, 2015, Section 4.3). Mathematically, they mean that every elasticity tensor must be positive-definite. A tensor is positive-definite if and only if all its eigenvalues are positive. For any isotropic elasticity tensor, the inequalities

$$C_{33} \geq \tfrac{4}{3}\, C_{44} \geq 0\ , \tag{2.8}$$

ensure that all eigenvalues are positive; thus, the stability conditions are satisfied. The same inequalities can be rewritten in a different notation, using Lamé coefficients,

$$\lambda \geq -\tfrac{2}{3}\,\mu \qquad \text{and} \qquad \mu \geq 0\,. \tag{2.9}$$

To ensure that all eigenvalues of any TI tensor are positive, the following inequalities must be obeyed:

$$\begin{gathered}C_{66} \geq 0\,, \quad C_{44} \geq 0\,, \quad C_{33} \geq 0\,, \quad C_{12}+C_{66} \geq 0\,, \\ \text{and} \quad \left(C_{12}+C_{66}\right) C_{33} \geq \left(C_{13}\right)^{2}\,.\end{gathered} \tag{2.10}$$

2.2.3 Thomsen anisotropy parameters

To examine the strength of anisotropy of an equivalent TI medium, we use the Thomsen (1986) parameters,

$$\epsilon := \frac{C_{11}^{\overline{\mathrm{TI}}} - C_{33}^{\overline{\mathrm{TI}}}}{2C_{33}^{\overline{\mathrm{TI}}}}\,, \tag{2.11}$$

$$\delta := \frac{\left(C_{13}^{\overline{\mathrm{TI}}} + C_{44}^{\overline{\mathrm{TI}}}\right)^{2} - \left(C_{33}^{\overline{\mathrm{TI}}} - C_{44}^{\overline{\mathrm{TI}}}\right)^{2}}{2C_{33}^{\overline{\mathrm{TI}}}\left(C_{33}^{\overline{\mathrm{TI}}} - C_{44}^{\overline{\mathrm{TI}}}\right)}\,, \tag{2.12}$$

$$\gamma := \frac{C_{66}^{\overline{\mathrm{TI}}} - C_{44}^{\overline{\mathrm{TI}}}}{2C_{44}^{\overline{\mathrm{TI}}}}\,. \tag{2.13}$$

As shown by Adamus et al. (2018)—for Backus averaging—increasing anisotropy of such a medium implies the increase of inhomogeneity among isotropic layers.†

2.2.4 Anisotropy parameter φ

Let us invoke the conditions on the elasticity coefficient of a transversely isotropic medium that are necessary and sufficient for such medium to be isotropic,

$$C_{11}^{\overline{\mathrm{TI}}} = C_{33}^{\overline{\mathrm{TI}}}\,, \tag{2.14}$$

$$C_{44}^{\overline{\mathrm{TI}}} = C_{66}^{\overline{\mathrm{TI}}}\,, \tag{2.15}$$

†Readers interested in the relation between inhomogeneity and anisotropy in Backus average may refer to the aforementioned paper (Adamus et al., 2018) included in Appendix A, on page 249.

$$C_{12}^{\overline{\mathrm{TI}}} = C_{13}^{\overline{\mathrm{TI}}} = C_{11}^{\overline{\mathrm{TI}}} - 2C_{66}^{\overline{\mathrm{TI}}} \,. \tag{2.16}$$

If we assume the arithmetic average, we can show that the last condition is satisfied if λ is constant in layers. We rewrite condition (2.16) as

$$\left(\frac{1}{n}\sum_{i=1}^{n}\frac{\lambda_i}{\lambda_i+2\mu_i}\right)\left(\frac{1}{n}\sum_{i=1}^{n}\frac{1}{\lambda_i+2\mu_i}\right)^{-1}\left[\frac{1}{n}\left(\sum_{i=1}^{n}\frac{\lambda_i}{\lambda_i+2\mu_i}\right)-1\right] + \frac{1}{n}\sum_{i=1}^{n}\frac{2\lambda_i\mu_i}{\lambda_i+2\mu_i} = 0 \,, \tag{2.17}$$

where n is the number of layers and i denotes the i-th layer. For two layers, as may be verified after direct calculation,

$$\begin{gathered}\lambda_1\mu_1\left(\lambda_1+2\mu_1\right)\left(\lambda_2+2\mu_2\right)+\lambda_2\mu_2\left(\lambda_1+2\mu_1\right)\left(\lambda_2+2\mu_2\right)= \\ \lambda_1\mu_2\left(\lambda_1+2\mu_1\right)\left(\lambda_2+2\mu_2\right)+\lambda_2\mu_1\left(\lambda_1+2\mu_1\right)\left(\lambda_2+2\mu_2\right) \,.\end{gathered} \tag{2.18}$$

From stability conditions, $\lambda + 2\mu \neq 0$, thus, after division,

$$\lambda_1\mu_1 + \lambda_2\mu_2 = \lambda_1\mu_2 + \lambda_2\mu_1 \,. \tag{2.19}$$

Hence, condition (2.16) is satisfied if $\lambda_1 = \lambda_2$ and/or if $\mu_1 = \mu_2$. As shown by Backus (1962), every stable, three-layered, isotropic medium is equivalent to n-layered isotropic medium. However, it is not true for every two-layered isotropic medium. Therefore, we consider a general, three-layered case. After laborious computations, we obtain

$$\begin{gathered}\lambda_1\lambda_2\mu_1+\lambda_1\lambda_3\mu_1+\lambda_1\lambda_2\mu_2+\lambda_2\lambda_3\mu_2+\lambda_1\lambda_3\mu_3+\lambda_2\lambda_3\mu_3+ \\ 2\lambda_1\mu_1\mu_2+2\lambda_2\mu_1\mu_2+2\lambda_1\mu_1\mu_3+2\lambda_3\mu_1\mu_3+2\lambda_2\mu_2\mu_3+2\lambda_3\mu_2\mu_3= \\ 2\lambda_2\lambda_3\mu_1+2\lambda_1\lambda_3\mu_2+2\lambda_1\lambda_2\mu_3+4\lambda_3\mu_1\mu_2+4\lambda_2\mu_1\mu_3+4\lambda_1\mu_2\mu_3 \,.\end{gathered} \tag{2.20}$$

For three-layered medium, condition (2.16) is satisfied if $\lambda_1 = \lambda_2 = \lambda_3$ and/or if $\mu_1 = \mu_2 = \mu_3$. Thus, for n-layered medium, the same condition is true if $\lambda = \mathrm{const}$ and/or if $\mu = \mathrm{const}$.

Let us define a new anisotropy parameter,

$$\varphi := \frac{C_{12}^{\overline{\mathrm{TI}}} - C_{13}^{\overline{\mathrm{TI}}}}{2C_{12}^{\overline{\mathrm{TI}}}}, \tag{2.21}$$

which, similarly to expressions (2.11)–(2.13), is equal to zero in the case of isotropy of an equivalent medium. However, as opposed to the Thomsen parameters, φ is equal to zero also in the case of constant λ in layers; since, as discussed above, $C_{12}^{\overline{\mathrm{TI}}} - C_{13}^{\overline{\mathrm{TI}}} = 0$ if $\lambda = \mathrm{const}$. The latter property might be particularly useful in the detection of variations of λ—thus, in possible detection of fluids. The choice of the denominator makes the parameter dimensionless and analogous in its form to the Thomsen parameters. Based on stability conditions, φ may have either a positive or negative value.

We can rewrite φ in terms of Lamé coefficients.

$$\varphi = \frac{\overline{\left(\frac{\lambda}{\lambda+2\mu}\right)}^2\,\overline{\left(\frac{1}{\lambda+2\mu}\right)}^{-1} + \overline{\left(\frac{2\lambda\mu}{\lambda+2\mu}\right)} - \overline{\left(\frac{\lambda}{\lambda+2\mu}\right)}\;\overline{\left(\frac{1}{\lambda+2\mu}\right)}^{-1}}{2\overline{\left(\frac{\lambda}{\lambda+2\mu}\right)}^2\,\overline{\left(\frac{1}{\lambda+2\mu}\right)}^{-1} + 2\overline{\left(\frac{2\lambda\mu}{\lambda+2\mu}\right)}} \tag{2.22}$$

and after short algebraic manipulations, we write

$$\varphi = \frac{1}{2} - \frac{1}{2}\left[\overline{\left(\frac{\lambda}{\lambda+2\mu}\right)} + \overline{\left(\frac{\lambda}{\lambda+2\mu}\right)}^{-1}\overline{\left(\frac{1}{\lambda+2\mu}\right)}\;\overline{\left(\frac{2\lambda\mu}{\lambda+2\mu}\right)}\right]^{-1}. \tag{2.23}$$

The above expression has probably the simplest form. Each term in the square brackets is dependent on both λ and μ. However, the first two terms seem to be more affected by λ.

Hence, we see that the magnitude of expression (2.23) depends significantly on variations of λ in layers. The great dependence on λ is even more visible if we consider two periodic layers of the same thickness. (For three periodic layers the result is more complicated, involves dozens of terms, and is less intuitive; thus, we do not invoke it in this paper). In such a case, we obtain

$$\varphi = \frac{(\lambda_1 - \lambda_2)(\mu_1 - \mu_2)}{2\left(2\lambda_1\lambda_2 + \lambda_1\mu_1 + \lambda_1\mu_2 + \lambda_2\mu_1 + \lambda_2\mu_2\right)} \tag{2.24}$$

and we notice that due to term $2\lambda_1\lambda_2$, the denominator is more influenced by λ than by μ. Parameters ϵ and δ seem to be less dependent on λ than φ is, since we get

$$\epsilon = \frac{(\mu_1 - \mu_2)\left(\lambda_1 - \lambda_2 + \mu_1 - \mu_2\right)}{2(\lambda_1 + 2\mu_1)(\lambda_2 + 2\mu_2)} \tag{2.25}$$

and

$$\delta = \frac{(\mu_1 - \mu_2)\left(\lambda_1\mu_2 - \lambda_2\mu_1\right)\left(2\lambda_1\lambda_2 + 3\lambda_1\mu_2 + 3\lambda_2\mu_1 + 4\mu_1\mu_2\right)}{2\left[\mu_1\left(\lambda_2 + \mu_2\right)\left(\lambda_1 + 2\mu_2\right) + \mu_2\left(\lambda_1 + \mu_1\right)\left(\lambda_2 + 2\mu_2\right)\right]\left(\lambda_1 + 2\mu_1\right)\left(\lambda_2 + 2\mu_2\right)}\,. \tag{2.26}$$

The numerators of expressions (2.25) and (2.26) seem to be strongly dependent on μ, in particular due to their first term, $(\mu_1 - \mu_2)$.

To have more insight into φ, let us express it in terms of the Thomsen parameters. To do so, we use the property of a TI medium, namely, $C_{12}^{\overline{\rm TI}} = C_{11}^{\overline{\rm TI}} - 2C_{66}^{\overline{\rm TI}}$. First, we extract $C_{11}^{\overline{\rm TI}}$, $C_{66}^{\overline{\rm TI}}$, and $C_{13}^{\overline{\rm TI}}$ from ϵ, γ, and δ, respectively,

$$\begin{gathered} C_{11}^{\overline{\rm TI}} = C_{33}^{\overline{\rm TI}} + 2C_{33}^{\overline{\rm TI}}\epsilon\,, \qquad C_{66}^{\overline{\rm TI}} = C_{44}^{\overline{\rm TI}} + 2C_{44}^{\overline{\rm TI}}\gamma\,, \qquad \text{and} \\ C_{13}^{\overline{\rm TI}} = -C_{44}^{\overline{\rm TI}} \pm \left[C_{44}^{2\,\overline{\rm TI}} - 2C_{33}^{\overline{\rm TI}}C_{44}^{\overline{\rm TI}}(1+\delta) + C_{33}^{2\,\overline{\rm TI}}(1+2\delta)\right]^{\frac{1}{2}}\,. \end{gathered} \tag{2.27}$$

If $\delta << 1$, which is usually the case in seismology, then

$$\begin{aligned} C_{13}^{\overline{\mathrm{TI}}} &\approx -C_{44}^{\overline{\mathrm{TI}}} \pm \left[\left(C_{44}^{\overline{\mathrm{TI}}} \right)^2 - 2C_{33}^{\overline{\mathrm{TI}}} C_{44}^{\overline{\mathrm{TI}}} (1+\delta) + \left(C_{33}^{\overline{\mathrm{TI}}} \right)^2 (1 + 2\delta + \delta^2) \right]^{\frac{1}{2}} \\ &= -C_{44}^{\overline{\mathrm{TI}}} \pm \left[C_{44}^{\overline{\mathrm{TI}}} - C_{33}^{\overline{\mathrm{TI}}} (1+\delta) \right] . \end{aligned} \tag{2.28}$$

Finally, we can express φ . If $C_{13}^{\overline{\mathrm{TI}}} \approx -C_{33}^{\overline{\mathrm{TI}}} (1+\delta)$, then $C_{13}^{\overline{\mathrm{TI}}}$ is negative and

$$\begin{aligned} \varphi &\approx \frac{C_{33}^{\overline{\mathrm{TI}}} - C_{44}^{\overline{\mathrm{TI}}} + 2C_{33}^{\overline{\mathrm{TI}}}\epsilon - 4C_{44}^{\overline{\mathrm{TI}}}\gamma + C_{33}^{\overline{\mathrm{TI}}}(1+\delta)}{2\left(C_{33}^{\overline{\mathrm{TI}}} - 2C_{44}^{\overline{\mathrm{TI}}} + 2C_{33}^{\overline{\mathrm{TI}}}\epsilon - 4C_{44}^{\overline{\mathrm{TI}}}\gamma \right)} \\ &= \frac{1}{2} + \frac{C_{33}^{\overline{\mathrm{TI}}}(1+\delta)}{2C_{33}^{\overline{\mathrm{TI}}}(1+2\epsilon) - 4C_{44}^{\overline{\mathrm{TI}}}(1+2\gamma)} . \end{aligned} \tag{2.29}$$

If we substitute, $g = V_{P0}^2 / V_{S0}^2$, where V_{P0} and V_{S0} are the vertical quasi P and S velocities,

$$\varphi \approx \frac{1}{2} + \frac{1+\delta}{2(1+2\epsilon) - 4g(1+2\gamma)} . \tag{2.30}$$

If $C_{13}^{\overline{\mathrm{TI}}} \approx -2C_{44}^{\overline{\mathrm{TI}}} + C_{33}^{\overline{\mathrm{TI}}} (1+\delta)$, then $C_{13}^{\overline{\mathrm{TI}}}$ is either negative or positive and

$$\varphi \approx \frac{1}{2} + \frac{1+\delta}{2(1+2\epsilon) - 4g(1+2\gamma)} + \frac{g - \delta - 1}{1 + 2\epsilon - 2g\,(1+2\gamma)} \tag{2.31}$$

is corrected by the third term.

We see that φ might be expressed in terms of three Thomsen parameters; thus, it is dependent on them. Mathematically, the introduction of φ as an additional anisotropy parameter is not reasonable since the Thomsen parameters already express all the independent TI coefficients. The justification might be gained while using φ in place of δ . Both parameters provide coefficient $C_{13}^{\overline{\mathrm{TI}}}$ that is furnished by neither ϵ nor γ . Physically, the usage of φ as an additional anisotropy parameter is justified; it is sensitive to constant or near-constant λ

in layers. Hence, it provides another physical property.

As shown in expressions (2.1)–(2.6), all five independent TI coefficients depend on variations of μ in layers. Also, Postma (1955) or Backus (1962) prove that constant μ in isotropic layers renders the equivalent medium to be isotropic. Therefore, φ and the Thomsen parameters depend highly on changes of μ. In equivalent media, no parameter shows the strength of anisotropy and is independent of these variations. In other words, φ, as demonstrated in expressions (2.30) and (2.31), is directly dependent on γ; which expresses the changes of μ in layers purely, namely,

$$\gamma = \frac{\overline{\mu} - \overline{\left(\frac{1}{\mu}\right)}^{-1}}{2\overline{\left(\frac{1}{\mu}\right)}^{-1}}\,. \tag{2.32}$$

Since ϵ and δ are affected by μ, they also depend on γ; although in an indirect manner.

2.3 Response of anisotropy parameters to changes of λ and μ

In this section, we analyse the relations among anisotropy parameters, φ, ϵ, and δ, in equivalent TI media. During our investigation, we verify the approach shown in Berryman et al. (1999) by checking if negative values of ϵ, or small positive values of ϵ and δ, correspond to large changes of λ in layers. Concurrently, we attempt to find the other indicators that might characterise the variation of the fluid content in layered Earth. By doing so, we improve the prior method.

We examine only the ranges of Lamé coefficients that are relevant to sandstones (brine sands, gas sands, and others). Based on works of Castagna and Smith (1994) and Wanniarachichi et al. (2017), the approximate ranges of these coefficients are $\lambda \in [-3\,,\,20]\,\mathrm{GPa}$ and $\mu \in [1\,,\,30]\,\mathrm{GPa}$, where GPa are gigapascals. However, taking into consideration that the values of λ that are close to zero might cause the issue within Backus averaging (Bos et al. (2018) and Kudela and Stanoev (2018)), we set the ranges to be $\lambda \in [3\,,\,20]\,\mathrm{GPa}$ and $\mu \in [1\,,\,30]\,\mathrm{GPa}$. These ranges might also correspond to shales and other sedimentary rocks.

We consider six types of variations of λ and μ. As a quantitative tool of these changes, we use their relative standard deviations (RSD),

$$
\begin{aligned}
RSD_\lambda &= \overline{\lambda}^{\,-1}\left(\frac{1}{n}\sum_{i=1}^{n}\left(\overline{\lambda}-\lambda_i\right)^2\right)^{\frac{1}{2}} \times 100\%\,, \quad \text{and} \\
RSD_\mu &= \overline{\mu}^{\,-1}\left(\frac{1}{n}\sum_{i=1}^{n}\left(\overline{\mu}-\mu_i\right)^2\right)^{\frac{1}{2}} \times 100\%\ ,
\end{aligned}
\tag{2.33}
$$

where n is the number of layers, $\overline{\lambda}$ and $\overline{\mu}$ are the arithmetic mean values of λ and μ in a stack of layers, and λ_i, μ_i, are the values for individual layers.

We divide this section into two parts. In Section 2.3.1, we consider the case of near-constant rigidity ($RSD_\mu < 2\,\%$), which is equivalent to near-constant μ in layers, or γ close to zero. In Section 2.3.2, we analyse the case of varying shear modulus, μ ($RSD_\mu > 2\,\%$). In each part, we examine three different variations of λ, namely, $RSD_\lambda < 2\,\%$, $RSD_\lambda \in (2\,,\,20)\%$, and $RSD_\lambda > 20\,\%$. Table 2.1 illustrates the aforementioned division of this section. Throughout the paper, the notion "near-constant rigidity" or "near-constant μ" is denoted by $RSD_\mu < 2\,\%$, whereas $RSD_\mu > 2\,\%$ refers to "varying μ". Similarly, "near-constant λ" is denoted by $RSD_\lambda < 2\,\%$, whereas $RSD_\lambda > 2\,\%$ refers to "varying λ". Additionally, "moderately varying λ" refers to $RSD_\lambda \in (2\,,\,20)\%$, and "strongly varying λ" refers to $RSD_\lambda > 20\,\%$.

Table 2.1: Plan of examination of six different variations of Lamé coefficients

	$RSD_\lambda < 2\,\%$	$RSD_\lambda \in (2\,,\,20)\%$	$RSD_\lambda > 2\,\%$
$RSD_\mu < 2\,\%$	Section 2.3.1	Section 2.3.1	Section 2.3.1
$RSD_\mu > 2\,\%$	Section 2.3.2	Section 2.3.2	Section 2.3.2

2.3.1 Near-constant rigidity

Let us perform MC simulations to obtain examples of equivalent TI media and to compute their respective φ, ϵ, and δ. We receive randomly sampled $s = 1000$ examples of TI media, equivalent to $n = 3$ isotropic layers of sandstones having the Lamé coefficients within ranges mentioned in the previous section. The choice of the set of examples is restricted by $RSD_\mu < 2\,\%$. Thus, we consider only near-constant μ in layers, which—in our case—corresponds to $\gamma < 1.4 \times 10^{-4}$.

$RSD_\lambda < 2\,\%$

Herein, apart from $RSD_\mu < 2\,\%$, we include an additional restriction of $RSD_\lambda < 2\,\%$ to the simulations. The anisotropy parameters for 1000 examples of equivalent TI media are shown in a form of cross-plots in Figures 2.1a and 2.1b.

In $5.5\,\%$ of examples, $\varphi > \epsilon$; this result is expected due to near-constant λ that strongly diminishes the values of φ. In $38\,\%$ of cases, $|\varphi| > |\epsilon|$; φ is much more likely to have negative values than ϵ is. In $8\,\%$ of examples, ϵ is negative; this is unexpected since—according to Berryman et al. (1999)—negative ϵ is characteristic for variations of λ. In $11\,\%$ of cases, δ is positive, hence, there are some examples that present small positive ϵ and small positive δ; again—in view of Berryman et al. (1999) method—this is an unexpected result. Thus, viewing negative values of ϵ, or small positive values of ϵ and δ, as possible fluid indicators might lead to inaccuracy. We notice that Figure 2.1b, clearly presents

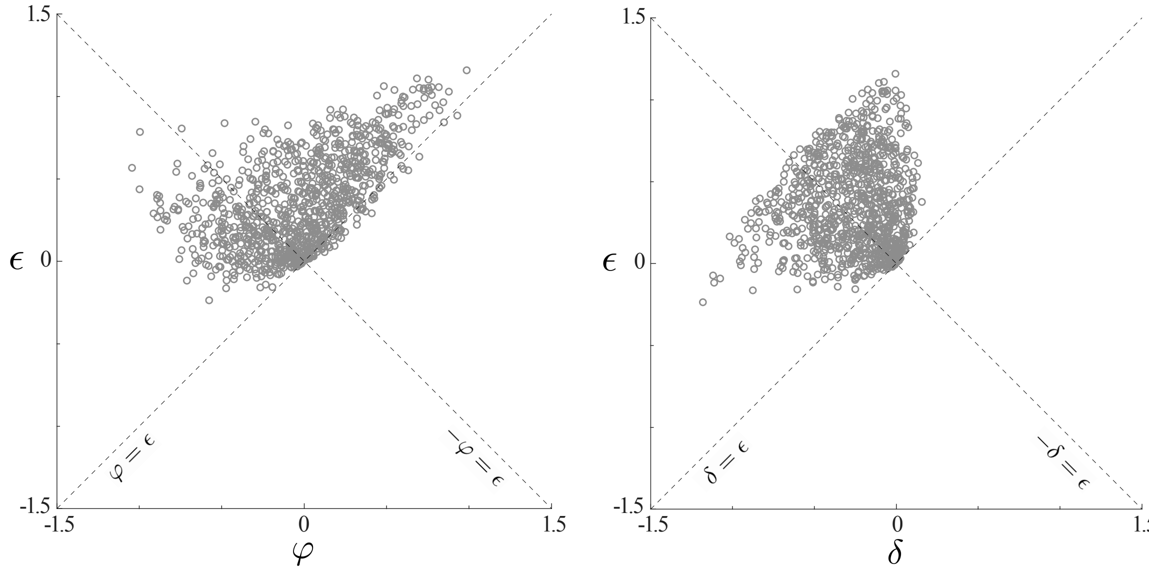

(a) φ versus ϵ **(b)** δ versus ϵ

Figure 2.1: φ, ϵ, and δ for 1000 examples of equivalent TI media restricted by $RSD_\mu < 2\,\%$ and $RSD_\lambda < 2\,\%$. Values are scaled by a factor of 10^4.

well-known relation for equivalent media, $\delta < \epsilon$ (Berryman, 1979).

In every example the absolute values of anisotropy parameters are smaller than 1.5×10^{-4}. In only one out of 1000 cases $|\varphi|$ is larger than 10^{-4}, whereas it occurs more frequently for $|\epsilon|$ or $|\delta|$.

$RSD_\lambda \in (2\,,\,20)\%$

Herein, we consider examples of moderately varying λ. The anisotropy parameters for 1000 examples of equivalent TI media are shown in a form of cross-plots in Figures 2.2a and 2.2b.

In $43.7\,\%$ of cases, $\varphi > \epsilon$; thus, the growth of variations of λ, significantly increases the amount of examples that satisfy this relation. In $88.9\,\%$ of examples, $|\varphi| > |\epsilon|$; this indicator has been even more influenced by the increase of variations of λ, as compared to

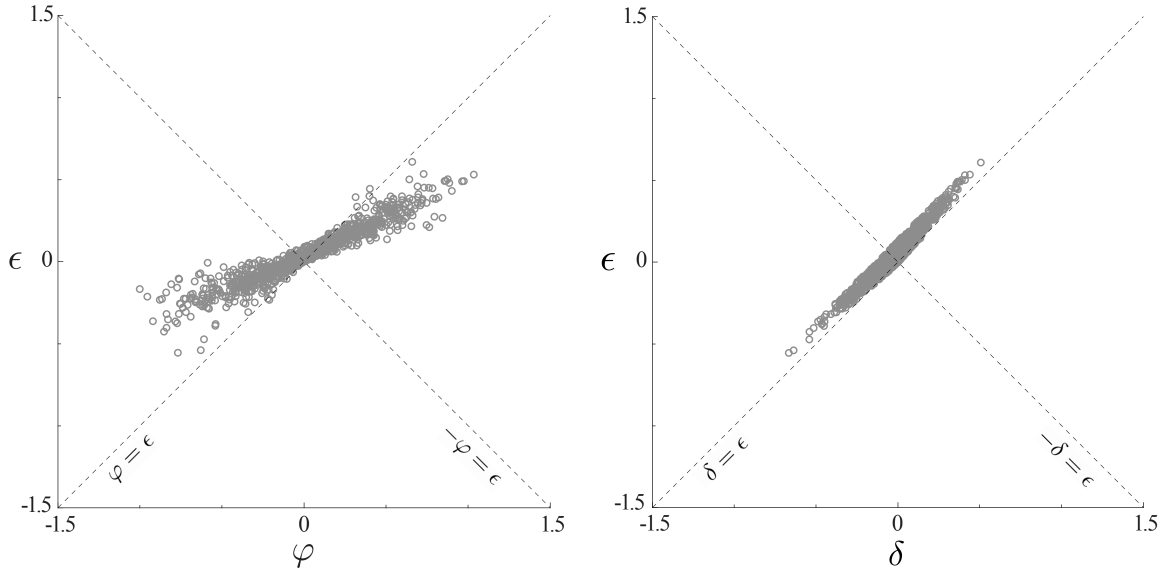

(a) φ versus ϵ

(b) δ versus ϵ

Figure 2.2: φ, ϵ, and δ for 1000 examples of equivalent TI media restricted by $RSD_\mu < 2\,\%$ and $RSD_\lambda \in (2\,,\,20)\%$. Values are scaled by a factor of 10^3.

$\varphi \geq \epsilon$. In $42.4\,\%$ of cases, ϵ is negative; also in $47.2\,\%$ of examples δ is positive. Taking into account that always $\delta < \epsilon$, it means that in $89.6\,\%$ of examples either ϵ is negative or δ is positive, which—in view of Berryman et al. (1999) approach—is a desired result. In other words, in $10.4\,\%$ of cases ϵ is positive and δ is negative, which—according to Berryman et al. (1999)—is characteristic for weak variations of λ. The aforementioned case might correspond to near-constant μ and to variations of λ with $RSD_\lambda < 5\,\%$.

The shape of the set of data points in Figure 2.2a is elongated more in the horizontal direction as opposed to the vertical one, which means that the values of φ grow more significantly due to the the increased variations of λ than the values of ϵ. In addition, in Figure 2.2b we notice that ϵ and δ have very similar values. Based on that figure, we expect that φ is also more sensitive to variations of λ than δ is.

$RSD_\lambda > 20\,\%$

Herein, we consider examples of strongly varying λ. The anisotropy parameters for 1000 examples of equivalent TI media are shown in a form of cross-plots in Figures 2.3a and 2.3b.

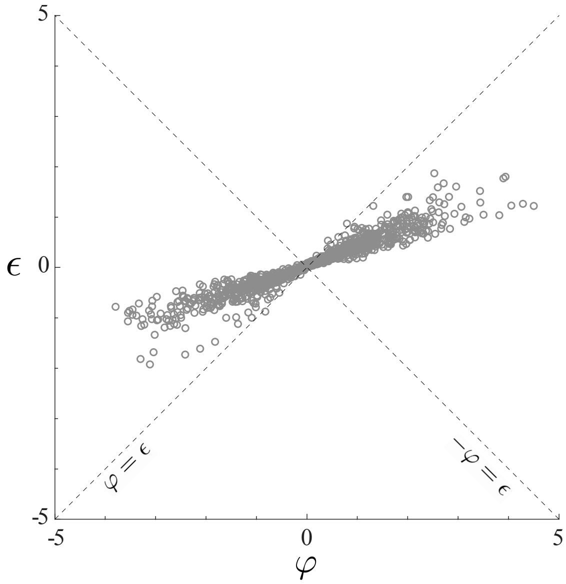

(a) φ versus ϵ

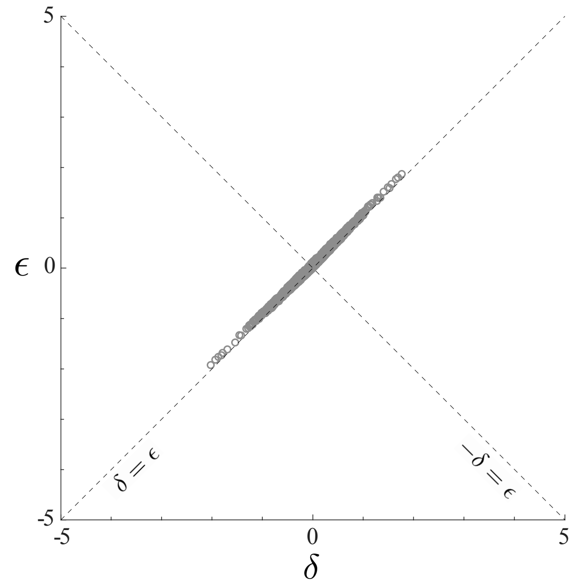

(b) δ versus ϵ

Figure 2.3: φ, ϵ, and δ for 1000 examples of equivalent TI media restricted by $RSD_\mu < 2\,\%$ and $RSD_\lambda > 20\,\%$. Values are scaled by a factor of 10^3.

In $50.9\,\%$ of cases, $\varphi > \epsilon$; we notice that the further increase of the strength of variations of λ does not significantly affect this indicator. In $97.6\,\%$ of examples, $|\varphi| > |\epsilon|$; thus, there is a large probability that if we encounter $|\varphi| \leq |\epsilon|$, then the variations of λ are not strong. In only $3.3\,\%$ of cases, ϵ is positive and δ is negative, which means that in a great majority of cases Berryman et al. (1999) approach is correct.

Figure 2.3a confirms our statement that φ is more sensitive to variations of λ than ϵ or δ. In Figure 2.3b, values of ϵ and δ are again very similar.

2.3.2 Varying rigidity

In a similar manner to Section 2.3.1, we receive 1000 randomly sampled TI media that are equivalent to $n = 3$ isotropic layers, corresponding to sandstones. In this section, the choice of the set of examples is restricted by $RSD_\mu > 2\,\%$. Hence, we consider only varying μ in layers, which—in our case—corresponds to $\gamma > 1.4 \times 10^{-4}$.

$RSD_\lambda < 2\,\%$

Herein, apart from $RSD_\mu > 2\,\%$, we include an additional restriction of $RSD_\lambda < 2\,\%$ to the simulations. The anisotropy parameters for 1000 examples of equivalent TI media are shown in a form of cross-plots in Figures 2.4a and 2.4b.

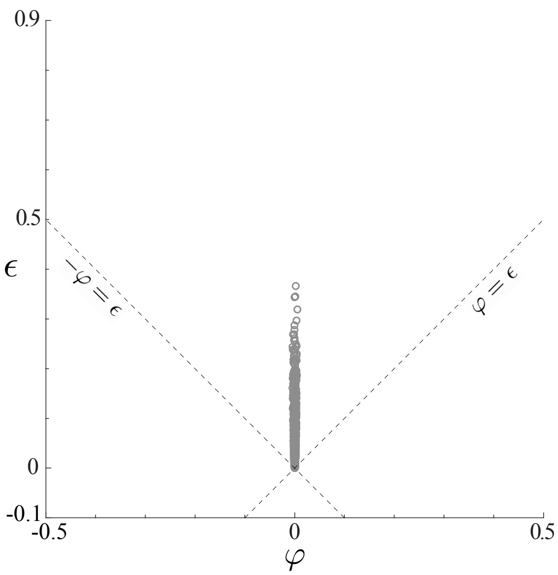

(a) φ versus ϵ

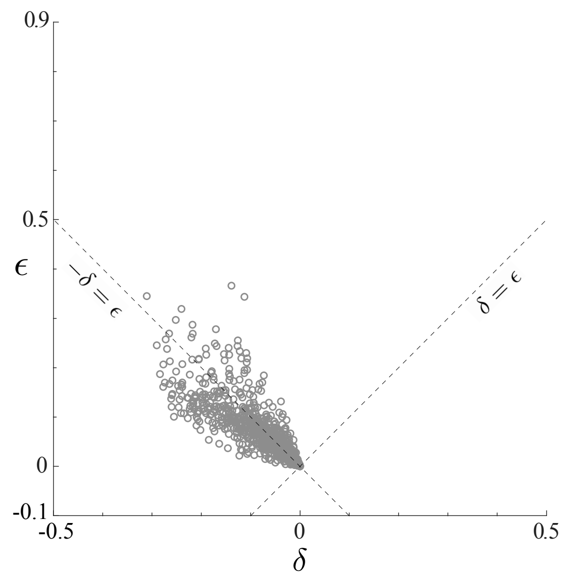

(b) δ versus ϵ

Figure 2.4: φ, ϵ, and δ for 1000 examples of equivalent TI media restricted by $RSD_\mu > 2\,\%$ and $RSD_\lambda < 2\,\%$

None of examples present either $\varphi > \epsilon$, $|\varphi| > |\epsilon|$, $\epsilon < 0$, or $\delta > 0$. If we compare these results to the ones from Figures 2.1a and 2.1b, we notice that the change of the strength of variations of μ has a significant impact on the fluid indicators. That change, however, does not affect φ as much as it affects ϵ and δ, since φ still has relatively small values. Again, small range of φ is caused by near-constant λ in layers. Only in one example is $|\varphi| > 5 \times 10^{-3}$.

$RSD_\lambda \in (2\,,\,20)\%$

Herein, we consider examples of moderately varying λ. The anisotropy parameters for 1000 examples of equivalent TI media are shown in a form of cross-plots in Figures 2.5a and 2.5b.

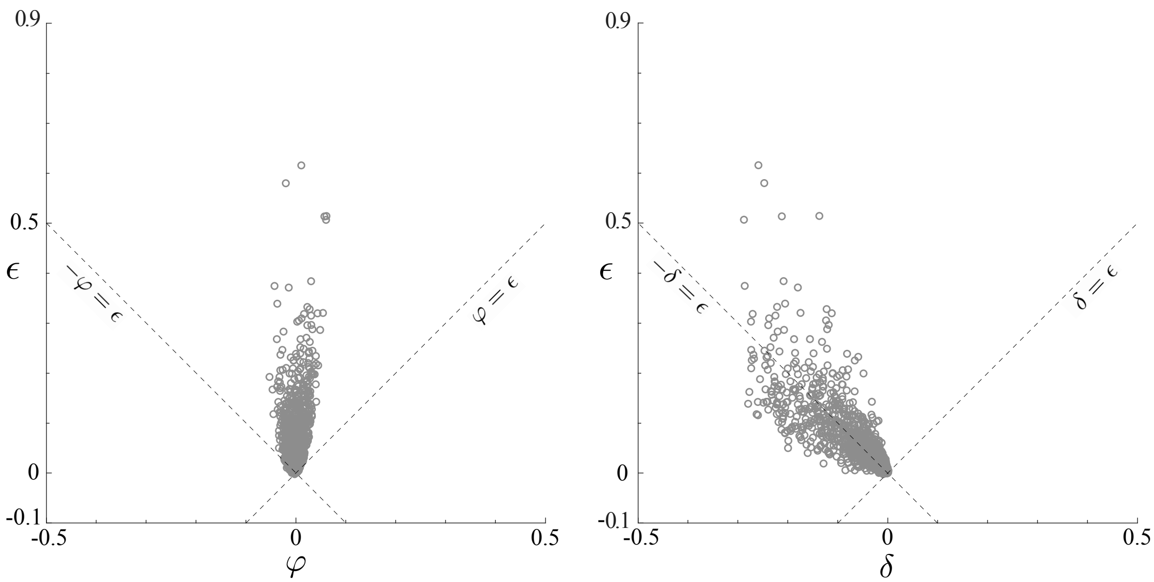

(a) φ versus ϵ **(b)** δ versus ϵ

Figure 2.5: φ, ϵ, and δ for 1000 examples of equivalent TI media restricted by $RSD_\mu > 2\,\%$ and $RSD_\lambda \in (2\,,\,20)\%$

All three indicators, namely, $\varphi > \epsilon$, $\epsilon < 0$, and $\delta > 0$, occur very rarely; none of them is presented in more than 13 examples. In $6.1\,\%$ of cases, $|\varphi| > |\epsilon|$; thus this fluid indicator is slightly more sensitive on variations of λ than the aforementioned three ones. If we compare Figures 2.4b and 2.5b, we notice that ϵ or δ, for a great majority of examples, are within similar ranges. However, if we look at Figures 2.4a and 2.5a, we find out that the set of points has a much wider shape in the latter one. In other words, the absolute value of φ is grately affected by the strength of variations of λ. As a result of that, in $64.7\,\%$ of cases $|\varphi| > 5 \times 10^{-3}$.

$RSD_\lambda > 20\,\%$

Herein, we consider examples of strongly varying λ. The anisotropy parameters for 1000 examples of equivalent TI media are shown in a form of cross-plots in Figures 2.6a and 2.6b.

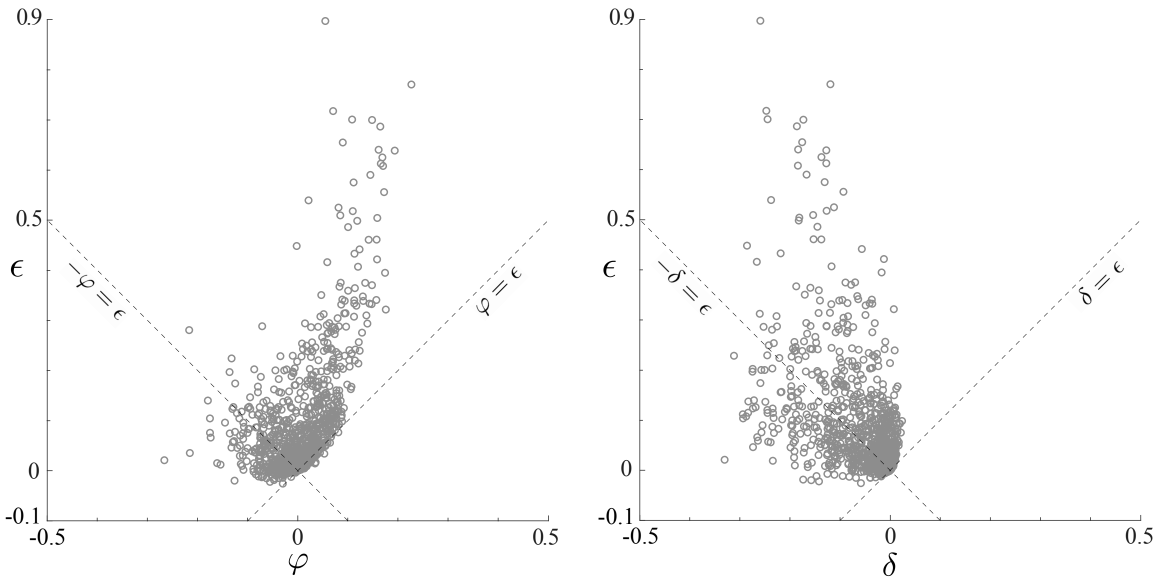

(a) φ versus ϵ

(b) δ versus ϵ

Figure 2.6: φ, ϵ, and δ for 1000 examples of equivalent TI media restricted by $RSD_\mu > 2\,\%$ and $RSD_\lambda > 20\,\%$

In $6.8\,\%$ of cases, $\varphi > \epsilon$; we notice that the further increase of the strength of variations of λ does not significantly affect this indicator, which still remains unreliable. In $34.3\,\%$ of examples, $|\varphi| > |\epsilon|$, since large negative values of φ often correspond to small positive ϵ. In only $13.8\,\%$ of cases, ϵ and δ are both small positive. Further, ϵ is negative in only

$6.8\,\%$ of examples. The low percentage of occurrence of the two above indicators renders the Berryman et al. (1999) approach unreliable in the varying rigidity case.

In $90.5\,\%$ of examples, $|\varphi| > 5\times10^{-3}$, which means that $|\varphi|$ is sensitive on further increases of the strength of variations of λ. We notice that large values of ϵ are characteristic only for strongly or moderately varying λ, however, such cases occur rarely.

2.4 Summary of results

In this section, we summarise the results presented in Section 2.3. Additionally, we consider certain fluid indicators that have not been taken into account therein. Moreover, we present Table 2.3 that consists of computed ranges of anisotropy parameters that correspond to six different cases of variations of Lamé coefficients.

Table 2.2 illustrates the indicators that show the change of variations of λ in layers. Smaller values in the $RSD_\lambda < 2\,\%$ column along with larger values in the $RSD_\lambda \in (2\,,\,20)\,\%$ and $RSD_\lambda > 20\,\%$ columns, indicate greater sensitivity to variations of λ; thus, the efficiency of these fluid indicators. Herein, in addition to Section 2.3, we consider $\varphi < \delta$ and $|\varphi| > |\delta|$, which present similar results to the ones of $\varphi > \epsilon$ and $|\varphi| > |\epsilon|$, respectively. We explain these similarities by using the fact that in every case of variations examined by us, the proportion between $|\delta| < |\epsilon|$ and $|\delta| > |\epsilon|$, and between $\varphi < 0$ and $\varphi > 0$, is almost one to one.

We have exhibited the results for relations

$$|\epsilon|\vee|\delta| > 10^{-4}\,, \quad |\epsilon|\vee|\delta| > 1.5\times10^{-4}\,, \quad |\varphi|\vee|\epsilon|\vee|\delta| > 10^{-4}\,, \quad \text{and} \quad |\varphi| > 10^{-4}\,, \tag{2.34}$$

where $\vee$ is the logical symbol “or”. These results have been exposed to show that—in

Table 2.2: Potential fluid indicators and its occurrence in 1000 examples of equivalent TI media (in %). For each case of variations of μ, the occurrence of the most efficient indicator is highlighted in bold.

	$RSD_\mu < 2\,\%$			$RSD_\mu > 2\,\%$		
	$RSD_\lambda < 2\,\%$	$RSD_\lambda \in (2\,,\,20)\,\%$	$RSD_\lambda > 20\,\%$	$RSD_\lambda < 2\,\%$	$RSD_\lambda \in (2\,,\,20)\,\%$	$RSD_\lambda > 20\,\%$
$\varphi > \epsilon$	5.50	43.7	50.9	0.00	1.00	6.80
$\varphi < \delta$	14.1	42.6	46.9	0.00	1.30	12.9
$\|\varphi\| > \|\epsilon\|$	38.0	88.9	97.6	0.00	6.10	34.3
$\|\varphi\| > \|\delta\|$	46.2	92.6	98.4	0.30	9.20	45.7
$\epsilon < 0$	8.00	42.4	45.6	0.00	0.50	6.80
$\delta > 0$	11.0	47.2	51.1	0.00	1.30	13.8
$\|\epsilon\| \vee \|\delta\| > 10^{-4}$	2.10	63.8	88.8	99.8	100	100
$\|\epsilon\| \vee \|\delta\| > 1.5 \times 10^{-4}$	0.00	46.8	82.7	99.8	100	100
$\|\varphi\| \vee \|\epsilon\| \vee \|\delta\| > 10^{-4}$	2.20	76.7	94.6	99.8	100	100
$\|\varphi\| > 10^{-4}$	**0.10**	**75.8**	**94.4**	91.1	99.5	100
$\|\varphi\| > 5 \times 10^{-3}$	0.00	0.00	0.20	**0.10**	**64.7**	**90.5**

near-constant rigidity case—the absolute values of φ are more sensitive to variations of λ than the absolute values of ϵ or δ together. Also, it is clear that consideration of $|\epsilon|$ or $|\delta|$ as additional indicators to $|\varphi|$ gives almost no improvement in possible detection of fluids. In the case of varying rigidity, the absolute values of ϵ or δ are decidedly less sensitive than $|\varphi|$. Therefore, they are not presented in Table 2.2.

In the case of $RSD_\mu < 2\,\%$, the most-efficient indicator that suggests variations of λ is $|\varphi| > 10^{-4}$. Additionally, we might try to check relations $|\varphi| > |\delta|$, $|\varphi| > |\epsilon|$, $\varphi > \epsilon$, $\varphi < \delta$, $\epsilon < 0$, and $\delta > 0$. Unfortunately, they are not very reliable since they also might be satisfied in the case of near-constant λ. Conversely, if we encounter $|\varphi| < |\delta|$ or $|\varphi| < |\epsilon|$, there is a very large probability that we have detected the case of near-constant λ in layers. Moreover, taking into consideration that $\delta < \epsilon$ always holds, another relations strongly suggesting near-constant λ are $(\varphi < \epsilon) \vee (\varphi > \delta)$ and $(\epsilon > 0) \vee (\delta < 0)$.

In the case of $RSD_\mu > 2\,\%$, the most efficient indicator is $|\varphi| > 5 \times 10^{-3}$. Its reliability might be improved by considering the additional indicators, such as $|\varphi| > |\delta|$ or $|\varphi| > |\epsilon|$. Also, we could take into account relations $(\varphi > \epsilon) \vee (\varphi < \delta)$ and $(\epsilon < 0) \vee (\delta > 0)$. If one of these relations is satisfied then there is a very large probability that there is moderately or strongly varying λ in layers.

Table 2.3 shows the ranges and dominants of the anisotropy parameters corresponding to 1000 examples of equivalent TI media obtained by the MC method. To estimate the most frequent values of φ, ϵ, and δ, we choose the highest bin—out of 25 bins—of their distributions and compute the mean value within that bin. The content of this table helps to display the relations among the anisotropy parameters and may be treated as supplement information to the cross-plots from the previous section.

Table 2.3: Dominants and ranges of anisotropy parameters for 1000 examples of equivalent TI media

	$RSD_\mu < 2\,\%$					
	$RSD_\lambda < 2\,\%$		$RSD_\lambda \in (2\,,\,20)\,\%$		$RSD_\lambda > 20\,\%$	
	Dominant $\left[\times 10^{-5}\right]$	Range $\left[\times 10^{-3}\right]$	Dominant $\left[\times 10^{-5}\right]$	Range $\left[\times 10^{-3}\right]$	Dominant $\left[\times 10^{-5}\right]$	Range $\left[\times 10^{-3}\right]$
φ	0.259	$(-0.105\,,\,0.099)$	0.313	$(-1.001\,,\,1.034)$	1.339	$(-5.384\,,\,4.499)$
ϵ	1.784	$(-0.024\,,\,0.116)$	-2.004	$(-0.555\,,\,0.608)$	-21.48	$(-1.926\,,\,1.868)$
δ	-0.737	$(-0.118\,,\,0.016)$	1.587	$(-0.667\,,\,0.506)$	15.02	$(-2.027\,,\,1.763)$
	$RSD_\mu > 2\,\%$					
	$RSD_\lambda < 2\,\%$		$RSD_\lambda \in (2\,,\,20)\,\%$		$RSD_\lambda > 20\,\%$	
	Dominant $\left[\times 10^{-3}\right]$	Range $\left[\times 10^{-3}\right]$	Dominant $\left[\times 10^{-3}\right]$	Range $\left[\times 10^{-3}\right]$	Dominant $\left[\times 10^{-3}\right]$	Range $\left[\times 10^{-3}\right]$
φ	-0.064	$(-4.626\,,\,5.252)$	-1.878	$(-53.06\,,\,61.08)$	-0.985	$(-266.3\,,\,226.6)$
ϵ	6.566	$(0.060\,,\,365.9)$	18.06	$(-2.252\,,\,615.6)$	24.57	$(-25.78\,,\,897.2)$
δ	-5.398	$(-310.9\,,\,-0.040)$	-3.701	$(-288.1\,,\,1.144)$	1.973	$(-330.7\,,\,23.45)$

Comparing the results shown in Table 2.3 for both near-constant rigidity and varying rigidity case, we notice that the values of φ, ϵ, and δ strongly depend on the strength of variations of μ in layers. That dependence is reflected in the relations among these anisotropy parameters in Table 2.2. In other words, there is no fluid indicator that would be of similar reliability in both $RSD_\mu < 2\,\%$ and $RSD_\mu > 2\,\%$ cases. To detect the change of the fluid content, we should consider different indicators for different variations of μ in layers.

Due to the aforementioned strong dependence of fluid indicators on changes of μ in layers, let us consider more specific ranges of these variations. We express them in terms of γ, which, as shown in expression (2.32), depends solely on μ. The advantage of such representation is that in the inverse problems, in which we know only the equivalent TI elasticity coefficients, we can compute γ, whereas μ remains unknown. In Table 2.4, we consider the most efficient indicator, $|\varphi|$. We show how its various values respond to different ranges of γ and variations of λ in layers.

Hence, if we have elasticity coefficients, $C_{12}^{\overline{\rm TI}}$, $C_{13}^{\overline{\rm TI}}$, $C_{44}^{\overline{\rm TI}}$, $C_{66}^{\overline{\rm TI}}$, and we use Table 2.4, we can quite precisely predict the variations of λ; thus, possible change of fluid content. The advantage of $|\varphi|$ over ϵ and δ, apart from being more efficient as discussed above, is that combination $|\varphi|$ and γ requires the knowledge of four elasticity coefficients, whereas ϵ, δ, and γ need five of them.

2.5 Discussion

We have examined various relations among the anisotropy parameters of their respective equivalent TI media sampled using Monte Carlo method. The aforementioned media correspond to layered sandstones and other layered sedimentary rocks.

Table 2.4: Values of $|\varphi|$ and their occurrence in 1000 examples of equivalent TI media (in %). For each range of γ, the occurrence of the most efficient indicator is highlighted in bold.

		$\|\varphi\| > 10^{-4}$	$\|\varphi\| > 5 \cdot 10^{-4}$	$\|\varphi\| > 10^{-3}$	$\|\varphi\| > 5 \cdot 10^{-3}$	$\|\varphi\| > 10^{-2}$
$\gamma < 10^{-4}$	$RSD_\lambda < 2\,\%$	**0.0**	0.0	0.0	0.0	0.0
	$RSD_\lambda \in (2\,\%\,,\,20\,\%)$	**73.6**	11.3	0.0	0.0	0.0
	$RSD_\lambda > 20\,\%$	**93.6**	68.1	37.2	0.0	0.0
$\gamma \in [10^{-4}\,,\,5 \cdot 10^{-4})$	$RSD_\lambda < 2\,\%$	18.8	**0.0**	0.0	0.0	0.0
	$RSD_\lambda \in (2\,\%\,,\,20\,\%)$	89.8	**50.4**	17.4	0.0	0.0
	$RSD_\lambda > 20\,\%$	98.6	**89.4**	78.7	7.9	0.0
$\gamma \in [5 \cdot 10^{-4}\,,\,10^{-3})$	$RSD_\lambda < 2\,\%$	44.3	**0.0**	0.0	0.0	0.0
	$RSD_\lambda \in (2\,\%\,,\,20\,\%)$	94.4	**70.6**	43.8	0.0	0.0
	$RSD_\lambda > 20\,\%$	98.4	**94.3**	87.8	31.6	1.7
$\gamma \in [10^{-3}\,,\,5 \cdot 10^{-3})$	$RSD_\lambda < 2\,\%$	70.4	0.9	**0.0**	0.0	0.0
	$RSD_\lambda \in (2\,\%\,,\,20\,\%)$	96.9	83.3	**66.8**	1.5	0.0
	$RSD_\lambda > 20\,\%$	99.0	96.5	**93.3**	62.3	27.8
$\gamma \in [5 \cdot 10^{-3}\,,\,10^{-2})$	$RSD_\lambda < 2\,\%$	81.1	16.6	**0.0**	0.0	0.0
	$RSD_\lambda \in (2\,\%\,,\,20\,\%)$	98.1	91.8	**83.1**	17.6	0.1
	$RSD_\lambda > 20\,\%$	99.5	98.4	**95.8**	79.7	52.0
$\gamma \geq 10^{-2}$	$RSD_\lambda < 2\,\%$	93.4	69.9	47.5	**0.2**	0.0
	$RSD_\lambda \in (2\,\%\,,\,20\,\%)$	99.7	97.5	95.0	**72.9**	49.4
	$RSD_\lambda > 20\,\%$	99.9	99.7	99.1	**94.7**	89.7

In our work, we have been particularly focused on the analysis of the dependence of values and relations among φ , ϵ , and δ with respect to variations of Lamé coefficient λ . Parameter φ seems to be the most sensitive to these changes; hence, its consideration might be useful in fluid detection in layered Earth. If $\gamma < 10^{-4}$, then we propose to verify that $|\varphi| > 10^{-4}$. If $\gamma \in [10^{-4}\,,\,10^{-3})$, $\gamma \in [10^{-3}\,,\,10^{-2})$, or if $\gamma \geq 10^{-2}$, then we encourage to verify that $|\varphi| > 5 \times 10^{-4}$, $|\varphi| > 10^{-3}$, $|\varphi| > 5 \times 10^{-3}$, respectively. In the case of satisfied relations—in sedimentary rocks—the change of fluid content is very probable.

To have better accuracy in detecting fluids, we suggest taking into account additional indicators discussed in Section 2.4. However, it is important to emphasise that all the examined fluid indicators greatly depend on variations of μ , which—in equivalent TI media—can be expressed as the dependance on γ .

Additionally, we have shown that viewing negative values of ϵ or small positive values of ϵ and δ as fluid indicators might lead to inaccuracy. Hence, the approach shown in Berryman et al. (1999) seems to be unreliable.

In general, the variations of λ strongly suggest the change of fluid content in layers for which λ—in the no-fluid case—is very similar. Thus, the possibility of distinguishing between dry and fluid saturated rocks appears to be reliable within the same rock formation, *ceteris paribus*. In other words, our approach seems to be more useful in the case of near-constant rigidity. In the case of varying μ , there is a chance that the variations of λ are caused by different elasticity properties of different rocks, instead of the change of fluid content.

The presented fluid indicators may be useful, for instance, in inverse problems, where we only know the elasticity coefficients of equivalent TI media, and we want to estimate the variations of λ . In forward problems, they may provide—based on well-log data—

insightful information on fluids, which could be a valuable reference to amplitude-versus-offset (AVO) analysis.

We expect to examine the fluid indicators in the real data case. They could be acquired from equivalent TI media obtained from well-log measurements. In turn, these indicators might be related to seismic data, in particular, the aforementioned AVO analysis.

Acknowledgments

We wish to acknowledge consultations with supervisors Michael A. Slawinski and Tomasz Danek. We thank Theodore Stanoev for the editorial work along with fruitful discussions. Also, we wish to thank Associate Editor, Yuriy Ivanov, and dear Reviewers for their insightful comments. This research was performed in the context of The Geomechanics Project supported by Husky Energy. Also, this research is partially supported by the Natural Sciences and Engineering Research Council of Canada, grant 202259. The author has no conflict of interest to declare.

2.6 References

Adamus, F. P., Slawinski, M. A., and Stanoev, T. (2018). "On effects of inhomogeneity on anisotropy in Backus average". *arXiv*, 1802.04075 [physics.geo-ph].

Backus, G. E. (1962). "Long-Wave Elastic Anisotropy Produced by Horizontal Layering". *J. Geophys. Res.* 67 (11), 4427–4440.

Berryman, J. G. (1979). "Long-wave elastic anisotropy in transversely isotropic media". *Geophysics*, 44 (5), 896–917.

Berryman, J. G., Grechka, V. Y., and Berge, P. A. (1999). "Analysis of Thomsen parameters for finely layered VTI media". *Geophysical Prospecting*, 47 (6), 959–978.

Bos, L., Dalton, D. R., Slawinski, M. A., and Stanoev, T. (2017). "On Backus average for generally anisotropic layers". *Journal of Elasticity*, 127 (2), 179–196.

Bos, L., Danek, T., Slawinski, M. A., and Stanoev, T. (2018). "Statistical and numerical considerations of Backus-average product approximation". *Journal of Elasticity*, 132 (1), 141–159.

Castagna, J. P. and Smith, S. W. (1994). "Comparison of AVO indicators: A modeling study". *Geophysics*, 59 (12), 1849–1855.

Gassmann, F. (1951). "Über die Elastizität poröser Medien". *Vierteljahrsschrift der Naturforschenden Gesellschafy in Zurich*, 96 (1), 1–23.

Kudela, I. and Stanoev, T. (2018). "On possibile issues of Backus average". *arXiv*, 1804.01917 [physics.geo-ph].

Kumar, D. (2013). "Applying Backus averaging for deriving seismic anisotropy of a long-wavelength equivalent medium from well-log data". *J. Geophys. Eng.* 10 (5), 1–15.

Postma, G. W. (1955). "Wave Propagation in a Stratified Medium". *Geophysics*, 20 (4), 780–806.

Schoenberg, M. and Muir, F. (1989). "A calculus for finely layered anisotropic media". *Geophysics*, 54 (5), 581–589.

Slawinski, M. A. (2015). *Waves and rays in elastic continua*. 3rd edn. World Scientific.

Thomsen, L. (1986). "Weak elastic anisotropy". *Geophysics*, 51 (10), 1954–1966.

Wanniarachichi, W. A. M., Ranjith, P. G., Perera, M. S. A., Rathnaweera, T. D., Lyu, Q., and Mahanta, B. (2017). "Assessment of dynamic material properties of intact rocks using seismic wave attenuation: an experimental study". *R. Soc. Open Sci.* 4 (10), 170896.

Post-publication comments

In the Introduction of this paper, we mention that the φ method is not valid for layers that exhibit lower symmetries than the isotropic one. Upon presenting this method at the EAGE 2020 Annual Conference, I got the question from Benjamin Roure regarding the applicability of the technique to the TI layers with a vertical symmetry axis (VTI). It is true that the method was designed to detect large variations of λ in the isotropic layers. However, it is to be expected that the method can be still applicable if the intrinsic anisotropy of the layers is very weak—the layers could be described as isotropic ones with negligible anisotropic correction terms. We can presume that the φ method is irrelevant in case of strong anisotropy of the layers. Nevertheless, φ has an interesting quality also in the case of VTI constituents. It equals to zero if both C_{12} and C_{13} are constant in layers. This is a natural extension of the isotropic case since for isotropy φ equals to zero for constant $\lambda = C_{12} = C_{13}$.

Note that, in this paper, we do not assume density-scaled parameters; the stiffnesses have units of stress rather than velocity squared. Thus, in Section 2.2.1, the formula for the average mass density of the equivalent medium, ρ^{eq}, should be stated. Specifically, $\rho^{\mathrm{eq}} = \overline{\rho_i}$, where the overbar stands for the weighted average of a density varying in layers.

In Section 2.2.2, we discuss the stability conditions for an isotropic and TI elasticity tensor. It is important to clarify that these conditions require the matrix representation of the elasticity tensor—not the tensor itself—to be positive semi-definite.

In Section 2.2.4, we prove that the isotropic condition, $C_{12}^{\overline{\mathrm{TI}}} = C_{13}^{\overline{\mathrm{TI}}}$, is satisfied if $\lambda = \mathrm{const}$ and/or $\mu = \mathrm{const}$ in layers. First, we show the proof for a two-layered periodic medium. Subsequently, we consider a three-layered material, which makes the proof valid for n-layers; since, as stated by Backus (1962), any stable HTI[‡] material which can be modeled for long waves by a stable, isotropic, layered medium can be modeled by a stack of isotropic stable, homogeneous (ISH) layers of just three different types.

However, as noticed by Dr. Mikhail Kotchetov, we can omit the two or three-layered case and consider n-layered medium immediately. Using

$$\frac{1}{n}\left(\sum_{i=1}^{n}\frac{\lambda_i}{\lambda_i+2\mu_i}\right)-1=\frac{1}{n}\sum_{i=1}^{n}\frac{-2\mu_i}{\lambda_i+2\mu_i} \tag{2.35}$$

we can rewrite expression (2.17) to get

$$\left(\sum_{i=1}^{n}\frac{\lambda_i}{\lambda_i+2\mu_i}\right)\left(\sum_{i=1}^{n}\frac{\mu_i}{\lambda_i+2\mu_i}\right)=\left(\sum_{i=1}^{n}\frac{1}{\lambda_i+2\mu_i}\right)\left(\sum_{i=1}^{n}\frac{\lambda_i\mu_i}{\lambda_i+2\mu_i}\right). \tag{2.36}$$

If $\lambda_i=\lambda$ for all i, then λ can be factored out from the first sum and moved to the second. Similarly, if $\mu_i=\mu$ for all i, then μ can be factored out from the second sum and moved to the first, which completes the proof. Further, on page 21, we state that—based on stability conditions—φ is allowed to have negative or positive values. However, we did not mention about the specific feasible range. For a two layered case, expression (2.21) can be written as

$$\varphi=\frac{(\mu_1-\mu_2)\left(\dfrac{\mu_1\mu_2}{xy}-x-(\mu_1-\mu_2)\right)}{4(xy-\mu_1\mu_2)}, \tag{2.37}$$

where subscripts denote the layer, $x:=\lambda_1+\mu_2$ and $y:=\lambda_2+\mu_1$. In the case of xy being infinitesimally larger than $\mu_1\mu_2$ and very small x (or, similarly, xy being infinitesimally smaller than $\mu_1\mu_2$ and large x), expression (2.37) tends to ∞. In the case of xy being infinitesimally larger than $\mu_1\mu_2$ and large x (or xy being infinitesimally smaller than $\mu_1\mu_2$ and very small x), expression (2.37) tends to $-\infty$. Hence, the range of φ is $\in\mathbb{R}$.

[‡]Abbreviation HTI stands for a "homogeneous transversely isotropic" medium.

In Section 2.4, we summarise the results and propose fluid indicators. Specific absolute values of φ appear to be the most efficient in detecting variations of λ, as exhibited in Table 2.4. It should be clarified that the ideal, most efficient indicator is the one that never occurs for near-constant λ ($RSD_\lambda < 2\%$), but appears in 100% of cases if λ varies strongly ($RSD_\lambda > 20\%$). To assure strong—but not moderate—fluctuations of λ, also 0% of occurrence for $RSD_\lambda \in (2\%, 20\%)$ should be expected. Therefore, the indicators in bold from Table 2.4 suggest moderate or strong variations; they do not imply strong fluctuations only. It is worth noticing that moderate fluctuations can be caused by different elastic properties of rocks, especially if μ is varying. To assure that the λ variations are caused by the presence of fluids—in case of bigger γ indicating varying μ—we suggest checking even larger values of $|\varphi|$ than the ones indicated in bold. This way strong variations, not moderate ones, are implied. The rule of thumb is that larger $|\varphi|$ indicates stronger λ fluctuations. Finally, we should notice that other ranges of $|\varphi|$ are indicative of fluids in felsic or mafic rocks. In this paper, we have examined stiffnesses corresponding to the sedimentary rocks only.

Chapter 3

On the problematic case of product approximation in Backus average*

Abstract

Elastic anisotropy might be a combined effect of the intrinsic anisotropy and the anisotropy induced by thin-layering. The Backus average, a useful mathematical tool, allows us to describe such an effect quantitatively. The results are meaningful only if the underlying physical assumptions are obeyed, such as static equilibrium of the material. We focus on the only mathematical assumption of the Backus average, namely, product approximation. It states that the average of the product of a varying function with a nearly constant function is approximately equal to the product of the averages of those functions. We analyse particular problematic case for which the aforementioned assumption is inaccurate. Furthermore, we focus on the seismological context. We examine the inaccuracy's effect on the wave

*This chapter consists of the original research paper and the post-publication comments. Herein, we invoke the following paper: Adamus, F. P. (2021). "On the problematic case of product approximation in Backus average". *Journal of Elasticity*, 144(1), 55–80.

propagation in a homogenous medium—obtained using the Backus average—equivalent to thin layers. Numerical simulations indicate clearly that the product approximation inaccuracy has negligible effect on wave propagation; irrespective of layers' symmetries. To give the results a practical focus, we show that the problematic case of product approximation is strictly related to the negative Poisson's ratio of constituents layers. We discuss the laboratory and well-log cases in which such a ratio has been noticed. Upon thorough literature review, it occurs that examples of so-called auxetic materials (media that have negative Poisson's ratio) are not extremely rare exceptions as thought previously. The investigation and derivation of Poisson's ratio for materials exhibiting symmetry classes up to monoclinic become a significant part of this paper. In addition to the main objectives, we also show that the averaging of cubic layers results in an equivalent medium with tetragonal (not cubic) symmetry. We present concise formulations of stability conditions for low symmetry classes, such as trigonal, orthotropic, and monoclinic.

Keywords: Backus averaging, Continuum mechanics, Approximation, Poisson's ratio, Numerical analysis.

3.1 Introduction

The assumption of material isotropy is convenient but often inaccurate. For instance, in the context of the elasticity of rocks, individual crystals have to be neither of the same types nor oriented randomly. In case they are not, we encounter so-called intrinsic anisotropy. Further, due to geological processes, the formation of rocks can be arranged in a non-random manner forming a foliated structure. In such a situation, we consider anisotropy induced by thin layers.

The Backus average is a useful mathematical tool that provides us with a quantitative description of the anisotropy produced by thin layering (Backus, 1962). The isotropic layers can be replaced by the transversely-isotropic, equivalent (or, so-called, effective, or replacement) medium. The anisotropy of such a medium is a consequence of the inhomogeneity of the stack of layers only (e.g., Slawinski, 2018, Chapter 4). Further, as also shown by Backus (1962), the transversely-isotropic constituents may be approximated by a transversely-isotropic medium, which anisotropy is a combined effect of the intrinsic anisotropy and the anisotropy induced by thin-layering (Bakulin et al., 2000). The Backus average can be extended to lower symmetry classes. We can either follow a procedure analogous to the one shown by Backus (1962) or use the efficient matrix formalism presented by Schoenberg and Muir (1989).

The equivalent medium obtained using the Backus average is a good analogy of a layered material only if the underlying assumptions of the average are satisfied. In the literature, numerous authors dedicate their works to the assumption of the material's static equilibrium. Among many of them are Helbig (1984), Carcione et al. (1991), and Liner and Fei (2007). Another assumption, but a mathematical one this time, introduced by Backus (1962) is the one of product approximation, which states that the average of the product of a rapidly-varying function with nearly-constant function is approximately equal to the product of the averages of those functions. For more than a half-century, the researchers have taken the product assumption for granted. Bos et al. (2017) are the first authors to discuss its validity in the context of the Backus average. A year later, Bos et al. (2018) find and examine statistically a particular case for which the product approximation results in spurious values. They conclude that this problematic case is physically possible, but not likely to appear in seismology. The aforementioned authors examine a single example of a rapidly-varying function that corresponds to isotropic layers only.

This paper aims to continue the investigation on this particular problematic case of product approximation. However, we do not limit ourselves to the examples of rapidly-varying functions corresponding to isotropic layers, but we also check their analogous forms valid for anisotropic constituents. We discuss in detail the possibility of the occurrence of inaccurate product approximation in the context of seismology. We relate it to the presence of negative Poisson's ratio in individual thin layers. Rocks that exhibit such a ratio are called auxetic; in this work, we pay special attention to them. Finally, we perform several simulations of a wave propagating in thinly-layered and equivalent media. Upon comparison of the results, we notice that the problematic case of product approximation has negligible effect on the accuracy of the averaging process—at least in the seismological context.

To be able to perform the investigation on product approximation and negative Poisson's ratio, first, we need to introduce the necessary tools and notions that we use later in the text. Therefore, in Section 3.2, we discuss symmetry classes of elasticity tensors, the conditions that must be obeyed to make these tensors stable, and details of the Backus average. Section 3.3 consists of the main body of the paper.

3.2 Theory

3.2.1 Symmetry classes of elasticity tensor

In the theory of linear elasticity, the forces applied to a single point are expressed in terms of a stress tensor and their resultant deformations in terms of a strain tensor. The definition of the strain tensor for infinitesimal displacements in three dimensions is

$$\varepsilon_{ij} := \frac{1}{2}\left(\frac{\partial u_i}{\partial x_j} + \frac{\partial u_j}{\partial x_i}\right) \qquad i,j \in \{1,2,3\}\,, \tag{3.1}$$

where subscripts i and j, denote Cartesian coordinates, and u_i are the components of the displacement vector describing the deformations in the i-th direction. The constitutive equation relating stresses and strains is Hooke's law, namely,

$$\sigma_{ij} = \sum_{k=1}^{3}\sum_{\ell=1}^{3} c_{ijk\ell}\varepsilon_{k\ell} \qquad i,j \in \{1,2,3\}\,, \tag{3.2}$$

which states that the applied load at a point is linearly related to the deformation by the elasticity tensor, $c_{ijk\ell}$. Due to the index symmetries of $c_{ijk\ell}$, we can replace it by C_{mn}, where $m,n \in \{1,...,6\}$, by following

$$\begin{cases} m = i & \text{if } i = j \\ n = \ell & \text{if } \ell = k \end{cases} \quad \text{and} \quad \begin{cases} m = 9-(i+j) & \text{if } i \neq j \\ n = 9-(\ell+k) & \text{if } \ell \neq k \end{cases} \,. \tag{3.3}$$

In this way, we can represent the elasticity tensor by a 6×6 matrix. C_{mn} can be invariant to different groups of transformations of the coordinate system. The invariance to the orientation of the coordinate system is called material symmetry. There are eight possible symmetry classes. Herein, we focus on monoclinic, orthotropic, tetragonal, trigonal, transversely-isotropic (TI), cubic, and isotropic classes.

We call a tensor to be monoclinic if its symmetry group contains a reflection about a plane through the origin. Herein, for convenience, we choose x_3 to be the axis along which we perform the reflection. If we additionally rotate the coordinates by angle θ about the x_3-axis, where $\tan(2\theta) = 2C_{45}/(C_{44}-C_{55})$, we can express the monoclinic tensor in its natural coordinate system (Helbig, 1994, p.83). In such an orientation, the elasticity matrix has the lowest possible number of the nonzero entries (Slawinski, 2015, Section 5.6.3).

We obtain the following stress-strain relation expressed in a matrix form,

$$\begin{bmatrix} \sigma_{11} \\ \sigma_{22} \\ \sigma_{33} \\ \sigma_{23} \\ \sigma_{13} \\ \sigma_{12} \end{bmatrix} = \begin{bmatrix} C_{11} & C_{12} & C_{13} & 0 & 0 & C_{16} \\ C_{12} & C_{22} & C_{23} & 0 & 0 & C_{26} \\ C_{13} & C_{23} & C_{33} & 0 & 0 & C_{36} \\ 0 & 0 & 0 & C_{44} & 0 & 0 \\ 0 & 0 & 0 & 0 & C_{55} & 0 \\ C_{16} & C_{26} & C_{36} & 0 & 0 & C_{66} \end{bmatrix} \begin{bmatrix} \varepsilon_{11} \\ \varepsilon_{22} \\ \varepsilon_{33} \\ 2\varepsilon_{23} \\ 2\varepsilon_{13} \\ 2\varepsilon_{12} \end{bmatrix}. \tag{3.4}$$

The elasticity tensor whose symmetry group contains a two-fold, three-fold, four-fold, or n-fold rotation is called orthotropic, trigonal, tetragonal, or TI, respectively. Their matrix representations having the least nonzero independent entries are the following.

$$\boldsymbol{C}^{\text{ort}} = \begin{bmatrix} C_{11} & C_{12} & C_{13} & 0 & 0 & 0 \\ C_{12} & C_{22} & C_{23} & 0 & 0 & 0 \\ C_{13} & C_{23} & C_{33} & 0 & 0 & 0 \\ 0 & 0 & 0 & C_{44} & 0 & 0 \\ 0 & 0 & 0 & 0 & C_{55} & 0 \\ 0 & 0 & 0 & 0 & 0 & C_{66} \end{bmatrix}, \tag{3.5}$$

$$\boldsymbol{C}^{\text{trig}} = \begin{bmatrix} C_{11} & C_{12} & C_{13} & 0 & C_{15} & 0 \\ C_{12} & C_{11} & C_{13} & 0 & -C_{15} & 0 \\ C_{13} & C_{13} & C_{33} & 0 & 0 & 0 \\ 0 & 0 & 0 & C_{44} & 0 & -C_{15} \\ C_{15} & -C_{15} & 0 & 0 & C_{44} & 0 \\ 0 & 0 & 0 & -C_{15} & 0 & \frac{C_{11}-C_{12}}{2} \end{bmatrix}, \tag{3.6}$$

$$
\boldsymbol{C}^{\mathrm{tetr}} = \begin{bmatrix} C_{11} & C_{12} & C_{13} & 0 & 0 & 0 \\ C_{12} & C_{11} & C_{13} & 0 & 0 & 0 \\ C_{13} & C_{13} & C_{33} & 0 & 0 & 0 \\ 0 & 0 & 0 & C_{44} & 0 & 0 \\ 0 & 0 & 0 & 0 & C_{44} & 0 \\ 0 & 0 & 0 & 0 & 0 & C_{66} \end{bmatrix}, \tag{3.7}
$$

$$
\boldsymbol{C}^{\mathrm{TI}} = \begin{bmatrix} C_{11} & C_{12} & C_{13} & 0 & 0 & 0 \\ C_{12} & C_{11} & C_{13} & 0 & 0 & 0 \\ C_{13} & C_{13} & C_{33} & 0 & 0 & 0 \\ 0 & 0 & 0 & C_{44} & 0 & 0 \\ 0 & 0 & 0 & 0 & C_{44} & 0 \\ 0 & 0 & 0 & 0 & 0 & \frac{C_{11}-C_{12}}{2} \end{bmatrix}. \tag{3.8}
$$

Again, we choose the x_3-axis to be the rotation axis. A cubic symmetry group contains four-fold rotations about two axes that are orthogonal to one another, whereas an isotropic elasticity tensor is invariant under any rotation. Their matrix representations are

$$
\boldsymbol{C}^{\mathrm{cub}} = \begin{bmatrix} C_{11} & C_{13} & C_{13} & 0 & 0 & 0 \\ C_{13} & C_{11} & C_{13} & 0 & 0 & 0 \\ C_{13} & C_{13} & C_{11} & 0 & 0 & 0 \\ 0 & 0 & 0 & C_{44} & 0 & 0 \\ 0 & 0 & 0 & 0 & C_{44} & 0 \\ 0 & 0 & 0 & 0 & 0 & C_{44} \end{bmatrix} \tag{3.9}
$$

and

$$
\boldsymbol{C}^{\text{iso}} = \begin{bmatrix} C_{11} & C_{11}-2C_{44} & C_{11}-2C_{44} & 0 & 0 & 0 \\ C_{11}-2C_{44} & C_{11} & C_{11}-2C_{44} & 0 & 0 & 0 \\ C_{11}-2C_{44} & C_{11}-2C_{44} & C_{11} & 0 & 0 & 0 \\ 0 & 0 & 0 & C_{44} & 0 & 0 \\ 0 & 0 & 0 & 0 & C_{44} & 0 \\ 0 & 0 & 0 & 0 & 0 & C_{44} \end{bmatrix} . \tag{3.10}
$$

3.2.2 Stability conditions for various symmetries

The stability conditions embody the fact that it is necessary to expend energy to deform a material. To satisfy these conditions, a 6×6 matrix that represents an elasticity tensor must be positive semi-definite. A real symmetric matrix is positive semi-definite if and only if all its eigenvalues (or, equivalently, its principal minors) are nonnegative. Any isotropic tensor is stable if

$$
C_{11} \geq \frac{4}{3} C_{44} \geq 0 \, . \tag{3.11}
$$

A cubic tensor must satisfy

$$
C_{11} - C_{13} \geq 0 \, , \quad C_{11} + 2C_{13} \geq 0 \, , \quad \text{and} \quad C_{44} \geq 0 \, . \tag{3.12}
$$

For a TI and tetragonal tensor we require

$$
C_{11} - |C_{12}| \geq 0 \, , \quad C_{33}(C_{11} + C_{12}) \geq 2C_{13}^2 \, , \quad C_{44} \geq 0 \, , \quad \text{and} \quad C_{66} \geq 0 \, . \tag{3.13}
$$

The last inequality is redundant for the TI case, due to relation $2C_{66} = C_{11} - C_{12}$. A trigonal tensor expressed in a natural coordinate system is stable if

$$C_{11} - |C_{12}| \geq 0\,, \quad C_{33}(C_{11} + C_{12}) \geq 2C_{13}^2\,, \quad C_{44} \geq 0\,, \quad \text{and} \quad C_{11} - C_{12} \geq 2\frac{C_{15}^2}{C_{44}}\,. \tag{3.14}$$

These inequalities are more complicated if a trigonal tensor is not expressed with respect to its natural coordinate system. In such a case, not analysed herein, $C_{14} \neq 0$. So far we have obtained the above stability conditions by verifying the requirements for nonnegative eigenvalues. In the case of orthotropic and monoclinic symmetry classes, due to complicated forms of eigenvalues, we follow the nonnegative, principal-minors criterion. For the orthotropic tensor, we get

$$C_{11} \geq 0\,, \quad C_{11}C_{22} \geq C_{12}^2\,, \quad C_{44} \geq 0\,, \quad C_{55} \geq 0\,, \quad C_{66} \geq 0\,, \quad \text{and} \tag{3.15}$$

$$C_{11}C_{22}C_{33} + 2C_{12}C_{13}C_{23} - C_{11}C_{23}^2 - C_{22}C_{13}^2 - C_{33}C_{12}^2 \geq 0\,. \tag{3.16}$$

A monoclinic tensor is stable if inequalities (3.15), (3.16), and

$$\begin{aligned} C_{11}C_{22}C_{33} + 2C_{12}C_{13}C_{23} - C_{11}C_{23}^2 - C_{22}C_{13}^2 - C_{33}C_{12}^2 \geq C_{16}^2(C_{22}C_{33} - C_{23}^2) \\ +C_{26}^2(C_{11}C_{33} - C_{13}^2) + C_{36}^2(C_{11}C_{22} - C_{12}^2) + 2C_{16}C_{26}(C_{13}C_{23} - C_{33}C_{12}) \\ +2C_{16}C_{36}(C_{12}C_{23} - C_{22}C_{13}) + 2C_{26}C_{36}(C_{12}C_{13} - C_{11}C_{23}) \end{aligned} \tag{3.17}$$

are satisfied. The inequalities are even more complicated for a non-natural coordinate system, where $C_{45} \neq 0$. We notice that for any symmetry class all the main-diagonal entries of the elasticity matrix must be nonnegative, which is simple to prove (e.g. Slawinski, 2015, Exercise 4.5). Notice that the stability conditions for some of the symmetry classes are discussed in Mouchat and Coudert (2014).

3.2.3 Backus average

The procedure of Backus averaging is based on the assumption that the averaged medium is in static equilibrium. If the top and bottom of such a medium is subjected to the same stresses, and we set the Cartesian coordinate system in such a manner that the x_3-axis is vertical, then

$$\sigma_{i3}\,, \quad \frac{\partial u_i}{\partial x_2}\,, \quad \frac{\partial u_i}{\partial x_1}\,, \qquad i \in \{1,\, 2,\, 3\} \tag{3.18}$$

are vertically constant. The remaining stresses or strains may vary significantly along the x_3-axis.

Physically, the above assumption is satisfied, and the Backus average makes sense, if the thickness of the averaged stack of layers, l', is much smaller than the wavelength. In other words, lower the wave frequency, the better accuracy of the average. For purposes of our numerical tests, performed in Section 3.3.3, we choose l' to be at least ten times shorter than the dominant wavelength of primary wave, λ_0^P, which assures that the long-wave assumption is satisfied (Carcione et al., 1991).

Mathematically, the Backus average is correct if the only one mathematical assumption introduced by Backus, namely, the product approximation, remains true. As Backus states in his paper,

$$\overline{f(x_3)g(x_3)} \approx \overline{f(x_3)}\;\overline{g(x_3)}\,, \tag{3.19}$$

where, overbar denotes the average weighted by the layer thicknesses. $f(x_3)$ is a nearly-constant function that stands for stresses and displacements from expression (3.18). $g(x_3)$ describes combinations of elasticity parameters, which can vary significantly from layer to layer. If the above approximation holds, the elasticity coefficients of a stack of isotropic layers are long-wave equivalent to

$$
\begin{aligned}
C_{11}^{\mathrm{TI}} &= \overline{\left(\frac{C_{11}-2C_{44}}{C_{11}}\right)}^{2}\,\overline{\left(\frac{1}{C_{11}}\right)}^{-1} + \overline{\left(\frac{4(C_{11}-C_{44})C_{44}}{C_{11}}\right)}\,,\\
C_{13}^{\mathrm{TI}} &= \overline{\left(\frac{C_{11}-2C_{44}}{C_{11}}\right)}\,\overline{\left(\frac{1}{C_{11}}\right)}^{-1}\,,\\
C_{33}^{\mathrm{TI}} &= \overline{\left(\frac{1}{C_{11}}\right)}^{-1}\,,\\
C_{44}^{\mathrm{TI}} &= \overline{\left(\frac{1}{C_{44}}\right)}^{-1}\,,\\
C_{66}^{\mathrm{TI}} &= \overline{C_{44}}\,,
\end{aligned}
\tag{3.20}
$$

where C_{11} and C_{44} describe each isotropic layer. The five independent coefficients on the left-hand side are the equivalent transversely-isotropic parameters. In Appendix 3.A, we present formulations of the Backus average for layers that exhibit lower symmetry classes.

3.3 Problematic case of product approximation

As discussed by Bos et al. (2018), the assumption of product approximation may be inaccurate only in the case of $\overline{g}\approx 0$, since, in such a situation, the relative error,

$$
err = \frac{\overline{fg}-\overline{f}\,\overline{g}}{\overline{fg}}\times 100\%\,, \tag{3.21}
$$

is around 100%. Predominantly, g is positive (Bos et al., 2018). Therefore, in this section, we look for the possibilities of negative, or low positive g's in layers so that the averaged medium has a chance to represent the problematic case of $\overline{g}\approx 0$. First, in Section 3.3.1, we study the problem from a theoretical point of view. We analyse various examples of functions g that describe combinations of elasticity coefficients corresponding to different symmetry classes. Subsequently, in Section 3.3.2, we look into the close relationship between Poisson's ratio and g. Based on this relation, we discuss the possibility of occurrence of $\overline{g} \approx 0$ in the real seismological cases. Lastly, in Section 3.3.3, we choose theoretically and practically possible values of elasticity parameters for each layer, such that the resulting $\overline{g} \approx 0$. Based on numerical experiments, we compare the simulation of a wave propagating in a layered and long-wave equivalent medium.

3.3.1 Negative g

Let us examine to which combinations of elasticity parameters function g corresponds. Herein, we consider symmetry classes up to monoclinic. To derive g, as an example, we perform the standard procedure to get Backus average for the monoclinic symmetry. First, we write the stress-strain relations in such medium as

$$\sigma_{11} = C_{11}\varepsilon_{11} + C_{12}\varepsilon_{22} + C_{13}\varepsilon_{33} + 2C_{16}\varepsilon_{12}\,, \tag{3.22}$$

$$\sigma_{22} = C_{12}\varepsilon_{11} + C_{22}\varepsilon_{22} + C_{23}\varepsilon_{33} + 2C_{26}\varepsilon_{12}\,, \tag{3.23}$$

$$\sigma_{33} = C_{13}\varepsilon_{11} + C_{23}\varepsilon_{22} + C_{33}\varepsilon_{33} + 2C_{36}\varepsilon_{12}\,, \tag{3.24}$$

$$\sigma_{23} = C_{44}\frac{\partial u_2}{\partial x_3} + C_{44}\frac{\partial u_3}{\partial x_2}\,, \tag{3.25}$$

$$\sigma_{13} = C_{55}\frac{\partial u_1}{\partial x_3} + C_{55}\frac{\partial u_3}{\partial x_1}\,, \tag{3.26}$$

$$\sigma_{12} = C_{16}\varepsilon_{11} + C_{26}\varepsilon_{22} + C_{36}\varepsilon_{33} + 2C_{66}\varepsilon_{12}\,. \tag{3.27}$$

Then, we rewrite the above equations. We want to have one component of a stress tensor or displacement vector that may vary along the x_3-axis on one side of the equations, and on the other side the components that are nearly constant. We can directly do it with equations (3.24)–(3.26), namely,

$$\varepsilon_{33} = \sigma_{33}\underbrace{\left(\frac{1}{C_{33}}\right)}_{g_1} - \underbrace{\left(\frac{C_{13}}{C_{33}}\right)}_{g_2}\varepsilon_{11} - \underbrace{\left(\frac{C_{23}}{C_{33}}\right)}_{g_3}\varepsilon_{22} - \underbrace{\left(\frac{C_{36}}{C_{33}}\right)}_{g_{m_1}} 2\varepsilon_{12}\,, \tag{3.28}$$

$$\frac{\partial u_2}{\partial x_3} = \sigma_{23}\underbrace{\left(\frac{1}{C_{44}}\right)}_{g_4} - \frac{\partial u_3}{\partial x_2}\,, \tag{3.29}$$

$$\frac{\partial u_1}{\partial x_3} = \sigma_{13}\underbrace{\left(\frac{1}{C_{55}}\right)}_{g_5} - \frac{\partial u_3}{\partial x_1}\,. \tag{3.30}$$

Now, we insert the right-hand side of equation (3.28) into equations (3.22), (3.23), and (3.27), to get,

$$\sigma_{11} = \sigma_{33}\left(\frac{C_{13}}{C_{33}}\right) + \underbrace{\left(C_{11} - \frac{C_{13}^2}{C_{33}}\right)}_{g_6}\varepsilon_{11} + \underbrace{\left(C_{12} - \frac{C_{13}C_{23}}{C_{33}}\right)}_{g_7}\varepsilon_{22} + \underbrace{\left(C_{16} - \frac{C_{13}C_{36}}{C_{33}}\right)}_{g_{m_2}} 2\varepsilon_{12}\,, \tag{3.31}$$

$$\sigma_{22} = \sigma_{33}\left(\frac{C_{23}}{C_{33}}\right) + \left(C_{12} - \frac{C_{13}C_{23}}{C_{33}}\right)\varepsilon_{11} + \underbrace{\left(C_{22} - \frac{C_{23}^2}{C_{33}}\right)}_{g_8}\varepsilon_{22} + \underbrace{\left(C_{26} - \frac{C_{23}C_{36}}{C_{33}}\right)}_{g_{m_3}} 2\varepsilon_{12}\,, \tag{3.32}$$

$$\sigma_{12} = \sigma_{33}\left(\frac{C_{36}}{C_{33}}\right) + \left(C_{16} - \frac{C_{13}C_{36}}{C_{33}}\right)\varepsilon_{11} + \left(C_{26} - \frac{C_{23}C_{36}}{C_{33}}\right)\varepsilon_{22} + \underbrace{\left(C_{66} - \frac{C_{36}^2}{C_{33}}\right)}_{g_9} 2\varepsilon_{12}\,. \tag{3.33}$$

Equations (3.28)–(3.33) are ready to be averaged. However, to be able to proceed with the Backus average, from now on, we need to introduce the assumption of product approximation (see Appendix 3.A). Terms in parentheses in equations (3.28)–(3.33) correspond to various g ; we denote them as g_i or g_{m_i} . Terms outside of parentheses correspond to slowly varying function f . Expressions g_i are also presented in higher symmetry classes, and if we follow the procedure shown above, they occupy places analogous to those in equations (3.28)–(3.33). On the other hand, g_{m_i}, are typical for a monoclinic symmetry class only; they do not have the analogous terms in higher symmetry classes. As shown in Appendix 3.B, in trigonal symmetry there is a special case of g that also does not have the analogy in other symmetries. We denote it by g_t. In Table 3.1, we indicate all possibilities of g's for seven symmetry classes.

Table 3.1: Specific g's for symmetry classes up to monoclinic

	monoclinic (g^{mon})	orthotropic (g^{ort})	trigonal (g^{trig})	tetragonal (g^{tetr})
g_1	$1/C_{33}$	$1/C_{33}$	$1/C_{33}$	$1/C_{33}$
g_2	C_{13}/C_{33}	C_{13}/C_{33}	C_{13}/C_{33}	C_{13}/C_{33}
g_3	C_{23}/C_{33}	C_{23}/C_{33}	g_2^{trig}	g_2^{tetr}
g_4	$1/C_{44}$	$1/C_{44}$	$1/C_{44}$	$1/C_{44}$
g_5	$1/C_{55}$	$1/C_{55}$	g_4^{trig}	g_4^{tetr}
g_6	$C_{11}-C_{13}^2/C_{33}$	$C_{11}-C_{13}^2/C_{33}$	$C_{11}-C_{13}^2/C_{33}-C_{15}^2/C_{44}$	$C_{11}-C_{13}^2/C_{33}$
g_7	$C_{12}-C_{13}C_{23}/C_{33}$	$C_{12}-C_{13}C_{23}/C_{33}$	$C_{12}-C_{13}^2/C_{33}+C_{15}^2/C_{44}$	$C_{12}-C_{13}^2/C_{33}$
g_8	$C_{22}-C_{23}^2/C_{33}$	$C_{22}-C_{23}^2/C_{33}$	g_6^{trig}	g_6^{tetr}
g_9	$C_{66}-C_{36}^2/C_{33}$	C_{66}	$(C_{11}-C_{12})/2-C_{15}^2/C_{44}$	C_{66}
g_{m_1}	C_{36}/C_{33}			
g_{m_2}	$C_{16}-C_{13}C_{36}/C_{33}$			
g_{m_3}	$C_{26}-C_{23}C_{36}/C_{33}$			
g_t			C_{15}/C_{44}	
	TI (g^{TI})	cubic (g^{cub})	isotropic (g^{iso})	
g_1	$1/C_{33}$	$1/C_{11}$	$1/C_{11}$	
$g_2=g_3$	C_{13}/C_{33}	C_{13}/C_{11}	$(C_{11}-2C_{44})/C_{11}$	
$g_4=g_5$	$1/C_{44}$	$1/C_{44}$	$1/C_{44}$	
$g_6=g_8$	$C_{11}-C_{13}^2/C_{33}$	$C_{11}-C_{13}^2/C_{11}$	$4(C_{11}-C_{44})C_{44}/C_{11}$	
g_7	$C_{12}-C_{13}^2/C_{33}$	$C_{13}-C_{13}^2/C_{11}$	$2(C_{11}-2C_{44})C_{44}/C_{11}$	
g_9	$(C_{11}-C_{12})/2$	C_{44}	C_{44}	

Based on stability conditions and analysis performed below, in Table 3.2, we present which g's the negative values are allowed for. As can be easily verified numerically, the stability conditions allow C_{13} and C_{23} to be negative, thus, g_2 and g_3 are not necessarily positive. Since it is required that $C_{ii} \geq 0$ (for $i \in \{1, ..., 6\}$), we conclude that all g_1, g_4, g_5, and

Table 3.2: Possibly negative g's for symmetry classes up to monoclinic

monoclinic	orthotropic	trigonal	tetragonal	TI	cubic	isotropic
g_2^{mon}	g_2^{ort}	g_2^{trig}	g_2^{tetr}	g_2^{TI}	g_2^{cub}	g_2^{iso}
g_3^{mon}	g_3^{ort}	g_7^{trig}	g_7^{tetr}	g_7^{TI}		g_7^{iso}
g_7^{mon}	g_7^{ort}	g_t				
g_{m_1}						
g_{m_2}						
g_{m_3}						

particular g_9 must be nonnegative. Below, we analyse only the cases in which it is non-trivial to decide if g's are allowed to be negative. Since, the verdicts of possible negativity of g's are obvious in cases of isotropic and cubic symmetries, let us discuss g_6 and g_7 for TI and tetragonal symmetries. We invoke condition

$$C_{33}(C_{11}+C_{12}) \geq 2C_{13}^2\,. \tag{3.34}$$

We know also that $C_{11} \geq C_{12}$. From the both conditions we obtain

$$C_{33}C_{11} \geq C_{13}^2\,, \tag{3.35}$$

and we infer that

$$C_{33}C_{12} \geq C_{13}^2 \tag{3.36}$$

is not necessarily true, hence, g_7^{TI} and g_7^{tetr} may be negative, whereas g_6^{TI} and g_6^{tetr} are always nonnegative. For trigonal symmetry, the situation is more complicated, due to parameter C_{15}. g_9^{trig} is always nonnegative, due to condition

$$\frac{(C_{11}-C_{12})}{2} \geq \frac{C_{15}^2}{C_{44}}\,. \tag{3.37}$$

Now we can analyse g_6^{trig} . We know that $C_{11}-C_{13}^2/C_{33}$ is nonnegative. To make it negative we try to subtract something greater or equal than C_{15}^2/C_{44} , which is $(C_{11}-C_{12})/2$. We obtain

$$C_{11}-\frac{C_{13}^2}{C_{33}}-\frac{C_{11}-C_{12}}{2}=\frac{\frac{1}{2}C_{33}(C_{11}+C_{12})}{C_{33}}-\frac{C_{13}^2}{C_{33}}\geq 0\,. \tag{3.38}$$

Thus, g_6^{trig} must be nonnegative. If $C_{15}=0$ then $g_7^{\mathrm{trig}}=g_7^{\mathrm{tetr}}=g_7^{\mathrm{TI}}$ which means that g_7^{trig} can be negative the same way that g_7^{tetr} and g_7^{TI} can. The additional stability condition (3.37) for trigonal symmetry—its other conditions are the same for TI and tetragonal symmetry—does allow it. Also, we numerically check that C_{15}/C_{44} can be negative; thus, g_t may be negative as well.

Let us discuss the orthotropic and monoclinic case. Due to the complexity of inequalities (3.16) and (3.17), to decide whether particular g are allowed to be negative, we perform numerical—instead of analytical—analysis only. For each symmetry class, we choose ten–thousand stable elasticity matrices (with nonnegative eigenvalues), where stiffnesses are sampled from uniformly distributed ranges. The range of each elasticity parameter was set to $[-10\,\mathrm{km/s}^2\,,\,50\,\mathrm{km/s}^2\,]$. Based on Monte Carlo (MC) simulations described above, we notice that g_7^{ort} , g_7^{mon}, g_{m_1} , g_{m_2} , or g_{m_3} can be negative while the eigenvalues of the tensors are still positive. However, we neither have found an orthotropic matrix with six nonnegative eigenvalues, where $g_6^{\mathrm{ort}}<0$ or $g_8^{\mathrm{ort}}<0$, nor a monoclinic, semipositive matrix, where $g_6^{\mathrm{mon}}<0$, $g_8^{\mathrm{mon}}<0$, or $g_9^{\mathrm{mon}}<0$. Thus, we conclude that the above g's are very unlikely to be encountered as negative in practical situations, so we do not include them in Table 3.2.

3.3.2 Negative Poisson's ratio

Relation between g and Poisson's ratio

In this section, we look for the alternative elastic moduli that may indicate negative g. We especially focus on the relationship between $g < 0$ and negative Poisson's ratio. First, let us discuss the isotropic symmetry class. To have more physical insight into possibly negative $g_2^{\rm iso}$ and $g_7^{\rm iso}$, we can express them in terms of Lamé parameters or bulk modulus and rigidity. Knowing that $\lambda := C_{11} - 2C_{44}$ and $\mu := C_{44}$, we rewrite

$$g_2^{\rm iso} = \frac{\lambda}{\lambda + 2\mu} = \frac{K - \frac{2}{3}\mu}{K + \frac{4}{3}\mu} \qquad \text{and} \qquad g_7^{\rm iso} = \frac{2\lambda\mu}{\lambda + 2\mu} = \frac{2(K - \frac{2}{3}\mu)\mu}{K + \frac{4}{3}\mu}\,, \tag{3.39}$$

where $K := \lambda + (2/3)\mu$ denotes incompressibility and μ stands for sole rigidity. The material is stable if $\lambda \geq -(2/3)\mu$, $\mu \geq 0$, and $K \geq 0$. Thus, the denominators of expression (3.39) must be positive. Therefore, $g_2^{\rm iso}$ and $g_7^{\rm iso}$ are negative if and only if

$$\lambda < 0 \qquad \text{or} \qquad \frac{\text{incompressibility}}{\text{rigidity}} := \frac{K}{\mu} < \frac{2}{3}\,. \tag{3.40}$$

The magnitudes of $g_2^{\rm iso}$ and $g_7^{\rm iso}$ are incomparable, since $g_2^{\rm iso}$ is dimensionless, whereas $g_7^{\rm iso}$ is not. We can express Poisson's ratio, ν, in terms of Lamé parameters, or primary and secondary waves, namely,

$$\nu_{31} := -\frac{\varepsilon_{11}}{\varepsilon_{33}} = \frac{\lambda}{2(\lambda + \mu)} = \frac{V_P^2 - 2V_S^2}{2(V_P^2 - V_S^2)} = \nu_{ij} \qquad i\,, j\, \in \{1,\, 2,\, 3\}\,. \tag{3.41}$$

The above expression is derived for uniaxial stress in the x_3 direction, but is valid for any direction. We denote the axial strain by letter i, while j stands for the lateral strain. Poisson's ratio is stable if the denominator $2(\lambda + \mu)$ is positive. Hence, negative numerator,

λ, implies negative ν. Therefore, negative Poisson's ratio is another indicator of negative g_2^{iso} and g_7^{iso}. Also, notice that $\nu < 0$ if $V_P/V_S < \sqrt{2}$. Let us discuss, the cubic symmetry. In such a case, g is negative if and only if C_{13} is negative, which is tantamount to negative Poisson's ratio, since we have

$$\nu_{ij} = \frac{C_{13}}{C_{11} + C_{13}} \tag{3.42}$$

and to satisfy the stability condition the denominator must be positive. For TI and tetragonal symmetries, Poisson's ratio

$$\nu_{31} = \nu_{32} = \frac{C_{13}}{C_{11} + C_{12}}\,, \qquad \nu_{13} = \nu_{23} = \frac{C_{13}(C_{11} - C_{12})}{C_{33}C_{11} - C_{13}^2} \tag{3.43}$$

is negative if and only if g_2 is negative (C_{13} must be less than zero) and

$$\nu_{21} = \nu_{12} = \frac{C_{33}C_{12} - C_{13}^2}{C_{33}C_{11} - C_{13}^2} \tag{3.44}$$

is negative if and only if g_7 is negative. Note that expressions (3.41), (3.43), and (3.44) are also derived in Mavko et al. (2009). For the trigonal symmetry class, we get the following Poisson's ratios.

$$\nu_{31} = \nu_{32} = \frac{C_{13}\left(C_{11} - C_{12} - 2\dfrac{C_{15}^2}{C_{44}}\right)}{C_{11}\left(C_{11} - 2\dfrac{C_{15}^2}{C_{44}}\right) - C_{12}\left(C_{12} + 2\dfrac{C_{15}^2}{C_{44}}\right)}\,, \tag{3.45}$$

$$\nu_{21} = \nu_{12} = \frac{C_{12} - \dfrac{C_{13}^2}{C_{33}} + \dfrac{C_{15}^2}{C_{44}}}{C_{11} - \dfrac{C_{13}^2}{C_{33}} - \dfrac{C_{15}^2}{C_{44}}} = \frac{g_7^{\mathrm{trig}}}{g_6^{\mathrm{trig}}}\,, \tag{3.46}$$

$$\nu_{13} = \nu_{23} = \frac{\dfrac{C_{13}}{C_{33}}\left(C_{11} - C_{12} - 2\dfrac{C_{15}^2}{C_{44}}\right)}{C_{11} - \dfrac{C_{13}^2}{C_{33}} - \dfrac{C_{15}^2}{C_{44}}} = \frac{g_2^{\mathrm{trig}}a}{g_6^{\mathrm{trig}}}\,. \tag{3.47}$$

Let us discuss expression (3.45). The term in the numerator in parentheses, to which we later refer as a, must be nonnegative due to the last inequality in condition (3.14). Thus, the expression in the first set of parentheses in the denominator must be also positive and equal or larger than C_{12}. The expression in the second set of parentheses must be equal or smaller than C_{11}. Therefore, the denominator must be positive. Due to the above analysis, we notice that ν_{31} and ν_{32} are negative if and only if C_{13} is negative. In other words, negative $g_2^{\rm trig}$ is tantamount to negative ν_{31} or ν_{32}. On the other hand, according to expression (3.46), negative $g_7^{\rm trig}$ is tantamount to negative ν_{21}. Lastly, ν_{13} and ν_{23} are negative if and only if $g_2^{\rm trig} < 0$. For orthotropic symmetry class we get

$$\nu_{31} = \frac{C_{13}C_{22} - C_{12}C_{23}}{C_{11}C_{22} - C_{12}^2} = \frac{n_1}{d_3}\,, \tag{3.48}$$

$$\nu_{32} = \frac{C_{23}C_{11} - C_{12}C_{13}}{C_{11}C_{22} - C_{12}^2} = \frac{n_2}{d_3}\,, \tag{3.49}$$

$$\nu_{21} = \frac{C_{12}C_{33} - C_{13}C_{23}}{C_{11}C_{33} - C_{13}^2} = \frac{n_3}{d_2}\,, \tag{3.50}$$

$$\nu_{23} = \frac{C_{23}C_{11} - C_{12}C_{13}}{C_{11}C_{33} - C_{13}^2} = \frac{n_2}{d_2}\,, \tag{3.51}$$

$$\nu_{12} = \frac{C_{12}C_{33} - C_{13}C_{23}}{C_{22}C_{33} - C_{23}^2} = \frac{n_3}{d_1}\,, \tag{3.52}$$

$$\nu_{13} = \frac{C_{13}C_{22} - C_{12}C_{23}}{C_{22}C_{33} - C_{23}^2} = \frac{n_1}{d_1}\,, \tag{3.53}$$

where denominators d_1, d_2, and d_3 must be positive due to the stability conditions. Numerator $n_3 = C_{33}\, g_7^{\rm ort}$, hence, negative $g_7^{\rm ort}$ implies negative ν_{21} and ν_{12}. The analysis of numerators n_1 and n_2 is more complicated since we cannot simply express it in terms of $g_i^{\rm ort}$. Therefore, herein, we state the following Lemma only, whereas the proof is included in Appendix 3.C.

Lemma 3.3.1. *If $g_2^{\rm ort} < 0$ and $g_3^{\rm ort} < 0$ then n_1 and n_2 cannot be both positive. If $g_2^{\rm ort} < 0$ then $n_1 > 0$ together with $n_2 < 0$ are not allowed. If $g_3^{\rm ort} < 0$ then $n_1 < 0$ together with*

$n_2 > 0$ *are not allowed. If either* $g_2^{\mathrm{ort}} > 0$ *or* $g_3^{\mathrm{ort}} > 0$ *then* n_1 *and* n_2 *cannot be both negative.*

Notice that the above Lemma implies that if $g_2^{\mathrm{ort}} < 0$ and $g_3^{\mathrm{ort}} < 0$ then both n_1 and n_2 must be negative. That is tantamount to ν_{31} , ν_{32} , ν_{23} , and ν_{13} being negative.

For a monoclinic symmetry we get

$$\nu_{31} = \frac{C_{13}C_{26}^2 - C_{16}C_{23}C_{26} - C_{12}C_{26}C_{36} + C_{16}C_{22}C_{36} + C_{12}C_{23}C_{66} - C_{13}C_{22}C_{66}}{C_{66}C_{12}^2 - 2C_{12}C_{16}C_{26} + C_{22}C_{16}^2 + C_{11}C_{26}^2 - C_{11}C_{22}C_{66}} = \frac{n_1}{d_3}\,, \tag{3.54}$$

$$\nu_{32} = \frac{C_{16}^2C_{23} - C_{13}C_{16}C_{26} - C_{12}C_{16}C_{36} + C_{11}C_{26}C_{36} + C_{12}C_{13}C_{66} - C_{11}C_{23}C_{66}}{C_{66}C_{12}^2 - 2C_{12}C_{16}C_{26} + C_{22}C_{16}^2 + C_{11}C_{26}^2 - C_{11}C_{22}C_{66}} = \frac{n_2}{d_3}\,, \tag{3.55}$$

$$\nu_{21} = \frac{C_{12}C_{36}^2 - C_{13}C_{26}C_{36} - C_{16}C_{23}C_{36} + C_{16}C_{26}C_{33} + C_{13}C_{23}C_{66} - C_{12}C_{33}C_{66}}{C_{66}C_{13}^2 - 2C_{13}C_{16}C_{36} + C_{33}C_{16}^2 + C_{11}C_{36}^2 - C_{11}C_{33}C_{66}} = \frac{n_3}{d_2}\,, \tag{3.56}$$

$$\nu_{23} = \frac{C_{16}^2C_{23} - C_{13}C_{16}C_{26} - C_{12}C_{16}C_{36} + C_{11}C_{26}C_{36} + C_{12}C_{13}C_{66} - C_{11}C_{23}C_{66}}{C_{66}C_{13}^2 - 2C_{13}C_{16}C_{36} + C_{33}C_{16}^2 + C_{11}C_{36}^2 - C_{11}C_{33}C_{66}} = \frac{n_2}{d_2}\,, \tag{3.57}$$

$$\nu_{12} = \frac{C_{12}C_{36}^2 - C_{13}C_{26}C_{36} - C_{16}C_{23}C_{36} + C_{16}C_{26}C_{33} + C_{13}C_{23}C_{66} - C_{12}C_{33}C_{66}}{C_{66}C_{23}^2 - 2C_{23}C_{26}C_{36} + C_{33}C_{26}^2 + C_{22}C_{36}^2 - C_{22}C_{33}C_{66}} = \frac{n_3}{d_1}\,, \tag{3.58}$$

$$\nu_{13} = \frac{C_{13}C_{26}^2 - C_{16}C_{23}C_{26} - C_{12}C_{26}C_{36} + C_{16}C_{22}C_{36} + C_{12}C_{23}C_{66} - C_{13}C_{22}C_{66}}{C_{66}C_{23}^2 - 2C_{23}C_{26}C_{36} + C_{33}C_{26}^2 + C_{22}C_{36}^2 - C_{22}C_{33}C_{66}} = \frac{n_1}{d_1}\,. \tag{3.59}$$

Due to complicated forms of Poisson's ratios, we again are not able to analytically express the relationship between the sign of ν and its influence on g . Based on repeated random simulations of ten–thousand stable elasticity matrices (where the stiffnesses are distributed uniformly within the same ranges as in the previously described MC sampling), we notice that the negative sign of any of g_2^{mon} , g_3^{mon} , g_7^{mon} , g_{m_1} , g_{m_2} , or g_{m_3} does not restrict the sign of any ν_{ij} . Also, all negative or all positive Poisson's ratios do not imply the negative sign of any g . There are, however, some combinations of negative g that are likely to imply negative sign of certain ν_{ij} . For instance, negative g_2^{mon} , g_3^{mon} , and g_7^{mon} , or negative g_7^{mon} , g_{m_2} , and g_{m_3} , or negative g_3^{mon} , g_{m_1} , and g_{m_3} , imply that certain ν_{ij} , in all simulated cases, are negative.

To conclude, for isotropic, cubic, TI, and tetragonal symmetries, negative Poisson's ratio in any axial direction implies some negative g, and any negative g implies some $\nu_{ij} < 0$. The above is not always true for trigonal and orthotropic symmetries. In case of a trigonal symmetry class, negative g_t , and in case of an orthotropic class, negative g_2^{ort} or negative g_3^{ort} , do not imply that certain $\nu_{ij} < 0$. In monoclinic case, negative ν (in all axial directions) does not imply negative sign of any g , but some combinations of negative g's are likely to imply that certain $\nu_{ij} < 0$.

Crystals, minerals, and rocks with negative Poisson's ratio

Since, in the majority of symmetry classes examined by us, the presence of negative Poisson's ratio is tantamount to some negative g , it is reasonable to check the sign of this ratio for the layered rocks. The appearance of $g < 0$ in some individual layers may lead to $\overline{g} \approx 0$ of the equivalent medium that, in turn, can cause inaccuracy in the Backus approximation. In general, $\nu < 0$ is not likely to occur in geophysical data, however, as Zaitsev et al. (2017) state,

> rocks with negative Poisson ratios are not rare exceptions, in contrast to conventional belief.

As numerically shown by Kudela and Stanoev (2018), negative Poisson's ratio does not occur in the global seismological case exemplified by the Preliminary reference Earth model (Dziewoński and Anderson, 1981). However, there are some laboratory and well-log cases in which $\nu < 0$ has been noticed locally. By doing a detailed literature review, we invoke them below.

First, let us discuss naturally occurring auxetic crystals and minerals that have been investigated in a laboratory. Using spectroscopic techniques, Yeganeh-Haeri et al. (1992) show that α-cristobalite, which is a low-temperature modification of a crystalline form of silica (SiO_2), exhibits negative Poisson's ratio. Due to its elastic anisotropy, the value of ν varies with the direction of uniaxial stress. Poisson's ratio occurs in a range from -0.5 to 0.08, although it remains predominantly negative. Cristobalite occurs widely in nature (Yeganeh-Haeri et al., 1992). It forms in volcanic lava domes and often can be found in acidic volcanic rocks (Damby et al., 2014). Also, it can occur in soils (Mizota et al., 1987), deep-sea cherts and porcelanites (Calvert et al., 1977), or other sedimentary rocks (Beljankin and Petrov, 1938). Therefore, one should not disregard its potential influence on the rock's Poisson's ratio. A mineral that also may have $\nu < 0$ is zeolite (Grima et al. (2000), Grima et al. (2007), Sanchez-Valle et al. (2008)). It naturally occurs, for instance, in deep-sea sediments or geothermal systems (Hay, 1986). Moreover, very rare auxetic minerals are indicated by Baughman et al. (1998). Also, as stated by Lakes (2017), it is more likely for the highly anisotropic minerals or crystals to have negative Poisson's ratio, than for the isotropic ones. For instance, single crystal forms of anisotropic arsenic, antimony, and bismuth exhibit $\nu < 0$ in certain directions. However, there is a case of an auxetic mineral that is isotropic. Depending on the temperature, polycrystalline quartz exhibits low, very low, or negative Poisson's ratio (McKnight et al., 2008). According to to Ji et al. (2010), the presence of this mineral may cause some rocks to be auxetic. At ambient conditions, the Poisson's ratio of quartz is $\nu = 0.08$ (Ji et al., 2018).

Let us invoke some laboratory examples of various auxetic rocks. Nur and Simmons (1969) have noticed that very small or negative values of ν are exhibited by dry rocks at very low pressure. They observed that, if there is no external pressure, Casco and Westerly granites present $\nu = -0.100$ and $\nu = -0.094$, respectively. Twenty years later, Hommand-Etienne and Houpert (1989) examine Senones and Remiremont granites with thermally induced cracks. These rocks occur to have negative Poisson's ratio for various directions of uniaxial stresses, which is probably caused, as authors state, by numerous microcracks. The investigation of Zaitsev et al. (2017) confirm that negative ν can primarily occur in cracked rocks at low pressures. Based on the works of Coyner (1984), Freund (1992), and Mavko and Jizba (1994), they describe thirty–four rock samples of cracked rocks with $\nu < 0$ at $8\,\mathrm{MPa}$ confining pressure. Gregory (1976) examines twenty samples of sedimentary rocks at different pressures and at ambient temperature. He notices that apart from the low pressure, $\nu < 0$ (presented in many examined samples) is caused by gas saturation and low porosity. The above statement is confirmed by the experiments of Han (1986) and Jizba (1991). In their works, negative Poisson's ratio is exhibited only by low-porous sedimentary rocks; consolidated sandstones and gas sandstones, respectively. Such results were obtained, *inter alia*, for the approximate effective pressure in the well, that is, for $20\,\mathrm{MPa}$ (Dvorkin et al., 1999). Ji et al. (2010) show that ν decreases with increasing temperature due to thermal effects. According to the authors, quartz-rich rocks at a temperature approaching the α–β quartz transition (such as granite, diorite, quartz-rich sandstone, etc.) may display negative values of Poisson's ratio. They use quartzite as an example to illustrate the effect of phase transition on ν . The quartz-transition temperature is at about $600\,^\circ\mathrm{C}$, however, quartzite has $\nu = 0$ at the temperature of $450\,^\circ\mathrm{C}$ only. Between $450\,^\circ\mathrm{C}$ and $600\,^\circ\mathrm{C}$ it exhibits $\nu < 0$ (Ji et al., 2010, Figure 3b). Recently, the topic of auxetic natural rocks has been studied carefully by Ji et al. (2018). They state that

> none of the crystalline igneous and metamorphic rocks (e.g., amphibolite, gabbro, granite, peridotite, and schist) display auxetic behaviour at pressures of $> 5\,\mathrm{MPa}$ and room temperature. Our experimental measurements showed that quartz-rich sedimentary rocks (i.e., sandstone and siltstone) are most likely to be the only rocks with negative Poisson's ratios at low confining pressures ($\leq 200\,\mathrm{MPa}$) because their main constituent mineral, α-quartz, already has extremely low Poisson's ratio ($\nu = 0.08$) and they contain microcracks, micropores, and secondary minerals.

In the most recent work on auxetic rocks, Ji et al. (2019) state that

> negative Poisson's ratio cannot occur in wet volcanic rocks but may appear in a dry basalt with such an extremely high porosity $(\geq 70\%)$ that a re-entrant foam structure has formed.

Hence, apart from the laboratory experiments, we expect to detect the negative ν in the seismological studies, in the quartz-rich continental crust with a high geothermal gradient (Ji et al., 2010), quartz-rich and gas-bearing sedimentary rocks, or in dry, highly porous basalts.

Finally, we invoke the examples of auxetic rocks obtained from well-log measurements. Let us consider the work of Castagna and Smith (1994), where a worldwide collection of twenty–five sets of velocity and density measurements is exhibited. These measurements of brine sands, shales and gas sands, are based on well-log and laboratory data and occur in close in-situ proximity. Based on the velocities of primary and secondary waves, along with the densities, we compute ν . Two samples of gas sands occur to have negative Poisson's ratio, whereas another sample has a positive value, but very close to zero. Their values are $\nu = -0.18$, $\nu = -0.0162$, and $\nu = 1.02 \times 10^{-4}$, respectively. We find another example of well-log data with negative Poisson's ratio in Goodway (2001, Table 2). The ostracod shale from the Mannville Group in Western Canadian Sedimentary Basin (WCSB), is auxetic. The ostracod beds are used in the gas and oil exploration (Hayes et al., 1994), and in particular, oils are sourced from the ostracod shales (Fay et al., 2012). Hence, this is an important case from the explorational point of view. Based on the density, along with the P and S velocities, we again compute Poisson's ratio and obtain $\nu = -0.11$. Further, Emery and Stewart (2006) present a substantial collection of data from twelve wells in offshore Newfoundland, Eastern Canada. Based on the P and S wave velocities from their Figure 5, we infer that subsets of a dataset from at least two wells present $\nu < 0$.

The above real-data examples confirm most of the expectations coming from the laboratory measurements. To conclude, the ideal conditions for a rock to be auxetic are high temperature and low pressure. Additionally, the chances for the auxetic behaviour are larger if the rock is dry or gas-bearing, quartz-rich, has numerous cracks, and low porosity.

3.3.3 Numerical examples

Let us consider some numerical examples to check if the signal that propagates through thin layers would change its shape and magnitude if propagating through the equivalent medium with $\overline{g} \approx 0$. In cases that we examine, Poisson's ratio of each layer is low. In turn, g's of individual constituents are close to zero, which causes the average $\overline{g} \approx 0$. We use some practical examples of ν from Section 3.3.2.

Wave propagation modelling

In this paper, we analyse the wave propagation in two dimensions, namely, in the x_3x_1-plane. In such a case the elastic equations of motion have the following form.

$$\rho\frac{\partial^2 u_i}{\partial t^2} = \frac{\partial \sigma_{i1}}{\partial x_1} + \frac{\partial \sigma_{i3}}{\partial x_3} + f_i\,, \qquad i \in \{1,\,3\}\,, \tag{3.60}$$

where ρ is a mass density and f is a body force. To obtain the wave equations, we need to insert—into the equations of motion above—the 2D stress-strain relations and expression (3.1). To do so, we first reduce relations (3.4) to two dimensions, namely,

$$\begin{bmatrix} \sigma_{11} \\ \sigma_{33} \\ \sigma_{13} \end{bmatrix} = \begin{bmatrix} C_{11} & C_{13} & 0 \\ C_{13} & C_{33} & 0 \\ 0 & 0 & C_{55} \end{bmatrix} \begin{bmatrix} \varepsilon_{11} \\ \varepsilon_{33} \\ 2\varepsilon_{13} \end{bmatrix}\,, \tag{3.61}$$

which are the strain-stress relations valid not only for monoclinic, but also orthogonal, tetragonal, and TI symmetry classes. For the cubic case, $C_{33} = C_{11}$, whereas for the isotropic class of symmetry, additionally, $C_{13} = C_{11} - 2C_{55}$. (Herein, we do not consider a trigonal class). We solve the resulting elastic wave equations using the open-source seismic modelling code *ewefd2d* in the Madagascar package (Fomel et al., 2013). The code implements a time-domain finite difference method.

To be able to solve the wave equations numerically, we need to define a computational mesh. We model seismic data on a $N_{x_1} \times N_{x_3} = 1500^2$ mesh at uniform $\Delta x_1 = \Delta x_3 = 2\,\mathrm{m}$ spacing. We assume low-frequency stress source injected in the x_3-axis only. For this purpose, we use the Ricker wavelet with a dominant frequency of $12\,\mathrm{Hz}$. We locate the source at $(x_1,\,x_3) = (1500\,\mathrm{m},\,1500\,\mathrm{m})$ and a receiver at $(x_1,\,x_3) = (1500\,\mathrm{m},\,1620\,\mathrm{m})$.

In our simulations, we consider a periodic, three-layered system, to which we refer as a PL medium. We propose five different examples of PL media that we denote by roman letters. Media I–III represent isotropic layers. Medium IV consists of cubic layers, whereas V is composed of layers that exhibit either monoclinic, orthotropic, tetragonal or TI symmetry classes. Layers are placed horizontally and uniformly separated by $2\Delta x_3 = 4\,\mathrm{m}$. Hence, the receiver is separated from the source by a PL medium that consists of ten sets of three layers (in total $120\,\mathrm{m}$). Elasticity coefficients and densities of the layers are presented in Table 3.3.

Table 3.3: Five different elastic PL media. Elasticity parameters are in GPa, whereas density in $\mathrm{kg/m^3}$.

	I (iso)	II (iso)	III (iso)	IV (cubic)	V (mon/ort/tetr/TI)
layer 1	$C_{11} = 37.79$ $C_{55} = 18.89$ $\rho = 2410$	$C_{11} = 37.79$ $C_{55} = 18.89$ $\rho = 2410$	$C_{11} = 40$ $C_{55} = 20$ $\rho = 2410$	$C_{11} = 45 \quad C_{55} = 10$ $C_{13} = 1.2 \times 10^{-7}$ $\rho = 2200$	$C_{11} = 45 \quad C_{55} = 10$ $C_{13} = 1.2 \times 10^{-7}$ $C_{33} = 35 \quad \rho = 2200$
layer 2	$C_{11} = 5.93$ $C_{55} = 2.78$ $\rho = 2100$	$C_{11} = 20.29$ $C_{55} = 10.14$ $\rho = 2300$	$C_{11} = 20$ $C_{55} = 10$ $\rho = 2300$	$C_{11} = 20 \quad C_{55} = 5$ $C_{13} = 1.0 \times 10^{-7}$ $\rho = 1800$	$C_{11} = 20 \quad C_{55} = 5$ $C_{13} = 1.0 \times 10^{-7}$ $C_{33} = 15 \quad \rho = 1800$
layer 3	$C_{11} = 62.44$ $C_{55} = 28.21$ $\rho = 2590$	$C_{11} = 37.79$ $C_{55} = 18.89$ $\rho = 2410$	$C_{11} = 40$ $C_{55} = 20$ $\rho = 2410$	$C_{11} = 30 \quad C_{55} = 8$ $C_{13} = 0.8 \times 10^{-7}$ $\rho = 2000$	$C_{11} = 30 \quad C_{55} = 8$ $C_{13} = 0.8 \times 10^{-7}$ $C_{33} = 22 \quad \rho = 2000$

Also, using expression (3.20) and formulas from Appendix 3.A, we compute the elastic coefficients of the media equivalent to I–V. The equivalent density is the arithmetic average of densities of individual layers. To model the wave propagation—similarly to the PL case—we insert the computed parameters of the equivalent media into the wave equations. We compare the displacement propagation in PL and equivalent media by using the following semblance.

$$S = \frac{\sum_i (a_i + b_i)^2}{2\sum_i (a_i^2 + b_i^2)} \times 100\%\,, \tag{3.62}$$

where a_i and b_i are the discrete values of displacement changing with time in both media.

Results

Medium I consists of isotropic layers corresponding to gas-bearing sandstones presented in Castagna and Smith (1994) (sets 6, 15, and 12, respectively). Poisson's ratio of each layer is low, namely, $\nu_1 \approx 2.6 \times 10^{-4}$, $\nu_2 \approx 0.06$, and $\nu_3 \approx 0.10$. As a result, the averaged $\overline{g_2} \approx 0.05$ is low as well. We present the propagation of displacement (x_3-component) recorded by the receiver in Figure 3.1a. In Figure 3.2, we additionally show the snapshots of wave propagation in both components recorded at time $t = 0.3\,\mathrm{s}$. We notice that displacements are almost identical for both PL and equivalent media, which is confirmed by $S \approx 99.99\%$. Hence, the product approximation, even if $\overline{g}$ is low, seems to be correct, and the average works properly.

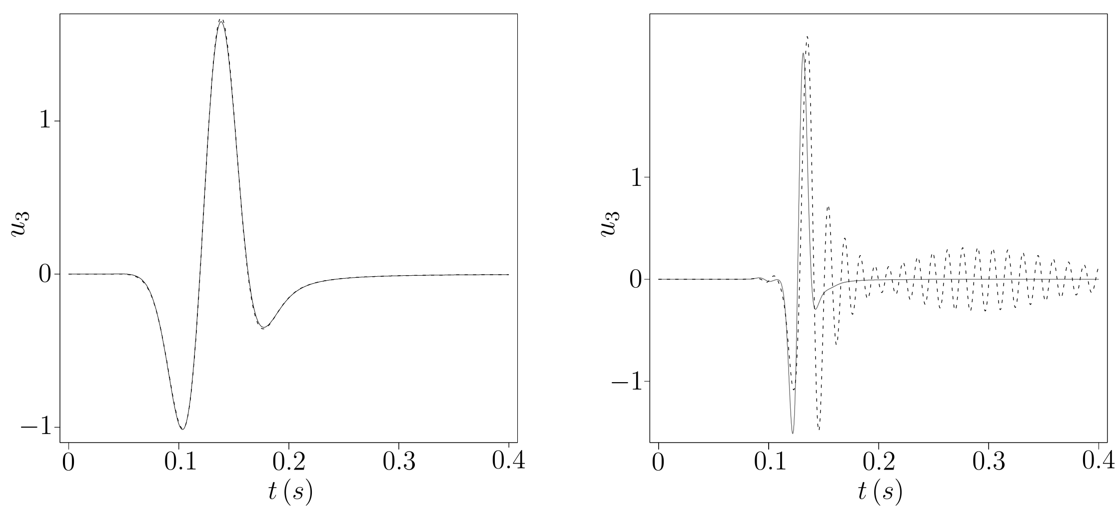

(a) 12 Hz dominant frequency

(b) 48 Hz dominant frequency

Figure 3.1: Displacement u_3 recorded by the receiver. Signal in PL and equivalent medium I is denoted by dashed and solid line, respectively.

The properties of Medium II are similar to gas sandstone from Castagna and Smith (1994) (layer 1 and 3) and ostracod shale from Goodway (2001) (layer 2). In this example, however, we choose the elasticity parameters in such a way that the resulting $\overline{g_2} \approx 3 \times 10^{-4}$ is very low, but still possible to occur in real data case. The semblance of displacement

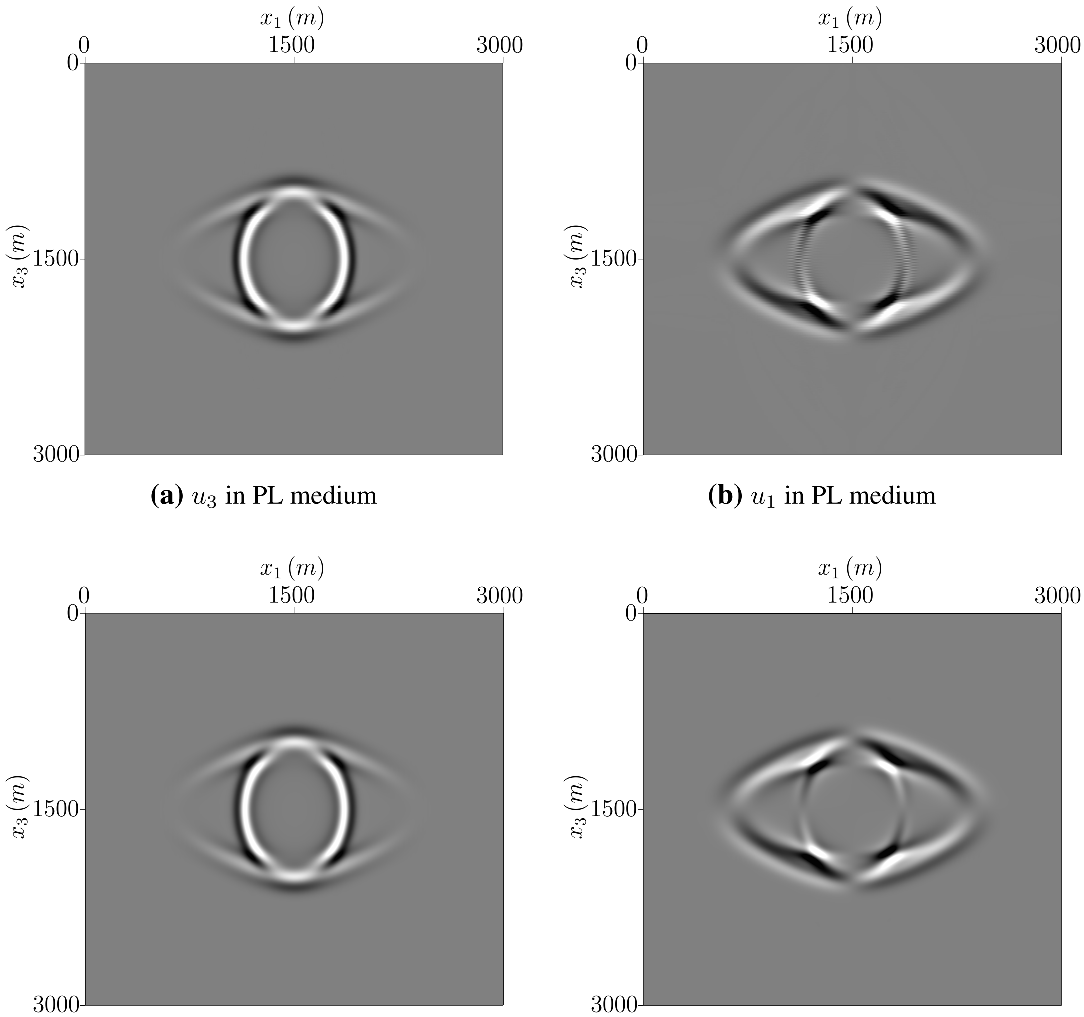

(a) u_3 in PL medium

(b) u_1 in PL medium

(c) u_3 in equivalent medium

(d) u_1 in equivalent medium

Figure 3.2: Snapshots of displacement u_3 and u_1 in PL and equivalent medium I at time $t = 0.3\,\mathrm{s}$

propagation recorded by the receiver in PL and equivalent medium is high, $S \approx 100\%$. Again, the Backus approximation appears to be accurate.

Medium III is the idealised version of the previous example. We slightly change the elasticity parameters in a way that $\overline{g_2}$ is precisely zero, which is probably impossible to achieve in a real seismological case. Thus, in this example, the relative error of the product approximation is 100%. Perhaps surprisingly, the aforementioned error does not influence the accuracy of the Backus average, since $S \approx 100\%$.

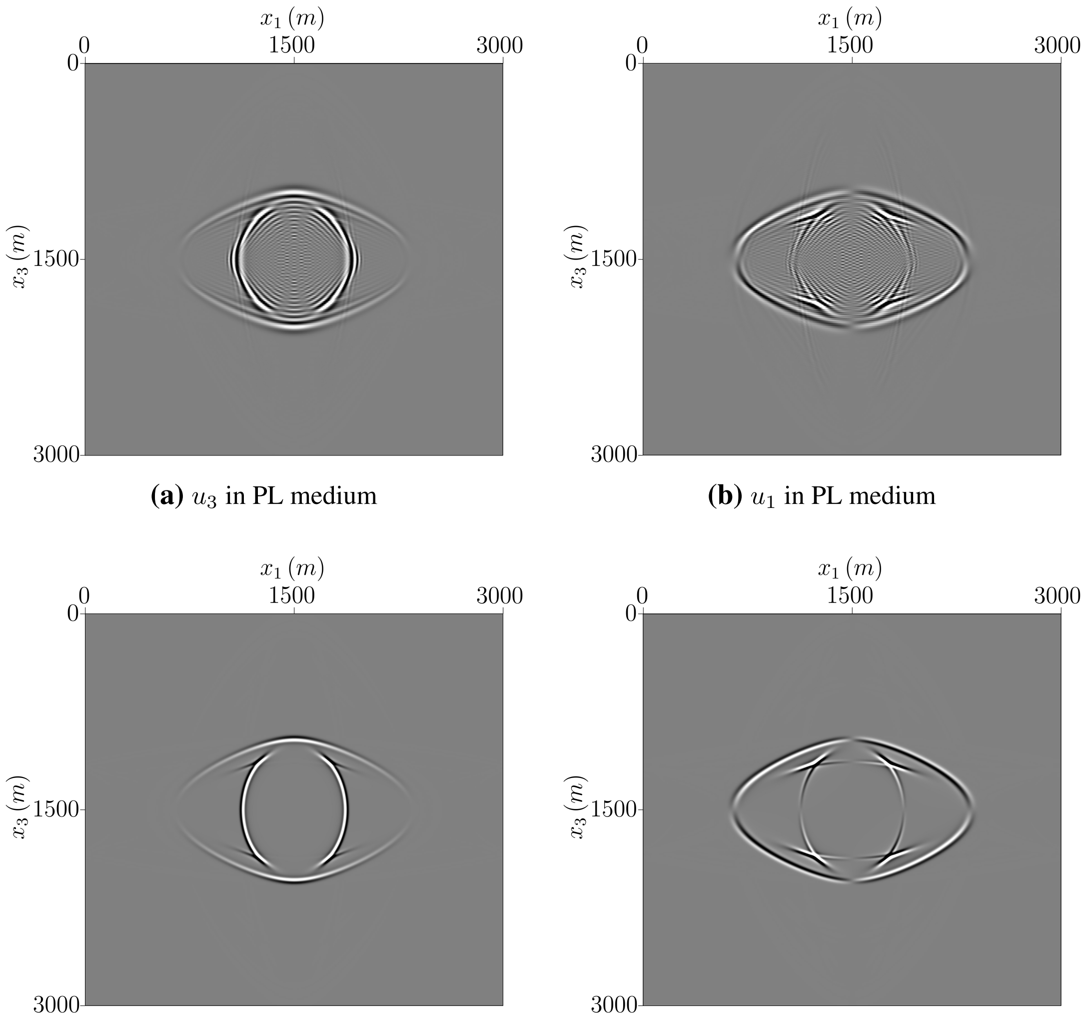

(a) u_3 in PL medium

(b) u_1 in PL medium

(c) u_3 in equivalent medium

(d) u_1 in equivalent medium

Figure 3.3: Snapshots of displacement u_3 and u_1 in PL and equivalent medium I^* at time $t = 0.3\,\mathrm{s}$

Previous examples regarded isotropic layers only. From now on, however, we focus on anisotropic constituents. Medium IV presents cubic layering. The medium equivalent to cubic layers has a tetragonal symmetry class, as we show in Appendix 3.A. This fact might not be evident for the readers since we have not encountered the above statement or analogical examples in the existing literature. We set C_{13} to have very small values, so that $\overline{g_2} \approx 3 \times 10^{-9}$ appears to be extremely low. As in previous examples, Backus average works properly ($S \approx 100\%$), which is illustrated by Figures 3.4 and 3.5. The last

Medium V represents layers that can exhibit monoclinic, orthotropic, tetragonal, or TI symmetry class. The product approximation is inaccurate due to $\overline{g_2} \approx 5 \times 10^{-9}$. However, again it does not affect the Backus approximation that is still accurate since $S \approx 100\%$.

It occurs that the low-frequency assumption seems to raise more concerns than the product assumption. To support the above statement, let us again consider Medium I , but exceptionally change the dominant frequency of the Ricker wavelet to $48\,\mathrm{Hz}$; thus, let us increase it four times. Figures 3.1b and 3.3 illustrate the inaccuracy of the averaging process confirmed by $S \approx 82.81\%$ only. Later in the text, we refer to this higher-frequency example as to the case I^* . For reference, in Table 3.4, we present more accurate values of semblances and $\overline{g_2}$ for all cases I–V .

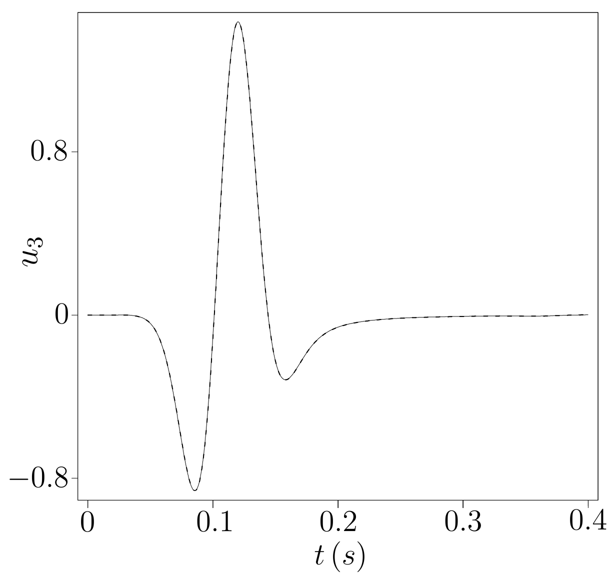

Figure 3.4: Displacement u_3 recorded by the receiver. Signal in PL and equivalent medium IV is denoted by dashed and solid line, respectively.

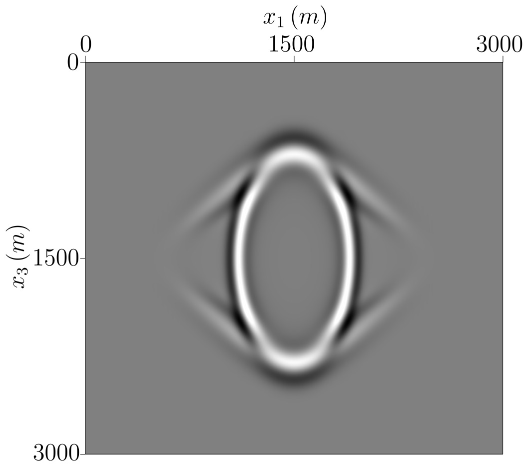

(a) u_3 in PL medium

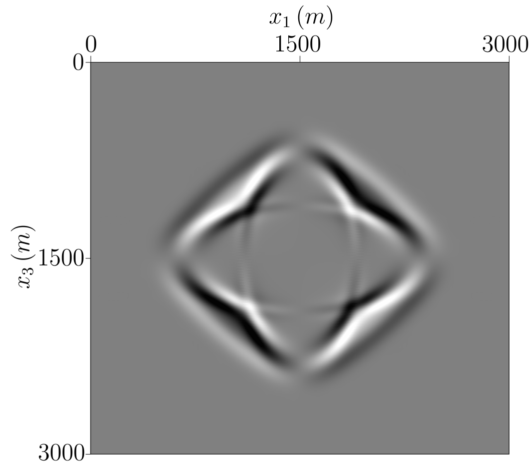

(b) u_1 in PL medium

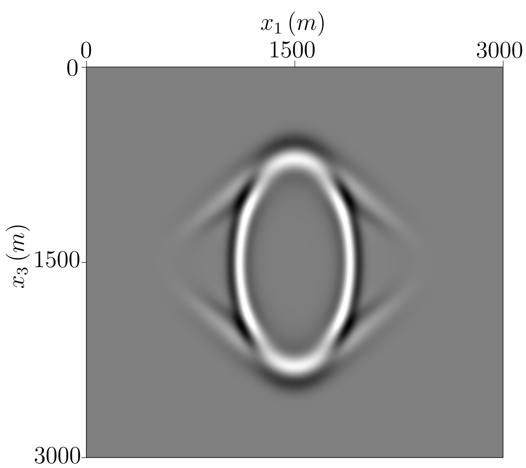

(c) u_3 in equivalent medium

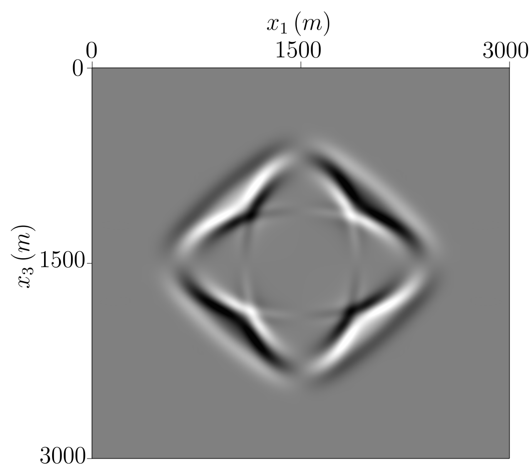

(d) u_1 in equivalent medium

Figure 3.5: Snapshots of displacement u_3 and u_1 in PL and equivalent medium IV at time $t = 0.3\,\mathrm{s}$

Table 3.4: Approximate values of semblances (in %) of signals propagating through thin layers and equivalent media for cases I–V discussed in the main text. The approximate values of averaged $\overline{g_2}$ are also presented.

	I	I^*	II	III	IV	V
semb.	99.9940	82.8138	99.9996	99.9992	99.9993	99.9988
$\overline{g_2}$	0.0530	0.0530	3.41×10^{-4}	0	3.44×10^{-9}	4.58×10^{-9}

3.4 Conclusions

We focus on the case of product approximation that leads to inaccurate results. We discuss a possibility of its occurrence in physics, in general, and in applied seismology, in particular. We examine numerically the effect of such an inaccuracy on wave propagation in a medium obtained by the Backus average.

In Section 3.3.1, we present Table 3.1 that consists of all the possibilities (up to monoclinic class) of rapidly-varying functions g. Table 3.2 indicates which g may be negative and still obey the stability conditions. In turn, negative g (or positive, but low values of g) in certain layers may lead to the average $\overline{g} \approx 0$, which makes the product approximation inaccurate. As discussed in Section 3.3.2, for isotropic, cubic, TI, and tetragonal symmetry classes, negative g is tantamount to negative Poisson's ratio in some direction. Based on the literature review, we show that there are numerous examples in which $\nu < 0$ occurs in practice. Thus, the problematic case of product approximation is likely to occur in real seismological cases, not as assumed previously (Bos et al., 2018). In general, the chances for negative, or low positive Poisson's ratio are larger if the rock is dry or gas-bearing, is quartz-rich, has numerous cracks and low porosity, occurs in a high-temperature or low-pressure environment.

In Section 3.3.3, we perform several 2D numerical simulations of wave propagation in layered and equivalent media with $\overline{g} \approx 0$. Based on these examples, we conclude that the problematic case of product approximation that causes the Backus average to be inaccurate does not affect the wave propagation in a meaningful manner. The product assumption seems to be much less critical than the long-wave and thin layers assumption.

Please note that our numerical analysis is not entirely complete. We neither consider 3D examples, nor the cases of layers exhibiting generally-anisotropic or trigonal symmetry classes. However, given our simulations, we expect that the influence of $\overline{g} \approx 0$ on the wave propagation in equivalent medium obtained by the Backus average should also be marginal in these, low-symmetry or 3D examples.

Acknowledgements

We wish to thank Michael A. Slawinski and David Dalton for their comments. Also, we acknowledge Reviewers' comments and the proofreading of David Dalton. The research was done in the context of The Geomechanics Project partially supported by the Natural Sciences and Engineering Research Council of Canada, grant 202259. The author has no conflict of interests to declare.

Data Availability Statement

The data that support the findings of this study are available from the author upon reasonable request.

3.5 References

Backus, G. E. (1962). "Long-Wave Elastic Anisotropy Produced by Horizontal Layering". *J. Geophys. Res.* 67 (11), 4427–4440.

Bakulin, A., Grechka, V., and Tsvankin, I. (2000). "Estimation of fracture parameters from reflection seismic data–Part II: Fractured models with orthorhombic symmetry". *Geophysics*, 65 (6), 1803–1817.

Baughman, R. H., Stafstrom, S., Cui, C., and Dantas, S. O. (1998). “Materials with Negative Compressibilities in One or More Dimensions”. *Science*, 279 (5356), 1522–1524.

Beljankin, D. S. and Petrov, V. P. (1938). “Occurrence of Cristobalite in A Sedimentary Rock”. *American Mineralogist*, 23 (3), 153–155.

Bos, L., Dalton, D. R., Slawinski, M. A., and Stanoev, T. (2017). “On Backus average for generally anisotropic layers”. *Journal of Elasticity*, 127 (2), 179–196.

Bos, L., Danek, T., Slawinski, M. A., and Stanoev, T. (2018). “Statistical and numerical considerations of Backus-average product approximation”. *Journal of Elasticity*, 132 (1), 141–159.

Calvert, S. E., Burns, R. G., Smith, J. V., and Kempe, D. R. C. (1977). “Mineralogy of Silica Phases in Deep-Sea Cherts and Porcelanites [and Discussion]”. *Phil. Trans. Roy. Soc. Lond. Math. Phys. Sci.,* 286 (1336), 239–252.

Carcione, J. M., Kosloff, D., and Behle, A. (1991). “Long-wave anisotropy in stratified media: A numerical test”. *Geophysics*, 56 (2), 245–254.

Castagna, J. P. and Smith, S. W. (1994). “Comparison of AVO indicators: A modeling study”. *Geophysics*, 59 (12), 1849–1855.

Coyner, K. B. (1984). “Effects of stress, pore pressure, and pore fluids on bulk strain, velocity, and permeability in rocks”. PhD thesis. Massachusetts Institute of Technology.

Damby, D. E., Llewellin, E. W., Horwell, C. J., Williamson, B. J., Najorka, J., Cressey, G., and Carpenter, M. (2014). “The α—β phase transition in volcanic cristobalite”. *J. Appl. Crystallogr.* 47 (4), 1205–1215.

Dvorkin, J., Moos, D., Packwood, J. L., and Nur, A. M. (1999). “Identifying patchy saturation from well logs”. *Geophysics*, 64 (6), 1756–1759.

Dziewoński, A. M. and Anderson, D. L. (1981). “Preliminary reference Earth model”. *Phys. Earth Planet. Inter.* 25 (4), 297–356.

Emery, D. J. and Stewart, R. R. (2006). "Using VP/VS to explore for sandstone reservoirs: well log and synthetic seismograms from the Jeanne d'Arc basin, offshore Newfoundland". *CREWES Research Report*, 18 (1), 1–20.

Fay, M., Larter, S., Bennett, B., Snowdon, L., and Fowler, M. (2012). "Petroleum Systems and Quantitative Oil Chemometric Models for Heavy Oils in Alberta and Saskatchewan to Characterize Oil-Source Correlations". *GeoConvention 2012:Vision*.

Fomel, S., Sava, P., Vlad, I., .Liu, Y, and Bashkardin, V. (2013). "Madagascar: Open-source software project for multidimensional data analysis and reproducible computational experiments". *J. Open Res. Softw.* 1 (1), e8.

Freund, D. (1992). "Ultrasonic compressional and shear velocities in dry clastic rocks as a function of porosity, clay content, and confining pressure". *Geophys. J. Int.* 108 (1), 125–135.

Goodway, B. (2001). "AVO and Lamé constants for rock parameterization and fluid detection". *CSEG Recorder*, 26 (6), 39–60.

Gregory, A. R. (1976). "Fluid saturation effect on dynamic elastic properties of sedimentary rocks". *Geophysics*, 41 (5), 895–921.

Grima, J. N., Gatt, R., Zammit, V., Williams, J. J., Evans, K. E., Alderson, A., and Walton, R. I. (2007). "Natrolite: a zeolite with negative Poisson's ratios". *J. Appl. Phys.* 101 (8), 086102.

Grima, J. N., Jackson, R., Alderson, A., and Evans, K. E. (2000). "Do Zeolites Have Negative Poisson's Ratios?" *Advanced Materials*, 12 (24), 1912–1918.

Han, D.-H. (1986). "Effects of porosity and clay content on acoustic properties of sandstones and unconsolidated sediments:" PhD thesis. Stanford University.

Hay, R. L. (1986). "Geologic Occurrence of Zeolites and Some Associated Minerals". *Stud. Surf. Sci. Catal.* 28 (1), 35–40.

Hayes, B. J. R., Christopher, J. R., Rosenthal, L., Los, G., McKercher, B., Minken, D., Tremblay, Y. M., and Fennel, J. (1994). “Cretaceous Mannville Group of the Western Canada Sedimentary Basin; in Geological Atlas of the Western Canada Sedimentary Basin”. *Canadian Society of Petroleum Geologists and Alberta Research Council*, 19 (URL: https://ags.aer.ca/publications/chapter-19-cretaceous-mannville-group.htm).

Helbig, K. (1984). “Anisotropy and dispersion in periodically layered media”. *Geophysics*, 49 (4), 364–373.

— (1994). *Foundations of anisotropy for exploration seismics*. Pergamon Press.

Hommand-Etienne, F. and Houpert, R. (1989). “Thermally Induced Microcracking in Granites: Characterization and Analysis”. *Int. J. Rock Mech. Min. Sci. Geomech. Abstr.* 26 (2), 125–134.

Ji, S., Li, L., Motra, H. B., Wuttke, F., Sun, S., Michibayashi, K., and Salisbury, M. H. (2018). “Poisson’s Ratio and Auxetic Properties of Natural Rocks”. *J. Geophys. Res. Solid Earth*, 123 (2), 1161–1185.

Ji, S., Sun, S., Wang, Q., and Marcotte, D. (2010). “Lamé parameters of common rocks in the Earth’s crust and upper mantle”. *J. Geophys. Res.* 115(B6), 1–15.

Ji, S., Wang, Q., and Li, L. (2019). “Seismic velocities, Poisson’s ratios and potential auxetic behavior of volcanic rocks”. *Tectonophysics*, 766 (1), 270–282.

Jizba, D. (1991). “Mechanical and acoustical properties of sandstones and shales”. PhD thesis. Stanford University.

Kudela, I. and Stanoev, T. (2018). “On possibile issues of Backus average”. *arXiv*, 1804.01917 [physics.geo-ph].

Lakes, R. S. (2017). “Negative-Poisson’s-Ratio Materials: Axetic Solids”. *Annu. Rev. Mater. Res.* 47 (1), 63–81.

Liner, C. and Fei, T. (2007). “The Backus number”. *Lead. Edge*, 26 (4), 420–426.

Mavko, G. and Jizba, D. (1994). “The relation between seismic P- and S-wave velocity dispersion in saturated rocks”. *Geophysics*, 59 (1), 87–92.

Mavko, G., Mukerji, T., and Dvorkin, J. (2009). *The rock physics handbook: Tools for seismic analysis of porous media*. 2nd edn. Cambridge University Press.

McKnight, R. E. A., Moxon, T., Buckley, A., Taylor, P. A., Darling, T. W., and Carpenter, M. A. (2008). “Grain size dependence of elastic anomalies accompanying the α–β phase transition in polycrystalline quartz”. *J. Phys. Condens. Matter*, 20 (7), 075229.

Mizota, C., Toh, N., and Matsuhisa, Y. (1987). “Origin of cristobalite in soils derived from volcanic ash in temperate and tropical regions”. *Geoderma*, 39 (4), 323–330.

Mouchat, F. and Coudert, F. X. (2014). “Necessary and Sufficient Elastic Stability Conditions in Various Crystal Systems”. *Phys. Rev. B*, 90 (22), 1–4.

Nur, A. and Simmons, G. (1969). “The effect of saturation on velocity in low porosity rocks”. *Earth Planet. Sci. Lett.* 7 (2), 183–193.

Sanchez-Valle, C., Lethbridge, Z. A. D., Sinogeikin, S. V., Williams, J. J., Walton, R. I., Evans, K. E., and Bass, J. D. (2008). “Negative Poisson’s ratios in siliceous zeolite MFI-silicalite”. *J. Chem. Phys.* 128 (18), 184503.

Schoenberg, M. and Muir, F. (1989). “A calculus for finely layered anisotropic media”. *Geophysics*, 54 (5), 581–589.

Slawinski, M. A. (2015). *Waves and rays in elastic continua*. 3rd edn. World Scientific.

— (2018). *Waves and rays in seismology: Answers to unasked questions*. 2nd edn. World Scientific.

Ting, T. C. T. and Chen, T. (2005). “Poisson’s ratio for anisotropic elastic materials can have no bounds”. *Q. J. Mech. Appl. Math.* 58 (1), 73–82.

Yeganeh-Haeri, A, Weidner, D. J., and Parise, J. B. (1992). “Elasticity of α-Cristobalite: A Silicon Dioxide with a Negative Poisson’s Ratio”. *Science*, 257 (5070), 650–652.

Zaitsev, V. Y., Radostin, A. V., Pasternak, E., and Dyskin, A. (2017). "Extracting real-crack properties from non-linear elastic behaviour of rocks: abundance of cracks with dominating normal compliance and rocks with negative Poisson ratios". *Nonlinear Process. Geophys.* 24 (3), 543–551.

3.A Backus average for anisotropic layers

Let us write the strain-stress relations in two dimensions (x_3x_1-plane), namely,

$$\sigma_{11} = C_{11}\varepsilon_{11} + C_{13}\varepsilon_{33}\,, \tag{3.63}$$

$$\sigma_{33} = C_{13}\varepsilon_{11} + C_{33}\varepsilon_{33}\,, \tag{3.64}$$

$$\sigma_{13} = 2C_{55}\varepsilon_{13}\,, \tag{3.65}$$

which are the relations valid for the monoclinic, orthotropic, tetragonal, and TI symmetry class. Upon a rearrangement, we get

$$\sigma_{11} = \left(C_{11} - \frac{C_{13}^2}{C_{33}}\right)\varepsilon_{11} + \left(\frac{C_{13}}{C_{33}}\right)\sigma_{33}\,, \tag{3.66}$$

$$\varepsilon_{33} = -\left(\frac{C_{13}}{C_{33}}\right)\varepsilon_{11} + \left(\frac{1}{C_{33}}\right)\sigma_{33}\,, \tag{3.67}$$

$$\frac{\partial u_1}{\partial x_3} = \left(\frac{1}{C_{55}}\right)\sigma_{13} - \frac{\partial u_3}{\partial x_1}\,. \tag{3.68}$$

Let us treat the above equations as the stress-strain relations that correspond to many individual constituents that we want to average. To perform the averaging process, we use the three following properties: the average of the sum is a sum of the average, the average of the derivative is a derivative of the average, and, finally, the product approximation.

We obtain

$$\overline{\sigma_{11}} = \left[\overline{\left(C_{11} - \frac{C_{13}^2}{C_{33}}\right)} + \overline{\left(\frac{C_{13}}{C_{33}}\right)}^2 \overline{\left(\frac{1}{C_{33}}\right)}^{-1}\right] \overline{\varepsilon_{11}} + \overline{\left(\frac{C_{13}}{C_{33}}\right)}\,\overline{\left(\frac{1}{C_{33}}\right)}^{-1} \overline{\varepsilon_{33}}\,, \tag{3.69}$$

$$\overline{\sigma_{33}} = \overline{\left(\frac{C_{13}}{C_{33}}\right)}\,\overline{\left(\frac{1}{C_{33}}\right)}^{-1} \overline{\varepsilon_{11}} + \overline{\left(\frac{1}{C_{33}}\right)}^{-1} \overline{\varepsilon_{33}}\,, \tag{3.70}$$

$$\overline{\sigma_{13}} = \overline{\left(\frac{1}{C_{55}}\right)}^{-1} 2\,\overline{\varepsilon_{13}}\,. \tag{3.71}$$

Comparing equations (3.69)–(3.71) with equations (3.63)–(3.65), we see that the equivalent elasticity parameters are equal to

$$C_{11}^{\overline{\mathrm{eq}}} = \overline{\left(C_{11} - \frac{C_{13}^2}{C_{33}}\right)} + \overline{\left(\frac{C_{13}}{C_{33}}\right)}^2 \overline{\left(\frac{1}{C_{33}}\right)}^{-1}, \tag{3.72}$$

$$C_{13}^{\overline{\mathrm{eq}}} = \overline{\left(\frac{C_{13}}{C_{33}}\right)}\,\overline{\left(\frac{1}{C_{33}}\right)}^{-1}, \tag{3.73}$$

$$C_{33}^{\overline{\mathrm{eq}}} = \overline{\left(\frac{1}{C_{33}}\right)}^{-1}, \tag{3.74}$$

$$C_{55}^{\overline{\mathrm{eq}}} = \overline{\left(\frac{1}{C_{55}}\right)}^{-1}, \tag{3.75}$$

and the resulting medium is either monoclinic, orthotropic, tetragonal, or TI. If layers have cubic symmetry, then $C_{33} = C_{11}$. In such a case, $C_{33}^{\overline{\mathrm{eq}}} \neq C_{11}^{\overline{\mathrm{eq}}}$, which means that the equivalent medium is not cubic. To understand what is the symmetry class of the medium equivalent to cubic layers, we need to derive the analogous equivalent parameters, but for a 3D case. Upon an analogous procedure, shown above, we get

$$C_{11}^{\overline{\mathrm{eq}}} = \overline{\left(C_{11} - \frac{C_{13}^2}{C_{11}}\right)} + \overline{\left(\frac{C_{13}}{C_{11}}\right)}^2 \overline{\left(\frac{1}{C_{11}}\right)}^{-1}, \tag{3.76}$$

$$C_{12}^{\overline{\mathrm{eq}}} = \overline{\left(C_{13} - \frac{C_{13}^2}{C_{11}}\right)} + \overline{\left(\frac{C_{13}}{C_{11}}\right)}^2 \overline{\left(\frac{1}{C_{11}}\right)}^{-1} , \tag{3.77}$$

$$C_{13}^{\overline{\mathrm{eq}}} = \overline{\left(\frac{C_{13}}{C_{11}}\right)}\,\overline{\left(\frac{1}{C_{11}}\right)}^{-1} , \tag{3.78}$$

$$C_{33}^{\overline{\mathrm{eq}}} = \overline{\left(\frac{1}{C_{11}}\right)}^{-1} , \tag{3.79}$$

$$C_{55}^{\overline{\mathrm{eq}}} = \overline{\left(\frac{1}{C_{55}}\right)}^{-1} , \tag{3.80}$$

$$C_{66}^{\overline{\mathrm{eq}}} = \overline{C_{55}} \, , \tag{3.81}$$

where $C_{11}^{\overline{\mathrm{eq}}} = C_{22}^{\overline{\mathrm{eq}}}$, $C_{13}^{\overline{\mathrm{eq}}} = C_{23}^{\overline{\mathrm{eq}}}$, and $C_{55}^{\overline{\mathrm{eq}}} = C_{44}^{\overline{\mathrm{eq}}}$. The equivalent medium has six independent elasticity parameters and exhibits the tetragonal symmetry class.

3.B Backus procedure for a trigonal tensor

First, we write the stress-strain relations in a trigonal medium (expressed in a natural coordinate system) as

$$\sigma_{11} = C_{11}\varepsilon_{11} + C_{12}\varepsilon_{22} + C_{13}\varepsilon_{33} + C_{15}\frac{\partial u_1}{\partial x_3} + C_{15}\frac{\partial u_3}{\partial x_1} , \tag{3.82}$$

$$\sigma_{22} = C_{12}\varepsilon_{11} + C_{11}\varepsilon_{22} + C_{13}\varepsilon_{33} - C_{15}\frac{\partial u_1}{\partial x_3} - C_{15}\frac{\partial u_3}{\partial x_1} , \tag{3.83}$$

$$\sigma_{33} = C_{13}\varepsilon_{11} + C_{13}\varepsilon_{22} + C_{33}\varepsilon_{33} \, , \tag{3.84}$$

$$\sigma_{23} = C_{44}\frac{\partial u_2}{\partial x_3} + C_{44}\frac{\partial u_3}{\partial x_2} - 2C_{15}\varepsilon_{12} \, , \tag{3.85}$$

$$\sigma_{13} = C_{44}\frac{\partial u_1}{\partial x_3} + C_{44}\frac{\partial u_3}{\partial x_1} + C_{15}\varepsilon_{11} - C_{15}\varepsilon_{22} \, , \tag{3.86}$$

$$\sigma_{12} = (C_{11} - C_{12})\varepsilon_{12} - C_{15}\frac{\partial u_2}{\partial x_3} - C_{15}\frac{\partial u_3}{\partial x_2} \,. \tag{3.87}$$

We can directly rewrite equations (3.84)–(3.86) in a manner that the nearly-constant stresses and strains are on the right-hand side, whereas the sole varying function of displacements is on the left-hand side. We get,

$$\varepsilon_{33} = \sigma_{33}\underbrace{\left(\frac{1}{C_{33}}\right)}_{g_1} - \underbrace{\left(\frac{C_{13}}{C_{33}}\right)}_{g_2}\varepsilon_{11} - \underbrace{\left(\frac{C_{13}}{C_{33}}\right)}_{g_3}\varepsilon_{22} \,, \tag{3.88}$$

$$\frac{\partial u_2}{\partial x_3} = \sigma_{23}\underbrace{\left(\frac{1}{C_{44}}\right)}_{g_4} - \frac{\partial u_3}{\partial x_2} - \underbrace{\left(\frac{C_{15}}{C_{44}}\right)}_{g_t} 2\varepsilon_{12} \,, \tag{3.89}$$

$$\frac{\partial u_1}{\partial x_3} = \sigma_{13}\underbrace{\left(\frac{1}{C_{44}}\right)}_{g_5} - \frac{\partial u_3}{\partial x_1} - \left(\frac{C_{15}}{C_{44}}\right)\varepsilon_{11} + \left(\frac{C_{15}}{C_{44}}\right)\varepsilon_{22} \,. \tag{3.90}$$

Now, we insert the right-hand side of equation (3.88) and (3.90) into equations (3.82) and (3.83). Also, we insert the right-hand side of (3.89) into (3.87). Upon simple calculations, we obtain

$$\sigma_{11} = \sigma_{33}\left(\frac{C_{13}}{C_{33}}\right) + \sigma_{13}\left(\frac{C_{15}}{C_{44}}\right) + \underbrace{\left(C_{11} - \frac{C_{13}^2}{C_{33}} - \frac{C_{15}^2}{C_{44}}\right)}_{g_6}\varepsilon_{11} + \underbrace{\left(C_{12} - \frac{C_{13}^2}{C_{33}} + \frac{C_{15}^2}{C_{44}}\right)}_{g_7}\varepsilon_{22} \,, \tag{3.91}$$

$$\sigma_{22} = \sigma_{33}\left(\frac{C_{13}}{C_{33}}\right) - \sigma_{13}\left(\frac{C_{15}}{C_{44}}\right) + \left(C_{12} - \frac{C_{13}^2}{C_{33}} + \frac{C_{15}^2}{C_{44}}\right)\varepsilon_{11} + \underbrace{\left(C_{11} - \frac{C_{13}^2}{C_{33}} - \frac{C_{15}^2}{C_{44}}\right)}_{g_8}\varepsilon_{22} \,, \tag{3.92}$$

$$\sigma_{12} = -\sigma_{23}\left(\frac{C_{15}}{C_{44}}\right) - \underbrace{\left(\frac{C_{11} - C_{12}}{2} - \frac{C_{15}^2}{C_{44}}\right)}_{g_9} 2\varepsilon_{12} \,. \tag{3.93}$$

Terms in parentheses in equations (3.88)–(3.93) correspond to various g; we denote them as g_i or g_t. We notice that in case of trigonal symmetry, $g_2 = g_3$, $g_4 = g_5$, and $g_6 = g_8$.

3.C Proof of Lemma 3.3.1

Proof. Let us consider first part of Lemma 3.3.1, which states that

> *if* $g_2^{\rm ort} < 0$ *and* $g_3^{\rm ort} < 0$ *then* n_1 *and* n_2 *cannot be both positive.*

To prove it, let us assume that $g_2^{\rm ort} < 0$ and $g_3^{\rm ort} < 0$. Since, according to stability conditions, $C_{33} \geq 0$, the above assumption is tantamount to $C_{13} < 0$ and $C_{23} < 0$. Also, assume that $n_1 > 0$ and $n_2 > 0$, which is tantamount to

$$C_{13}C_{22} - C_{12}C_{23} > 0 \tag{3.94}$$

and

$$C_{23}C_{11} > C_{12}C_{13}\,, \tag{3.95}$$

respectively. From stability conditions, we also know that $C_{22} \geq 0$. Hence, to satisfy expression (3.94), C_{12} must be positive. Therefore, we can rewrite inequality (3.94) as

$$\frac{C_{13}C_{22}}{C_{12}} > C_{23}\,. \tag{3.96}$$

Now, let us consider inequality (3.95). Upon inserting some larger value in the place of C_{23} the inequality will remain true. However, if we insert there the left-hand side of inequality (3.96), we obtain

$$C_{11}C_{22} < C_{12}^2\,, \tag{3.97}$$

which is mathematically correct, but not allowed by the stability conditions.

Second part of Lemma 3.3.1 states that

> *if* $g_2^{\rm ort} < 0$ *then* $n_1 > 0$ *together with* $n_2 < 0$ *are not allowed.*

To prove it, let us assume that $g_2^{\mathrm{ort}} < 0$, which is tantamount to $C_{13} < 0$. Also, assume that $n_1 > 0$ and $n_2 < 0$. We get,

$$\frac{C_{12}C_{23}}{C_{22}} < C_{13} \tag{3.98}$$

and

$$\frac{C_{12}C_{13}}{C_{11}} > C_{23}\,. \tag{3.99}$$

Herein, we have invoked the so-called strict stability conditions (the matrix representing the elasticity tensor must be positive definite instead of positive semidefinite), which constitute the fact that C_{11} and C_{22} are greater than zero. We insert the left-hand side of inequality (3.99) in place of C_{23} inside inequality (3.98) to again obtain

$$C_{11}C_{22} < C_{12}^2\,. \tag{3.100}$$

To prove third part of Lemma 3.3.1 stating that

if $g_3^{\mathrm{ort}} < 0$ *then* $n_1 < 0$ *together with* $n_2 > 0$ *are not allowed*

we assume $g_3^{\mathrm{ort}} < 0$ and consider $n_1 < 0$ and $n_2 > 0$. We obtain

$$\frac{C_{12}C_{23}}{C_{22}} > C_{13} \tag{3.101}$$

and

$$\frac{C_{12}C_{13}}{C_{11}} < C_{23}\,. \tag{3.102}$$

If we insert the left-hand side of inequality (3.101) in place of C_{13} from inequality (3.102), which is a mathematically justified operation, we again obtain expression not allowed by the stability conditions.

The last part stating that

if either $g_2^{\mathrm{ort}} > 0$ *or* $g_3^{\mathrm{ort}} > 0$ *then* n_1 *and* n_2 *cannot be both negative,*

can be proved trivially using same strategy as for the previous parts of Lemma 3.3.1. □

Post-publication comments

Upon suggestions of the thesis examiners, let us add a few comments on this chapter.

In the paper, we mention the Backus average physical assumption of static equilibrium. To be more precise, G. Backus assumed a quasi-static instead of static equilibrium. In other words, vertical stresses are meant to be approximately, instead of exactly, constant through thin layers.

Between expressions (3.4) and (3.5), we state that the elasticity tensor whose symmetry group contains a two-fold rotation is called orthotropic. This statement is not precise since a monoclinic symmetry group also contains a two-fold symmetry. Hence, to be correct, we should restate that the orthotropic symmetry group contains two-fold rotations about rotational axes orthogonal to one another. Also, in expression (3.6), we propose a matrix representation of a trigonal tensor having the least non-zero entries. It should be clarified that this is one of four possible representations. Specifically, rotation of $\theta = 60^\circ$ about the symmetry x_3-axis leads to the change of the C_{15} sign. Another trigonal matrix with least non-zero entries can be obtained if we rotate a matrix from expression (3.6) by $\theta = 30^\circ$. In such a case, parameter C_{14} appears, whereas C_{15} is absent. Similarly, additional rotation of $\theta = 60^\circ$ would change the sign of C_{14}.

Further, in Section 3.2.2, we derive the stability conditions for various symmetry classes. We claim that for orthotropic and monoclinic symmetries, we follow the nonnegative, principal-minors criterion due to complicated forms of the eigenvalues. However, in expressions (3.15)–(3.17), we examined leading principal minors only. This criterion would be correct when considering the so-called strict stability conditions tantamount to positive-definite matrices (additionally, the equality signs in relations (3.15)–(3.17) should be removed). Therefore, in our positive semi-definite case, there are few inequalities missing, such as $C_{11}C_{33} \geq C_{13}^2$ or $C_{22}C_{33} \geq C_{23}^2$. The above-mentioned missing inequalities would lead to a simplification of the stability analysis performed to extract possibly negative g's, shown in Table 3.2. For example, it can be seen immediately—without performing the MC simulations—that g_6^{ort} , g_6^{mon} , g_6^{ort} , g_6^{mon} cannot be negative. Nevertheless, missing inequalities have no impact on the final results.

Also, in Section 3.3.1, we should clarify that in the derivations of g's (see Table 3.1), we assumed the same coordinate orientation of Hookean solids in layers. Different orientations would lead to a lower symmetry of the equivalent medium.

In Section 3.3.2, we discuss the relationship between negative Poisson's ratio and negative g's. Let us add a few comments on Poisson's ratio expressions. Poisson's ratio of a medium having any symmetry is defined as

$$\nu_{ij} := \frac{\varepsilon_{jj}}{\varepsilon_{ii}}\,, \tag{3.103}$$

where i stands for the uniaxial stress direction and j denotes perpendicular direction to this stress. Commonly, Poisson's ratio is expressed in terms of compliance matrix coefficients, where the compliance matrix is an inverse of the elasticity matrix. Specifically,

$$\nu_{ij} := \frac{S_{ij}}{S_{ii}}\,, \tag{3.104}$$

where S_{ij} are the entries of a 6×6 symmetric compliance matrix expressed in Voigt's notation. The compliance matrix, similarly to the stiffness matrix, must obey stability conditions (Ting and Chen, 2005). Hence, S_{ii} must be greater than zero, which excludes potentially problematic cases of zero denominators of the Poisson's ratios. In the paper, we proposed more complicated forms of ν using elasticity parameters since g's were also expressed in terms of stiffnesses. Our expressions can be derived using the inverse of the elasticity matrix and relating the combinations of stiffnesses to the compliances from expression (3.104). Further, as shown in Section 3.3.2, isotropic and cubic symmetries have a single Poisson's ratio, TI, trigonal, and tetragonal symmetries have three distinct Poisson's ratios, whereas orthotropic and monoclinic media have six. To clarify, in all these cases, we have assumed that Hookean solids are expressed in a natural coordinate system. We did not consider a generally anisotropic class that, similarly to the orthotropic and monoclinic class, also have six distinct Poisson's ratios, which is the maximum number. Let us comment on the stability conditions. These conditions are the only requirements that restrict Poisson's ratio range. In the case of isotropy, $\nu \in [-1\,,\, 0.5]$ that can be easily derived using expression (3.41) and stability condition $\lambda \geq -(2/3)\mu$. In the case of any anisotropic class, there are no bonds for Poisson's ratio. Hence, as proved by Ting and Chen (2005), ν can have an arbitrarily large positive or negative value.

In the conclusions of this chapter, we state that the product approximation inaccuracy does not influence wave propagation in a meaningful manner. To understand why it is the case, we need to take a closer look at the examples of layered media considered in our simulations, presented in Table 3.3. In our examples, we allowed g to vary significantly from layer to layer only if its values were not substantially negative. As we have discussed, large negative values are related to large negative Poisson's ratio that is not realistic to occur in nature. Therefore, practical cases of $\overline{g} \approx 0$ corresponded to small variations of g in layers only. In turn, 100% relative error of the product approximation had a negligible effect on the wave propagation due to a very small absolute discrepancy between $\overline{fg}$ and $\overline{f}\,\overline{g}$. Nevertheless, we believe that one could propose a geologically and seismologically non-realistic case of $\overline{g} \approx 0$ corresponding to very large variations of g in layers, where the product approximation inaccuracy would affect the wave propagation in a noticeable manner.

Chapter 4

Orthotropic anisotropy: on contributions of elasticity parameters to a difference in quasi-P-wave-squared velocities resulted from propagation in two orthogonal symmetry planes*

Abstract

We investigate the dependence of quasi P-wave phase velocity propagating in orthotropic media on particular elasticity parameters. Specifically, due to mathematical facilitation,

*This chapter consists of the original research paper and the post-publication comments. Herein, we invoke the following paper: Adamus, F. P. (2020). "Orthotropic anisotropy: on contributions of elasticity parameters to a difference in quasi-P-wave-squared velocities resulted from propagation in two orthogonal symmetry planes". *Geophysical Prospecting*, 68(8), 2361–2378.

we consider the squared-velocity difference, s^2, resulted from propagation in two mutually perpendicular symmetry planes. In the context of the effective medium theory, s^2 may be viewed as a parameter evaluating the influence of cracks—embedded in the background medium—parallel to one or both of the aforementioned planes. Our investigation is both theoretical and numerical. Based on Christoffel's equations, we propose two accurate approximations of s^2. Thanks to them, we interpret the aforementioned squared-velocity difference as being twice more dependent on $C_{55}-C_{44}$, than on $C_{13}-C_{23}$. To describe the magnitude of the dependence, we consider the proportions between the partial derivatives of s^2. Further, it occurs that s^2 is influenced by the ratio of vertically propagating quasi P-wave to vertically propagating quasi S-wave. Anomalously high s^2 might be caused by the low P/S ratio, which in turn can be an indicator of the presence of gas in natural fractures or aligned porosity. Also, we carry out numerical sensitivity study, according to which s^2 is approximately twice more dependent on C_{55} than on C_{13}, twice more sensitive to C_{44} than to C_{23}, and equally dependent on $-C_{33}$ as on $C_{13}+C_{23}$. The dependence on C_{11} and C_{22} can be neglected, especially for small phase angles. We verify the approximations and perform the sensitivity study, using eight examples of the elasticity tensors.

Keywords: Anisotropy, Numerical study, Theory, Velocity analysis, Elasticity parameters.

4.1 Introduction

An orthotropic material is a medium that possesses three mutually orthogonal symmetry planes (e.g., Helbig, 1994, p. 92). In practical studies, a good approximation of such anisotropy is a parallel-layered rock with perpendicular set of cracks (e.g., Slawinski, 2018, p. 124) or a layered rock with two sets of aligned cracks, orthogonal to the layers and each other (Bakulin et al., 2000). In such situations, the layering and cracks are the analogy to the orthogonal symmetry planes.

The theory furnishes us with Christoffel's equations, which help to theoretically predict the changes in phase velocity depending on the direction of wave propagation in shales, layered sandstones with cracks, or other rocks exhibiting the orthotropic anisotropy. The analytical solutions of Christoffel's equations for orthotropic media are complicated. If we know the values of density and elasticity parameters, we can numerically show how the velocity is expected to change with various polar and azimuthal phase angles. Such an analysis was performed, for instance, in Schoenberg and Helbig (1997) or Osinowo et al. (2017). However, it is a more difficult task to grasp how much the particular elasticity parameters contribute to the magnitude of phase velocity in general; especially, when we do not know their values.

To understand it, in this paper, we perform a theoretical and numerical analysis of quasi P-wave velocity in orthotropic media. We exclude the factor of changing azimuth so that the solutions of Christoffel's equations depend on the combined influence of density, elasticity coefficients, and polar angle only. In this way, we decrease the number of unknowns. To do so, we focus our attention on the difference between squared velocities propagating in two mutually-perpendicular vertical planes. We set the coordinate axes to coincide with symmetry planes, so we reduce the number of dependent elasticity parameters. We consider squared velocities instead of just velocities, due to mathematical simplicity. Also, we restrict our consideration to quasi P-waves only, to which, throughout the paper, we refer to simply P-waves.

To analyse the relations between P-wave velocity and particular elasticity coefficients, we consider some approximations to solutions of Christoffel's equations. Also, we perform the sensitivity study based on a series of numerical experiments and illustrate some of them graphically.

Such an analysis may help to understand which elasticity parameters or which relations between these parameters are the least or the most responsible for the changes in phase velocity in orthotropic media. In other words, we attempt to—in the context of elasticity parameters—grasp the meaning of different magnitudes of phase velocities of P-waves propagating along or perpendicularly to set of cracks, presented in real-data. Such data can be obtained upon azimuthal measurements, shown in, for instance, the work of Lynn (2014). Thus, we hope that our analysis can be used as a tool to understand the influence of particular elasticity coefficients on P-waves from real data cases. The more specific goal of this article is to comprehend the dependence of these waves on shear moduli. Especially, we want to determine the influence of C_{55} and C_{44} .

4.2 Squared-velocity difference

4.2.1 Introductory analysis of Christoffel's equations

The Christoffel's equations provide us with the phase velocities of the three waves that propagate within an anisotropic medium. We can write the solvability condition of a system of these equations,

$$\det\left[\sum_{j=1}^{3}\sum_{\ell=1}^{3} c_{ijk\ell}(\boldsymbol{x})n_j n_\ell - \rho(\boldsymbol{x})V^2\delta_{ik}\right] = \mathbf{0}\,, \qquad i,\, k = 1,\, 2,\, 3\,, \tag{4.1}$$

where tensor $c_{ijk\ell}(\boldsymbol{x})$ describes the elastic properties of an inhomogeneous medium and $\mathbf{n}$ is the unit vector normal to the wavefront. Density is denoted by $\rho(\boldsymbol{x})$, phase velocity by V , whereas δ_{ik} is Kronecker's delta. The above determinental equation is an eigenvalue equation. Three eigenvalues correspond to the phase velocities of quasi P-wave and two independent quasi S-waves. We should be aware that in the process of derivation of equation (4.1), we use a trial solution that assumes plane-wave propagation. Such an assumption is good for distant sources only. In Appendix 4.A, we present the solutions to equation (4.1) for orthotropic medium. Therein and in other parts of the paper, we use convenient Voigt's notation, C_{mn}, instead of tensorial notation, $c_{ijk\ell}$, while referring to the elasticity parameters.

Let us initially analyse the solutions of Christoffel's equations for P-wave propagating in symmetry planes of orthotropic medium. The velocity of P-wave propagating in the x_3x_1-plane (see Figure 4.1) depends on four elasticity parameters; C_{33}, C_{11}, C_{55}, and C_{13}. In the x_3x_2-plane, the velocity is influenced by C_{33}, C_{22}, C_{44}, and C_{23}. If P-wave propagates horizontally, then its velocity depends on C_{11}, C_{22}, C_{66}, and C_{12}. We may view the P-wave propagation in the x_3x_1-plane and the x_3x_2-plane of orthotropic medium as the propagation in a symmetry plane of two distinct tetragonal or (if additionally $C_{11} = C_{12} + 2C_{66}$) transversely isotropic media with the x_3 symmetry axis and common C_{33}. Further, we notice that coefficient C_{33} has a decreasing effect on P-wave velocity, V_P, when the polar angle grows (measured from the x_3-axis), whereas it starts to be influenced more by either C_{11} or C_{22}. In the horizontal plane, if azimuthal angle grows (measured from x_1), then V_P loses dependence on C_{11} and gains dependence on C_{22}. We illustrate the above considerations in Figure 4.1. From the solutions of Christoffel's equations in an arbitrary direction, we know that if P-wave propagates in-between symmetry planes, it depends on each of nine independent elasticity parameters. However, we do not know what is the strength of dependence on each elasticity coefficient or the relation between them, in neither an arbitrary propagation nor the symmetry–plane propagation. In the next sections, we limit ourselves to the analysis of P-wave propagating in the x_3x_1 and x_3x_2 symmetry planes. In this way, we reduce the number of elasticity parameters to seven only (three parameters for each vertical symmetry plane and C_{33} that is common for both of

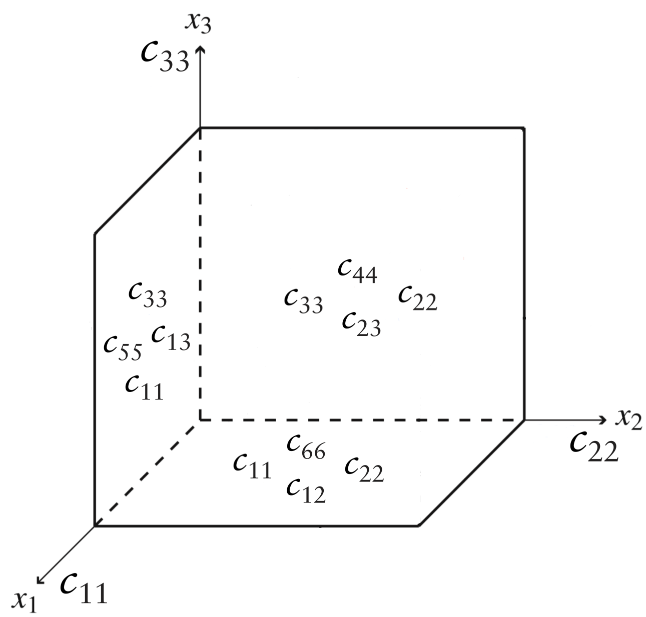

Figure 4.1: Dependence of V_P on elasticity parameters in three axis and symmetry planes

them). We try to consider the approximations to solutions of Christoffel's equations to understand the phase–velocity dependence better. In Appendix 4.A, we further discuss the orthotropic symmetry class. We view it in the context of Christoffel's equations and the relationship between elasticity parameters in typical, real-data scenarios. In Appendix 4.B, we present the examples of orthotropic tensors that, throughout the paper, we use in the numerical experiments.

4.2.2 Approximated squared-velocity difference

Weak anisotropy approximation for small polar angles

In this section, we focus on discrepancies between velocities of P-wave propagating in the x_3x_1-plane and the x_3x_2-plane. To get rid of some square roots present in equations for P-wave velocity, we focus on the difference between squared velocities. Thus, throughout this paper, we consider

$$s^2 := V_{P_{31}}^2 - V_{P_{32}}^2 \tag{4.2}$$

to which we refer as "squared-velocity difference". Subscripts P_{31} and P_{32} denote the plane of P-wave propagation.

First, let us invoke a weak-anisotropy approximation of orthotropic media, shown in Tsvankin (1997). $V_{P_{31}}$ and $V_{P_{32}}$ are approximately equal to

$$V_{P_{31}} \approx \sqrt{\frac{C_{33}}{\rho}\left(1 + 2\sin^4\theta_1\,\epsilon^{(2)} + 2\sin^2\theta_1\,\cos^2\theta_1\,\delta^{(2)}\right)}\,, \tag{4.3}$$

$$V_{P_{32}} \approx \sqrt{\frac{C_{33}}{\rho}\left(1 + 2\sin^4\theta_2\,\epsilon^{(1)} + 2\sin^2\theta_2\,\cos^2\theta_2\,\delta^{(1)}\right)}\,, \tag{4.4}$$

where $\epsilon^{(1)}$, $\epsilon^{(2)}$, $\delta^{(1)}$, and $\delta^{(2)}$ are the anisotropy parameters similar to Thomsen's (1986) parameters and defined in Tsvankin (1997). Symbols θ_1 and θ_2 stand for the polar angles measured from the vertical axis in the x_3x_1-plane and the x_3x_2-plane, respectively. Due to mathematical simplicity, throughout the paper, we consider a particular case of $\theta_1 = \theta_2 = \theta$. Note that in such a situation, the corresponding group (ray) angles, ψ_1, and ψ_2 occur to be approximately equal. To verify it, we use well-known relation (e.g., Tsvankin, 1997)

$$\tan\psi = \frac{\tan\theta + \dfrac{1}{V_P}\dfrac{\partial V_P}{\partial\theta}}{1 - \dfrac{\tan\theta}{V_P}\dfrac{\partial V_P}{\partial\theta}}\,. \tag{4.5}$$

Upon inserting exact values of $V_{P_{31}}$ or $V_{P_{32}}$ (see Appendix 4.A) and computing arcus tangens of the left-hand side of the above equation, we get ψ_1 or ψ_2, respectively. For any phase angle θ and P-wave velocity based on any matrix from Appendix 4.B, we obtain $|\psi_1 - \psi_2| < 0.015°$. Thus, in the context of real-data measurements, $\psi_1 \approx \psi_2$.

Now, we can use equations (4.3) and (4.4) to write the weak anisotropy approximation of s^2, namely,

$$\begin{aligned} s^2 =& V_{P_{31}}^2 - V_{P_{32}}^2 \approx \frac{C_{33}}{\rho}\left[2\sin^2\theta\,\left(\delta^{(2)}-\delta^{(1)}\right)+2\sin^4\theta\,\left(\epsilon^{(2)}-\epsilon^{(1)}+\delta^{(1)}-\delta^{(2)}\right)\right] \\ =& \frac{C_{33}}{\rho}\left\{2\sin^2\theta\,\left[\frac{(C_{13}+C_{55})^2-(C_{33}-C_{55})^2}{2C_{33}(C_{33}-C_{55})}-\frac{(C_{23}+C_{44})^2-(C_{33}-C_{44})^2}{2C_{33}(C_{33}-C_{44})}\right]\right. \\ & +2\sin^4\theta\left[\frac{C_{11}-C_{33}}{2C_{33}}-\frac{C_{22}-C_{33}}{2C_{33}}+\frac{(C_{23}+C_{44})^2-(C_{33}-C_{44})^2}{2C_{33}(C_{33}-C_{44})}\right. \\ & \left.\left.-\frac{(C_{13}+C_{55})^2-(C_{33}-C_{55})^2}{2C_{33}(C_{33}-C_{55})}\right]\right\}. \end{aligned} \tag{4.6}$$

If we abandon the term with $\sin^4\theta$, then we obtain the weak anisotropy approximation for small polar angles,

$$s^2 \approx t := \frac{1}{\rho}\sin^2\theta\,(C_{55}-C_{44})+\frac{1}{\rho}\sin^2\theta\,\left[\frac{(C_{13}+C_{55})^2}{(C_{33}-C_{55})}\right]-\frac{1}{\rho}\sin^2\theta\,\left[\frac{(C_{23}+C_{44})^2}{(C_{33}-C_{44})}\right]. \tag{4.7}$$

For later convenience, we can call the respective three terms

$$t := t_1 + t_2 - t_3\,. \tag{4.8}$$

Also, we can rewrite expression (4.7) as

$$\begin{aligned} t &= \frac{1}{\rho}\sin^2\theta\,\left[C_{55}-C_{44}+a(C_{13}+C_{55})-b(C_{23}+C_{44})\right] \\ &= \frac{1}{\rho}\sin^2\theta\,\left[(a+1)C_{55}-(b+1)C_{44}+aC_{13}-bC_{23}\right], \end{aligned} \tag{4.9}$$

where

$$a = \frac{C_{13}+C_{55}}{C_{33}-C_{55}}\,, \qquad b = \frac{C_{23}+C_{44}}{C_{33}-C_{44}}\,. \tag{4.10}$$

Figure 4.2 illustrates that weak-anisotropy approximation and approximation t are precise

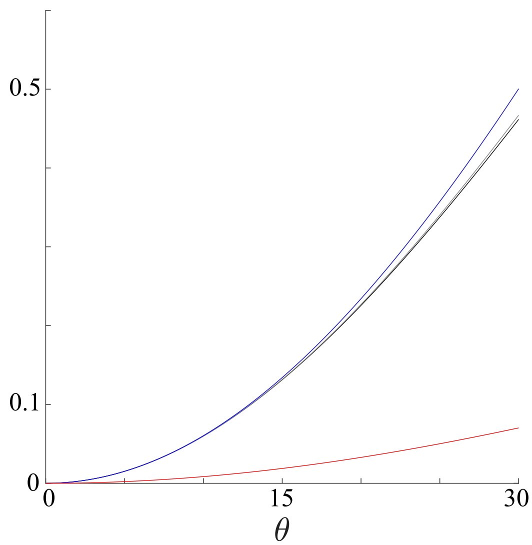

(a) Discrepancy for $C^{C\&al}$ †

(b) Discrepancy for $C^{D\&G}$

Figure 4.2: Discrepancy between estimated and true squared-velocity difference in $\mathrm{km}^2/\mathrm{s}^2$. Bottom axis denotes polar angle $[^\circ]$. Black line shows values of s^2, grey values of weak anisotropy approximation, blue t and red t_1.

for polar angles $\leq 15^\circ$. According to t, the squared-velocity difference can be scaled by $\sin^2\theta$ and depends on a combination of C_{33}, C_{44}, C_{55}, C_{13}, and C_{23}; neither on C_{11} nor on C_{22}. The lack of dependence on C_{11} and C_{22} is the result of dropping the $\sin^4\theta$ term that has a strong influence on large polar angles only.

Approximation based on shear moduli only

Now, let us not to consider a weak anisotropy approximation, but try to derive an approximation from exact solutions of $V_{P_{31}}$ and $V_{P_{32}}$ (see Appendix 4.A). We obtain

$$V_{P_{31}}^2 - V_{P_{32}}^2 = \frac{1}{2\rho}\bigg[(C_{55} - C_{44})\cos^2\theta + (C_{55} - C_{44})\sin^2\theta \\ + (C_{11} - C_{22})\sin^2\theta + \sqrt{D_{31}} - \sqrt{D_{32}}\bigg], \tag{4.11}$$

† Notations $C^{C\&al}$ and $C^{D\&G}$ stand for the orthotropic elasticity matrices presented in Appendix 4.B. In the paper, we will also invoke another matrices, namely, $C^{T\&al}$, $C^{S\&al}$, C^{lime}, C^{sand}, $C^{M\&al}$, and $C^{S\&H}$.

where $\sqrt{D_{31}}$ and $\sqrt{D_{32}}$ can be expressed in the following form.

$$\begin{aligned}\sqrt{D_{31}} &= \left[(C_{11}-C_{55})\sin^2\theta-(C_{33}-C_{55})\cos^2\theta\right]^2+4(C_{55}+C_{13})^2\sin^2\theta\cos^2\theta\,,\\ \sqrt{D_{32}} &= \left[(C_{22}-C_{44})\sin^2\theta-(C_{33}-C_{44})\cos^2\theta\right]^2+4(C_{44}+C_{23})^2\sin^2\theta\cos^2\theta\,.\end{aligned} \tag{4.12}$$

To simplify equation (4.11), we introduce the following intuitive assumptions.

$$\begin{aligned}&\left[(C_{11}-C_{55})\sin^2\theta-(C_{33}-C_{55})\cos^2\theta\right]^2\gg 4(C_{55}+C_{13})^2\sin^2\theta\cos^2\theta\,,\\ &\left[(C_{22}-C_{44})\sin^2\theta-(C_{33}-C_{44})\cos^2\theta\right]^2\gg 4(C_{44}+C_{23})^2\sin^2\theta\cos^2\theta\,.\end{aligned} \tag{4.13}$$

The above intuitive assumptions are based on the fact that for sufficiently small angles

$$(\cos^2\theta-\sin^2\theta)^2\gg 4\sin^2\theta\cos^2\theta\,, \tag{4.14}$$

which can be rewritten as

$$\cos^2(2\theta)\gg\sin^2(2\theta)\quad\to\quad\tan^2(2\theta)\ll 1\quad\to\quad\tan(2\theta)\ll 1\quad\to\quad\theta\ll\frac{\pi}{8}=22.5^\circ\,. \tag{4.15}$$

Assuming that inequalities (4.13) are correct, we rewrite expressions (4.12), namely,

$$\begin{aligned}\sqrt{D_{31}} &\approx \left[(C_{11}-C_{55})\sin^2\theta-(C_{33}-C_{55})\cos^2\theta\right]^2\,,\\ \sqrt{D_{32}} &\approx \left[(C_{22}-C_{44})\sin^2\theta-(C_{33}-C_{44})\cos^2\theta\right]^2\,.\end{aligned} \tag{4.16}$$

We insert expressions (4.16) into (4.11). We further assume that

$$(C_{11}-C_{55})\sin^2\theta<(C_{33}-C_{55})\cos^2\theta\quad\text{and}\quad(C_{22}-C_{44})\sin^2\theta<(C_{33}-C_{44})\cos^2\theta\,. \tag{4.17}$$

For instance, even if $C_{11}-C_{55}=3(C_{33}-C_{55})$ and $C_{22}-C_{44}=3(C_{33}-C_{44})$, which—in view of Appendix 4.B—is not expected to occur in practice, then the above assumption is not valid only for very large angles $\theta \geq 30°$. Taking into consideration expression (4.17), we finally obtain

$$s^2 \approx \frac{1}{\rho}\sin^2\theta\,(C_{55}-C_{44}) \tag{4.18}$$

that is equal to t_1, or to expression (4.9) with $a, b=0$; defined in previous section.

Let us validate the assumptions from expression (4.13) for matrices $C^{C\&al}$ and $C^{D\&G}$ and for increasing polar angles. The results are presented in Table 4.1.

Table 4.1: Assumptions (4.13) associated with $\sqrt{D_{31}}$ and $\sqrt{D_{32}}$. Numerical results for $C^{C\&al}$ and $C^{D\&G}$.

		$\theta=0°$	$\theta=1°$	$\theta=5°$	$\theta=10°$	$\theta=15°$
$C^{C\&al}$	$\sqrt{D_{31}}$	$35.72>0$	$35.67>0.073$	$34.27>1.796$	$30.13>6.966$	$23.95>14.89$
	$\sqrt{D_{32}}$	$39.16>0$	$39.10>0.063$	$37.72>1.555$	$33.61>6.034$	$27.40>12.90$
$C^{D\&G}$	$\sqrt{D_{31}}$	$9.000>0$	$8.987>0.015$	$8.670>0.369$	$7.728>1.433$	$6.305>3.063$
	$\sqrt{D_{32}}$	$10.11>0$	$10.10>0.009$	$9.783>0.212$	$8.836>0.821$	$7.394>1.756$

We notice that t_1 seems to be good approximation for very small polar angles only. The results from the table are confirmed in Figure 4.2. However, in the anomalous case discussed by Helbig and Schoenberg (1987), where $C_{55}\approx -C_{13}$ and $C_{44}\approx -C_{23}$, the right-hand sides of assumptions (4.13) are around zero, which makes the approximation (4.18) correct. Nonetheless, in a great majority of cases, sole dependence on shear moduli seems to be too significant simplification while trying to understand the difference in squared velocity. To better approximate s^2, we need to consider more elasticity parameters than the sole pair of C_{55} and C_{44}.

Intuitive approximation

Let us consider another approximation based on sole intuition rather than on mathematical derivation that is still difficult due to the presence of square roots $\sqrt{D_{31}}$ and $\sqrt{D_{32}}$.

While examining previous approximations, we have noticed that they are expressed in terms of scaling factor, $\sin^2\theta$, and the combination of elasticity parameters. If we analyse expression (4.11), we notice that s^2 depends on differences in pairs C_{55}, C_{44} and C_{11}, C_{22}. Also, expression (4.12) indicates that both roots differ from each other only by having C_{55} in places of C_{44}, C_{11} in place of C_{22}, or C_{13} in place of C_{23}. We see that C_{33} behaves as a constant that acts on both roots in the same manner. Let us neglect C_{33} and focus on pairs of elasticity parameters that render both roots different, namely, C_{55}, C_{44}, and C_{11}, C_{22}, and C_{13}, C_{23}. Having in mind that if $C_{55} = C_{44}$, $C_{11} = C_{22}$, and $C_{13} = C_{23}$, then $s^2 = 0$, we look for an approximation that—in such a situation—also equals to zero. Therefore, we propose

$$q^* := \frac{1}{\rho}\sin^2\theta\,(C_{55} - C_{44} + C_{11} - C_{22} + C_{13} - C_{23})\,, \tag{4.19}$$

which has similar form to expression (4.9), but has no coefficients a, $a+1$, b, $b+1$ in front of the elasticity parameters. Let us divide the above estimator into three components that will be useful in a later investigation.

$$q^* := q_1^* + q_2^* + q_3^*\,, \tag{4.20}$$

where

$$q_1^* := \frac{1}{\rho}\sin^2\theta\,(C_{55} - C_{44})\,, \quad q_2^* := \frac{1}{\rho}\sin^2\theta\,(C_{11} - C_{22})\,, \quad q_3^* := \frac{1}{\rho}\sin^2\theta\,(C_{13} - C_{23})\,. \tag{4.21}$$

Notice that $q_1^* = t_1$. To quantify the discrepancy between q^* and s^2, we compute the relative error,

$$err = \frac{1}{i_{\max}} \sum_i \frac{|s^2(\theta^{(i)}) - q^*(\theta^{(i)})|}{s^2(\theta^{(i)})}\,, \qquad i \in \{1\,, 2,\,\ldots\,,\, i_{\max}\}\,, \tag{4.22}$$

where, $\theta^{(i)}$, denotes a single polar angle. Relative errors calculated for various angles are shown in Table 4.2. Also, the contributions of q_1^* , q_2^* , and q_3^* presented as ratios of q^* are exposed in Table 4.3. The results are shown for both elasticity tensors, $C^{C\&al}$ and $C^{D\&G}$.

Table 4.2: Relative error in $\%$ between q^* and s^2 for various polar angles

	$\theta = 1^\circ$	$\theta = 3^\circ$	$\theta = 5^\circ$	$\theta = 10^\circ$	$\theta = 15^\circ$
$C^{C\&al}$	0.05	0.02	0.17	0.88	2.07
$C^{D\&G}$	20.67	20.60	20.46	19.77	18.55

Table 4.3: Contributions of q_1^* , q_2^* , and q_3^* presented as ratios of q^*

	q_1^*/q^*	q_2^*/q^*	q_3^*/q^*
$C^{C\&al}$	0.140	0.732	0.127
$C^{D\&G}$	0.110	0.479	0.411

In the case of elasticity tensor $C^{C\&al}$, the square-velocity difference seems to be precisely approximated by q^* . For $C^{D\&G}$, however, err for angles $\theta \in (0^\circ\,,\, 15^\circ]$ is $\approx 20\%$; hence, it seems to be high.

According to approximation q^* , the difference between squared-velocity propagating in the x_3x_1-plane and the x_3x_2-plane depends on the polar angle and equally on some values of C_{55} , C_{44} , C_{11} , C_{22} , C_{13} , and C_{23} . However, if we take into consideration the specific values of these parameters, it occurs that—as shown in Table 4.3—q^* mainly depends on the value of $C_{11} - C_{22}$. It also depends on $C_{55} - C_{44}$ and $C_{13} - C_{23}$, but in a smaller manner. The removal of C_{33} in the approximation may be incorrect, especially that this parameter has an essential role as a scaling factor, for instance, in the weak-anisotropy approximation from Section 4.2.2. In the next section, we try to illustrate and quantify the dependence of P-wave on each parameter, including C_{33}. As a result, we verify the correctness and modify approximation q^*.

4.2.3 Sensitivity study: changes of single elasticity parameter

Graphical analysis

In this section, we graphically analyse the values from tensor $C^{C\&al}$ only. In Figure 4.3a, we present how the squared-velocity difference is changing with polar angle, if every elasticity parameter is fixed (meaning that they have original values from $C^{C\&al}$). For later reference, in the same figure in red, we exhibit the velocity difference, $V_{P_{31}}(\theta) - V_{P_{32}}(\theta)$. Notice that ratio

$$\frac{s^2(\theta)}{V_{P_{31}}(\theta) - V_{P_{32}}(\theta)} = \frac{V_{P_{31}}^2(\theta) - V_{P_{32}}^2(\theta)}{V_{P_{31}}(\theta) - V_{P_{32}}(\theta)} = V_{P_{31}}(\theta) + V_{P_{32}}(\theta) \neq \text{const}. \tag{4.23}$$

Additionally, in Figure 4.3b, we illustrate the velocity changing with polar and azimuthal phase angles. These figures might be useful as a reference while studying the next paragraphs.

The relation between elasticity parameters and P-wave velocity can be illustrated in several ways. Below, we focus on showing the influence of a single parameter on velocity. Therefore, one coefficient changes, whereas we fix the rest of the elasticity parameters. The value of a particular elasticity coefficient varies with respect to velocity, polar, and azimuthal phase angle. To be able to show the variation on the 3–D graph, we additionally fix one of the variables. To do so, we again focus on the difference in squared-velocities, s^2; thus, we fix the azimuthal angle.

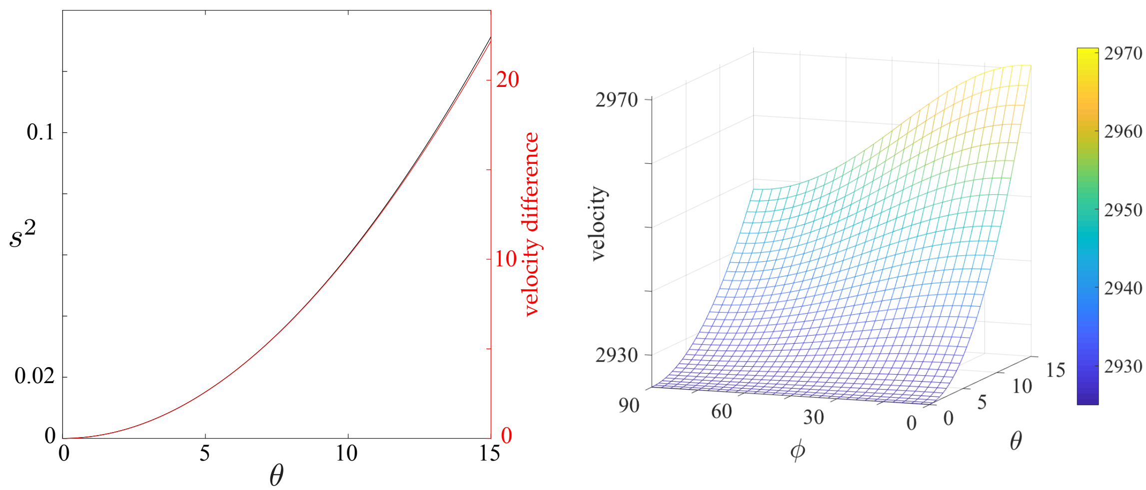

(a) s^2 $[\mathrm{km}^2/\mathrm{s}^2]$ in black and $V_{P_{31}} - V_{P_{32}}$ $[\mathrm{m/s}]$ in red vs. polar angle θ $[°]$

(b) V_P $[\mathrm{m/s}]$ vs. polar θ $[°]$ and azimuthal ϕ $[°]$ angle

Figure 4.3: Velocity dependence on direction of propagation for Cheadle et al. (1991) rock

On the graphs, we show only the values of elasticity parameters that obey the stability conditions. These conditions constitute the fact that it is necessary to expand energy to deform a material (e.g., Slawinski, 2018, Chapter 4.3). To satisfy them, a 6×6 matrix that represents an elasticity tensor must be positive semi-definite. A real symmetric matrix is positive semi-definite if and only if all its eigenvalues (or, equivalently, its principal minors) are nonnegative. Thus, in case of the orthotropic symmetry, the inequalities

$$C_{11} \geq 0\,, \quad C_{11}C_{22} \geq C_{12}^2\,, \quad C_{44} \geq 0\,, \quad C_{55} \geq 0\,, \quad C_{66} \geq 0\,, \quad \text{and}$$
$$C_{11}C_{22}C_{33} + 2C_{12}C_{13}C_{23} - C_{11}C_{23}^2 - C_{22}C_{13}^2 - C_{33}C_{12}^2 \geq 0 \qquad (4.24)$$

must be obeyed (Mouchat and Coudert, 2014).

Only seven elasticity parameters contribute to s^2 ; hence, we present seven figures. Figures 4.4–4.7 illustrate the variations of C_{55} , C_{44} , C_{11} , C_{22} , C_{13} , C_{23} , and C_{33} , respectively. The velocities are calculated for $\theta \in [0° \,, 15°]$ with a step of one degree, and for elasticity parameters $\in [0\,\mathrm{km}^2/\mathrm{s}^2 \,, 20\,\mathrm{km}^2/\mathrm{s}^2]$ with a step of one $\mathrm{km}^2/\mathrm{s}^2$ (for illustration purposes, apart from conditions (4.24), we have additionally assumed that $C_{13} > 0$ and $C_{23} > 0$, which does not influence later investigations). The original values of squared-velocity difference for all fixed parameters—hence, the black curve from Figure 4.3a—are shown on each graph as a thick line. In general, the higher the discrepancy between original s^2 from Figure 4.3a and s^2 computed for modified $C^{C\&al}$—which has one specific elasticity parameter changed—the larger the dependence of s^2 on this particular coefficient.

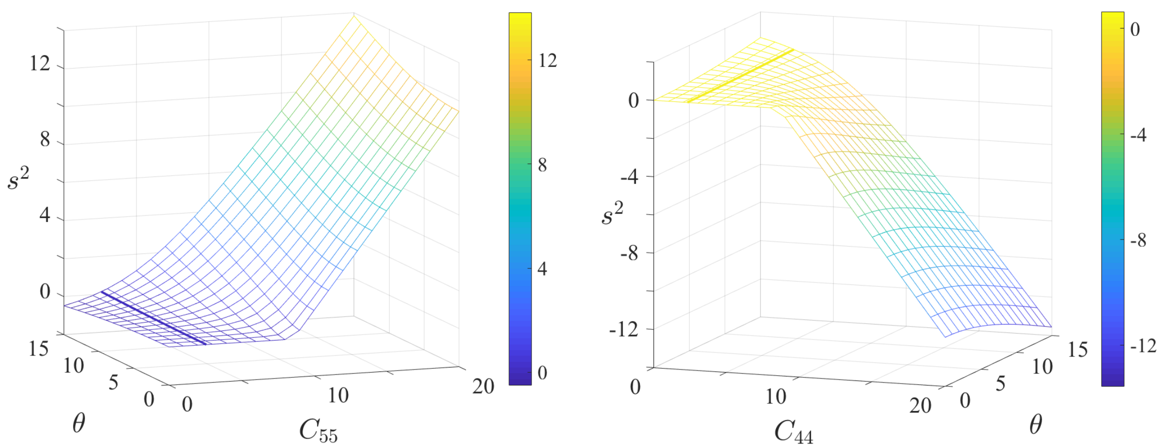

(a) C_{55} **(b)** C_{44}

Figure 4.4: s^2 [km^2/s^2] dependence on polar angle θ [°] and either C_{55} [km^2/s^2] or C_{44} [km^2/s^2]

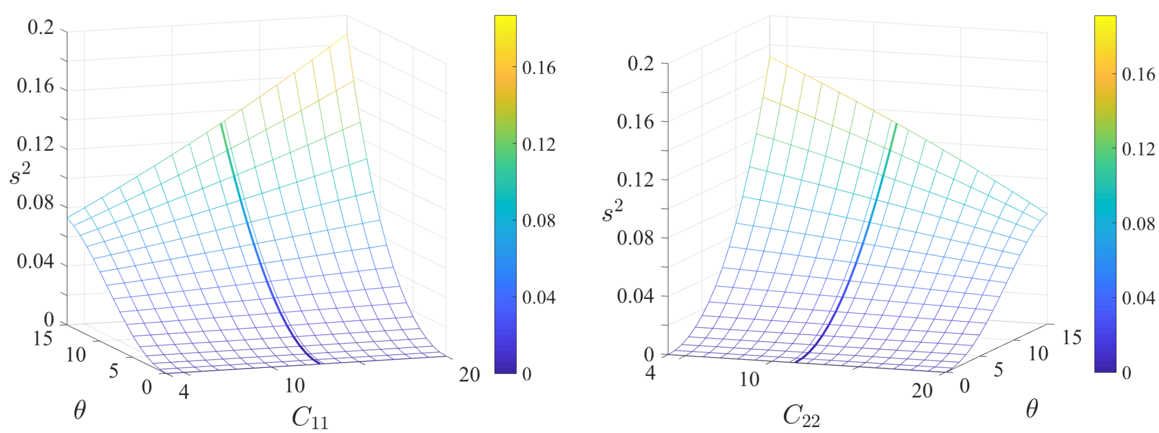

(a) C_{11} **(b)** C_{22}

Figure 4.5: s^2 [km^2/s^2] dependence on polar angle θ [°] and either C_{11} [km^2/s^2] or C_{22} [km^2/s^2]

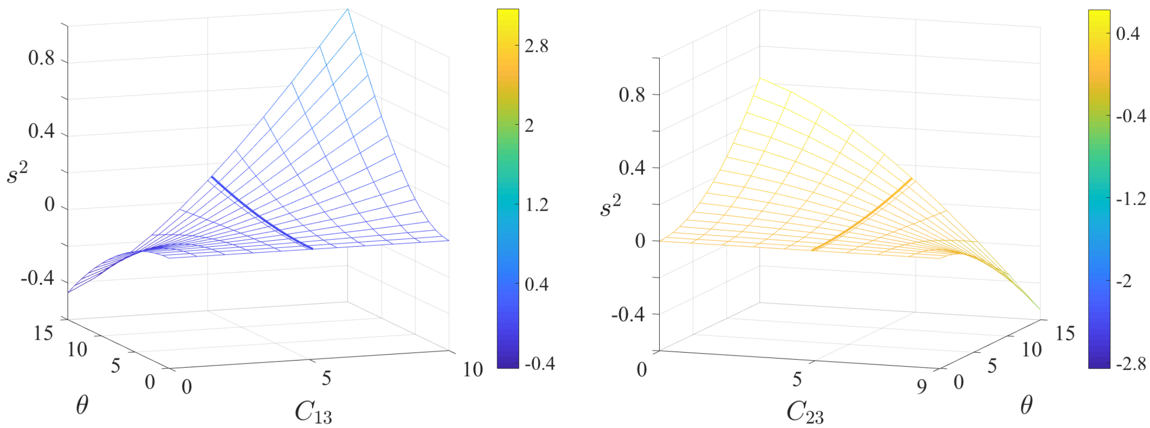

(a) C_{13} **(b)** C_{23}

Figure 4.6: s^2 $[\mathrm{km}^2/\mathrm{s}^2]$ dependence on polar angle θ $[°]$ and either C_{13} $[\mathrm{km}^2/\mathrm{s}^2]$ or C_{23} $[\mathrm{km}^2/\mathrm{s}^2]$

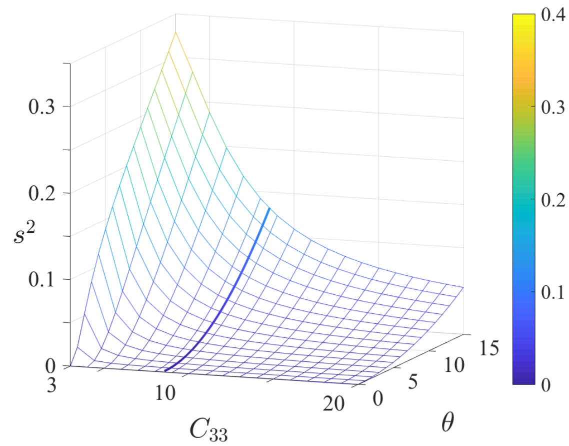

Figure 4.7: s^2 $[\mathrm{km}^2/\mathrm{s}^2]$ dependence on polar angle θ $[°]$ and C_{33} $[\mathrm{km}^2/\mathrm{s}^2]$

Let us analyse Figures 4.4–4.7. Pairs C_{55} and C_{44}, or C_{11} and C_{22}, or C_{13} and C_{23}, occupy analogical places in expressions for $V_{P_{31}}$ and $V_{P_{32}}$ (see Appendix 4.A). To some extent, the coefficients in pairs are related to each other. Therefore, we present Figures 4.4a and 4.4b, or Figures 4.5a and 4.5b, or Figures 4.6a and 4.6b, in pairs. Greater C_{55}, C_{11}, or C_{13} cause $V_{P_{31}}^2$ to be larger, similarly larger C_{44}, C_{22}, or C_{23}, make $V_{P_{32}}^2$ greater (see Appendix 4.A). Therefore, growing C_{55}, C_{11}, or C_{13} have a positive contribution to s^2. On the other hand, increasing C_{44}, C_{22}, or C_{23}, have a negative contribution to $V_{P_{31}}^2 - V_{P_{32}}^2$. All the above statements are reflected in quasi mirror symmetries between figures in pairs.

In the case of Figure 4.4, we cannot see it, because the thick line denoting s^2 for original values of elasticity parameters—common for both graphs—is not near the middle of the horizontal axis. Quasi-mirror symmetry between C_{55} and C_{44} can be seen in Figure 4.8. Mirror symmetries in Figures 4.4–4.6 are not ideal. The small differences in pair graphs are caused by slight differences in original values between pairs C_{55} , C_{44} , or C_{11} , C_{22} , or C_{13} , C_{23} (see values of $C^{C\&al}$). Due to quasi-mirror symmetries, we can conclude that the magnitude of the dependence of s^2 on coefficients in pairs is similar, only the sign differs.

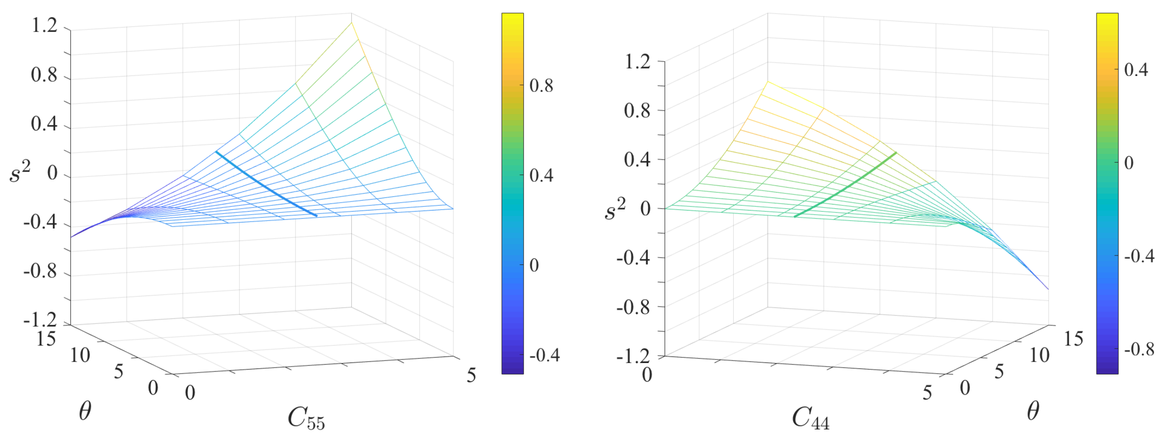

(a) C_{55} **(b)** C_{44}

Figure 4.8: s^2 [$\mathrm{km}^2/\mathrm{s}^2$] dependence on polar angle θ [°] and either C_{55} [$\mathrm{km}^2/\mathrm{s}^2$] or C_{44} [$\mathrm{km}^2/\mathrm{s}^2$]

We notice that the largest magnitude of s^2—either positive or negative—is presented in Figure 4.4. Gradually smaller magnitudes are shown in Figures 4.6, 4.7, and 4.5, respectively. It means that s^2 is the most dependent on changes in pair C_{55} and C_{44}, but the least dependent on C_{11} and C_{22}. We notice that in Figures 4.4–4.7, the slope of each surface is not linear. It means that dependence of s^2 on changes of the magnitude of each elasticity parameter would be different, depending on the value of these parameters. Therefore, the analysis of the graphs shown herein is not universal; figures can differ for other elasticity tensors. To make our analysis more universal, in the next section, we numerically quantify the aforementioned dependence of s^2 to changes of C_{ij} using values of $C^{D\&G}$ and other tensors shown in Appendix 4.B. We try to find the universal relations between these dependencies.

Numerical analysis

Throughout the paper, we use the following notions synonymously: sensitivity, influence, dependence, or contribution. Let us attempt to quantify the contribution of each elasticity parameter to the squared-velocity difference. In other words, we want to confirm the graphical analysis of the dependence of s^2 on particular C_{ij} . To get these contributions, we propose to compute the partial derivatives of s^2 with respect to a particular elasticity parameter for different polar angles. In other words, we treat the ratio of slightly changed, Δs^2 , to slightly changed elasticity parameter, ΔC_{ij} , as a contribution of parameter C_{ij} to s^2 . To compare the magnitudes of these contributions, we verify the proportions between the derivatives. For instance, if $s^2 \approx 2C_{55} + C_{13}$, we interpret it as s^2 being twice more dependent on some value of C_{55} than on some value of C_{13} since $\partial_{C_{55}} s^2 = 2\partial_{C_{13}} s^2$.

To avoid the ambiguity, note that in Section 4.2.2, we have already mentioned a different interpretation of contributions. If we consider the method of derivatives ratios, then coefficients q_1^* , q_2^* , and q_3^* equally contribute to q^* . However, if we do not regard derivatives, but just insert specific values of C_{ij} inside q_i^* terms, then q^* can be interpreted as the most dependent on q_2^* . Herein, however, we decide to focus on a probably more general method of interpretation that uses partial derivatives.

As an example, let us compute $\partial_{C_{55}} s^2$ for values of $C^{C\&al}$ and $\theta = 10^\circ$. We get,

$$\frac{\partial s^2}{\partial C_{55}} = \frac{1}{2} - \frac{f}{4\sqrt{g}} \, , \tag{4.25}$$

where

$$
\begin{aligned}
f &= \cos^4\theta\,(2C_{33}-2C_{55}) + \sin^4\theta\,(2C_{11}-2C_{55}) \\
&\qquad - 2\cos^2\theta\sin^2\theta\,(C_{11}+4C_{13}+C_{33}+2C_{55})\,, \\
g &= \cos^4\theta\,(C_{33}-C_{55})^2 + \sin^4\theta(C_{11}-C_{55})^2 \\
&\qquad + 2\cos^2\theta\sin^2\theta\,(2C_{13}^2+C_{55}^2-C_{11}C_{33}+C_{11}C_{55}+4C_{13}C_{55}+C_{33}C_{55})\,.
\end{aligned}
\tag{4.26}
$$

Upon inserting the values for C_{ij} and θ, we obtain $\partial_{C_{55}}s^2 \approx 0.151$. The rest of the derivatives calculated for $C^{C\&al}$ are presented in Table 4.4. We notice that the changes, Δs^2, are more significant for larger polar angles. The table confirms the analysis of Figures 4.4–4.7. The squared-velocity difference is the most sensitive to the changes in pair C_{55} and C_{44}, whilst the least to pair C_{11} and C_{22}.

Table 4.4: Derivatives $\partial_{C_{ij}}s^2$ computed for $C^{C\&al}$ and various polar angles

	$\theta = 1°$	$\theta = 3°$	$\theta = 5°$	$\theta = 10°$	$\theta = 15°$
$\partial_{C_{55}}s^2$	$1.598 \cdot 10^{-3}$	$14.314 \cdot 10^{-3}$	$39.385 \cdot 10^{-3}$	0.151	0.315
$\partial_{C_{44}}s^2$	$-1.404 \cdot 10^{-3}$	$-12.593 \cdot 10^{-3}$	$-34.721 \cdot 10^{-3}$	-0.134	-0.284
$\partial_{C_{11}}s^2$	$0.155 \cdot 10^{-6}$	$12.486 \cdot 10^{-6}$	$95.760 \cdot 10^{-6}$	$1.489 \cdot 10^{-3}$	$7.194 \cdot 10^{-3}$
$\partial_{C_{22}}s^2$	$-0.122 \cdot 10^{-6}$	$-9.880 \cdot 10^{-6}$	$-75.958 \cdot 10^{-6}$	$-1.195 \cdot 10^{-3}$	$-5.875 \cdot 10^{-3}$
$\partial_{C_{13}}s^2$	$0.786 \cdot 10^{-3}$	$7.041 \cdot 10^{-3}$	$19.374 \cdot 10^{-3}$	0.074	0.155
$\partial_{C_{23}}s^2$	$-0.699 \cdot 10^{-3}$	$-6.266 \cdot 10^{-3}$	$-17.277 \cdot 10^{-3}$	-0.068	-0.141
$\partial_{C_{33}}s^2$	$-0.106 \cdot 10^{-3}$	$-0.949 \cdot 10^{-3}$	$-2.587 \cdot 10^{-3}$	-0.009	-0.018

In Table 4.5, we show the simplified proportions between partial derivatives for each angle. To get these proportions, we divide each derivative by $\partial_{C_{13}}s^2$. We notice that with growing polar angle, s^2 starts to be proportionally more sensitive to C_{55}, C_{44}, C_{11}, C_{22}, C_{13}, and C_{23}, but less sensitive to C_{33}. The last column shows the mean proportions between derivatives so that we can disregard the angle.

Table 4.5: Simplified proportions between derivatives $\partial_{C_{ij}} s^2$ for different polar angles. The last column presents mean proportions.

	$\theta = 1^\circ$	$\theta = 3^\circ$	$\theta = 5^\circ$	$\theta = 10^\circ$	$\theta = 15^\circ$	mean
$\partial_{C_{55}} s^2$	2.0328	2.0328	2.0329	2.0331	2.0335	2.0331
$\partial_{C_{44}} s^2$	-1.7864	-1.7884	-1.7922	-1.8096	-1.8369	-1.8036
$\partial_{C_{11}} s^2$	0.0002	0.0018	0.0049	0.0201	0.0465	0.0153
$\partial_{C_{22}} s^2$	-0.0002	-0.0014	-0.0039	-0.0161	-0.0379	-0.0123
$\partial_{C_{13}} s^2$	1	1	1	1	1	1
$\partial_{C_{23}} s^2$	-0.8890	-0.8899	-0.8918	-0.9003	-0.9136	-0.8974
$\partial_{C_{33}} s^2$	-0.1354	-0.1348	-0.1335	-0.1278	-0.1187	-0.1297

We notice the following relations between derivatives,

$$\partial_{C_{55}} s^2 \approx 2\partial_{C_{13}} s^2 \,, \qquad \partial_{C_{44}} s^2 \approx 2\partial_{C_{23}} s^2 \quad \text{and} \quad -\partial_{C_{33}} s^2 \approx \partial_{C_{13}} s^2 + \partial_{C_{23}} s^2 \,. \quad (4.27)$$

Approximation based on derivatives ratios

Due to the very small dependance of squared-velocity difference on C_{11} or C_{22}, the intuitive approximation (4.19) seems not to be right. Let us improve q^*. We can try to introduce the scaling coefficients in front of the elasticity parameters, as it is done in expression (4.9). In this way, we take into consideration different strength of dependence of s^2 on particular parameters, namely,

$$s^2 \approx \frac{1}{\rho} \sin^2\theta \left(a_1 C_{55} + a_2 C_{44} + a_3 C_{11} + a_4 C_{22} + a_5 C_{13} + a_6 C_{23}\right). \quad (4.28)$$

Also, we should consider the dependence of squared-velocity difference on C_{33}, due to its nonnegligible contribution. We can assume that some of the scaling factors, a_i, depend on C_{33}, so its contribution is considered in approximation (4.28). To be able to estimate a_i, we first need to know the estimated contribution of each elasticity parameter to s^2. Let us use the values from the last column of Table 4.5. The most simple approximation that preserves the proportionality between partial derivatives is

$$s^2 \approx \frac{k}{\rho}\sin^2\theta\,(2.0331C_{55} - 1.8036C_{44} + 0.0153C_{11} \\ - 0.0123C_{22} + C_{13} - 0.8974C_{23} - 0.1297C_{33})\,, \tag{4.29}$$

where k allows us to find the best fit between this approximation and s^2. Let us use the fact that $\partial_{C_{55}}s^2 \approx 2\partial_{C_{13}}s^2$ and $\partial_{C_{44}}s^2 \approx 2\partial_{C_{23}}s^2$. Also, C_{11} and C_{22} have a very small contribution, so let us neglect it. We can rewrite expression (4.29) as,

$$s^2 \approx \frac{k}{\rho}\sin^2\theta\;[2C_{55} + C_{13} - 0.9(2C_{44} + C_{23}) - 0.13C_{33}]\;. \tag{4.30}$$

To obtain the form of the approximation shown in expression (4.28), we need to get rid of the last term. Since in this particular case, $C_{33} \approx 0.9\,(2C_{44} + C_{23})$, we can estimate

$$s^2 \approx \frac{k}{\rho}\sin^2\theta\;[2(C_{55} - C_{44}) + C_{13} - C_{23}]\;. \tag{4.31}$$

The relative error, err, between expessions (4.29) and (4.31) for $\theta \in (0^\circ\,,\,15^\circ]$ is $\approx 2.20\%$. According to expression (4.31), $a_1 = a_2 = 2k$, $a_3 = a_4 = 0$, $a_5 = a_6 = k$, which means that $C_{55} - C_{44}$ has twice larger contribution to s^2 than $C_{13} - C_{23}$ has. In this particular case, the best fit is for $k \approx 2.44$.

Let us check if expressions (4.29)–(4.31) are universal or not. To do so, we compute the derivatives (see Table 4.9) and perform the analogous procedure for $C^{D\&G}$. We get

$$s^2 \approx \frac{k}{\rho}\sin^2\theta\,(2.012C_{55} - 1.473C_{44} + 0.013C_{11} - 0.007C_{22} + C_{13} - 0.731C_{23} - 0.276C_{33}) \tag{4.32}$$

and we can see that the above approximation is different from expression (4.29). Especially the contribution of C_{33} is much greater. We again notice that $\partial_{C_{55}}s^2 \approx 2\partial_{C_{13}}s^2$

and $\partial_{C_{44}} s^2 \approx 2\partial_{C_{23}} s^2$, and we neglect a very small contribution of C_{11} and C_{22} . We obtain

$$s^2 \approx \frac{k}{\rho} \sin^2\theta \; [2C_{55} + C_{13} - 0.73(2C_{44} + C_{23}) - 0.276C_{33}] \; . \tag{4.33}$$

Since in this particular case, $C_{33} \approx 1.15(2C_{44} + C_{23})$ we again can estimate

$$s^2 \approx \frac{k}{\rho} \sin^2\theta \; [2(C_{55} - C_{44}) + C_{13} - C_{23}] \; , \tag{4.34}$$

where the best fit we get if $k \approx 1.98$. The relative error between expessions (4.32) and (4.34) for $\theta \in (0^\circ\,,\,15^\circ]$ is $\approx 14.58\%$. In this case, even if C_{33} has much greater contribution to changes of s^2 than in $C^{C\&al}$ case, again $a_1 = a_2 = 2k$, $a_3 = a_4 = 0$, $a_5 = a_6 = k$. We can follow the analogical procedure for elasticity tensors from Appendix 4.B, that is for $C^{T\&al}$, $C^{S\&al}$, C^{lime} , C^{sand} , $C^{M\&al}$, and $C^{S\&H}$. For every tensor we can obtain the approximation (4.31) with $err < 15\%$.

Let us attempt to choose one common value of k for each tensor in order to make the approximation (4.31) universal. Table 4.6 shows the relative error between approximation and s^2 for each tensor for $\theta \in (0^\circ\,,\,15^\circ]$. We calculate err for different candidates k. If $k = 1.95$ then $err < 20\%$ for each eight elasticity tensors. The smallest k that gives

Table 4.6: Relative error (in $\%$) between expression (4.31) and s^2 for various k

	$k = 1.7$	$k = 1.8$	$k = 1.9$	$k = 1.95$	$k = 2.0$	$k = 2.1$
$C^{C\&al}$	30.18	26.07	21.97	19.91	17.86	13.75
$C^{D\&G}$	13.99	8.93	3.87	1.38	1.19	6.25
$C^{T\&al}$	7.65	2.21	3.22	5.94	8.65	14.09
$C^{S\&al}$	3.41	9.49	15.58	18.62	21.66	27.74
C^{lime}	3.02	3.66	9.42	12.30	15.18	20.94
C^{sand}	1.86	7.30	13.26	16.24	19.22	25.19
$C^{M\&al}$	2.00	8.00	14.00	17.00	20.00	26.00
$C^{S\&H}$	15.41	10.44	5.46	2.97	0.49	4.49

perfect fit is for $C^{S\&al}$, where $k \approx 1.64$. The largest k that gives perfect fit is for $C^{C\&al}$, where $k \approx 2.44$. Hence, based on results from eight elasticity tensors, we can write an approximation that might fit also other orthotropic tensors, namely,

$$s^2 \approx \frac{2 \pm 0.5}{\rho} \sin^2\theta \; [2(C_{55} - C_{44}) + C_{13} - C_{23}] \; . \tag{4.35}$$

It seems that there is no accurate universal approximation akin to expression (4.28), where a_i would be constants. To make it more universal, we need to express a_i in terms of C_{33} and other coefficients.

Let us analyse approximation (4.31). We want to express k in terms of a combination of elasticity parameters—including C_{33}—so that expression (4.31) precisely approximates s^2 with no known *a priori* value of k. By doing numerical experiments, we notice that if $k \approx a + b$ (parameters a and b are previously defined in expression (4.10)), then the aforementioned approximation has always a very good fit. Thus, we propose to consider

$$s^2 \approx q = \frac{a+b}{\rho} \sin^2\theta \; [2(C_{55} - C_{44}) + C_{13} - C_{23}] \; , \tag{4.36}$$

which can be rewritten as

$$\frac{1}{\rho} \sin^2\theta \; [a(C_{13} + C_{55}) - b(C_{23} + C_{44}) + (C_{55} - C_{44}) - c] = t - \frac{c}{\rho} \sin^2\theta \, , \tag{4.37}$$

where

$$c = \frac{(C_{55} - C_{44})(C_{33} - 2C_{55} - C_{13})(C_{33} - 2C_{44} - C_{23})}{(C_{33} - C_{55})(C_{33} - C_{44})} \, . \tag{4.38}$$

The relative error of this approximation is low and is shown in Table 4.7. Let us comment on expression (4.37). Specifically, we focus on relation between c and terms of t. In a weak anisotropy approximation, $\delta^{(1)} << 1$ and $\delta^{(2)} << 1$. In such a case, C_{33} must be close to

Table 4.7: Relative error in $\%$ between q and s^2

	$C^{C\&al}$	$C^{D\&G}$	$C^{T\&al}$	$C^{S\&al}$	C^{lime}	C^{sand}	$C^{M\&al}$	$C^{S\&H}$
err for $\theta \in (0°\,,\,10°]$	0.36	0.62	0.54	0.38	0.97	0.78	0.91	0.20
err for $\theta \in (0°\,,\,15°]$	0.53	1.11	1.17	0.50	2.46	1.78	1.43	0.38

$2C_{55} + C_{13}$ and to $2C_{44} + C_{23}$. Therefore, the absolute value of $C_{33} - 2C_{55} - C_{13}$ is much smaller than the value of $C_{33} - C_{55}$. In analogous way, $|C_{33} - 2C_{44} - C_{23}|$ is much smaller than $C_{33} - C_{44}$. Thus, in a weak anisotropy case $C_{55} - C_{44}$ is much greater than c . Based on a calculation of each elasticity tensor, this is true even in the case of stronger anisotropy. Also, we notice that $a(C_{13} + C_{55}) - b(C_{23} + C_{44})$ is much greater than $C_{55} - C_{44}$. In other words, the last term in squared parenthesis in approximation,

$$q = \frac{1}{\rho} \sin^2\theta \; [a(C_{13} + C_{55}) - b(C_{23} + C_{44}) + (C_{55} - C_{44}) - c] \; , \tag{4.39}$$

in comparison to the rest of the terms, is very small and can be neglected. Hence, we can write

$$q = \frac{a+b}{\rho} \sin^2\theta \; [2(C_{55} - C_{44}) + C_{13} - C_{23}] = t - \frac{c}{\rho} \sin^2\theta \approx t \, . \tag{4.40}$$

The relative error between approximation t and s^2, shown in Table 4.8, is very similar to the one between q and s^2 from Table 4.7, as expected.

Table 4.8: Relative error $(\text{in } \%)$ between t and s^2

	$C^{C\&al}$	$C^{D\&G}$	$C^{T\&al}$	$C^{S\&al}$	C^{lime}	C^{sand}	$C^{M\&al}$	$C^{S\&H}$
err for $\theta \in (0°\,,\,10°]$	0.32	0.38	0.53	0.10	1.30	1.01	0.43	0.25
err for $\theta \in (0°\,,\,15°]$	0.71	0.87	1.15	0.22	3.02	2.29	0.95	0.51

Let us follow a different approach to verify the correctness of approximations q and t again. We propose to check if their partial derivatives preserve similar proportions as the partial derivatives computed for s^2 and shown in Table 4.5. The calculated partial derivatives for

s^2, q, and t are shown in Table 4.9. We notice that s^2, q, and t have similar proportions between derivatives. This is true for each eight elasticity tensors. Thus, the correct proportions of derivatives and tiny relative errors between q and s^2, or t and s^2, indicate that we formulate approximations q and t correctly. We also notice that each tensor obeys the relations from expression (4.27); hence, these relations seem to be universal.

Table 4.9: Simplified proportions between derivatives $\partial_{C_{ij}} s^2$, $\partial_{C_{ij}} q$ and $\partial_{C_{ij}} t$, computed for eight different elasticity tensors. The proportions calculated for s^2 are averaged for angles $\theta \in (0^\circ\,,\,15^\circ]$.

	$C^{C\&al}$	$C^{D\&G}$	$C^{T\&al}$	$C^{S\&al}$	C^{lime}	C^{sand}	$C^{M\&al}$	$C^{S\&H}$
$\partial_{C_{55}} s^2$	2.0331	2.0121	2.0002	2.0097	2.0082	2.0061	2.0464	2.0052
$\partial_{C_{44}} s^2$	−1.8036	−1.4726	−1.7308	−1.7960	−2.0474	−1.8135	−2.4536	−2.4919
$\partial_{C_{11}} s^2$	0.0153	0.0133	0.0115	0.0099	0.0100	0.0101	0.0084	0.0106
$\partial_{C_{22}} s^2$	−0.0123	−0.0073	−0.0086	0.0077	−0.0104	−0.0082	−0.0127	−0.0160
$\partial_{C_{13}} s^2$	1	1	1	1	1	1	1	1
$\partial_{C_{23}} s^2$	−0.8974	−0.7309	−0.8597	−0.8820	−1.0208	−0.8955	−1.2240	−1.2408
$\partial_{C_{33}} s^2$	−0.1297	−0.2764	−0.1320	−0.0979	0.0188	−0.0900	0.1874	0.2513
$\partial_{C_{55}} q$	2.0156	2.0249	1.9986	1.9919	2.0017	1.9936	2.0312	2.0140
$\partial_{C_{44}} q$	−1.7856	−1.4538	−1.7177	−1.7666	−2.0534	−1.7552	−2.4751	−2.5316
$\partial_{C_{13}} q$	1	1	1	1	1	1	1	1
$\partial_{C_{23}} q$	−0.8965	−0.7153	−0.8529	−0.8761	−1.0273	−0.8714	−1.2434	−1.2577
$\partial_{C_{33}} q$	−0.1264	−0.2860	−0.1339	−0.1014	0.0243	−0.1097	0.2003	0.2597
$\partial_{C_{55}} t$	2.0330	2.0123	2.0002	2.0097	2.0086	2.0056	2.0471	2.0073
$\partial_{C_{44}} t$	−1.7866	−1.4407	−1.7211	−1.7902	−2.0520	−1.7976	−2.4631	−2.5260
$\partial_{C_{13}} t$	1	1	1	1	1	1	1	1
$\partial_{C_{23}} t$	−0.8890	−0.7143	−0.8538	−0.8793	−1.0230	−0.8876	−1.2284	−1.2589
$\partial_{C_{33}} t$	−0.1354	−0.2856	−0.1330	−0.0987	0.0204	−0.0956	0.1875	0.2595

Let us analyse the meaning of $a+b$, namely,

$$a+b=\frac{C_{13}+C_{55}}{C_{33}-C_{55}}+\frac{C_{23}+C_{44}}{C_{33}-C_{44}}\,. \tag{4.41}$$

If we multiply each elasticity parameter by the same value, $a+b$ remains unchanged. Therefore, we should focus our attention on proportions between the elasticity parameters, not on their magnitudes. Larger values of C_{33} cause $a+b$ to be smaller. On the other hand, greater C_{55} , C_{44} , C_{13} , or C_{23} , cause $a+b$ to be larger. Hence, we deduce that larger C_{55}/C_{33} , C_{44}/C_{33} , C_{13}/C_{33} , or C_{23}/C_{33} , make $a+b$ bigger. Further, proportions C_{55}/C_{33} or C_{44}/C_{33} seem to influence $a+b$ much more, in comparison to C_{13}/C_{33} , or C_{23}/C_{33} . This is because C_{55} and C_{44} decrease the denominators and increase numerators, whereas C_{13} and C_{23} only increase numerators. The aforementioned dominance of C_{55} over C_{13} and C_{44} over C_{23} is confirmed if we compare their derivatives, namely,

$$\frac{\partial(a+b)}{\partial C_{55}} = \frac{1}{C_{33}-C_{55}} + \frac{C_{13}+C_{55}}{(C_{33}-C_{55})^2}\,, \tag{4.42}$$

$$\frac{\partial(a+b)}{\partial C_{13}} = \frac{1}{C_{33}-C_{55}}\,, \tag{4.43}$$

$$\frac{\partial(a+b)}{\partial C_{44}} = \frac{1}{C_{33}-C_{44}} + \frac{C_{23}+C_{44}}{(C_{33}-C_{44})^2}\,, \tag{4.44}$$

$$\frac{\partial(a+b)}{\partial C_{23}} = \frac{1}{C_{33}-C_{44}}\,. \tag{4.45}$$

We see clearly that expression (4.42) is larger than expression (4.43) by the second term. In analogous way, expression (4.44) is larger than expression (4.45). Therefore, we can state that the magnitude of $a+b$ depends mostly on C_{55}/C_{33} and C_{44}/C_{33} . To a lesser extent, it also depends on C_{13}/C_{33} and C_{23}/C_{33} .

4.2.4 Sensitivity study: changes of anisotropy parameters

In the previous section, we have quantified the contributions of each elasticity parameter to the squared-velocity difference. Herein, we want to obtain the analogical results, but for the anisotropy parameters defined in Tsvankin (1997). To do so, we again check the proportions between partial derivatives. In this section, however, we compute the derivatives with respect to the anisotropy parameters, instead of elasticity parameters.

First, let us consider a weak-anisotropy approximation. Since, expression (4.6) contains unwanted elasticity parameter C_{33} , we propose to consider a normalised value,

$$\frac{s^2}{C_{33}} = \frac{V_{P_{31}}^2 - V_{P_{32}}^2}{V_{P_3}^2} \approx \left(2\sin^2\theta - 2\sin^4\theta\right)\left(\delta^{(2)} - \delta^{(1)}\right) + 2\sin^4\theta\left(\epsilon^{(2)} - \epsilon^{(1)}\right) \,, \tag{4.46}$$

where V_{P_3} is a P-wave velocity propagating along the x_3-axis. The partial derivatives of s^2/C_{33} computed with respect to each anisotropy parameter depend on angle solely. For small angles, the above expression is sensitive to the difference $\delta^{(2)} - \delta^{(1)}$. The epsilons contribute significantly for large polar angles only. For instance, if $\theta = 15^\circ$, then the contribution of $\delta^{(2)} - \delta^{(1)}$ is around fourteen times larger than the contribution of $\epsilon^{(2)} - \epsilon^{(1)}$. However, if $\theta = 30^\circ$, then it is only three times larger.

Due to the simple form of expression (4.46), the analysis of the weak-anisotropy case is trivial. The situation becomes more complicated if we study the exact value of s^2/C_{33} , since we get

$$\begin{aligned}\frac{s^2}{C_{33}} = \sin^2\theta\left(\epsilon^{(2)} - \epsilon^{(1)}\right) + \frac{f^{(2)}}{2}&\left[\sqrt{\left(1 + \frac{2\epsilon^{(2)}\sin^2\theta}{f^{(2)}}\right)^2 - \frac{2\left(\epsilon^{(2)} - \delta^{(2)}\right)\sin^2(2\theta)}{f^{(2)}}} - 1\right] \\ - \frac{f^{(1)}}{2}&\left[\sqrt{\left(1 + \frac{2\epsilon^{(1)}\sin^2\theta}{f^{(1)}}\right)^2 - \frac{2\left(\epsilon^{(1)} - \delta^{(1)}\right)\sin^2(2\theta)}{f^{(1)}}} - 1\right] ,\end{aligned} \tag{4.47}$$

where

$$f^{(2)} := 1 - \frac{C_{55}}{C_{33}} = 1 - \frac{V_{S_V}^2}{V_{P_3}^2} \,, \qquad f^{(1)} := 1 - \frac{C_{44}}{C_{33}} = 1 - \frac{V_{S_H}^2}{V_{P_3}^2} \,. \tag{4.48}$$

The superscript refers to the axis direction that defines the orientation of the symmetry plane for which given parameter is obtained. V_{S_V} and V_{S_H} denote velocities of S-waves propagating vertically with displacements polarised in x_1 and x_2 directions, respectively.

The partial derivatives do not depend on the angle solely. They are also sensitive to the values of the elasticity tensor that we use. Note that expression (4.47) consists of six coefficients $\epsilon^{(1)}$, $\epsilon^{(2)}$, $\delta^{(1)}$, $\delta^{(2)}$, $f^{(1)}$, and $f^{(2)}$ that in total depend on seven (not six) distinct elasticity parameters, as expected. In Table 4.10, we show the simplified proportions between the partial derivatives. The derivatives are computed with respect to the anisotropy parameters obtained from $C^{C\&al}$.

Table 4.10: Partial derivatives of s^2/C_{33} with respect to anisotropy parameters. Values of parameters are obtained from $C^{C\&al}$. Normalised derivatives are computed for various polar angles.

	$\theta = 1°$	$\theta = 5°$	$\theta = 15°$	$\theta = 30°$
$\partial_{\epsilon^{(2)}}(s^2/C_{33})$	1	1	1	1
$\partial_{\epsilon^{(1)}}(s^2/C_{33})$	-0.790	-0.793	-0.817	-0.134
$\partial_{\delta^{(2)}}(s^2/C_{33})$	$1.969 \cdot 10^3$	78.349	8.333	1.784
$\partial_{\delta^{(1)}}(s^2/C_{33})$	$-1.969 \cdot 10^3$	-78.606	-8.565	-1.945
$\partial_{f^{(2)}}(s^2/C_{33})$	0.012	0.012	0.012	0.010
$\partial_{f^{(1)}}(s^2/C_{33})$	-0.008	-0.008	-0.007	-0.005

We see that the exact value of s^2/C_{33} depends mostly on $\delta^{(1)}$ and $\delta^{(2)}$. Only for large angles, the contribution of epsilons is more significant. The contribution of $f^{(1)}$ and $f^{(2)}$ is small and can be omitted. Similar results can be obtained for other elasticity tensors from Appendix 4.B.

4.3 Summary and discussion

In Section 4.2.1, we discuss the solutions of Christoffel's equations to understand the general relationship between elasticity parameters and P-wave velocity propagating in axis planes. Also, we present this dependence graphically. Subsequently, in Section 4.2.2, we focus on the squared-velocity difference. Due to a complicated form of s^2, we consider its approximations. We show the approximation t, which simplifies the terms in s^2. However, t occurs not to be intuitive enough to understand which parameters or simple relations between parameters—such as addition or subtraction—influence the squared-velocity difference more. For instance, it is difficult to interpret the meaning of $t_2 - t_3$ unambiguously. We do not know what the influence of, for instance, $C_{13} - C_{23}$, or C_{33} is. We propose other, more simple, estimators. The approximations t_1 and q^* occur not to be accurate, but give us an insight on how to improve them. Therefore, in Section 4.2.3, we make the next step and perform a sensitivity study. Based on a numerical experiment, we present Figures 4.4–4.7 that show the dependence of s^2 on each elasticity parameter. Subsequently, we formulate the aforementioned dependence in terms of partial derivatives of s^2 with respect to each elasticity coefficient. If we look at the derivatives exposed in Table 4.9, we notice the following relations between them. In general,

$$\partial_{C_{55}} s^2 \approx 2\partial_{C_{13}} s^2 \,, \qquad \partial_{C_{44}} s^2 \approx 2\partial_{C_{23}} s^2 \quad \text{and} \quad -\partial_{C_{33}} s^2 \approx \partial_{C_{13}} s^2 + \partial_{C_{23}} s^2 \,. \tag{4.49}$$

Also, based on eight numerical experiments, we notice that $\partial_{C_{33}} s^2 / \partial_{C_{13}} s^2 \in (0\,,\, 0.28)$.

Further, we use the computed derivatives to formulate a new, improved approximation, q, which—similarly to t—has the general form shown in expression (4.28). We have proposed

$$s^2(\theta \leq 15^\circ) \approx q = \frac{\sin^2\theta}{\rho}\left(\frac{C_{13}+C_{55}}{C_{33}-C_{55}} + \frac{C_{23}+C_{44}}{C_{33}-C_{44}}\right)(2C_{55} - 2C_{44} + C_{13} - C_{23})\,, \tag{4.50}$$

which preserves similar proportions between derivatives, as t and s^2 do. Approximation q is accurate for $\theta \leq 15^\circ$, but it does not necessarily always give better results than t. However, it shows the relations between elasticity coefficients more clearly and simply. In other words, the aim of proposing q is not to find the most accurate approximation of s^2, but to show clearly on which simple relations between elasticity parameters the squared-velocity difference depends. First-term on the left in expression (4.50) considers the influence of polar angle and mass density. The first parenthesis tells us about the dependence on proportions of C_{55}/C_{33}, C_{44}/C_{33}, C_{13}/C_{33}, and C_{23}/C_{33}. The second parenthesis corresponds to the differences between pairs C_{55}, C_{44}, and C_{13}, C_{23}. It is worth to notice that C_{55}/C_{33} and C_{44}/C_{33} are the velocity ratios of vertically propagating S-waves to P-wave. The larger the ratio, the higher s^2. The above statement can be of a great significance in the context of practical studies. In particular, it means that the azimuthal measurement of P-wave velocity can give us information on, for instance, zones with anomalously high S/P-wave ratio. As commonly known, such zones may be porous, gas-saturated sandstone rocks. Hence, anomalously high s^2 might indicate the presence of gas in natural fractures or aligned porosity. In general, the magnitude of s^2 tells us about the strength of the orthotropic anisotropy, for instance, induced by fractures (see differences $2C_{55} - 2C_{44}$ and $C_{13} - C_{23}$ presented in q). However, if we perform some azimuthal measurements in the zone, in which we expect similar strength of orthotropic anisotropy and the results would differ significantly from each other, we can expect that these differences are caused by the presence of gas in some part of the zone (see first parenthesis of q). Additionally, in Section 4.2.4, we have examined the influence of each traditional anisotropy parameter on squared-velocity difference normalised by C_{33}.

To compute the derivatives of s^2 for particular elasticity or anisotropy parameters, we have performed numerical experiments on eight elasticity tensors. These tensors differ from each other in a meaningful manner. Some of them represent relation $C_{44} > C_{55}$, others $C_{44} < C_{55}$. Also, the proportions between C_{11}, C_{22}, and C_{33} are different for every tensor. Further, C_{13} is either larger than C_{23}, or smaller. Some tensors are strongly anisotropic, whereas the others are not. They represent a variety of situations in the context of elasticity or geology. Therefore, their examination gives sufficiently universal results. However, consideration of more examples would give even more reliability to the conclusions.

To sum up, we use two combined strategies to understand the dependence of P-wave phase velocity on elasticity parameters in orthotropic media. We look for an insightful approximation of s^2 and perform a sensitivity study based on the proportions between partial derivatives of s^2 with respect to the individual parameters. Thus, we focus on consideration of the squared-velocity difference resulted from the wave propagation in two mutually-orthogonal vertical symmetry planes. However, to some extent, this consideration is also valid for the velocity difference. As shown in Figure 4.3a, the ratio $s^2/(V_{P_{31}} - V_{P_{32}})$ is similar for the angles $\theta \in [0^\circ\,,\,15^\circ]$. Also, the proportions between derivatives computed for s^2 or $V_{P_{31}} - V_{P_{32}}$ occur to be similar. On the other hand, the approximations derived herein are not valid for the velocity difference. In the future, we should check to which extent the conclusions reasonable for squared-velocity difference are valid for $V_{P_{31}} - V_{P_{32}}$. Also, we believe that the partial-derivatives strategy should be easily implemented in the context of wave propagation beyond symmetry planes.

4.4 Conclusions

Let us enumerate the main results obtained in this paper, which concern the influence of elasticity parameters on s^2; thus, on the difference between squared-velocity propagating in the x_3x_1-plane and the x_3x_2-plane of the orthotropic medium. In the context of the effective medium theory (e.g., Bakulin et al., 2000), s^2 can be regarded as a parameter evaluating the influence of cracks—embedded in the background medium—parallel to one or both of the aforementioned planes.

1. Based on derivatives of s^2 with respect to C_{ij}, we conclude that s^2 depends:

- around twice more on C_{55} in comparison to the influence of C_{13} ,
- around twice more on C_{44} in comparison to the influence of C_{23} ,
- around equally on $-C_{33}$ as on the contribution of the sum of C_{13} and C_{23} , or analogously, around twice less on $-C_{33}$ than on the contribution of the sum of C_{55} and C_{44} ,
- in a small manner on C_{11} and C_{22} (which is true for small θ only),
- on the polar angle. We notice that the contributions of each elasticity parameter are changing with angle. The contribution of C_{55} , C_{44} , C_{13} , C_{23} , C_{11} , and C_{22} grow with polar angle, whereas the contribution of C_{33} decreases.

2. We have presented approximations t and q , which, based on eight examples, estimate s^2 with a relative error $err \leq 1.3\,\%$ for polar angle $\theta \in (0^\circ\,,\,10^\circ]$, and with $err < 3.1\,\%$ for $\theta \in (0^\circ\,,\,15^\circ]$.

3. Based on approximation q , we can state that s^2 depends on:
   - difference $2C_{55} - 2C_{44}$. The larger difference causes s^2 to be larger.
   - difference $C_{13} - C_{23}$. Again, a larger difference causes s^2 to be larger.
   - proportions of C_{33} to C_{55} , C_{44} , C_{13} , and C_{23} . We notice that s^2 is more influenced by C_{55}/C_{33} and C_{44}/C_{33} , than by C_{13}/C_{33} and C_{23}/C_{33} . Larger ratios cause s^2 to be larger.

4. As mentioned above, s^2 does not depend on sole magnitudes of the elasticity coefficients, but on the relations between them, such as differences and proportions. It much depends on the velocity difference between vertical S-wave with vertical displacements, V_{S_V} , and vertical S-wave with horizontal displacements, V_{S_H} . Also, it much depends on the proportion of the aforementioned velocities with the velocity

of vertically propagating P-wave, V_{P_3}. In other words, if $V_{S_V} - V_{S_H}$ is large and V_{S_V}/V_{P_3}, V_{S_H}/V_{P_3} are large, then we expect high s^2. Thus, in real-data cases, we should observe larger azimuthal fluctuations of P-wave in the presence of gas than in the case of its absence. In practice, we can treat high value of s^2 as a gas indicator.

5. We have not find the universal approximation of the simple form $s^2 \approx \sin^2\theta/\rho\,(a_1C_{55} + a_2C_{44} + a_3C_{11} + a_4C_{22} + a_5C_{13} + a_6C_{23})$, where a_i would be constants. Estimators $s^2 \approx q^* = \sin^2\theta/\rho\,(C_{55} - C_{44} + C_{11} - C_{22} + C_{13} - C_{23})$ and $s^2 \approx t_1 = \sin^2\theta/\rho\,(C_{55} - C_{44})$ usually do not work. The most universal is $s^2 \approx \sin^2\theta/\rho\,(k = 2 \pm 0.5)(2C_{55} - 2C_{44} + C_{13} - C_{23})$. However, the consideration of C_{33} is needed to make it more universal. If we express a_i in terms of C_{33} and other parameters, then we can obtain universal approximations q or t.

Additionally, we have examined the influence of the anisotropy parameters $\epsilon^{(1)}$, $\epsilon^{(2)}$, $\delta^{(1)}$, and $\delta^{(2)}$ on normalised squared-velocity difference, s^2/C_{33}. For small polar angles, say $\theta < 15^\circ$, only the difference $\delta^{(2)} - \delta^{(1)}$ has a significant contribution. For larger angles, the influence of the epsilons should be taken into account as well.

Acknowledgements

We want to thank Heloise Lynn, who inspired the author to pursue the topic of this paper. We are grateful for her numerous and insightful comments. Also, we wish to acknowledge consultations with supervisor Michael A. Slawinski. Reviews by Yuriy Ivanov and Igor Ravve helped to improve the manuscript. This research was performed in the context of The Geomechanics Project supported by Husky Energy. Also, this research is partially supported by the Natural Sciences and Engineering Research Council of Canada, grant 202259. The author has no conflict of interest to declare.

Data Availability Statement

The data that support the findings of this study are available from the corresponding author upon reasonable request.

4.5 References

Bakulin, A., Grechka, V., and Tsvankin, I. (2000). "Estimation of fracture parameters from reflection seismic data–Part II: Fractured models with orthorhombic symmetry". *Geophysics*, 65 (6), 1803–1817.

Cheadle, S. P., Brown, R. J., and Lawton, Don C. (1991). "Orthorhombic anisotropy: A physical seismic modeling study". *Geophysics*, 56 (10), 1603–1613.

Dewangan, P. and Grechka, V. (2003). "Inversion of multicomponent, multiazimuth, walkaway VSP data for the stiffness tensor". *Geophysics*, 68 (3), 1022–1031.

Helbig, K. (1994). *Foundations of anisotropy for exploration seismics*. Pergamon Press.

Helbig, K. and Schoenberg, M. (1987). "Anomalous polarization of elastic waves in transversely isotropic media". *J. Acoust. Soc. Am.* 81 (5), 1235–1245.

Koren, Z. and Ravve, I. (2017). "Fourth-order normal moveout velocity in elastic layered orthorhombic media – Part 2: Offset-azimuth domain". *Geophysics*, 82 (3), C113–C132.

Lynn, H. (2014). "Field data evidence of orthorhombic media: changes in the P-P bright azimuth with angle of incidence". *SEG Expanded Abstracts*.

Mahmoudian, F., Margrave, G., Daley, P. F., and Wong, J. (2012). "Estimation of stiffness coefficients of an orthorhombic physical model from group velocity measurements". *CREWES Research Report*, 24 (1), 1–16.

Mensch, T. and Rasolofosaon, P. (1997). “Elastic-wave velocities in anisotropic media of arbitrary symmetry–generalization of Thomsen’s parameters ϵ, δ and γ”. *Geophys. J. Int.* 128 (1), 43–64.

Mouchat, F. and Coudert, F. X. (2014). “Necessary and Sufficient Elastic Stability Conditions in Various Crystal Systems”. *Phys. Rev. B*, 90 (22), 1–4.

Osinowo, O. O., Chapman, M., Bell, R., and Lynn, H. B. (2017). “Modelling Orthorhombic Anisotropic Effects for Reservoir Fracture Characterization of a Naturally Fractured Tight Carbonate Reservoir, Onshore Texas, USA”. *Pure Appl. Geophys.* 174 (11), 4137–4152.

Schoenberg, M. and Helbig, K. (1997). “Orthorhombic media: Modeling elastic wave behavior in a vertically fractured earth”. *Geophysics*, 62 (6), 1954–1974.

Slawinski, M. A. (2018). *Waves and rays in seismology: Answers to unasked questions*. 2nd edn. World Scientific.

Svitek, T., Vavryčuk, V., Lokajíček, T., and Petružálek, M (2014). “Determination of elastic anisotropy of rocks from P- and S-wave velocities: numerical modelling and lab measurements”. *Geophys. J. Int.* 199 (3), 1682–1697.

Takanashi, M., Nishizawa, O., Kanagawa, K., and Yasunaga, K. (2001). “Laboratory measurements of elastic anisotropy parameters for the exposed crustal rocks from the Hidaka Metamorphic Belt, Central Hokkaido, Japan”. *Geophys. J. Int.* 145 (1), 33–47.

Thomsen, L. (1986). “Weak elastic anisotropy”. *Geophysics*, 51 (10), 1954–1966.

Tsvankin, I. (1997). “Anisotropic parameters and P-wave velocity for orthorhombic media”. *Geophysics*, 62 (4), 1292–1309.

4.A Christoffel's equations for orthotropic media

Let us invoke equation (4.1), namely,

$$\det\left[\sum_{j=1}^{3}\sum_{\ell=1}^{3} c_{ijk\ell}(\boldsymbol{x})n_j n_\ell - \rho(\boldsymbol{x})V^2\delta_{ik}\right] = \mathbf{0}\,, \qquad i,\, k = 1,\, 2,\, 3\,. \tag{4.51}$$

Herein, we solve the above equation for the orthotropic symmetry class. An orthotropic material with symmetry planes coinciding with the coordinate planes has the following elasticity parameters, expressed in Voigt's notation,

$$\boldsymbol{C}^{\mathrm{ort}} = \begin{bmatrix} C_{11} & C_{12} & C_{13} & 0 & 0 & 0 \\ C_{12} & C_{22} & C_{23} & 0 & 0 & 0 \\ C_{13} & C_{23} & C_{33} & 0 & 0 & 0 \\ 0 & 0 & 0 & C_{44} & 0 & 0 \\ 0 & 0 & 0 & 0 & C_{55} & 0 \\ 0 & 0 & 0 & 0 & 0 & C_{66} \end{bmatrix}. \tag{4.52}$$

To replace $c_{ijk\ell}$ by C_{mn} , we have used index symmetries of $c_{ijk\ell}$ and followed

$$\begin{cases} m = i & \text{if } i = j \\ n = \ell & \text{if } \ell = k \end{cases} \quad \text{and} \quad \begin{cases} m = 9-(i+j) & \text{if } i \neq j \\ n = 9-(\ell+k) & \text{if } \ell \neq k \end{cases}. \tag{4.53}$$

We assume that waves propagate through the point; therefore, we disregard the dependance on position, $\boldsymbol{x}$. We set x_3 to be the axis denoting the direction of depth. The solution of phase velocities propagating in an arbitrary direction is complicated to show in terms of the elasticity parameters. For instance, Appendix A in Tsvankin (1997) is dedicated to such representation. Herein, we present the solutions for the wave propagating in the:

x_3x_1-plane,

$$V_{P_{31},S_V}(\theta_1) = \sqrt{\frac{(C_{33}+C_{55})\cos^2\theta_1 + (C_{11}+C_{55})\sin^2\theta_1 \pm \sqrt{D(\theta_1)}}{2\rho}}\,, \tag{4.54}$$

$$V_{S_H}(\theta_1) = \sqrt{\frac{C_{44}\cos^2\theta_1 + C_{66}\sin^2\theta_1}{\rho}}\,, \tag{4.55}$$

$$\begin{aligned} D(\theta_1) = {} & (C_{33}-C_{55})^2\cos^4\theta_1 + (C_{11}-C_{55})^2\sin^4\theta_1 + \\ & 2\cos^2\theta_1\sin^2\theta_1\left(2C_{13}^2 + C_{55}^2 - C_{11}C_{33} + C_{11}C_{55} + C_{33}C_{55} + 4C_{13}C_{55}\right)\,, \end{aligned} \tag{4.56}$$

the x_3x_2-plane,

$$V_{P_{32},S_V}(\theta_2) = \sqrt{\frac{(C_{33}+C_{44})\cos^2\theta_2 + (C_{22}+C_{44})\sin^2\theta_2 \pm \sqrt{D(\theta_2)}}{2\rho}}\,, \tag{4.57}$$

$$V_{S_H}(\theta_2) = \sqrt{\frac{C_{55}\cos^2\theta_2 + C_{66}\sin^2\theta_2}{\rho}}\,, \tag{4.58}$$

$$\begin{aligned} D(\theta_2) = {} & (C_{33}-C_{44})^2\cos^4\theta_2 + (C_{22}-C_{44})^2\sin^4\theta_2 + \\ & 2\cos^2\theta_2\sin^2\theta_2\left(2C_{23}^2 + C_{44}^2 - C_{22}C_{33} + C_{22}C_{44} + C_{33}C_{44} + 4C_{23}C_{44}\right)\,, \end{aligned} \tag{4.59}$$

and the x_1x_2-plane,

$$V_{P_{12},S_H}(\phi) = \sqrt{\frac{(C_{11}+C_{66})\cos^2\phi + (C_{22}+C_{66})\sin^2\phi \pm \sqrt{D(\phi)}}{2\rho}}\,, \tag{4.60}$$

$$V_{S_V}(\phi) = \sqrt{\frac{C_{55}\cos^2\phi + C_{44}\sin^2\phi}{\rho}}\,, \tag{4.61}$$

$$D(\phi) = (C_{11} - C_{66})^2 \cos^4 \phi + (C_{22} - C_{66})^2 \sin^4 \phi +$$
$$2 \cos^2 \phi \sin^2 \phi \left(2C_{12}^2 + C_{66}^2 - C_{11}C_{22} + C_{11}C_{66} + C_{22}C_{66} + 4C_{12}C_{66}\right) . \tag{4.62}$$

$V_{P_{31}}$, $V_{P_{32}}$, and $V_{P_{12}}$ denote P-wave propagating in the x_3x_1-plane, the x_3x_2-plane, and the x_1x_2-plane, respectively. V_{S_V} denotes quasi S-wave with the particle displacement in the vertical plane. V_{S_H} denotes quasi S-wave with particle displacement in the horizontal plane. We denote the polar angle by θ_i , where $i = 1$ and $i = 2$ correspond to the inclination in the x_3x_1-plane and the x_3x_2-plane, respectively. The azimuthal angle, ϕ , expresses the angle inclined from x_1 towards x_2 . If $C_{55} = C_{44}$, $C_{11} = C_{22}$, and $C_{13} = C_{23}$, then $V_{P_{31}} = V_{P_{32}}$, which is the case of tetragonal or (if additionally $C_{11} = C_{12} + 2C_{66}$) transversely-isotropic media.

If in expressions (4.54)–(4.56) or (4.57)–(4.59), we set $\theta_i = 0°$, then the wave propagation is parallel to the x_3-axis and we obtain

$$V_{P_3} = \sqrt{\frac{C_{33}}{\rho}} , \quad V_{S_V} = V_{S_{31}} = \sqrt{\frac{C_{55}}{\rho}} , \quad V_{S_H} = V_{S_{32}} = \sqrt{\frac{C_{44}}{\rho}} . \tag{4.63}$$

Similarly, if in expressions (4.57)–(4.59) we set $\theta_2 = 90°$ (or in expressions (4.60)–(4.62) we set $\phi = 90°$), then the wave propagation is parallel to the x_2-axis and we get

$$V_{P_2} = \sqrt{\frac{C_{22}}{\rho}} , \quad V_{S_V} = V_{S_{23}} = \sqrt{\frac{C_{44}}{\rho}} , \quad V_{S_H} = V_{S_{21}} = \sqrt{\frac{C_{66}}{\rho}} . \tag{4.64}$$

Finally, if in expressions (4.54)–(4.56) we set $\theta_1 = 90°$ (or in expressions or (4.60)–(4.62) we set $\phi = 0°$), then the wave propagation is parallel to the x_1-axis and we obtain

$$V_{P_1} = \sqrt{\frac{C_{11}}{\rho}} , \quad V_{S_V} = V_{S_{13}} = \sqrt{\frac{C_{55}}{\rho}} , \quad V_{S_H} = V_{S_{12}} = \sqrt{\frac{C_{66}}{\rho}} . \tag{4.65}$$

The index of P-waves denotes the direction of propagation parallel to one axis. First index of S-waves denotes the direction of propagation, while the second index denotes the direction of particle displacement.

From a practical point of view, an orthotropic symmetry class can be, for instance, a good analogy to flat-layered sedimentary rocks with one set of vertical aligned fractures parallel to either the x_1-axis or the x_2-axis. We show both situations in Figures 4.9a and 4.9b. The velocity propagating in the horizontal plane is often larger than the velocity which propagates vertically. Also, the velocity of wave propagating in a parallel way to cracks is larger than the wave that propagates perpendicularly to cracks. Hence, if the cracks are set to be parallel to the x_1-axis (see Figure 4.9a), then $V_{P_1} > V_{P_2} > V_{P_3}$ and we expect $C_{11} > C_{22} > C_{33}$. Also, $V_{S_{31}} > V_{S_{32}}$, $V_{S_{12}} > V_{S_{13}}$, $V_{S_{21}} > V_{S_{23}}$; therefore, $C_{66} > C_{55} > C_{44}$. On the other hand, if cracks are parallel to x_2 (see Figure 4.9b), then $V_{P_2} > V_{P_1} > V_{P_3}$ and $C_{22} > C_{11} > C_{33}$. Also, $V_{S_{32}} > V_{S_{31}}$, $V_{S_{12}} > V_{S_{13}}$, $V_{S_{21}} > V_{S_{23}}$; therefore, $C_{66} > C_{44} > C_{55}$. The above considerations are in accordance with expressions (4.63)–(4.65).

4.B Examples of elasticity tensors

In this paper, we base our numerical studies on the values of elasticity parameters coming from the following eight matrices representing the orthotropic tensors. All the elasticity coefficients are density-scaled and are in $\mathrm{km}^2/\mathrm{s}^2$. We use parameters that correspond to

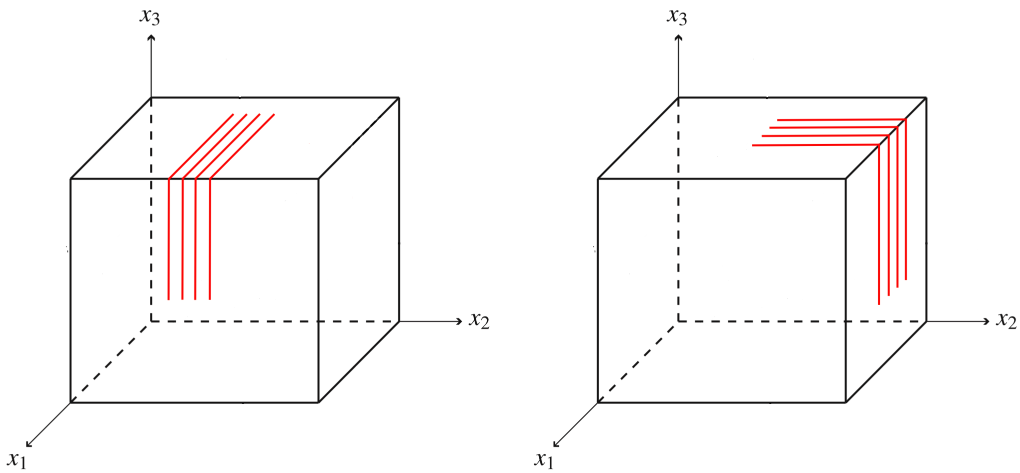

(a) $C_{11} > C_{22} > C_{33}$ and $C_{66} > C_{55} > C_{44}$ **(b)** $C_{22} > C_{11} > C_{33}$ and $C_{66} > C_{44} > C_{55}$

Figure 4.9: Flat-layered sedimentary rock with a set of cracks (in red) parallel to either the x_1-axis or the x_2-axis, as a good analogy of an orthotropic medium with symmetry planes coinciding with coordinate planes. We show typical relationships between elasticity parameters that we expect in real-data cases.

the orthotropic phenolic laminate shown in Cheadle et al. (1991),

$$C^{\mathrm{C\&al}} = \begin{bmatrix} 12.788 & 5.471 & 5.138 & 0 & 0 & 0 \\ 5.471 & 11.323 & 4.884 & 0 & 0 & 0 \\ 5.138 & 4.884 & 8.556 & 0 & 0 & 0 \\ 0 & 0 & 0 & 2.298 & 0 & 0 \\ 0 & 0 & 0 & 0 & 2.579 & 0 \\ 0 & 0 & 0 & 0 & 0 & 2.762 \end{bmatrix} . \tag{4.66}$$

Also, we consider the approximated values of orthotropic elasticity coefficients from Dewangan and Grechka (2003), shown in their figure 4,

$$C^{\mathrm{D\&G}} = \begin{bmatrix} 5.300 & 3.350 & 2.500 & 0 & 0 & 0 \\ 3.350 & 4.520 & 1.830 & 0 & 0 & 0 \\ 2.500 & 1.830 & 4.000 & 0 & 0 & 0 \\ 0 & 0 & 0 & 0.820 & 0 & 0 \\ 0 & 0 & 0 & 0 & 1.000 & 0 \\ 0 & 0 & 0 & 0 & 0 & 1.080 \end{bmatrix}. \tag{4.67}$$

In both matrices, $C_{11} > C_{22} > C_{33}$ and $C_{66} > C_{55} > C_{44}$. Thus, the cracks are parallel to the x_1-axis, as presented in Figure 4.9a. The other six matrices do not correspond to the typical situation of flat-layered sedimentary rock with a set of cracks parallel to the x_1-axis. It makes our work more universal since it is not only focused on the situation presented in Figure 4.9a. To support the conclusions coming from the numerical experiments, we also utilise,

$$C^{T\&al} = \begin{bmatrix} 39.313 & x & 10.935 & 0 & 0 & 0 \\ x & 34.810 & 8.552 & 0 & 0 & 0 \\ 10.935 & 8.552 & 27.773 & 0 & 0 & 0 \\ 0 & 0 & 0 & 8.009 & 0 & 0 \\ 0 & 0 & 0 & 0 & 8.237 & 0 \\ 0 & 0 & 0 & 0 & 0 & 12.709 \end{bmatrix}, \tag{4.68}$$

which values are based on the specification of orthotropic biotite schist analysed by Takanashi et al. (2001). The value of C_{12} is unknown, but we do not needed it for our purposes. Also, we perform calculations on

$$C^{S\&al} = \begin{bmatrix} 38.606 & 13.029 & 17.933 & 0 & 0 & 0 \\ 13.029 & 31.298 & 15.288 & 0 & 0 & 0 \\ 17.933 & 15.288 & 47.260 & 0 & 0 & 0 \\ 0 & 0 & 0 & 11.827 & 0 & 0 \\ 0 & 0 & 0 & 0 & 12.404 & 0 \\ 0 & 0 & 0 & 0 & 0 & 10.769 \end{bmatrix} . \tag{4.69}$$

We take the values above from Svitek et al. (2014). Therein, authors perform the laboratory measurements on a generally-anisotropic biotite gneiss under pressure of $0.1\mathrm{MPa}$. For purposes of our orthotropic analysis, we have assumed that $C_{14} = C_{15} = C_{16} = C_{24} = C_{25} = C_{26} = C_{34} = C_{35} = C_{36} = C_{45} = C_{46} = C_{56} = 0$. By using the same assumption, we have modified two more tensors from the work of Mensch and Rasolofosaon (1997). We use modified tensor of Saturated Lavoux limestone, namely,

$$C^{lime} = \begin{bmatrix} 11.005 & 5.342 & 6.164 & 0 & 0 & 0 \\ 5.342 & 10.731 & 5.753 & 0 & 0 & 0 \\ 6.164 & 5.753 & 12.100 & 0 & 0 & 0 \\ 0 & 0 & 0 & 2.694 & 0 & 0 \\ 0 & 0 & 0 & 0 & 2.374 & 0 \\ 0 & 0 & 0 & 0 & 0 & 2.511 \end{bmatrix} \tag{4.70}$$

and modified tensor of Dry Vosges sandstone,

$$C^{sand} = \begin{bmatrix} 4.952 & 0.433 & 0.625 & 0 & 0 & 0 \\ 0.433 & 5.096 & 1.010 & 0 & 0 & 0 \\ 0.625 & 1.010 & 6.779 & 0 & 0 & 0 \\ 0 & 0 & 0 & 2.452 & 0 & 0 \\ 0 & 0 & 0 & 0 & 2.885 & 0 \\ 0 & 0 & 0 & 0 & 0 & 2.356 \end{bmatrix}. \tag{4.71}$$

Also, we consider a tensor from Mahmoudian et al. (2012),

$$C^{M\&al} = \begin{bmatrix} 8.700 & 4.900 & 4.960 & 0 & 0 & 0 \\ 4.900 & 12.670 & 5.580 & 0 & 0 & 0 \\ 4.960 & 5.580 & 12.250 & 0 & 0 & 0 \\ 0 & 0 & 0 & 2.890 & 0 & 0 \\ 0 & 0 & 0 & 0 & 2.340 & 0 \\ 0 & 0 & 0 & 0 & 0 & 2.280 \end{bmatrix}, \tag{4.72}$$

which values are based on the experiments performed on the orthotropic laminate phenolic layer. Further, we use,

$$C^{S\&H} = \begin{bmatrix} 9.000 & 3.600 & 2.250 & 0 & 0 & 0 \\ 4.900 & 9.840 & 2.400 & 0 & 0 & 0 \\ 2.250 & 2.400 & 5.938 & 0 & 0 & 0 \\ 0 & 0 & 0 & 2.000 & 0 & 0 \\ 0 & 0 & 0 & 0 & 1.600 & 0 \\ 0 & 0 & 0 & 0 & 0 & 2.182 \end{bmatrix}, \tag{4.73}$$

shown in Schoenberg and Helbig (1997). Its parameters correspond to the situation illustrated in Figure 4.9b; they satisfy relations $C_{22} > C_{11} > C_{33}$ and $C_{66} > C_{44} > C_{55}$.

Post-publication comments

In this paper, we analyse the influence of each stiffness on the P-wave propagation in the symmetry planes of an orthotropic medium. The impact of the elasticity parameters is viewed in the context of

- the sensitivity analysis using the partial derivatives,
- the approximation of a squared-velocity difference, s^2, which evaluates the influence of cracks.

We should emphasise that the exact expression of s^2 is neither very complicated nor lengtty. However, it does not give enough physical insight into the contributions of stiffnesses; therefore, simple approximations are proposed.

In Section 4.2.2, we consider a squared-velocity difference in the context of a particular case of phase polar angles, where angles in both perpendicular planes are equal to each other, namely, $\theta_1 = \theta_2 = \theta$. Also, using expression (4.5), we check if the corresponding ray angles are approximately equal. However, as noticed by Dr. Zvi Koren, this expression can be rewritten in a more convenient form as

$$\tan(\psi - \theta) = \frac{dV/d\theta}{V(\theta)} \,, \tag{4.74}$$

where ψ denotes the ray angle.

Further, on page 101, we write

Now, let us not to consider a weak anisotropy approximation, but try to derive an approximation from exact solutions.

To be more precise, the weak anisotropy approximation of Tsvankin (1997) was also derived from exact solutions. However, in contrast to his approximation, we do not follow perturbation methods but propose assumption (4.13).

In expression (4.24), we invoke the stability conditions for orthotropic media that are indispensable to define the physically feasible ranges of stiffnesses. To be precise, the equal signs from this expression should be removed. As discussed in the Post-publication comments of Chapter 3, we have again followed the leading principal minors—instead of the principal minors—criterion that corresponds to the strict stability conditions of a positive definite—instead of semidefinite—matrix. Furthermore, in this paper, we also utilse the anisotropy parameters defined in Tsvankin (1997). Hence, it may be useful for the reader to express the stability conditions in terms of the above-mentioned coefficients. This is not a straightforward task, since C_{13} , C_{23} , C_{12} cannot be unequivocally determined. Specifically,

$$
\begin{aligned}
C_{13} &= \pm\sqrt{\left(V_{P_3}^2 - V_{S_{31}}^2\right)\left(V_{P_3}^2(1+2\delta^{(2)}) - V_{S_{31}}^2\right)} - V_{S_{31}}^2 := \pm\sqrt{\Delta^{(2)}} - V_{S_{31}}^2\,,\\
C_{23} &= \pm\sqrt{\left(V_{P_3}^2 - V_{S_{32}}^2\right)\left(V_{P_3}^2(1+2\delta^{(1)}) - V_{S_{32}}^2\right)} - V_{S_{32}}^2 := \pm\sqrt{\Delta^{(1)}} - V_{S_{32}}^2\,,\\
C_{12} &= \pm\sqrt{\left(V_{P_3}^2 - V_{S_{31}}^2\left(1+2\gamma^{(1)}\right)\right)\left(V_{P_3}^2(1+2\delta^{(3)}) - V_{S_{31}}^2\left(1+2\gamma^{(1)}\right)\right)}\\
&\qquad - V_{S_{31}}^2\left(1+2\gamma^{(1)}\right) := \pm\sqrt{\Delta^{(3)}} - V_{S_{31}}^2\left(1+2\gamma^{(1)}\right)\,.
\end{aligned}
\tag{4.75}
$$

$V_{P_3} = \sqrt{C_{33}/\rho}$, $V_{S_{31}} = \sqrt{C_{55}/\rho}$, and $V_{S_{32}} = \sqrt{C_{44}/\rho}$ denote phase velocities of waves propagating in the x_3 direction, where the second number in the subscript stands for the direction of particle displacement. The above expressions have negative signs in front of the squared roots if $C_{13} < -C_{55}$, $C_{23} < -C_{44}$, $C_{12} < -C_{66}$, respectively. These are very unlikely and anomalous—but physically feasible—relations, discussed by Helbig and Schoenberg (1987). Thus, instead of the classical stability conditions, we propose to consider even more strict conditions. In other words, apart from the leading principal criterion of the elasticity matrix expressed in terms of Tsvankin (1997) parameters, we also exclude the anomalous relations. Hence, we additionally assume $C_{13} > -C_{55}$, $C_{23} > -C_{44}$, $C_{12} > -C_{66}$, so that the terms in front of the squared roots are positive and C_{13}, C_{23}, C_{12} from expression (4.75) are determined uniquely. This way, we obtain the following conditions

$$
\begin{gathered}
\epsilon^{(1)}\,,\epsilon^{(2)}\,,\gamma^{(1)}\,,\gamma^{(2)} > -\frac{1}{2}\,, \qquad V_{P_3}\,,V_{S_{31}}\,,V_{S_{31}} > 0\,, \qquad \sqrt{\Delta^{(i)}} > 0\,, \\
4V_{P_3}^4\,\epsilon^{(1)}\epsilon^{(2)} - \left(V_{S_{31}}^2\left(1+2\gamma^{(1)}\right) - \sqrt{\Delta^{(3)}}\right)^2 > 0\,, \qquad \text{and} \\
4V_{P_3}^6\,\epsilon^{(1)}\epsilon^{(2)} - \left(\sqrt{\Delta^{(1)}} - V_{S_{32}}^2\right)\left(\sqrt{\Delta^{(2)}} - V_{S_{31}}^2\right)\left(2V_{S_{31}}^2\left(1+2\gamma^{(1)}\right) - 2\sqrt{\Delta^{(3)}}\right) \\
\qquad - 2V_{P_3}^2\,\epsilon^{(1)}\left(\sqrt{\Delta^{(2)}} - V_{S_{31}}^2\right)^2 - 2V_{P_3}^2\,\epsilon^{(2)}\left(\sqrt{\Delta^{(1)}} - V_{S_{32}}^2\right)^2 \\
\qquad - V_{P_3}^2\left(V_{S_{31}}^2\left(1+2\gamma^{(1)}\right) - \sqrt{\Delta^{(3)}}\right)^2 > 0\,.
\end{gathered}
\tag{4.76}
$$

Readers can use the inequalities from expression (4.76) to determine the non-anomalous, feasible conditions of an orthotropic matrix described by Tsvankin (1997) parameters. Additionally, note that certain parameters in expression (4.76) are not independent, namely,

$$
V_{S_{32}}^2 = V_{S_{31}}^2\left(\frac{1+2\gamma^{(1)}}{1+2\gamma^{(2)}}\right)\,. \tag{4.77}
$$

Our last comment concerns expression (4.47). Therein, we discuss the dependence of s^2/C_{33} on Tsvankin (1997) parameters, where we use $f^{(1)}$ and $f^{(2)}$, defined in expression (4.48). Although s^2/C_{33} is described by $\epsilon^{(1)}$, $\epsilon^{(2)}$, $\delta^{(1)}$, $\delta^{(2)}$, $f^{(1)}$ and $f^{(2)}$, we claim that it relies on seven, not six, independent parameters. In fact, $f^{(1)}$ and $f^{(2)}$ are not independent coefficients (Koren and Ravve, 2017), which can be seen upon rewriting relation (4.77), namely,

$$1 - f^{(1)} = \left(1 - f^{(2)}\right)\left(\frac{1+2\gamma^{(1)}}{1+2\gamma^{(2)}}\right) . \tag{4.78}$$

Hence, s^2/C_{33} depends on $\epsilon^{(1)}$, $\epsilon^{(2)}$, $\delta^{(1)}$, $\delta^{(2)}$, $\gamma^{(1)}$, $\gamma^{(2)}$, and $f^{(2)}$; number of parameters is augmented to seven, as expected.

Chapter 5

Cumulative moduli for orthotropic media: Parametrization for quasi P-wave phase velocity*

Abstract

We perform a numerical analysis of the solution of Christoffel's equations that correspond to quasi P-wave phase velocity propagating in an orthotropic medium. We focus on the relationships between all nine elasticity parameters. To describe these dependencies, we define "cumulative moduli" υ, λ, and μ that show the analogy to Lamé coefficients. Each module is responsible for the relations of a distinct group of three parameters. By introducing such a representation, in certain cases, we may predict quasi P-wave velocity for any incidence and azimuth angle, knowing less than required nine elasticity parameters.

*This chapter consists of the conference paper with corrected figures and the post-publication comments. Herein, we invoke the following paper: Adamus, F. P. (2020). "Cumulative moduli for orthotropic media: Parametrization for quasi P-wave phase velocity". *SEG Expanded Abstracts*, 181–185.

During the analysis, for simplification and analogy, we also utilise a cubic symmetry class. As a result of this, we additionally present a universal, strong anisotropy approximation of quasi P-wave velocity for cubic media.

5.1 Introduction

While willing to study the propagation of waves in elastic materials, we obtain the equations of motion. For anisotropic Hookean solids, these equations are complicated and difficult to solve analytically (which is not the case for isotropic solids). Therefore, we use a trial solution that leads to Christoffel's equations (e.g., Slawinski, 2015, Chapter 7). The three roots of the solubility condition of these equations correspond to phase velocities of three waves that propagate in an anisotropic medium. Herein, we focus on the root that describes the quasi P-wave phase velocity.

We are particularly interested in the study of the velocity in shales or other laminated rocks with parallel or perpendicular set of cracks to these laminations. A good theoretical analogy to such rocks is an orthotropic symmetry class of Hookean solids. To describe an orthotropic medium, we use nine elasticity parameters. We can theoretically predict the phase velocity changes for various incidence and azimuthal angles by computing the Christoffel's roots. To do so, we require knowledge of the values of all nine elasticity parameters. The values of parameters C_{11} , C_{22} , C_{33} can be obtained based on quasi P-wave velocity measurements in the vertical and horizontal directions (assuming that the laminations or cracks are horizontal). To get C_{55} , C_{44} , C_{66} , we need to measure quasi S-waves in the same directions of propagation. Finally, to acquire C_{13} , C_{23} , C_{12} , we measure the velocity of waves propagating in the oblique direction. In practice, it is often challenging to know all nine values. Therefore, an approximation of Christoffel's root that needs a smaller number of the elasticity coefficients may be useful. We attempt to find one.

The expression of Christoffel's root for quasi P-wave propagating in any direction of the orthotropic medium is complicated and lengthy. Its sensitivity to each elasticity parameter is not apparent. We quantify it by computing the partial derivative of Christoffel's root with respect to each elasticity parameter. We look for the patterns of dependencies within three groups of elasticity coefficients. We want to understand what are the relations between C_{11}, C_{22}, and C_{33}. We examine relations between C_{13}, C_{23}, C_{12}, and relations between shear moduli, C_{55}, C_{44}, C_{66}. We embrace the dependencies within the aforementioned three groups of parameters in terms of "cumulative moduli"υ, λ, and μ, respectively. The introduction of cumulative moduli allows us to intuitively grasp the physics contained in the expression of Christoffel's root. Also, they show that in some cases, we do not need nine elasticity parameters to quite accurately estimate the velocity of quasi P-wave propagating in any direction.

To obtain the results for orthotropic media, in some parts of the text, we also study a simplified model. We utilise a higher, cubic symmetry class, where, in addition to the orthotropic relations, $C_{11} = C_{22} = C_{33}$, $C_{13} = C_{23} = C_{12}$, and $C_{44} = C_{55} = C_{66}$.

5.2 Cumulative moduli

Let us denote the quasi P-wave phase velocity obtained for any direction of propagation as V, which exact expression is difficult to show analytically (e.g., Tsvankin, 1997). In orthotropic media, it depends on the incidence angle, θ, azimuthal angle, ϕ, density, and nine elasticity parameters mentioned above. To examine the angularly changing sensitivity of V to C_{11}, C_{22}, C_{33}, we propose to use the following expression based on the partial derivatives of V with respect to each elasticity parameter.

$$\upsilon^*(\theta,\phi) := \frac{C_{11}\,\partial_{C_{11}}V + C_{22}\,\partial_{C_{22}}V + C_{33}\,\partial_{C_{33}}V}{\partial_{C_{11}}V + \partial_{C_{22}}V + \partial_{C_{33}}V}\,, \tag{5.1}$$

where the denominator stands for a normalisation factor. To grasp the meaning of the expression (5.1), let us use the density-scaled values of elasticity parameters based on the work of Cheadle et al. (1991) (later, we refer to their work as $C\&al$). The values expressed in $\mathrm{km}^2/\mathrm{s}^2$ are: $C_{11} = 12.788\,, C_{22} = 11.323\,, C_{33} = 8.556\,, C_{13} = 5.138\,, C_{23} = 4.884\,,$ $C_{12} = 5.471\,, C_{44} = 2.298\,, C_{55} = 2.579\,, C_{33} = 2.762\,.$ Also, consider a spherical system, where we measure the incidence angle from a vertical axis x_3 and the azimuthal angle from the x_1-axis towards the x_2-axis. For instance, if $\theta = 45^\circ$ and $\phi = 0^\circ$, we get

$$\upsilon^* = 0.6322 C_{11} + 0.3678 C_{33} = 11.2316\,[\mathrm{km}^2/\mathrm{s}^2]\,. \tag{5.2}$$

We see that C_{22} does not appear in expression (5.2), which is the result of propagation in the x_3x_1-plane. Also, we notice that υ^* depends more on C_{11} than on C_{33} . This is the result of $C_{11} > C_{33}$. If $C_{11} = C_{33}$, for our chosen angles, the dependence on both parameters would be the same. Based on the simple example above, it is clear that υ^* describes the dependence of V on C_{11} , C_{22} , C_{33} as a single, cumulative dependence on one module only.

To obtain υ^* we need to compute partial derivatives of V . Thus, we require the knowledge of all nine elasticity parameters. We want to express the derivatives in terms of functions of incidence, f_θ , and azimuth, f_ϕ , so we can get υ^* knowing C_{11} , C_{22} , and C_{33} only. To do so, first, let us consider a special case in which orthotropic symmetry reduces to cubic one. We modify the values of elasticity parameters, namely, $C_{11} = 12.788 = C_{22} = C_{33}$, $C_{13} = 5.138 = C_{23} = C_{12}$, and $C_{44} = 2.298 = C_{55} = C_{66}$. We use these new values, however, we still perform the operations as there were nine elasticity parameters. We notice that in the x_3x_1-plane $\partial_{C_{33}}V \approx kf_\theta = k\cos^4\theta$, where k is a scaling factor. This is true also for the x_3x_2-plane and for any other plane that contains the vertical axis. We perform the analogous analysis for the derivatives with respect to C_{11} and C_{22}. We notice that in the x_3x_1-plane $\partial_{C_{11}}V \approx kf_\theta = k\sin^4\theta$. However, as oppose to the case of $\partial_{C_{33}}V$, the value of $\partial_{C_{11}}V$ decreases if we consider any other plane containing the vertical axis. To take into consideration the azimuthal influence, we take a look at the horizontal x_1x_2-plane, where $\partial_{C_{11}}V \approx kf_\phi = k\cos^4\phi$. Now we can take into account both incidence and azimuthal factors and scale it by k. Hence, we get $\partial_{C_{11}}V \approx kf_\theta f_\phi = k\sin^4\theta\cos^4\phi$ valid for any θ and ϕ. Analogously, we obtain $\partial_{C_{22}}V \approx k\sin^4\theta\sin^4\phi$ also valid for any angle. In the case of values based on $C\&al$, scaling factor $k = 0.14$. We illustrate the above analysis in Figure 5.1. Now, we can define

$$\upsilon(\theta,\phi) := \frac{C_{11}\,\sin^4\theta\cos^4\phi + C_{22}\,\sin^4\theta\sin^4\phi + C_{33}\,\cos^4\theta}{\sin^4\theta\cos^4\phi + \sin^4\theta\sin^4\phi + \cos^4\theta}\,. \tag{5.3}$$

The scaling factor k got canceled. For the cubic symmetry, the above expression makes little sense, since $\upsilon = \upsilon^* = C_{11}$. We utilise this high symmetry example only because it is more accurate to derive scaling factor k and functions f_θ and f_ϕ. However, υ is designed to work for the orthotropic symmetry, since it describes a cumulative effect of C_{11}, C_{22}, and C_{33} on V. It can be obtained knowing three elasticity parameters only, instead of all nine (as is the case of υ^*).

Let us check if υ accurately estimates υ^* in the case of the orthotropic symmetry class. We take the unmodified values from C&al, and from the works of Dewangan and Grechka (2003), Svitek et al. (2014), Mensch and Rasolofosaon (1997), Mahmoudian et al. (2012), and Schoenberg and Helbig (1997). While referring to these works, we denote them as $D\&G$, $S\&al$, $M\&R$, $M\&al$, and $S\&H$, respectively (we take two tensors from $M\&R$, corresponding to limestone, $\mathrm{M\&R_{lim}}$, and sandstone, $\mathrm{M\&R_{san}}$). To check the accuracy of

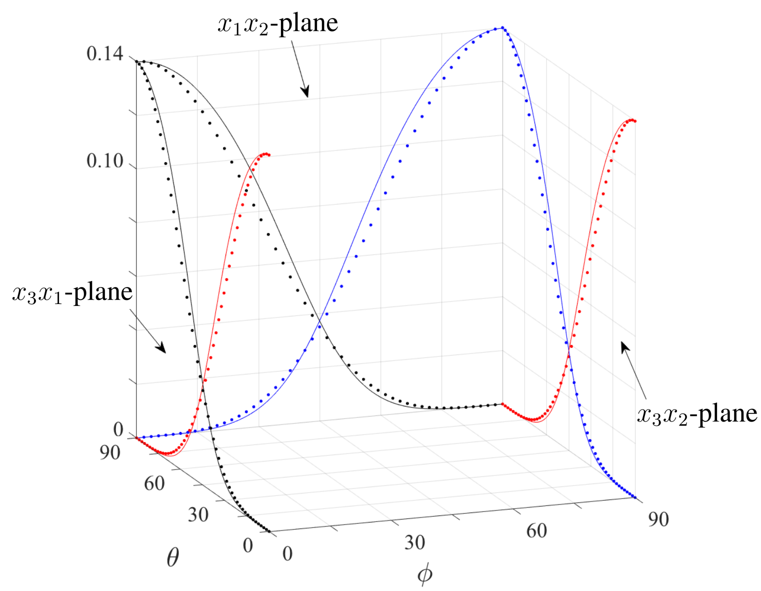

Figure 5.1: Partial derivatives of V with respect to C_{11} (solid black), C_{22} (solid blue) and C_{33} (solid red) computed for three symmetry planes. Dotted lines correspond to kf_θ and kf_ϕ. Angles expressed in cartesian, as opposed to spherical coordinates. Planes corresponding to the spherical system invoked in the main text are indicated by arrows. Values are based on C&al exhibiting cubic symmetry class.

the approximation of υ^* by υ, we compute their mean relative error, err (calculated for any incidence and azimuthal angle and averaged). Also, we want to describe the strength of the orthotropic anisotropy. To do so, we quantify the differences between cubic tensors (obtained upon modifications of elasticity parameters, as was done for $C\&al$) and their orthotropic counterparts. We use the ratio of Frobenius norms,

$$A := \frac{||C^{\mathrm{ort}} - C^{\mathrm{cub}}||}{||C^{\mathrm{ort}} + C^{\mathrm{cub}}||} \times 100\,, \tag{5.4}$$

where we subtract and add the components of orthotropic and cubic 6×6 matrices representing these tensors (e.g., Slawinski, 2018, Chapter 4). In other words, A describes the anisotropy arising from the change of cubic to orthotropic class. We present the errors and A for all seven tensors exhibiting orthotropic symmetry in Table 5.1.

Table 5.1: Mean relative errors $[\%]$ of cumulative moduli. Values of elasticity parameters used to calculate the moduli are taken from tensors exhibiting orthotropic symmetry. Differences between orthotropic tensors and their cubic counterparts are expressed by parameter $A\,[\%]$.

	$err(\upsilon^*, \upsilon)$	$err(\lambda^*, \lambda)$	$err(\mu^*, \mu)$	A
$C\&al$	1.16	0.18	0.30	9.93
$D\&G$	0.67	1.74	0.87	9.65
$S\&al$	1.20	0.64	0.28	8.32
$\mathrm{M\&R_{lim}}$	0.12	0.07	0.04	3.36
$\mathrm{M\&R_{san}}$	1.13	1.37	0.43	9.46
$M\&al$	1.03	0.32	0.54	13.6
$S\&H$	2.22	1.46	0.88	10.6

Let us discuss the errors. First, the shape of functions f_θ and f_ϕ that describe partial derivatives changing with angles, differ slightly from the ones in the cubic case. Also, scaling factor k is not the same for each partial derivative $\partial_{C_{ij}}V$. The above two issues affect err. However, the relative error still remains low. Even though υ was derived from a cubic example, it seems valuable for the orthotropic symmetry. Further, we notice that very small err is present for a tensor $\mathrm{M\&R_{lim}}$ that has low A. We can expect that weak orthotropic anisotropy assures higher accuracy of υ.

We have already discussed the cumulative dependence of V on elasticity parameters C_{11}, C_{22}, and C_{33}. In a similar way, we analyse the influence of a group C_{13}, C_{23}, C_{12} and C_{55}, C_{44}, C_{66}. We propose

$$\lambda^*(\theta,\phi) := \frac{C_{13}\,\partial_{C_{13}}V + C_{23}\,\partial_{C_{23}}V + C_{12}\,\partial_{C_{12}}V}{\partial_{C_{13}}V + \partial_{C_{23}}V + \partial_{C_{12}}V}\,, \tag{5.5}$$

and

$$\mu^*(\theta,\phi) := \frac{C_{55}\,\partial_{C_{55}}V + C_{44}\,\partial_{C_{44}}V + C_{66}\,\partial_{C_{66}}V}{\partial_{C_{55}}V + \partial_{C_{44}}V + \partial_{C_{66}}V}\,. \tag{5.6}$$

By doing analogical analysis to the one illustrated in Figure 5.1, we estimate the above moduli by

$$\lambda(\theta,\phi) := \frac{C_{13}\ \sin^2(2\theta)\cos^2\phi + C_{23}\ \sin^2(2\theta)\sin^2\phi + C_{12}\ \sin^4\theta\cos^2(2\phi)}{\sin^2(2\theta)\cos^2\phi + \sin^2(2\theta)\sin^2\phi + \sin^4\theta\cos^2(2\phi)} \tag{5.7}$$

and

$$\mu(\theta,\phi) := \frac{C_{55}\ \sin^2(2\theta)\cos^2\phi + C_{44}\ \sin^2(2\theta)\sin^2\phi + C_{66}\ \sin^4\theta\cos^2(2\phi)}{\sin^2(2\theta)\cos^2\phi + \sin^2(2\theta)\sin^2\phi + \sin^4\theta\cos^2(2\phi)}\,, \tag{5.8}$$

respectively. The relative error between expressions (5.5) and (5.7) or between (5.6) and (5.8) is low, as we show in Table 5.1.

5.3 Some possible applications

Let us try to express P-wave phase velocity V using the knowledge from the previous section. First, we focus on a cubic symmetry class. Upon dozens of numerical experiments, we notice that we can accurately estimate

$$V \approx 2\left(C_{11}\partial_{C_{11}}V + C_{13}\partial_{C_{13}}V + C_{44}\partial_{C_{44}}V\right)\,. \tag{5.9}$$

We also notice that

$$2\partial_{C_{13}}V \approx \partial_{C_{44}}V\,, \tag{5.10}$$

hence, we rewrite expression (5.9) as

$$V \approx 2C_{11}\partial_{C_{11}}V + (C_{13}+2C_{44})\partial_{C_{44}}V\,. \tag{5.11}$$

Note that if $C_{11} = C_{13} + 2C_{44}$, then we deal with an isotropic case and

$$V = C_{11}\left(2\partial_{C_{11}}V + \partial_{C_{44}}V\right) = \sqrt{C_{11}}\,, \tag{5.12}$$

as required. Further, let us rewrite expression (5.11) as

$$V \approx C_{11}\left(2\partial_{C_{11}}V + 2\partial_{C_{22}}V + 2\partial_{C_{33}}V\right) + \left(C_{13} + 2C_{44}\right)\left(\partial_{C_{55}}V + \partial_{C_{44}}V + \partial_{C_{66}}V\right)\,, \tag{5.13}$$

where $C_{11} = C_{22} = C_{33}$ and $C_{55} = C_{44} = C_{66}$, so in this special case we have used the relations

$$\partial_{C_{11}^{\mathrm{cub}}}V = \partial_{C_{11}^{\mathrm{ort}}}V + \partial_{C_{22}^{\mathrm{ort}}}V + \partial_{C_{33}^{\mathrm{ort}}}V \tag{5.14}$$

and

$$\partial_{C_{44}^{\mathrm{cub}}}V = \partial_{C_{55}^{\mathrm{ort}}}V + \partial_{C_{44}^{\mathrm{ort}}}V + \partial_{C_{66}^{\mathrm{ort}}}V \tag{5.15}$$

that can be easily verified numerically. Subsequently, we write

$$\begin{aligned} V \approx\ & 2k_1C_{11}\left(\sin^4\theta\cos^4\phi + \sin^4\theta\sin^4\phi + \cos^4\theta\right) \\ & + k_2\left(C_{13} + 2C_{44}\right)\left[\sin^2(2\theta)\cos^2\phi + \sin^2(2\theta)\sin^2\phi + \sin^4\theta\cos^2(2\phi)\right]\,, \end{aligned} \tag{5.16}$$

where k_1 and k_2 are two distinct scaling factors. Each derivative is described by the same k and various $f_\theta f_\phi$, as mentioned in the previous section. Now, we want to describe k_1 and k_2. We know that V for zero incidence and azimuth angle must equal $\sqrt{C_{11}}$. Estimation (5.16) reflects it only if $k_1 = \sqrt{C_{11}}/2C_{11}$. If $\theta = 45^\circ$ and $\phi = 45^\circ$, then the exact value is $V = \sqrt{0.5C_{11} + 0.5C_{13} + C_{44}}$. To reflect it, we require

$$k_2 = \frac{\sqrt{2C_{11} + 2C_{13} + 4C_{44}} - \sqrt{C_{11}}}{2C_{13} + 4C_{44}}\,. \tag{5.17}$$

Thus, we propose the following strong anisotropy approximation of P-wave phase velocity for cubic media,

$$
\begin{aligned}
V \approx V^* := & \sqrt{C_{11}}\left(\sin^4\theta\cos^4\phi + \sin^4\theta\sin^4\phi + \cos^4\theta\right) \\
& + 0.5\left(\sqrt{2C_{11} + 2C_{13} + 4C_{44}} - \sqrt{C_{11}}\right) \\
& \left[\sin^2(2\theta)\cos^2\phi + \sin^2(2\theta)\sin^2\phi + \sin^4\theta\cos^2(2\phi)\right] .
\end{aligned}
\tag{5.18}
$$

In Table 5.2 we present the mean relative error between exact V and the above approximation, V^*. The accuracy of V^* is high and seems to be satisfactory.

Table 5.2: Mean relative errors $[\%]$ of approximations V^* and $\sqrt{\upsilon}$. Also, standard deviation, $std\,[\mathrm{m/s}]$, of $\sqrt{\upsilon}$ is presented. Calculation based on elasticity parameters taken from seven cubic (approx. V^*) and orthotropic (approx. $\sqrt{\nu}$) tensors.

	$err(V, V^*)$	$err(V, \sqrt{\upsilon})$	$std(V, \sqrt{\upsilon})$
C&al	0.18	1.66	63.9
D&G	0.14	1.19	34.1
S&al	0.02	1.34	106
$\mathrm{M\&R_{lim}}$	0.01	0.83	34.9
$\mathrm{M\&R_{san}}$	0.05	1.38	43.7
M&al	0.13	1.80	73.5
S&H	0.34	2.70	101

Similarly, we attempt to approximate V for the orthotropic case. We can estimate

$$
\begin{aligned}
V \approx 2(& C_{11}\partial_{C_{11}}V + C_{22}\partial_{C_{22}}V + C_{33}\partial_{C_{33}}V \\
& + C_{13}\partial_{C_{13}}V + C_{23}\partial_{C_{23}}V + C_{12}\partial_{C_{12}}V \\
& + C_{55}\partial_{C_{55}}V + C_{44}\partial_{C_{44}}V + C_{66}\partial_{C_{66}}V) .
\end{aligned}
\tag{5.19}
$$

Subsequently, we notice that

$$
2\partial_{C_{13}}V \approx \partial_{C_{55}}V , \quad 2\partial_{C_{23}}V \approx \partial_{C_{44}}V , \quad 2\partial_{C_{12}}V \approx \partial_{C_{66}}V . \tag{5.20}
$$

We can rewrite expression (5.19) as

$$\begin{aligned}V &\approx \upsilon^*(2\partial_{C_{11}}V + 2\partial_{C_{22}}V + 2\partial_{C_{33}}V)\\ &+(\lambda^* + 2\mu^*)(\partial_{C_{55}}V + \partial_{C_{44}}V + \partial_{C_{66}}V)\,.\end{aligned} \tag{5.21}$$

It is important to interpret the approximation above. We notice that it corresponds to expression (5.12) for isotropy class and expression (5.13) for cubic class. Let us assume that $\upsilon^* \approx \lambda^* + 2\mu^*$ (or analogously $\upsilon \approx \lambda + 2\mu$), which is akin to $C_{11} = C_{13} + 2C_{44}$ for the isotropic case, where C_{13} and C_{44} are the Lamé coefficients. Then we obtain,

$$V \approx \upsilon^* \left(2\partial_{C_{11}}V + 2\partial_{C_{22}}V + 2\partial_{C_{33}}V + \partial_{C_{55}}V + \partial_{C_{44}}V + \partial_{C_{66}}V\right)\,, \tag{5.22}$$

which reduces to expression (5.12) if $C_{11} = C_{22} = C_{33}$ and $C_{55} = C_{44} = C_{66}$. Due to analogical form of expression (5.22) to expression (5.12), we expect that

$$V \approx \sqrt{\upsilon^*} \approx \sqrt{\upsilon} \tag{5.23}$$

may be true even for stronger anisotropy, but under the condition that $\upsilon \approx \lambda + 2\mu$. We presume that this approximation may be inaccurate in cases where the discrepancy between υ and $\lambda + 2\mu$ is larger. Figures 5.2 and 5.3 show that values for the exact solution of quasi P-wave velocity are often between values of $\sqrt{\upsilon}$ and $\sqrt{\lambda + 2\mu}$. In cases in which $\upsilon \approx \lambda + 2\mu$, the velocity is approximated quite accurately. In other words, the accuracy of $\sqrt{\upsilon}$ strongly depends on variations in shear moduli or parameters C_{13}, C_{23}, and C_{12}. In Table 5.2, we present the mean relative error for $\sqrt{\upsilon}$. Also, we show its standard deviation for seven examples of orthotropic tensors. It occurs that for most of the examples, $err \approx 1.5\%$, which might be considered as a good result since six out of nine elasticity parameters are absent in the approximation $\sqrt{\upsilon}$. Additionally, in Figure 5.4, we show the discrepancy between

V and $\sqrt{\upsilon}$ in three symmetry planes. Larger inaccuracy indicates greater influence of shear moduli and parameters C_{13} , C_{23} , C_{12} on phase velocity.

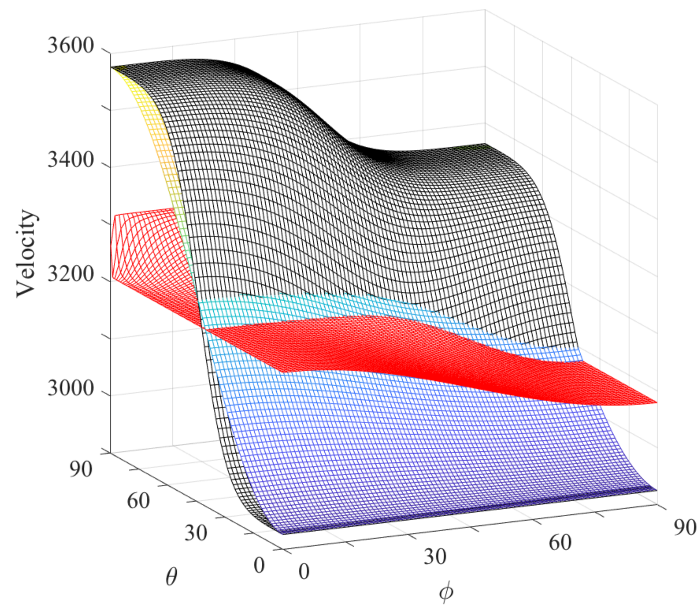

Figure 5.2: Exact values of quasi P-wave velocity $[\mathrm{m/s}]$ are in rainbow colours. Estimated $\sqrt{\upsilon}$ is in black, whereas $\sqrt{\lambda + 2\mu}$ in red. Calculation based on orthotropic tensor from $C\&al$.

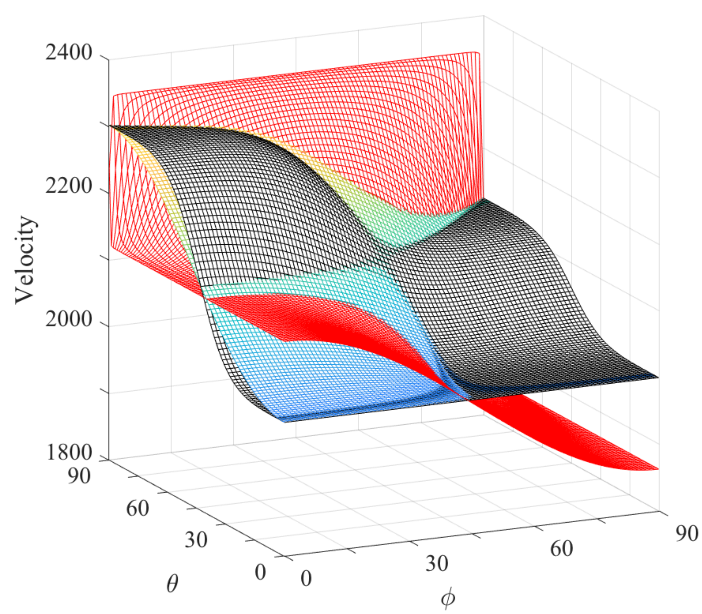

Figure 5.3: Exact values of quasi P-wave velocity $[\mathrm{m/s}]$ are in rainbow colours. Estimated $\sqrt{\upsilon}$ is in black, whereas $\sqrt{\lambda + 2\mu}$ in red. Calculation based on orthotropic tensor from $D\&G$.

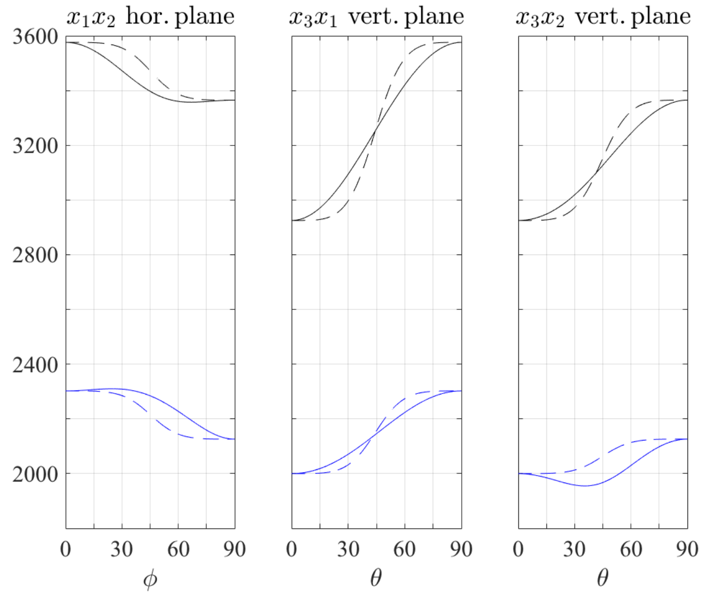

Figure 5.4: Exact values of quasi P-wave velocity $[\mathrm{m/s}]$ are in solid lines. Estimated $\sqrt{\upsilon}$ is in dashed lines. Results based on orthotropic tensors from $C\&al$ and $D\&G$ presented in black and blue, respectively. Symmetry planes correspond to the spherical system invoked in the main text and in Figure 5.1.

5.4 Conclusions

We have presented cumulative moduli υ, λ, and μ that allow us to understand the dependencies within three groups of elasticity parameters in the context of quasi P-wave velocity. To get each cumulative module, we need three different elasticity parameters. Having υ alone, we can estimate quasi P-wave velocity for any direction of propagation. The accuracy of the approximation is larger if υ is close to $\lambda + 2\mu$. We notice that for isotropic case $\upsilon = \lambda + 2\mu$ reduces to $C_{11} = C_{13} + 2C_{44}$, where C_{13} and C_{44} are Lamé coefficients. Having λ alone, we can understand the influence of elasticity parameters that can be obtained upon oblique measurements (with respect to symmetry planes). On the other hand, sole μ gives us information on the dependence of quasi P-wave velocity on shear moduli for any angle of propagation. We have used cumulative moduli to estimate V for cubic and orthotropic media, but there may be some other potential applications of υ, λ, and μ. In the future, we will investigate these applications.

Acknowledgements

We wish to thank Heloise Lynn and Michael A. Slawinski for precious comments and fruitful discussions.

5.5 References

Cheadle, S. P., Brown, R. J., and Lawton, Don C. (1991). “Orthorhombic anisotropy: A physical seismic modeling study”. *Geophysics*, 56 (10), 1603–1613.

Dewangan, P. and Grechka, V. (2003). “Inversion of multicomponent, multiazimuth, walkaway VSP data for the stiffness tensor”. *Geophysics*, 68 (3), 1022–1031.

Mahmoudian, F., Margrave, G., Daley, P. F., and Wong, J. (2012). “Estimation of stiffness coefficients of an orthorhombic physical model from group velocity measurements”. *CREWES Research Report*, 24 (1), 1–16.

Mensch, T. and Rasolofosaon, P. (1997). “Elastic-wave velocities in anisotropic media of arbitrary symmetry–generalization of Thomsen’s parameters ϵ, δ and γ”. *Geophys. J. Int.* 128 (1), 43–64.

Schoenberg, M. and Helbig, K. (1997). “Orthorhombic media: Modeling elastic wave behavior in a vertically fractured earth”. *Geophysics*, 62 (6), 1954–1974.

Slawinski, M. A. (2015). *Waves and rays in elastic continua*. 3rd edn. World Scientific.

— (2018). *Waves and rays in seismology: Answers to unasked questions*. 2nd edn. World Scientific.

Svitek, T., Vavryčuk, V., Lokajíček, T., and Petružálek, M (2014). “Determination of elastic anisotropy of rocks from P- and S-wave velocities: numerical modelling and lab measurements”. *Geophys. J. Int.* 199 (3), 1682–1697.

Tsvankin, I. (1997). “Anisotropic parameters and P-wave velocity for orthorhombic media”. *Geophysics*, 62 (4), 1292–1309.

Post-publication comments

This paper is a natural continuation of the investigation performed in Chapter 4. In both chapters, we analyse the dependence of quasi P-wave phase velocity propagating in orthotropic media on particular elasticity parameters. However, herein we do not limit ourselves to the propagation in the x_3x_1 and x_3x_2 planes; we consider any incidence and azimuthal angle. Due to the complicated form of the velocity expression, we divide the stiffnesses into three groups, which facilitates the analysis. Hence, similarly to Chapter 4, we introduce certain simplifications to the investigation. We again utilise the idea of expressing the parameter dependence on velocity by a partial derivative. The relations among derivatives for any incidence and azimuthal angle are analogous to the relations for squared-velocity difference s^2, as presented in expressions (4.49) and (5.20). To support this derivative relation, one could perform analogous lengthy numerical analysis, as it was done in Chapter 4. Due to the abstract form of this paper, we omit such an analysis.

As noted by Dr. Zvi Koren, the expressions for cumulative moduli can be arranged as the combination of particular three stiffnesses and their weights. For instance, expression (5.1) can be rewritten as

$$\upsilon^*(\theta\,,\phi) = \sum_{i=1}^{3} m_i w_i\,, \tag{5.24}$$

where m_i are the model parameters (in this case C_{11}, C_{22}, C_{33}) and w_i are their corresponding weights,

$$w_i = \frac{\partial_{m_i} V(\theta\,,\phi)}{\sum_{k=1}^{3} \partial_{m_k} V(\theta\,,\phi)}\,, \qquad \sum_{i=1}^{3} w_i = 1\,. \tag{5.25}$$

Naturally, expressions (5.5) and (5.6) can be arranged in a similar manner. However, an issue may arise in case of a cumulative module λ^* responsible for the relationship among C_{13}, C_{23}, and C_{12}. In contrast to the rest of the orthotropic parameters, C_{13}, C_{23}, and C_{12} are allowed to have—by the stability conditions—negative values, which can lead to negative values of partial derivatives. In turn, the denominator inside λ^* can be very small or equal to zero. Therefore, we propose to define the weights as

$$w_i = \frac{|\partial_{m_i} V(\theta\,,\phi)|}{\sum_{k=1}^{3} |\partial_{m_k} V(\theta\,,\phi)|}\,, \qquad \sum_{i=1}^{3} w_i = 1 \tag{5.26}$$

to cope with this problematic case; this way, the issue of very small denominator is solved. (Nevertheless, $C_{12} = C_{13} = C_{23} = 0$ still cause the problem). Subsequently, once the weights are computed, they become numbers. Hence, we obtain a linear combination of stiffnesses with clear influences of each parameter to the phase velocity, as shown in expression (5.2), namely,

$$\upsilon^* = 0.6322C_{11} + 0.3678C_{33}\,. \tag{5.27}$$

Further, one can compute the value of a cumulative module by substituting the values of stiffnesses. Here, an additional comment is needed. A larger value of a cumulative module does not necessarily mean a bigger impact of the particular group of three stiffnesses on the phase velocity. This is because elasticity parameters may be small for some specific cases, but their corresponding derivatives and influence— significant. Hence, cumulative moduli are not designed to be compared to each other. However, the values of υ^*, λ^*, and μ^* can be needed for P-wave velocity approximation, where they are treated as the orthotropic extensions of cubic C_{11}, C_{13}, C_{44} stiffnesses, respectively.

As discussed in the paragraph above, cumulative moduli are expressed in terms of the weights described by partial derivatives. However, in expressions (5.3) and (5.7)–(5.8), we propose the approximations of the weights using trigonometric functions (useful for P-wave velocity estimation). We should note that our approximations have a heuristic nature; they are based on dozens of numerical experiments. The trigonometric functions are not obtained based on the mathematical derivation—this is the work for the future. Further, there is a typo in the formulations of λ and μ. The last term in the numerator and denominator of expressions (5.7) and (5.8) should have $\sin^4\theta\sin^2(2\phi)$ instead of $\sin^4\theta\cos^2(2\phi)$. The same typo appears in the last term of expressions (5.16) and (5.18). Also, in the original conference paper, graphs corresponding to Figures 5.2 and 5.3 incorrectly illustrate the values of $\sqrt{\lambda+2\mu}$. In this thesis, the graphs are corrected.

A comment on approximation $\sqrt{\upsilon}$ is needed. Till expression (5.21), the P-wave velocity approximation has an excellent accuracy; the relative error is negligible. To reduce the number of elasticity parameters, we assume $\upsilon^*\approx\lambda^*+2\mu^*$ that is arguable, especially in view of the discrepancy between analogous $\sqrt{\upsilon}$ and $\sqrt{\lambda+2\mu}$ in Figures 5.2 and 5.3. To clarify this step, we should rewrite expression (5.21) as

$$
\begin{aligned}
V &\approx \upsilon^*(2\partial_{C_{11}}V+2\partial_{C_{22}}V+2\partial_{C_{33}}V)+(\lambda^*+2\mu^*)(\partial_{C_{55}}V+\partial_{C_{44}}V+\partial_{C_{66}}V)\\
&=\upsilon^*\left(2\partial_{C_{11}}V+2\partial_{C_{22}}V+2\partial_{C_{33}}V+\partial_{C_{55}}V+\partial_{C_{44}}V+\partial_{C_{66}}V\right)-\Delta_\upsilon\,,
\end{aligned}
\tag{5.28}
$$

where

$$
\Delta_\upsilon := (\upsilon^*-\lambda^*-2\mu^*)(\partial_{C_{55}}V+\partial_{C_{44}}V+\partial_{C_{66}}V)\,. \tag{5.29}
$$

The next step of expression (5.22) makes sense if $\Delta_\upsilon\approx 0$ that does not have to be tantamount to $\upsilon^*\approx\lambda^*+2\mu^*$. Hence, to be precise, $\Delta_\upsilon\approx 0$, not $\upsilon^*\approx\lambda^*+2\mu^*$, should have been assumed in the paper. Based on the numerical experiments, one can notice that for angles $(\theta \vee \phi) \to (0^\circ \vee 90^\circ)$, derivatives $\partial_{C_{55}} V$, $\partial_{C_{44}} V$, $\partial_{C_{66}} V \to 0$. Therefore, for very small or very large angles, υ^* is allowed to be different from $\lambda^* + 2\mu^*$; the assumption $\Delta_\upsilon \approx 0$ stays reasonable. In other words, $\Delta_\upsilon \approx 0$ is tantamount to $\upsilon^* \approx \lambda^* + 2\mu^*$ that holds for moderate polar and azimuthal angles (but not necessarily very small or very large angles). In the last step, in expression (5.23), we assume that $\upsilon^* \approx \upsilon$. This assumption seems to be more accurate for smaller orthotropic anisotropy described by the parameter A, as discussed in Section 5.2. To sum up, in the process of derivation of P-wave velocity approximation, we have assumed $\upsilon^* \approx \lambda^* + 2\mu^*$ for moderate angles and insignificant orthotropic anisotropy. Hence, the inaccuracy of approximation $\sqrt{\upsilon}$ can be caused by anomalous values of oblique parameters (λ^*), anomalous values of shear moduli (μ^*), or large orthotropic anisotropy (A). As illustrated in Figures 5.2 and 5.3, the discrepancy between $\sqrt{\upsilon}$ and $\sqrt{\lambda + 2\mu}$ is rather insignificant for both moderate angles and the orthotropic anisotropy is low; hence, a good accuracy of the P-wave approximation is apparent.

The P-wave velocity approximation using module υ might be helpful in the context of fluid detection. Let us consider a scenario, where C_{11}, C_{22}, and C_{33} are obtained from two vertical and horizontal measurements. Assume that the aforementioned stiffnesses do not differ significantly, meaning that the orthotropic anisotropy is small. Having C_{11}, C_{22}, and C_{33}, we compute $\sqrt{\upsilon}$ that approximates P-wave velocity for any angle. If predicted velocity differs significantly from the observations, the anomalous λ^* or μ^* is expected. Anomalously high μ^* implies a low P/S ratio that is typical for gas-bearing rocks. Hence, the gas presence may be one of the causes of a velocity-prediction large inaccuracy.

Chapter 6

Effective elasticity of a medium with many parallel fractures*

Abstract

We consider an alternative way of obtaining the effective elastic properties of a cracked medium. Similarly, to the popular linear-slip model, we assume flat, parallel fractures, and long wavelengths. However, we do not treat fractures as weakness planes of displacement discontinuity. In contrast to the classical models, we represent fractures by a thin layer embedded in the background medium. In other words, we follow the Schoenberg-Douma matrix formalism for Backus averaging, but we relax the assumptions of infinite weakness and marginal thickness of a layer so that it does not correspond to the linear-slip plane. To represent the properties of a fracture, we need a fourth order elasticity tensor and a thickness parameter. The effective tensor becomes more complicated, but it may describe

*This chapter is the original research paper of Adamus, F. P. (2020). "Effective elasticity of a medium with many parallel fractures". *arXiv*, 2006.10434v3 [physics.geo-ph] (submitted to *Geophysical Journal International*).

a higher concentration of parallel cracks more accurately. Apart from the derivations of the effective elasticity tensors, we perform numerical experiments in which we compare the performance of our approach with a linear-slip model in the context of highly fractured media. Our model becomes pertinent if filled-in or empty cracks occupy more than one percent of the effective medium.

Keywords: Anisotropy, Effective, Elastic, Fractures.

6.1 Introduction

The influence of cracks on the elastic properties of a medium has been a topic of interest for numerous researchers. There are various models used to describe the effective elasticity parameters of a fractured material. Some authors assume short wavelength compared to the cracked structure so that crack-pore microgeometry and the properties of a fluid are essential (e.g., O'Connell and Budiansky, 1977). Others often focus on long wavelengths that are more suitable for seismic frequencies (e.g., Garbin and Knopoff, 1973). Further, models differ depending on the shape of cracks assumed. If they are ellipsoidal (Eshelby (1957), Nishizawa (1982), Hudson (1994)), the analysis usually becomes quite complicated (Hudson, 1981). In practice, however, the aspect ratio of cracks is typically low. Also, the details of their microstructure are often neglected in the seismic fracture-detection studies. Therefore, cracks are not rarely described as flat (see Kachanov, 1992), which is a useful simplification, since in some cases the results do not change very much compared to the ellipsoidal shapes (Hudson (1981), Schoenberg and Douma (1988), Thomsen (1995)). Flat fractures may be planar (Schoenberg, 1980), elliptical (Hudson, 1980), or irregular (Grechka et al., 2006). Moreover, cracks can be distributed randomly (Hudson, 1980), can be aligned (Thomsen, 1995) or parallel (Schoenberg and Douma, 1988).

In this paper, we consider long-wave, effective elasticity of a medium that corresponds to the background rock with parallel sets of flat fractures. Due to long-wavelength assumption, our investigation is pertinent—but not limited—to seismic studies.

There are three widely investigated, effective models that assume long wavelength and flat fractures (Cui et al., 2017). These are the linear-slip model, penny-shaped crack model, and the combined model. Below, we shortly describe each of them.

The linear-slip stands for the fracture interface across which the traction vector is continuous, but the displacement is not (Schoenberg, 1980). The displacement discontinuity linearly depends on traction. This relation is governed by the second-order tensor, which authors often refer to as the excess fracture compliance. Schoenberg and Douma (1988) are first to use the linear-slip concept in modelling the effective elasticity. Their work is based on Backus (1962) average, in which the aforementioned discontinuity corresponds to an infinitely weak and thin, horizontal layer. The work of Schoenberg and Douma (1988) was further developed by Schoenberg and Sayers (1995) that considered any orientation of linear-slip interfaces, not only the horizontal one. Another, but penny-shaped crack model was proposed by Garbin and Knopoff (1973) and then further developed by Hudson (1980). They use scattering formalism, where circular cracks are treated as scatterers. Cracks can be either aligned in one direction or randomly distributed. The expressions of Garbin and Knopoff (1973) are accurate to the first order in the concentration of cracks, whereas the expressions of Hudson (1980) to the second order. The second-order expressions correspond to the interactions between cracks that are not included in the linear-slip model. The penny-shaped model is complicated but accounts for the microstructure properties. The combined model is tantamount to the linear-slip one, but additionally relates the micro characteristics to the interface. Such a model was shown, for instance, by Hudson et al. (1996). The authors use scattering formalism and assume that circular cracks are aligned and parallel. This way, they obtain the excess fracture compliance related to cracks' properties. Subsequently, this second-order tensor can be used in the linear-slip model (Hudson and Liu, 1999).

In this paper, we propose another long-wave model in which cracks are flat. However, we assume a neither planar nor circular shape. Herein, we treat fractures as sets of thin parallel layers. We follow the approach of Schoenberg and Douma (1988), where they use the matrix formalism based on the Backus average. As opposed to the aforementioned authors, we do not assume that layers corresponding to fractures are infinitely weak and thin. In other words, we abandon the linear-slip description. In this way, the properties of fractures are represented by fourth-order elasticity tensor and layer thickness, instead of excess fracture compliance only. In the text, we refer to this method as the generalised Schoenberg-Douma approach or, simply, the generalised approach. The linear slip model of Schoenberg and Douma (1988) can be extended to viscoelastic (Chichinina and Obolentseva, 2009) or poroelastic (Rubino et al., 2015) media. Analogously, the extension can be made to the generalised method. However, due to the complexity of expressions, we focus on the elastic effects only. Thus, we assume that fractures are filled with solidified material. The properties of the filling material affect the elasticity parameters of the crack.

The main advantage of the generalised approach over the linear-slip model is that a high concentration of cracks is explicitly taken into account. The relaxation of infinite weakness and marginal thickness of cracks allows the representation of the elastic properties of a medium with many parallel fractures or the background rock with harder inclusions. The main body of the paper is dedicated to the comparison between the two aforementioned approaches. A heavily fractured medium was also considered in the combined models. Therein, the high concentration of cracks is described by, for instance, crack density parameter. In the rest part of the paper, we discuss the generalised approach and the combined models in the context of the effective elasticity of a medium with many parallel fractures.

6.2 Generalised Schoenberg-Douma approach

Elastic properties of parallel layers can be accurately approximated by the effective stiffness parameters of a homogeneous medium, assuming a sufficiently long wavelength. To obtain these effective parameters, consider a well-known Voigt's representation of a fourth-order elasticity tensor of arbitrary anisotropy,

$$\boldsymbol{C}_i = \begin{bmatrix} c_{11_i} & c_{12_i} & c_{13_i} & c_{14_i} & c_{15_i} & c_{16_i} \\ c_{12_i} & c_{22_i} & c_{23_i} & c_{24_i} & c_{25_i} & c_{26_i} \\ c_{13_i} & c_{23_i} & c_{33_i} & c_{34_i} & c_{35_i} & c_{36_i} \\ c_{14_i} & c_{24_i} & c_{34_i} & c_{44_i} & c_{45_i} & c_{46_i} \\ c_{15_i} & c_{25_i} & c_{35_i} & c_{45_i} & c_{55_i} & c_{56_i} \\ c_{16_i} & c_{26_i} & c_{36_i} & c_{46_i} & c_{56_i} & c_{66_i} \end{bmatrix} . \tag{6.1}$$

Such a matrix describes the elastic properties of the i-th thin layer. The above parameters can also be represented by three matrices proposed by Helbig and Schoenberg (1987),

$$\boldsymbol{M}_i = \begin{bmatrix} c_{11_i} & c_{12_i} & c_{16_i} \\ c_{12_i} & c_{22_i} & c_{26_i} \\ c_{16_i} & c_{26_i} & c_{66_i} \end{bmatrix} , \quad \boldsymbol{N}_i = \begin{bmatrix} c_{33_i} & c_{34_i} & c_{35_i} \\ c_{34_i} & c_{44_i} & c_{45_i} \\ c_{35_i} & c_{45_i} & c_{55_i} \end{bmatrix} , \quad \boldsymbol{P}_i = \begin{bmatrix} c_{13_i} & c_{14_i} & c_{15_i} \\ c_{23_i} & c_{24_i} & c_{25_i} \\ c_{36_i} & c_{46_i} & c_{56_i} \end{bmatrix} . \tag{6.2}$$

These 3×3 matrices allow one to homogenise a stack of thin layers having arbitrary anisotropy, using process analogous to Backus (1962) average. Assume that layers are horizontal, and the x_3-axis denotes depth. The elasticity parameters of a homogenised, long-wave equivalent medium are

$$\boldsymbol{N}_e = \overline{(\boldsymbol{N}_i^{-1})}^{-1}\,, \tag{6.3}$$

$$\boldsymbol{P}_e = \overline{(\boldsymbol{P}_i\,\boldsymbol{N}_i^{-1})}\,\overline{(\boldsymbol{N}_i^{-1})}^{-1}\,, \tag{6.4}$$

$$\boldsymbol{M}_e = \overline{\boldsymbol{M}_i - \boldsymbol{P}_i\boldsymbol{N}_i^{-1}\boldsymbol{P}_i^T} + \overline{\boldsymbol{P}_i\boldsymbol{N}_i^{-1}}\,\overline{(\boldsymbol{N}_i^{-1})}^{-1}\,\overline{\boldsymbol{N}_i^{-1}\boldsymbol{P}_i^T}\,, \tag{6.5}$$

where bar denotes the average and ^{T} stands for a transpose. The average is weighted by the layer thickness. The above derivations are identical to the ones of Helbig and Schoenberg (1987), Schoenberg and Douma (1988), and Schoenberg and Muir (1989). For simplicity, throughout the paper, we assume density-scaled parameters.

We denote the relative thickness of a layer as h_i, where $i \in \{1,\ldots,n\}$ and $\sum_{i=1}^{n} h_i = 1$; thus, a medium is composed of numerous layers of various relative thicknesses. Some of these layers correspond to the background (host) medium, whereas the rest to the set of thin and long parallel fractures that are filled with a solidified material. Since the average is commutative in the layer order and associative (Schoenberg and Muir, 1989), we can use these properties to fold the set of fractures into a single layer of total thickness h_f and obtain its effective stiffnesses. Analogously, we treat the background medium of total thickness $1-h_f$. Below, we rewrite expressions (6.3)–(6.5) in terms of background and fracture elasticities, indexed by letter b and f, respectively.

$$\boldsymbol{N}_e = \left((1-h_f)\boldsymbol{N}_b^{-1} + h_f\boldsymbol{N}_f^{-1}\right)^{-1} = \left((1-h_f)\boldsymbol{N}_b^{-1} + \boldsymbol{Z}\right)^{-1}\,, \tag{6.6}$$

$$\boldsymbol{P}_e = \left((1-h_f)\boldsymbol{P}_b\boldsymbol{N}_b^{-1} + h_f\boldsymbol{P}_f\boldsymbol{N}_f^{-1}\right)\boldsymbol{N}_e\,, \tag{6.7}$$

$$\begin{aligned}\boldsymbol{M}_e &= (1-h_f)(\boldsymbol{M}_b - \boldsymbol{P}_b\boldsymbol{N}_b^{-1}\boldsymbol{P}_b^T) + h_f(\boldsymbol{M}_f - \boldsymbol{P}_f\boldsymbol{N}_f^{-1}\boldsymbol{P}_f^T)\\ &\quad + \left((1-h_f)\boldsymbol{P}_b\boldsymbol{N}_b^{-1} + h_f\boldsymbol{P}_f\boldsymbol{N}_f^{-1}\right)\boldsymbol{N}_e\left((1-h_f)\boldsymbol{N}_b^{-1}\boldsymbol{P}_b^T + h_f\boldsymbol{N}_f^{-1}\boldsymbol{P}_f^T\right)\,,\end{aligned} \tag{6.8}$$

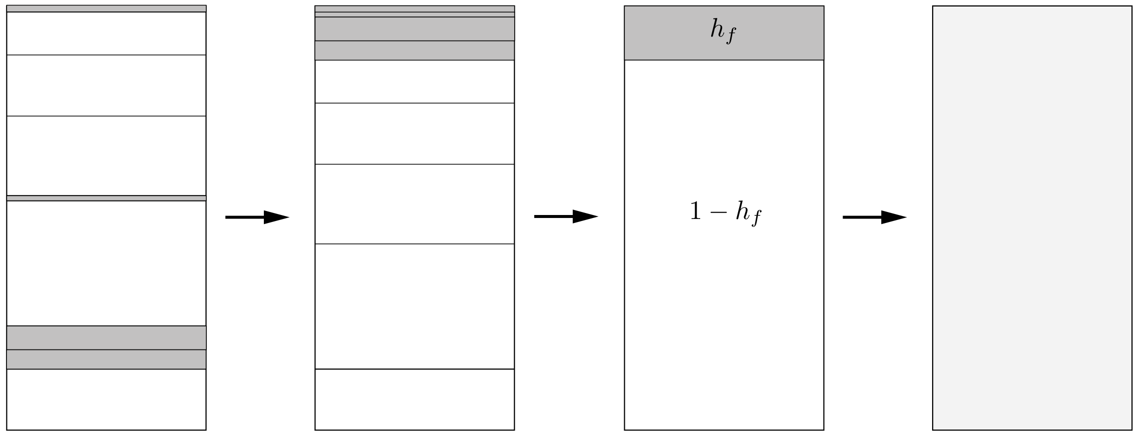

Figure 6.1: The illustration of commutative and associative properties of Helbig and Schoenberg (1987) average. The first column depicts the original layered medium, where grey colour denotes fractures filled with solidified material having different elastic properties. Subsequently, the layer sequence is interleaved so that fractures are cumulated in the upper part of the medium. Then, the effective parameters corresponding to fractures and background are obtained, respectively. In the last column, the effective parameters for the homogenised medium are calculated. The intermediate steps have no influence on the final results but are useful in the evaluation of the fracture's effect.

where $\boldsymbol{Z}$ is so-called fracture system compliance matrix (Schoenberg and Douma (1988), Schoenberg and Sayers (1995), Schoenberg and Helbig (1997)). We illustrate the homogenisation procedure used to obtain expressions (6.6)–(6.8) in Figure 6.1. Note that these expressions are the generalisations of Schoenberg and Douma (1988) derivation. The aforementioned authors assumed that the thickness of a system of fractures is marginal ($h_f \to 0$) and that fractures are infinitely weak $(\boldsymbol{M}_f, \boldsymbol{N}_f, \boldsymbol{P}_f \to 0)$. Upon introduction of such assumptions expressions (6.6)–(6.8) reduce to their results, namely,

$$\boldsymbol{N}_e \approx \left(\boldsymbol{N}_b^{-1} + h_f \boldsymbol{N}_f^{-1}\right)^{-1} = \left(\boldsymbol{N}_b^{-1} + \boldsymbol{Z}\right)^{-1} , \tag{6.9}$$

$$\boldsymbol{P}_e \approx \boldsymbol{P}_b \boldsymbol{N}_b^{-1} \left(\boldsymbol{N}_b^{-1} + \boldsymbol{Z}\right)^{-1} , \tag{6.10}$$

$$\boldsymbol{M}_e \approx \boldsymbol{M}_b - \boldsymbol{P}_b \boldsymbol{N}_b^{-1} \boldsymbol{P}_b^T + \boldsymbol{P}_b \boldsymbol{N}_b^{-1} \left(\boldsymbol{N}_b^{-1} + \boldsymbol{Z}\right)^{-1} \boldsymbol{N}_b^{-1} \boldsymbol{P}_b^T . \tag{6.11}$$

Let us discuss the physical meaning of expressions (6.9)–(6.11). The effect of fractures is expressed by $\boldsymbol{Z}$ only, which stands for the excess compliance caused by total displacement discontinuity (total linear slip) across weakness planes (Schoenberg and Douma, 1988). Thus, extremely thin layers are treated as planar discontinuities. The average of a background medium with a set of horizontal weakness planes becomes a particular case of a more general theory of Schoenberg and Sayers (1995), where planes of linear slip may have any orientation. Specifically, consider an equation of Schoenberg and Sayers (1995) that describes a background medium with one set of parallel weakness planes,

$$s_{ijk\ell} = s_{ijk\ell_b} + s_{ijk\ell_f} = s_{ijk\ell_b} + \frac{1}{4}\left(Z_{ik}n_\ell n_j + Z_{jk}n_\ell n_i + Z_{i\ell}n_k n_j + Z_{j\ell}n_k n_i\right) , \quad (6.12)$$

where $i, j, k, \ell \in \{1, 2, 3\}$, $s_{ijk\ell}$ denotes the compliances in a tensorial notation and n_i indicates the orientation of the planar slip. Note that if we insert vector $\boldsymbol{n} = [0, 0, 1]$, then we obtain the same result as from expressions (6.9)–(6.11). It is evident that in expressions (6.6)–(6.8), neither marginal thickness nor infinite weakness of a layer corresponding to fractures is assumed. Thus, expressions (6.6)–(6.8) are the generalisations of (6.9)–(6.11). In this generalised approach, we do not follow the theory of linear-slip excess compliances presented by Schoenberg and Sayers (1995). We treat a set of parallel fractures as thin and weak layers that does not have to be infinitely thin and weak but are allowed to be so. We believe that the aforementioned relaxation of linear-slip assumptions (no marginal thickness and infinite weakness) can be useful while willing to describe the effective elastic properties of a medium heavily cracked by weak fractures or a medium that contains few harder inclusions.

The physical meaning of the generalised approach can be extended to the influence of the set of parallel layers of any thickness and stiffness embedded in the background medium. Note that it depends on more unknowns than Schoenberg-Douma approximation; thus, it becomes more complicated. The influence of the fractures (or set of layers of any stiffness) is governed by thickness h_f and three matrices $\boldsymbol{M}_f$, $\boldsymbol{Z}$, and $\boldsymbol{P}_f$ (instead of $\boldsymbol{Z}$ only). Note that these three matrices represent a fourth-order elasticity tensor.

6.3 Examples of effective elasticity tensors

Let us consider quite a general example of a folded orthotropic layer of thickness h_f embedded in an orthotropic background medium of thickness $h_b = 1 - h_f$. We assume that tensors of both folded layer and background medium are expressed in a natural coordinate system. The elasticity parameters of a layer are

$$\boldsymbol{M}_f = \begin{bmatrix} f_{11} & f_{12} & 0 \\ f_{12} & f_{22} & 0 \\ 0 & 0 & f_{66} \end{bmatrix}, \quad \boldsymbol{P}_f = \begin{bmatrix} f_{13} & 0 & 0 \\ f_{23} & 0 & 0 \\ 0 & 0 & 0 \end{bmatrix}, \tag{6.13}$$

$$\boldsymbol{N}_f = \begin{bmatrix} f_{33} & 0 & 0 \\ 0 & f_{44} & 0 \\ 0 & 0 & f_{55} \end{bmatrix} = \begin{bmatrix} h_f Z_N^{-1} & 0 & 0 \\ 0 & h_f Z_{T_p}^{-1} & 0 \\ 0 & 0 & h_f Z_{T_q}^{-1} \end{bmatrix}, \tag{6.14}$$

where f_{ij} stand for stiffnesses of a folded layer representing parallel fractures. Subscript $_N$ denotes normal fracture system compliance, whereas $_{T_p}$ and $_{T_q}$ tangential compliances that, for horizontal layers, correspond to the x_2 and x_1 directions, respectively (see, Schoenberg and Douma, 1988). We assume neither marginal thickness nor infinite weakness of layers. To define the thickness of the folded layer, we use parameter h_f. Now, we need to introduce a new parameter that could refer to the relative weakness of the embedded layer.

We propose

$$w_{ij} \equiv 1 - \frac{f_{ij}}{c_{ij_b}}\,, \qquad i,j \in \{1,\dots,6\}\,, \tag{6.15}$$

where c_{ij_b} are stiffnesses of a background medium. Weakness w_{ij} is positive when the folded layer's elastic properties are weaker than the background, and negative when they are larger (we do not count unusual cases of negative stiffnesses). Infinitely weak layer (meaning that its stiffnesses are close to zero) gives $w_{ij} \to 1$. Note that if all $w_{ij} = 0$, then there is no distinction between background and folded layer. A stiffness tensor describing the elastic properties of a background medium with a set of parallel layers is

$$\boldsymbol{C}^{\text{eff}} = \begin{bmatrix} \boldsymbol{c}_1 & 0 \\ 0 & \boldsymbol{c}_2 \end{bmatrix}\,, \tag{6.16}$$

where

$$\boldsymbol{c}_1 = \begin{bmatrix} c_{11_b}\left(1-h_f w_{11}-h_b\frac{c_{13_b}^2}{c_{11_b}c_{33_b}}w_{13}\hat{\delta}_N\right) & c_{12_b}\left(1-h_f w_{12}-h_b\frac{c_{13_b}c_{23_b}}{c_{12_b}c_{33_b}}w_{13}w_{23}\hat{\delta}_N\right) & c_{13_b}(1-w_{13}\hat{\delta}_N) \\ c_{12_b}\left(1-h_f w_{12}-h_b\frac{c_{13_b}c_{23_b}}{c_{12_b}c_{33_b}}w_{13}w_{23}\hat{\delta}_N\right) & c_{22_b}\left(1-h_f w_{22}-h_b\frac{c_{23_b}^2}{c_{22_b}c_{33_b}}w_{23}\hat{\delta}_N\right) & c_{23_b}(1-w_{23}\hat{\delta}_N) \\ c_{13_b}(1-w_{13}\hat{\delta}_N) & c_{23_b}(1-w_{23}\hat{\delta}_N) & c_{33_b}(1-w_{33}\hat{\delta}_N) \end{bmatrix} \tag{6.17}$$

and

$$\boldsymbol{c}_2 = \begin{bmatrix} c_{44_b}(1-w_{44}\hat{\delta}_{T_p}) & 0 & 0 \\ 0 & c_{55_b}(1-w_{55}\hat{\delta}_{T_q}) & 0 \\ 0 & 0 & c_{66_b}\,(1-h_f w_{66}) \end{bmatrix}. \tag{6.18}$$

We define

$$0 \le \hat{\delta}_N \equiv \frac{Z_N c_{33_b}}{1 + Z_N c_{33_b} - h_f} \le 1\,, \tag{6.19}$$

$$0 \le \hat{\delta}_{T_p} \equiv \frac{Z_{T_p} c_{44_b}}{1 + Z_{T_p} c_{44_b} - h_f} \le 1\,, \tag{6.20}$$

$$0 \leq \hat{\delta}_{T_q} \equiv \frac{Z_{T_q} c_{55_b}}{1 + Z_{T_q} c_{55_b} - h_f} \leq 1 \, . \tag{6.21}$$

Coefficients $\hat{\delta}_N$, $\hat{\delta}_{T_p}$, and $\hat{\delta}_{T_q}$ are similar to deltas shown in Schoenberg and Helbig (1997). The essential difference is the presence of h_f in our expressions, which makes them more general. To indicate the above, we use hats over our parameters. If $h_f \to 0$ and $w_{ij} \to 1$, then matrix (6.16) represents the effective elasticity based on linear-slip theory. If we only assume the infinite weakness of folded layer, meaning that $h_f \not\to 0$ and $w_{ij} \to 1$, then the effective stiffnesses become weaker as compared to the stiffnesses based on linear-slip assumptions. For instance, $c_{66}^{\rm eff} = c_{66_b}(1 - h_f)$, whereas for linear-slip, $c_{66}^{\rm eff} = c_{66_b}$; it means that greater thickness of the folded layer, h_f, is responsible for the weakening of the effective medium. Note that to describe the infinitely weak folded layer that corresponds to thick cavity or very soft inclusion, we need only four parameters: Z_N, Z_{T_p}, Z_{T_q}, and h_f (see Appendix 6.A). On the other hand, if we set $h_f \to 0$ and $w_{ij} \not\to 1$, than the relaxed infinite weakness of the folded layer makes the effective medium stronger.

So far, we have discussed an example of an effective tensor corresponding to horizontal fractures embedded in a background medium. What if parallel fractures are not horizontal, but have a different orientation? What if there are more sets of fractures? We propose to follow the recipe presented in the last section of Schoenberg and Muir (1989). To model first set of fractures, we rotate the background medium to a desired coordinate system, then we calculate the effective parameters and rotate this tensor back. We repeat the process for other sets of fractures, where the background is the previously obtained effective medium. The interaction between fractures is neglected. Following the procedure of Schoenberg and Muir (1989), we obtain the effective tensor that corresponds to the orthotropic background medium with a set of orthotropic layers normal to the x_1-axis, namely,

$$\boldsymbol{c}_1^{(1)} = \begin{bmatrix} c_{11_b}\left(1-w_{11}^{33}\hat{\delta}_N^{(1)}\right) & c_{12_b}\left(1-w_{12}^{23}\hat{\delta}_N^{(1)}\right) & c_{13_b}\left(1-w_{13}\hat{\delta}_N^{(1)}\right) \\ c_{12_b}\left(1-w_{12}^{23}\hat{\delta}_N^{(1)}\right) & c_{22_b}\left(1-h_f w_{22}-h_b\frac{c_{12_b}^2}{c_{22_b}c_{11_b}}w_{12}^{23}\hat{\delta}_N^{(1)}\right) & c_{23_b}\left(1-h_f w_{23}^{12}-h_b\frac{c_{13_b}c_{12_b}}{c_{23_b}c_{33_b}}w_{13}w_{12}^{23}\hat{\delta}_N^{(1)}\right) \\ c_{13_b}\left(1-w_{13}\hat{\delta}_N^{(1)}\right) & c_{23_b}\left(1-h_f w_{23}^{12}-h_b\frac{c_{13_b}c_{12_b}}{c_{23_b}c_{33_b}}w_{13}w_{12}^{23}\hat{\delta}_N^{(1)}\right) & c_{33_b}\left(1-h_f w_{33}^{11}-h_b\frac{c_{13_b}^2}{c_{11_b}c_{33_b}}w_{13}\hat{\delta}_N^{(1)}\right) \end{bmatrix} \tag{6.22}$$

and

$$\boldsymbol{c}_2^{(1)} = \begin{bmatrix} c_{44_b}\left(1-h_f w_{44}^{66}\right) & 0 & 0 \\ 0 & c_{55_b}\left(1-w_{55}\hat{\delta}_{T_q}^{(1)}\right) & 0 \\ 0 & 0 & c_{66_b}\left(1-w_{66}^{44}\hat{\delta}_{T_p}^{(1)}\right) \end{bmatrix}, \tag{6.23}$$

where

$$w_{k\ell}^{ij} = 1 - \frac{f_{ij}}{c_{k\ell_b}}, \qquad \text{for} \quad (i,j) \neq (k,\ell), \quad \text{where} \quad i,j,k,\ell \in \{1,\ldots,6\} \tag{6.24}$$

and

$$0 \leq \hat{\delta}_N^{(1)} \equiv \frac{Z_N c_{11_b}}{1 + Z_N c_{11_b} - h_f} \leq 1, \tag{6.25}$$

$$0 \leq \hat{\delta}_{T_p}^{(1)} \equiv \frac{Z_{T_p} c_{66_b}}{1 + Z_{T_p} c_{66_b} - h_f} \leq 1, \tag{6.26}$$

$$0 \leq \hat{\delta}_{T_q}^{(1)} \equiv \frac{Z_{T_q} c_{55_b}}{1 + Z_{T_q} c_{55_b} - h_f} \leq 1. \tag{6.27}$$

Herein, subscripts $_{T_p}$ and $_{T_q}$ correspond to tangential compliances in horizontal (x_2) and vertical (x_3) directions, respectively. Schoenberg and Helbig (1997) denote them as $_{T_p} = {}_H$ and $_{T_q} = {}_V$. Superscript $^{(1)}$ indicates that the x_1-axis is normal to the set of embedded layers.

If fractures are normal to the x_2-axis, then we get

$$\boldsymbol{c}_1^{(2)} = \begin{bmatrix} c_{11_b}\left(1-h_f w_{11}-h_b \frac{c_{12_b}^2}{c_{11_b}c_{22_b}} w_{12}^{13}\hat{\delta}_N^{(2)}\right) & c_{12_b}\left(1-w_{12}^{13}\hat{\delta}_N^{(2)}\right) & c_{13_b}\left(1-h_f w_{13}^{12}-h_b \frac{c_{12_b}c_{23_b}}{c_{13_b}c_{22_b}} w_{12}^{13} w_{23}\hat{\delta}_N^{(2)}\right) \\ c_{12_b}\left(1-w_{12}^{13}\hat{\delta}_N^{(2)}\right) & c_{22_b}\left(1-w_{22}^{33}\hat{\delta}_N^{(2)}\right) & c_{23_b}\left(1-w_{23}\hat{\delta}_N^{(2)}\right) \\ c_{13_b}\left(1-h_f w_{13}^{12}-h_b \frac{c_{12_b}c_{23_b}}{c_{13_b}c_{22_b}} w_{12}^{13} w_{23}\hat{\delta}_N^{(2)}\right) & c_{23_b}\left(1-w_{23}\hat{\delta}_N^{(2)}\right) & c_{33_b}\left(1-h_f w_{33}^{22}-h_b \frac{c_{23_b}^2}{c_{22_b}c_{33_b}} w_{23}\hat{\delta}_N^{(2)}\right) \end{bmatrix} \tag{6.28}$$

and

$$\boldsymbol{c}_2^{(2)} = \begin{bmatrix} c_{44_b}\left(1-w_{44}\hat{\delta}_{T_p}^{(2)}\right) & 0 & 0 \\ 0 & c_{55_b}\left(1-h_f w_{55}^{66}\right) & 0 \\ 0 & 0 & c_{66_b}\left(1-w_{66}^{55}\hat{\delta}_{T_q}^{(2)}\right) \end{bmatrix}, \tag{6.29}$$

where

$$0 \le \hat{\delta}_N^{(2)} \equiv \frac{Z_N c_{22_b}}{1+Z_N c_{22_b}-h_f} \le 1\,, \tag{6.30}$$

$$0 \le \hat{\delta}_{T_p}^{(2)} \equiv \frac{Z_{T_p} c_{44_b}}{1+Z_{T_p} c_{44_b}-h_f} \le 1\,, \tag{6.31}$$

$$0 \le \hat{\delta}_{T_q}^{(2)} \equiv \frac{Z_{T_q} c_{66_b}}{1+Z_{T_q} c_{66_b}-h_f} \le 1\,. \tag{6.32}$$

Herein, subscripts $_{T_p}$ and $_{T_q}$ correspond to tangential compliances in vertical (x_3) and horizontal (x_1) directions, respectively. Superscript $^{(2)}$ indicates the normal to the set of embedded layers.

An example of effective tensor that corresponds to two sets of orthotropic layers normal to the x_1-axis and the x_2-axis that are embedded in the orthotropic background medium is complicated to present analytically. One of possible ways to obtain such a tensor is to treat coefficients of matrices $\boldsymbol{c}_1^{(1)}$ and $\boldsymbol{c}_2^{(1)}$ as background parameters and substitute them inside matrices $\boldsymbol{c}_1^{(2)}$ and $\boldsymbol{c}_2^{(2)}$.

All the examples discussed above can be easily reduced to cases of higher symmetry. For instance, if the background medium and folded layer are transversely isotropic with the x_3 symmetry axis (VTI), then $c_{11_b} = c_{22_b}$, $c_{13_b} = c_{23_b}$, $c_{44_b} = c_{55_b}$, $c_{11_b} = c_{12_b} + c_{66_b}$, and $w_{11} = w_{22}$, $w_{13} = w_{23}$, $w_{44} = w_{55}$, $w_{11} = w_{12} + w_{66}$. There are infinitely many examples of other effective tensors, which depend on the number of folded layers, their orientations and symmetry classes, and the symmetry class of the original background medium. These examples can be easily derived using expressions (6.6)–(6.8) and rotations of the coordinate system.

6.4 Numerical experiments

Let us discuss what may be the influence of thickness and stiffnesses of the folded layer that are neglected in the effective elasticity tensor obtained using linear-slip assumptions. To do so, we consider numerical experiments in which we focus on the relative error,

$$err = \frac{||(\boldsymbol{C}_b - \boldsymbol{C}_l^{\mathrm{eff}}) - (\boldsymbol{C}_b - \boldsymbol{C}^{\mathrm{eff}})||_2}{||\boldsymbol{C}_b - \boldsymbol{C}_l^{\mathrm{eff}}||_2} \times 100\% = \frac{||\Delta_l - \Delta||_2}{||\Delta_l||_2} \times 100\% \,, \tag{6.33}$$

where subscript $_l$ indicates the linear-slip approximation, and $\boldsymbol{C}_b$ denotes the background elasticity tensor. In the error above, we try to understand the discrepancy between linear-slip and generalised approach in estimating the influence of fractures. Therefore, to separate this influence from the background rock, we consider Δ_l not $\boldsymbol{C}_l^{\mathrm{eff}}$ in the denominator. We assume that the values of the background matrix $\boldsymbol{C}_b$ are known. We use a VTI background stiffness matrix from Schoenberg and Helbig (1997), namely,

$$\boldsymbol{C}_b = \begin{bmatrix} 10 & 4 & 2.5 & 0 & 0 & 0 \\ 4 & 10 & 2.5 & 0 & 0 & 0 \\ 2.5 & 2.5 & 6 & 0 & 0 & 0 \\ 0 & 0 & 0 & 2 & 0 & 0 \\ 0 & 0 & 0 & 0 & 2 & 0 \\ 0 & 0 & 0 & 0 & 0 & 3 \end{bmatrix} . \tag{6.34}$$

To describe the influence of cracks, in Schoenberg-Douma approximation, we need the excess fracture compliance 3×3 matrix $\boldsymbol{Z} = h_f \boldsymbol{N}_f^{-1}$ only. Hence, in general, we require the maximum number of six independent compliances or, equivalently, six independent stiffnesses, and one thickness parameter (both matrices are symmetric). However, to obtain the generalised formulas, apart from $\boldsymbol{Z}$, we need 3×3 matrices $\boldsymbol{M}_f$, $\boldsymbol{P}_f$, and thickness h_f ($\boldsymbol{P}_f$ is not symmetric). It gives the maximum number of twenty–one independent elasticity parameters (if the folded layer is generally anisotropic) and one thickness coefficient. In the numerical experiments, we assume that values of $\boldsymbol{Z}$ are the same for both approaches. In other words, $\boldsymbol{Z}$ does not influence err.

We assume one set of parallel fractures with a normal directed towards the x_1-axis. Herein, to manipulate the overall elastic properties of the folded layer easily and to understand its influence on err better, we also assume that the background and folded layer's stiffnesses are proportional. Hence, in our example, the fractures—same as the background—have VTI symmetry. We introduce,

$$\boldsymbol{C}_f = k\, \boldsymbol{C}_b\,, \tag{6.35}$$

where k is a scalar denoting hardness of the folded layer and $\boldsymbol{C}_f$ is a 6×6 matrix that consists of fracture stiffnesses f_{ij} (previously described by matrices $\boldsymbol{N}_f = h_f \boldsymbol{Z}^{-1}$, $\boldsymbol{M}_f$, and $\boldsymbol{P}_f$). Factor k is helpful, since one parameter governs all twenty–one stiffnesses of $\boldsymbol{C}_f$. Also, the simplicity of k can be physically justified when the folded layer is weak, and the exact values of specific stiffnesses do not matter so much. Hardness k can be understood as a simplification and an alternative to the previously defined weaknesses w_{ij}, where $k = 1 - w_{ij}$. In the context of the above expressions, the parameters needed for the fracture description in Scohenberg-Douma approximation are

$$\boldsymbol{Z} = h_f \begin{bmatrix} f_{33} & f_{34} & f_{35} \\ f_{34} & f_{44} & f_{45} \\ f_{35} & f_{45} & f_{55} \end{bmatrix}^{-1} = \frac{h_f}{k} \begin{bmatrix} c_{33_b} & c_{34_b} & c_{35_b} \\ c_{34_b} & c_{44_b} & c_{45_b} \\ c_{35_b} & c_{45_b} & c_{55_b} \end{bmatrix}^{-1} = \frac{h_f}{k} \begin{bmatrix} 1/6 & 0 & 0 \\ 0 & 1/2 & 0 \\ 0 & 0 & 1/2 \end{bmatrix}. \tag{6.36}$$

In the generalised formulation, we also have the same two unknowns that describe the fractures (see Appendix 6.B). Hence, the error depends only on the thickness h_f and hardness k. Below, we perform three numerical experiments in which we manipulate the values of h_f and k, so that either one or two of the linear-slip assumptions are relaxed. Specifically, we relax $k \to 0$, then $h_f \to 0$, and lastly, we relax them both. We check what the influence of the aforementioned relaxations on the relative error (6.33) is.

Let us make a brief comment on the volatility of $\boldsymbol{Z}$. As we see in expression (6.36), $\boldsymbol{Z}$ depends on hardness and thickness of fractures. In the inverse problems, it might be difficult to estimate its values precisely, especially when the layer is very thin and weak (linear-slip theory). If, say $h_f = 10^{-12}$, then it does not really matter—in terms of marginal differences in the absolute values—if $k = 100h_f$ or $k = 0.01h_f$, still k is very small, but its influence on $\boldsymbol{Z}$ is enormous. Hence, if fractures are very thin and weak, a small change in their compliances makes $\boldsymbol{Z}$ almost impossible to estimate (if we know the elastic properties of the effective medium, but do not know the background). Therefore, to make our experiments more realistic, we do not allow h_f and k to be smaller than 10^{-6} .

Relaxation of infinite weakness assumption

In this experiment, we fix a very small thickness $h_f = 10^{-5}$ and allow k to grow. Notice that when k increases, $\boldsymbol{Z}$ becomes smaller. Marginal h_f and growing k corresponds to the relaxation of the infinite weakness assumption of the linear-slip theory. In this way, we wish to isolate the influence of the hardness of the folded layer on err. Specifically, we check how much one can be wrong when in forward modelling assumes infinite weakness and marginal thickness of the folded layer, but the former assumption is incorrect. The results are illustrated in Figure 6.2.

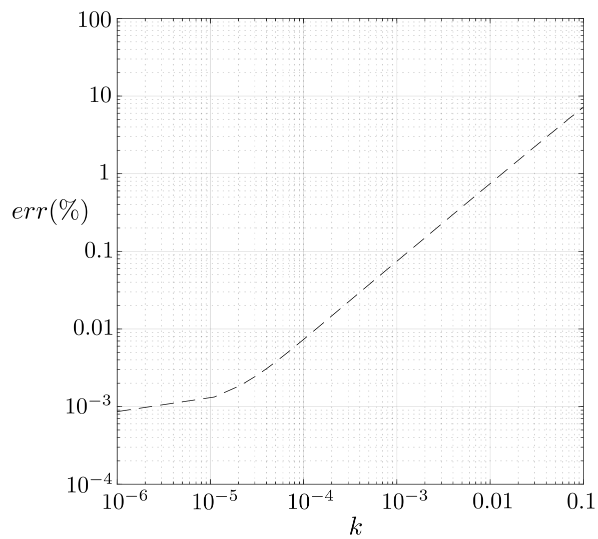

Figure 6.2: Dashed line illustrates the relative error, err, as a function of hardness, k , of folded layer. Thickness is fixed, $h_f = 10^{-5}$; hence, values of $\boldsymbol{Z}$ diminish when k grows. The axes are presented in a logarithmic scale.

We see that the relaxation of the infinite weakness assumption has quite substantial effect on the results. Let us think of extremely thin parallel inclusions that are ten times weaker than the background medium. The above-mentioned physical example corresponds to $k = 0.1$ for which err is around seven percent. Note that the error remains above one percent even for the inclusions fifty times weaker than the surroundings. Thus, despite the complexity of expressions (6.6)–(6.8), the application of these generalised equations might be worth consideration if fractures are not extremely weak. Matrix $\boldsymbol{Z}$ can have very low values if k is much larger than h_f, which corresponds to the right part of Figure 6.2.

Relaxation of marginal thickness assumption

Herein, we follow the infinite weakness assumption of the linear-slip theory. Thus, we fix a very small value of $k = 10^{-5}$. However, we relax the assumption of marginal thickness; therefore, we allow h_f to grow. Notice that as thickness increases, so do values of matrix $\boldsymbol{Z}$. Physically, minimal value of k and growing h_f may correspond to empty cavities or very soft inclusions embedded in the host medium. In this numerical experiment, we expect to isolate the effect of relative thickness h_f on err. Precisely, we examine how much one can be wrong when in forward modelling assumes the linear-slip deformation, but the assumption of marginal thickness is incorrect. The results are depicted by a dashed line in Figure 6.3.

The influence of h_f on the error seems to be quite significant and similar to the impact of k (compare Figures 6.2 and 6.3). Let us think of parallel cavities that take one percent of the effective medium's space and which stiffnesses are extremely weak. The aforementioned scenario corresponds to $h_f = 0.01$ for which err is almost one percent. The error becomes even more substantial for greater thicknesses of the folded layer. Again, the application of the generalised equations might be worth consideration if h_f is substantial. The situation of large h_f and extremely weak layer corresponds to very substantial values of $\boldsymbol{Z}$.

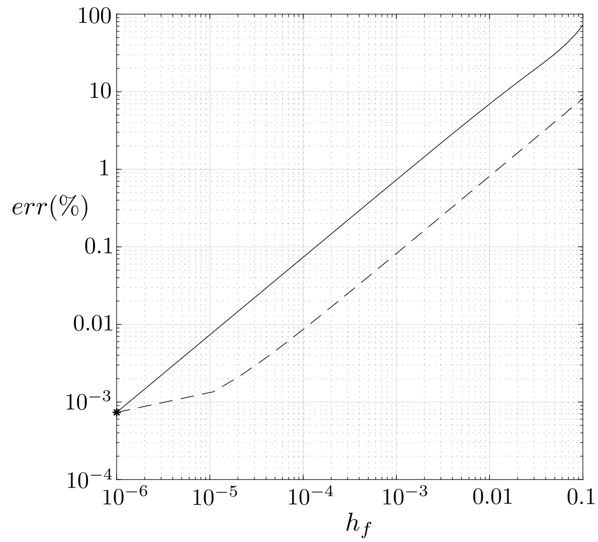

Figure 6.3: Both lines illustrate the relative error, err, as a function of thickness, h_f, of folded layer. For dashed line, hardness is fixed, $k = 10^{-5}$; hence, values of $\boldsymbol{Z}$ increase along with growing h_f. For solid line, $h_f = 0.1k$; thus, values of $\boldsymbol{Z}$ are fixed. Both lines present identical values in a star point, since $k = 10^{-5} = 10h_f$. As h_f grows the discrepancy between two lines is larger, which is caused by the influence of k (matrix $\boldsymbol{Z}$ has no influence on the error). The axes are presented in a logarithmic scale.

Relaxation of both assumptions

In this example, we choose specific values of $\boldsymbol{Z}$ so that h_f and k are both allowed to grow. Hence, we relax both assumptions of linear-slip deformation. We want realistic values of excess compliance matrix, similar to those of Schoenberg and Helbig (1997). Therefore, we choose $k = 10h_f$ and get

$$\boldsymbol{Z} = \begin{bmatrix} 1/60 & 0 & 0 \\ 0 & 1/20 & 0 \\ 0 & 0 & 1/20 \end{bmatrix}. \tag{6.37}$$

Having the above parameters set, we obtain $||\Delta_l||_2 \approx 1.8\,[\mathrm{km/s^2}]$, which indicates that the effect of fractures is relatively moderate. The solid line presents the cumulative influence of growing h_f and k on the error in Figure 6.3.

The result is similar to the previous numerical experiment, where k varied, but h_f was very small. For example, if $h_f = 0.01$ and $k = 0.1$, then $err \approx 6.95\%$. On the other hand, in Figure 6.2, $k = 0.1$ corresponds to $h_f = 10^{-5}$ and $err \approx 7.21\%$. Further, if $h_f = 10^{-4}$ and $k = 0.01$, then $err \approx 0.73\%$. In Figure 6.2, $k = 0.01$ corresponds to $h_f = 10^{-5}$ and $err \approx 0.75\%$. From our numerical example, we deduce that err does not augment if both assumptions, instead of one, are relaxed.

To sum up, in general, the larger the thickness or hardness of the layer of interest, the greater the error. Based on our example, thickness h_f and hardness k seem to have similar contributions to err. We believe that the linear-slip theory is relatively accurate if fractures of the effective medium take less than one percent of its space and are at least a hundred times weaker than the background. Otherwise, we recommend using the generalised approach. The number of parameters used in our method can be greatly reduced by introducing scaling factor k, as presented in the numerical experiments and exemplified in Appendix 6.B.

6.5 Comparison with other approaches

So far, we have discussed the generalised approach in the context of the linear-slip theory only. In this section, we compare it to the models that take into account the micro properties, such as the concentration of cracks. First, let us consider the penny-shaped crack models proposed by Hudson (1980) and Hudson and Liu (1999). As we have already discussed in Section 6.1, these models were derived based on the scattering formalism. The concentration of scatterers (cracks) is represented by the crack density parameter, e. The intrinsic limitation of the scattering approach is that scatterers must be diluted (Keller, 1960). Hence, the parameter responsible for the concentration of cracks, e, cannot be large.

This is a significant drawback compared to the generalised Schoenberg-Douma model since h_f has no limitation. Hudson models are derived for isotropic background and involve second rank tensor $\bar{\boldsymbol{U}}$ that represents the elastic properties of fractures. Following the works of Hudson, we consider isotropic background, cracks with normal towards the x_3-axis, and rotationally invariant $\bar{\boldsymbol{U}}$ and $\boldsymbol{Z}$ (meaning that $Z_{T_p} = Z_{T_q} = Z_T$). The elasticity parameters of the linear-slip model are tantamount to the parameters shown in Hudson (1980) and Hudson and Liu (1999). Specifically, using the linear-slip model, we get

$$\boldsymbol{C} = \begin{bmatrix} c_{11_b}\left(1-\frac{c_{12_b}^2}{c_{11_b}^2}\delta_N\right) & c_{12_b}\left(1-\frac{c_{12_b}}{c_{11_b}}\delta_N\right) & c_{12_b}(1-\delta_N) & 0 & 0 & 0 \\ c_{12_b}\left(1-\frac{c_{12_b}}{c_{11_b}}\delta_N\right) & c_{11_b}\left(1-\frac{c_{12_b}^2}{c_{11_b}^2}\delta_N\right) & c_{12_b}(1-\delta_N) & 0 & 0 & 0 \\ c_{12_b}(1-\delta_N) & c_{12_b}(1-\delta_N) & c_{11_b}(1-\delta_N) & 0 & 0 & 0 \\ 0 & 0 & 0 & c_{44_b}(1-\delta_T) & 0 & 0 \\ 0 & 0 & 0 & 0 & c_{44_b}(1-\delta_T) & 0 \\ 0 & 0 & 0 & 0 & 0 & c_{44_b} \end{bmatrix}, \tag{6.38}$$

where $c_{11_b} = c_{12_b} + 2c_{44_b}$ and

$$\delta_N = \frac{Z_N c_{11_b}}{1+Z_N c_{11_b}}, \quad \delta_T = \frac{Z_{T_q} c_{44_b}}{1+Z_{T_q} c_{44_b}}. \tag{6.39}$$

To obtain Hudson models, we insert either (see expressions (51)–(54) of Hudson (1980))

$$Z_N = \frac{\frac{c_{11_b}}{c_{44_b}} e\bar{U}_{33} + O(e^2)}{c_{11_b}\left(1-\frac{c_{11_b}}{c_{44_b}} e\bar{U}_{33} - O(e^2)\right)}, \qquad Z_T = \frac{e\bar{U}_{11} + O(e^2)}{c_{44_b}\left(1-e\bar{U}_{11}-O(e^2)\right)}, \tag{6.40}$$

or (see expression (8) of Hudson and Liu (1999))

$$Z_N = \frac{e\bar{U}_{33}}{c_{44_b}} + \Theta(e^2), \qquad Z_T = \frac{e\bar{U}_{11}}{c_{44_b}} + \Theta(e^2), \tag{6.41}$$

inside of $\boldsymbol{C}$. Both $O(e^2)$ and $\Theta(e^2)$ are second-order terms in crack density, responsible for the crack interactions. Hence, penny-shaped crack models, up to the first-order in e, can be treated as linear-slip models with parameters related to cracks' specific microstructure (we call them combined models). Assuming that cracks are infinitely weak—by means of Eshelby theory—components $\bar{U}_{11}$ and $\bar{U}_{33}$ can be related to the background stiffnesses (Eshelby (1957), Budiansky and O'Connell (1976), Hudson and Liu (1999)),

$$\bar{U}_{11} = \frac{16c_{11_b}}{3\left(3c_{11_b} - 2c_{44_b}\right)}\,, \qquad \bar{U}_{33} = \frac{4c_{11_b}}{3\left(c_{11_b} - c_{44_b}\right)}\,. \tag{6.42}$$

As indicated by Sayers and Kachanov (1991), second terms in the models of Hudson are not sufficient to account for higher concentration of cracks. From $e > 0.2$ they start to exhibit meaningless behaviour (the aforementioned limitation of the scattering approach). Most of the combined approaches neglect the second-order terms. Some of them do not assume interactions among cracks (non-interaction approximation), which is accurate for small (or, in some cases, moderate) concentrations of cracks only (Kachanov and Sevostianov, 2018). The other methods, such as the self-consistent, differential, or Mori-Tanaka schemes, tend to overestimate the impact of cracks on the effective stiffness (Kachanov, 1992). As shown by simulations of Saenger et al. (2006), the differential method seems to provide the best results for a high concentration of cracks. In the aforementioned schemes, density parameter e can be replaced by second and fourth-order tensors that cover all orientation distributions of cracks in a unified way (Kachanov, 1992). Below, for simplicity, we focus on e only.

The upside of the combined models is their ability to relate micro properties of cracks to excess fracture compliance $\boldsymbol{Z}$. Also, under certain conditions, they allow expressing $\boldsymbol{Z}$ in terms of the background stiffnesses (expression (6.42)). However, we need to emphasise their main downside in the context of heavily cracked media. The combined models assume that cracks are flat, meaning that their aspect ratio is very small ($\alpha \to 0$). To relate micro properties to the linear-slip, the volume fraction occupied by cracks, ϕ_f , must be also very small that is tantamount to $h_f \to 0$ assumed by Schoenberg and Douma (1988). Crack density combines both α and ϕ_f , namely,

$$e = \frac{3\phi_f}{4\pi\alpha} \, . \tag{6.43}$$

However, if the aspect ratio occurs to be small but not infinitely small, then a large number of e implies a significant value of ϕ_f . In turn, large ϕ_f is tantamount to a significant h_f that violates the assumption underlying the linear-slip theory. Therefore, the value of e seems to be limited intrinsically.

The generalised method seems to be more adequate in describing media with many parallel fractures than combined approaches since a large concentration of cracks corresponds to large h_f that does not violate the generalised method's assumptions. Perhaps, it is possible to utilise both parameters e and h_f jointly. In a particular case of flat but infinitely weak fractures (with no marginal thickness of the folded layer), we may use the Eshelby theory to express $\boldsymbol{Z}$ in terms of background elasticities and density parameter as it is done in the combined approaches. In other words, we conjecture that

$$Z_N = \frac{4c_{11_b}e}{3c_{44_b}\left(c_{11_b} - c_{44_b}\right)} \, , \qquad Z_T = \frac{16c_{11_b}e}{3c_{44_b}\left(3c_{11_b} - 2c_{44_b}\right)} \tag{6.44}$$

can be inserted inside matrices obtained using the generalised method (where $w_{ij} = 1$ and $h_f > 0$) . This conjecture needs to be verified by experimental studies.

To sum up, a higher concentration of cracks can be either described by a density parameter or by h_f, depending on whether the combined model or generalised method is used, respectively. Both methods give different effective elasticity parameters. For instance, if background is isotropic and cracks are aligned along the axis, e influences five independent effective stiffnesses (matrix (6.38)), whereas h_f influences six stiffnesses (simplified matrix (6.16)). Moreover, e is accurate for small numbers only, whereas h_f has no limitations. Perhaps it is possible to combine micro properties with a particular case of the generalised approach employing the Eshelby theory.

6.6 Conclusions

We have presented an alternative way of computing the effective elasticity tensor corresponding to a medium with parallel sets of fractures that are filled with a solidified material. We have discussed a traditional Schoenberg-Douma method that is based on the linear-slip approximation. Further, we have shown a generalisation of their approach and examined if consideration of more complicated expressions might be useful in the context of the approximation accuracy. The significant difference between the two aforementioned approaches is that the generalisation considers thickness and additional (to $\boldsymbol{Z}^{-1}$) elastic properties of the layer that corresponds to the system of parallel fractures. We believe that no assumption of linear-slip deformation in the generalised expressions can be useful while describing the effective elastic properties of a medium that is heavily fractured or contains a few harder inclusions.

In case a material includes numerous empty cavities, our model simplifies, so that the additional elastic properties of the folded layer are not taken into account (see Appendix 6.A). However, in such a case, our approach still differs from a traditional linear-slip method since the thickness parameter (h_f) is considered. Another simplification to our model is possible if we assume that the scaled background stiffnesses describe the elasticity of fractures. This way, only two additional parameters—thickness h_f and scaling factor k—are needed to consider the influence of parallel fractures (see Appendix 6.B). The linear-slip model can be simplified in a similar manner.

Numerical experiments have exposed that in forward problems, the consideration of parallel fractures intensity (equivalently, thickness h_f of the folded layer) and its additional elasticity parameters might be essential. We believe that also in the inverse problems, where we expect a heavily cracked medium, the generalised equations shown in this paper might be worth considering. It seems that the linear-slip approximation is quite accurate if fractures of the effective medium take less than one percent of its space and are at least a hundred times weaker than the background. If the fractures take more space or are harder, we recommend using the generalised Schoenberg-Douma approach that does not neglect the intensity of inclusions.

Other possible methods that take into account the high concentration of cracks are the combined, penny-shaped crack models. These approaches take into consideration the density and microstructure of cracks. The drawback of these methods is that they are limited intrinsically to the diluted concentration of cracks, and they are quite complicated. Also, their parameter responsible for the intensity of cracks (e) affects less number of the effective stiffnesses compared to the analogous parameter presented in the generalised approach (h_f). A combination of penny-shaped crack models with the generalised method seems possible. In this way, cracks are described by the background elasticities, density parameter and h_f.

Note that the generalised Schoenberg-Douma method is suitable for the computation of long-wave effective elasticity of any medium composed of parallel layers. Naturally, this approach is not limited to a very thin layer embedded in the background medium, which was the focus of this paper.

Acknowledgements

We wish to acknowledge discussions with Michael A. Slawinski. Also, we thank Elena Patarini for the graphical support. The research was done in the context of The Geomechanics Project partially supported by the Natural Sciences and Engineering Research Council of Canada, grant 202259. The author has no conflict of interest to declare.

6.7 References

Backus, G. E. (1962). “Long-Wave Elastic Anisotropy Produced by Horizontal Layering”. *J. Geophys. Res.* 67 (11), 4427–4440.

Budiansky, B. and O’Connell, R. J. (1976). “Elastic moduli of a cracked solid”. *Int. J. Solids Struct.* 12 (2), 81–97.

Chichinina, T. and Obolentseva, I. (2009). “Generalization of Schoenberg’s linear slip model to attenuative media: Physical modeling versus theory”. *SEG Expanded Abstracts*, 3451–3457.

Cui, X., Lines, L., Krebes, E. S., and Peng, S. (2017). *Seismic Forward Modeling of Fractures and Fractured Medium Inversion*. Springer.

Eshelby, J. D. (1957). “The determination of the elastic field of an ellipsoidal inclusion, and related problems”. *Proc. R. Soc. A*, 241 (1226), 376–396.

Garbin, H. D. and Knopoff, L. (1973). “The compressional modulus of a material permeated by a random distribution of circular cracks”. *Q. Appl. Math.* 30 (4), 454–464.

Grechka, V., Vasconcelos, I., and Kachanov, M. (2006). “The influence of crack shape on the effective elasticity of fractured rocks”. *Geophysics*, 71 (5), D153–D160.

Helbig, K. and Schoenberg, M. (1987). “Anomalous polarization of elastic waves in transversely isotropic media”. *J. Acoust. Soc. Am.* 81 (5), 1235–1245.

Hudson, J. A. (1980). “Overall properties of a cracked solid”. *Math. Proc. Cambridge Philos. Soc.* 88 (2), 371–384.

— (1994). “Overall properties of a material with inclusions or cavities”. *Geophys. J. Int.* 117 (2), 555–561.

— (1981). “Wave speeds and attenuation of elastic waves in material containing cracks”. *Geophys. J. R. Astron. Soc.* 64 (1), 133–150.

Hudson, J. A. and Liu, E. (1999). “Effective elastic properties of heavily faulted structures”. *Geophysics*, 64 (2), 479–485.

Hudson, J. A., Liu, E., and Crampin, S. (1996). “Transmission properties of a plane fault”. *Geophys. J. Int.* 125 (2), 559–566.

Kachanov, M. (1992). “Effective elastic properties of cracked solids: critical review of some basic concepts”. *Appl. Mech. Rev.* 45 (8), 304–335.

Kachanov, M. and Sevostianov, I. (2018). *Micromechanics of Materials, with Applications*. Springer.

Keller, J. B. (1960). *Wave Propagation in Random Media*. Tech. rep. EM–164. New York University, Institute of Mathematical Sciences Division of Electromagnetic Research.

Nishizawa, O. (1982). “Seismic velocity anisotropy in a medium containing oriented cracks—transversely isotropic case”. *Journal of Physics of the Earth*, 30 (4), 331–347.

O’Connell, R. J. and Budiansky, B. (1977). “Viscoelastic properties of fluid-saturated cracked solids”. *J. Geophys. Res.* 82 (36), 5719–5736.

Rubino, J. G., Castromán, G. A., Müller, T. M., Monachesi, L. B., Zyserman, F. I., and Holliger, K. (2015). “Including poroelastic effects in the linear slip theory”. *Geophysics*, 80 (2), 1–6.

Saenger, E. H., Kruger, O. S., and Shapiro, S. (2006). “Effective Elastic Properties of Fractured Rocks: Dynamic vs. Static Considerations”. *Int. J. Fract.* 139 (3), 569–576.

Sayers, C. and Kachanov, M. (1991). “A simple technique for finding effective elastic constants of cracked solids for arbitrary crack orientation statistics”. *Int. J. Solids Struct.* 7 (6), 671–680.

Schoenberg, M. (1980). “Elastic wave behavior across linear slip interfaces”. *J. Acoust. Soc. Am.* 68 (5), 1516–1521.

Schoenberg, M. and Douma, J. (1988). “Elastic wave propagation in media with parallel fractures and aligned cracks”. *Geophysical Prospecting*, 36 (6), 571–590.

Schoenberg, M. and Helbig, K. (1997). “Orthorhombic media: Modeling elastic wave behavior in a vertically fractured earth”. *Geophysics*, 62 (6), 1954–1974.

Schoenberg, M. and Muir, F. (1989). “A calculus for finely layered anisotropic media”. *Geophysics*, 54 (5), 581–589.

Schoenberg, M. and Sayers, C. M. (1995). “Seismic anisotropy of fractured rock”. *Geophysics*, 60 (1), 204–211.

Thomsen, L. (1995). “Elastic anisotropy due to aligned cracks in porous rock”. *Geophysical Prospecting*, 43 (6), 805–829.

6.A Effective elasticity with weakness assumption only

Consider an effective tensor that corresponds to the orthotropic background medium with a set of orthotropic layers normal to the x_1-axis. Layers are folded into one medium representing fractures. If we assume infinite weakness of the folded layer, but not its marginal thickness, then matrices (6.22) and (6.23) are simplified. We get

$$\boldsymbol{C}^{\text{eff}} = \begin{bmatrix} \boldsymbol{c}_1 & 0 \\ 0 & \boldsymbol{c}_2 \end{bmatrix}, \tag{6.45}$$

where

$$
\boldsymbol{c}_1 = \begin{bmatrix} c_{11_b}\left(1-\hat{\delta}_N\right) & c_{12_b}\left(1-\hat{\delta}_N\right) & c_{13_b}\left(1-\hat{\delta}_N\right) \\ c_{12_b}\left(1-\hat{\delta}_N\right) & c_{22_b}h_b\left(1-\frac{c_{12_b}^2}{c_{22_b}c_{11_b}}\hat{\delta}_N\right) & c_{23_b}h_b\left(1-\frac{c_{13_b}c_{12_b}}{c_{23_b}c_{33_b}}\hat{\delta}_N\right) \\ c_{13_b}\left(1-\hat{\delta}_N\right) & c_{23_b}h_b\left(1-\frac{c_{13_b}c_{12_b}}{c_{23_b}c_{33_b}}\hat{\delta}_N\right) & c_{33_b}h_b\left(1-\frac{c_{13_b}^2}{c_{11_b}c_{33_b}}\hat{\delta}_N\right) \end{bmatrix}, \qquad (6.46)
$$

$$
\boldsymbol{c}_2 = \begin{bmatrix} c_{44_b}h_b & 0 & 0 \\ 0 & c_{55_b}\left(1-\hat{\delta}_V\right) & 0 \\ 0 & 0 & c_{66_b}\left(1-\hat{\delta}_H\right) \end{bmatrix}, \qquad (6.47)
$$

and

$$
\hat{\delta}_N = \frac{Z_N c_{11_b}}{h_b + Z_N c_{11_b}}, \quad \hat{\delta}_V = \frac{Z_V c_{55_b}}{h_b + Z_V c_{55_b}}, \quad \hat{\delta}_H = \frac{Z_H c_{66_b}}{h_b + Z_H c_{66_b}}. \qquad (6.48)
$$

Excess fracture compliance that corresponds to displacement in normal, vertical, and horizontal direction is denoted by Z_N, Z_V, and Z_H, respectively. The elastic properties of a background medium are described by c_{ij_b}, whereas h_b stands for the relative thickness of such medium. The description of fractures needs only four parameters; Z_N, Z_V, Z_H, and h_b. Thickness $h_b \in (0,1]$ is the only coefficient that distinguishes the above matrices from the linear-slip description. If $h_b = 1$ than we get effective elasticity consistent with theory of Schoenberg and Douma (1988) or Schoenberg and Sayers (1995).

6.B Effective elasticity with scaling factor k

Again, consider an effective tensor that corresponds to the orthotropic background with an embedded set of orthotropic fractures normal to the x_1-axis. Assume that the elastic properties of folded fractures are equal to the scaled background stiffnesses. In other words, we invoke expression (6.35), namely, $C_f = kC_b$, where k is a scalar that relates 6×6 matrices describing fractures and the background, respectively. Due to the assumption above, the effective tensor represented by matrices (6.22) and (6.23) requires a lower number of parameters. To show it, first, we rewrite the weaknesses

$$w_{ij} = 1 - k\,, \qquad w^{ij}_{kl} = 1 - k c_{ij_b}/c_{kl_b} \tag{6.49}$$

and the excess compliances

$$Z_N = \frac{h_f}{c_{33_b} k}\,, \qquad Z_{T_p} = \frac{h_f}{c_{44_b} k}\,, \qquad Z_{T_q} = \frac{h_f}{c_{55_b} k}\,. \tag{6.50}$$

Subsequently, we insert expressions (6.49) and (6.50) into matrices (6.22) and (6.23), to obtain

$$\boldsymbol{C}^{\text{eff}} = \begin{bmatrix} c_{11} & c_{12} & c_{13} & 0 & 0 & 0 \\ c_{12} & c_{22} & c_{23} & 0 & 0 & 0 \\ c_{13} & c_{23} & c_{33} & 0 & 0 & 0 \\ 0 & 0 & 0 & c_{44} & 0 & 0 \\ 0 & 0 & 0 & 0 & c_{55} & 0 \\ 0 & 0 & 0 & 0 & 0 & c_{66} \end{bmatrix}, \tag{6.51}$$

where

$$c_{11} = \frac{c_{11_b} c_{33_b} k}{c_{11_b} h_f + c_{33_b} k - c_{33_b} h_f k}\,, \tag{6.52}$$

$$\begin{aligned} c_{22} = h_f k \left(c_{22_b} - \frac{c^2_{23_b}}{c_{33_b}} \right) + (1 - h_f) \left(c_{22_b} - \frac{c^2_{12_b}}{c_{11_b}} \right) \\ + \frac{c_{11_b} c_{33_b} k \left(\frac{c_{12_b}(1-h_f)}{c_{11_b}} + \frac{c_{23_b} h_f}{c_{33_b}} \right)^2}{c_{11_b} h_f + c_{33_b} k - c_{33_b} h_f k}\,, \end{aligned} \tag{6.53}$$

$$c_{33} = h_f k \left(c_{11_b} - \frac{c_{13_b}^2}{c_{33_b}} \right) + (1 - h_f) \left(c_{33_b} - \frac{c_{13_b}^2}{c_{11_b}} \right) + \frac{c_{11_b} c_{33_b} k \left(\frac{c_{13_b}(1-h_f)}{c_{11_b}} + \frac{c_{13_b} h_f}{c_{33_b}} \right)^2}{c_{11_b} h_f + c_{33_b} k - c_{33_b} h_f k} \,, \tag{6.54}$$

$$c_{12} = \frac{c_{12_b} c_{33_b} k + c_{11_b} c_{23_b} h_f k - c_{12_b} c_{33_b} h_f k}{c_{11_b} h_f + c_{33_b} k - c_{33_b} h_f k} \,, \tag{6.55}$$

$$c_{13} = \frac{c_{13_b} k \left(c_{33_b} + c_{11_b} h_f - c_{33_b} h_f \right)}{c_{11_b} h_f + c_{33_b} k - c_{33_b} h_f k} \,, \tag{6.56}$$

$$c_{23} = h_f k \left(c_{12_b} - \frac{c_{13_b} c_{23_b}}{c_{33_b}} \right) + (1 - h_f) \left(c_{23_b} - \frac{c_{12_b} c_{13_b}}{c_{11_b}} \right) + \frac{c_{11_b} c_{33_b} k \left(\frac{c_{13_b}(1-h_f)}{c_{11_b}} + \frac{c_{13_b} h_f}{c_{33_b}} \right) \left(\frac{c_{12_b}(1-h_f)}{c_{11_b}} + \frac{c_{23_b} h_f}{c_{33_b}} \right)}{c_{11_b} h_f + c_{33_b} k - c_{33_b} h_f k} \,, \tag{6.57}$$

$$c_{44} = c_{44_b} - c_{44_b} h_f + c_{66_b} h_f k \,, \tag{6.58}$$

$$c_{55} = \frac{c_{55_b} k}{h_f + k - h_f k} \,, \tag{6.59}$$

$$c_{66} = \frac{c_{66_b} c_{44_b} k}{c_{66_b} h_f + c_{44_b} k - c_{44_b} h_f k} \,. \tag{6.60}$$

The effective elasticity matrix (6.51) is described by the background stiffnesses c_{ij_b} and only two additional parameters k and h_f that are responsible for the set of parallel fractures.

Chapter 7

PP-wave reflection coefficient for vertically cracked media: Single set of aligned cracks*

Abstract

The main goal of this paper is to analyse the influence of cracks on the azimuthal variations of amplitude. We restrict our investigation to a single set of vertical, circular, and flat cavities aligned along a horizontal axis. Such cracks are embedded in either isotropic surroundings or transversely isotropic background with a vertical symmetry axis. We employ the effective medium theory to obtain either transversely-isotropic material with a horizontal symmetry axis or an orthotropic medium, respectively. To consider the amplitudes, we focus on a Vavryčuk-Pšenčík approximation of the PP-wave reflection coefficient. We as-

*This chapter is the original research paper of Adamus, F. P. (2020). "PP-wave reflection coefficient for vertically cracked media: Single set of aligned cracks". *arXiv*, 2010.08442v2 [physics.geo-ph] (submitted to *Geophysical Prospecting*).

sume that cracks are situated in one of the halfspaces being in welded contact. Azimuthal variations depend on the background stiffnesses, incidence angle, and crack density parameter. Upon analytical analysis, we indicate which factors (such as background's saturation) cause the reflection coefficient to have maximum absolute value in the direction parallel or perpendicular to cracks. We discuss the irregular cases, where such extreme values appear in the other than the aforementioned directions. Due to the support of numerical simulations, we propose graphic patterns of two-dimensional amplitude variations with azimuth. The patterns consist of a series of shapes that change with the increasing value of the crack density parameter. Schemes appear to differ depending on the incidence angle and the saturation. Finally, we extract these shapes that are characteristic of gas-bearing rocks. They may be treated as gas indicators. We support the findings and verify our patterns using real values of stiffnesses extracted from the sedimentary rocks' samples.

7.1 Introduction

Recently, the amplitude variations with azimuth (AVA) became a topic of interest for many seismologists. Such physical phenomena occur due to either intrinsic or induced azimuthal anisotropy of the medium. The latter kind is caused by thin layering or cracks embedded in the azimuthally-independent background, under the condition that at least one inhomogeneity is not parallel to the reference plane. The properties of cracks that induce AVA are essential from the exploration point of view since cracks may cause fluids, such as gas, to flow. Therefore, in this paper, we investigate the above-mentioned induced variations. We refer to them, in a singular form, as CAVA to emphasise that AVA is caused by cracks—not the layering or intrinsic anisotropy. To analyse such variations, we utilise effective medium theory and reflection coefficients.

The idea of homogenisation of elastic media containing inclusions dates back to Bruggeman (1937) and Eshelby (1957). A good summary of the micromechanics researchers' efforts can be found in Kachanov (1992). From a strictly geophysical perspective, the elastics of cracked media has been studied and popularised by Schoenberg and Douma (1988), Schoenberg and Sayers (1995), and Schoenberg and Helbig (1997). They treat cracks as infinitely weak and thin planes embedded in the background medium.

For over a century, researchers have been interested in finding the formulation of reflection and transmission coefficients at an interface between two elastic halfspaces. The exact solution to the plane wave reflection and transmission problem for isotropic media was shown by Zoeppritz (1919). An elegant extension of the explicit solution to monoclinic halfspaces was presented by Schoenberg and Protazio (1992). Due to the complexity of analytical formulations for both isotropic and anisotropic cases, researchers focused on various reflection and transmission coefficients' approximations. For the azimuthally-independent approximations, readers may refer to Chopra and Castagna (2014). If reflection and transmission coefficients do change with azimuth, the approximations become more complicated. Rüger (1998) proposed formulations for two transversely-isotropic halfspaces with a horizontal axis of symmetry. However, his derivations appear inaccurate if lower symmetries are considered. Halfspaces with an arbitrary symmetry were discussed by Ursin and Haugen (1996), Zillmer et al. (1997), and Vavryčuk and Pšenčík (1998). To obtain the approximations, Ursin and Haugen (1996) assumed weak elastic contrast at the interface only. On the other hand, Zillmer et al. (1997) allowed the contrast to be strong but assumed weak anisotropy. Both approximations are very complicated and lengthy. More user-friendly derivations were shown by Vavryčuk and Pšenčík (1998), who assumed both weak contrast interface and weak anisotropy. Upon introducing further linearisation, their approximations can be reduced to an elegant formulation shown by Pšenčík and Martins (2001), and then, it can be simplified to the aforementioned, popular approximation of Rüger (1998). Due to the convenience of analytical analysis and the accuracy of the approximation for low symmetry classes, we focus on the reflection coefficient estimated by Vavryčuk and Pšenčík (1998). Further, we restrict our analysis to PP-plane waves.

Numerous authors have employed the effective medium theory in the context of azimuthal variations of the reflection coefficient. Specifically, they often have used PP-amplitudes to predict the background and fracture parameters. Thus, they have focused on the solution of the inverse problem. However, due to a large number of unknowns, the azimuthal inversion becomes a difficult task. Some authors have considered isotropic background and the aforementioned Rüger's equations (e.g., Rüger and Gray, 2014). The others considered more sophisticated approximations, employing novel techniques to reduce the number of parameters, but still assuming an isotropic background (Chen et al. (2017) and Xie et al. (2019)). In contrast to the authors mentioned above, Ji and Zong (2019) have allowed the background to present lower than isotropic symmetry. However, they have utilised an additional linearisation of the reflection coefficient. In this paper, we do not focus on the explicit inversion of background and fracture parameters. This way, we can consider an anisotropic background and Vavryčuk-Pšenčík approximation, with no additional linearisations or assumptions. Using analytical and numerical methods, we try to better understand the nature of azimuthal variations of amplitude for cracked media. Specifically, we analyse the shapes of these variations. Thorough investigation allows us to notice not only the ellipse or peanut shapes, as assumed or indicated by the other authors (e.g., Xie et al., 2019). Further, some shapes occur to be more probable for specific saturations, incidences, and crack concentrations. Therefore, we also touch on the inverse problem; however, in an indirect, not explicit way. In other words, instead of focusing on the popular Bayesian framework, we investigate the patterns and characteristic attributes of CAVA. Principally, we are interested in the shapes that are typical for gas-bearing rocks.

7.2 Theory

7.2.1 Elasticity tensor and stability conditions

Consider a three-dimensional Cartesian coordinate system with x_i axes, where x_3 denotes the vertical axis. An elasticity tensor is a forth-rank Cartesian tensor that relates stress and strain second-rank tensors. A material whose elastic properties are rotationally invariant about one symmetry axes is called to be transversely isotropic (TI). This paper focuses on a TI medium with a rotation symmetry axis that coincides with the x_3-axis; we refer to such a medium as a VTI material. In Voigt's notation, an elasticity tensor of a VTI material is represented by

$$\boldsymbol{C} = \begin{bmatrix} C_{11} & C_{12} & C_{13} & 0 & 0 & 0 \\ C_{12} & C_{11} & C_{13} & 0 & 0 & 0 \\ C_{13} & C_{13} & C_{33} & 0 & 0 & 0 \\ 0 & 0 & 0 & C_{44} & 0 & 0 \\ 0 & 0 & 0 & 0 & C_{44} & 0 \\ 0 & 0 & 0 & 0 & 0 & C_{66} \end{bmatrix}, \tag{7.1}$$

where $C_{12} = C_{11} - 2C_{66}$. If additionally $C_{11} = C_{33}$, $C_{12} = C_{13}$, and $C_{44} = C_{66}$, medium becomes isotropic. An elasticity tensor is physically feasible if it obeys the stability conditions. These conditions (e.g., Slawinski, 2020a, Section 4.3) originate from the necessity of expending energy to deform a material. This necessity is mathematically expressed by the positive definiteness of the elasticity tensor. A tensor is positive definite if and only if all eigenvalues of its 6×6 matrix representation are positive. For a VTI elasticity tensor, this entails

$$C_{11} - |C_{12}| > 0\,, \quad C_{33}(C_{11}+C_{12}) > 2C_{13}^2\,, \quad \text{and} \quad C_{44} > 0\,. \tag{7.2}$$

For isotropic tensor, only one condition is required, namely,

$$C_{11} > \tfrac{4}{3}\,C_{44} > 0\,. \tag{7.3}$$

7.2.2 Elastic medium with a single ellipsoidal inclusion

Consider a linearly elastic material of volume V that contains a single region (inclusion) with different elastic properties occupying volume V_1. We denote the inhomogeneity surroundings with a subscript 0, whereas 1 indicates the embedded region. The strain of an effective (homogenised) material, averaged over volume V, can be expressed in terms of the strain average over the background surroundings $\overline{\varepsilon}_0$, and strain average over the inhomogeneity $\overline{\varepsilon}_1$, as follows.

$$\overline{\boldsymbol{\varepsilon}} = \frac{V-V_1}{V}\,\overline{\boldsymbol{\varepsilon}}_0 + \frac{V_1}{V}\,\overline{\boldsymbol{\varepsilon}}_1 = \phi_0 \boldsymbol{S}_0 : \overline{\boldsymbol{\sigma}}_0 + \phi_1 \boldsymbol{S}_1 : \overline{\boldsymbol{\sigma}}_1\,, \tag{7.4}$$

where $\boldsymbol{\varepsilon}$ stands for the second-rank strain tensor, $\boldsymbol{\sigma}$ denotes the second-rank stress tensor, $\boldsymbol{S}$ is the fourth-rank compliance tensor (the inverse of an elasticity tensor), and operator $:$ is the double-dot product. Volume fractions are denoted by ϕ. We assume an external stress at infinity that is uniform, namely,

$$\boldsymbol{\sigma}_\infty = \phi_0 \overline{\boldsymbol{\sigma}}_0 + \phi_1 \overline{\boldsymbol{\sigma}}_1\,. \tag{7.5}$$

The external stress can be related to the inhomogeneity stress solely, by using a fourth-rank stress concentration tensor $\boldsymbol{B}$, that is,

$$\overline{\boldsymbol{\sigma}}_1 = \boldsymbol{B} : \boldsymbol{\sigma}_\infty \,. \tag{7.6}$$

Combining equations (7.4)–(7.6), we get

$$\overline{\boldsymbol{\varepsilon}} = \boldsymbol{S}_0 : \boldsymbol{\sigma}_\infty + \phi_1(\boldsymbol{S}_1 - \boldsymbol{S}_0) : \boldsymbol{B} : \boldsymbol{\sigma}_\infty = \boldsymbol{S}_0 : \boldsymbol{\sigma}_\infty + \Delta\boldsymbol{\varepsilon} \,, \tag{7.7}$$

where $\Delta\boldsymbol{\varepsilon}$ is the extra strain of the material due to inclusion. Now, we can define fourth-rank compliance contribution tensor

$$\boldsymbol{H} := (\boldsymbol{S}_1 - \boldsymbol{S}_0) : \boldsymbol{B} \tag{7.8}$$

that is a key tensor since—upon inserting expression (7.8) into (7.7)—the contribution of an inhomogeneity can be expressed by $\boldsymbol{H}$ and volume fraction only. $\boldsymbol{H}$ depends on elastic properties of an inclusion and on $\boldsymbol{B}$ that, in turn, depends on inclusion's shape. If we assume the ellipsoidal shape of the inhomogeneity, we can express $\boldsymbol{B}$ in terms of fourth-rank Eshelby tensor, $\boldsymbol{s}$, which leads to a significant simplification of the so-called Eshelby problem (Eshelby, 1957). If different shapes are considered, the stresses and strain inside the inclusion are not constant. In turn, the contribution of such inclusions cannot be expressed in terms of Eshelby tensor, and more complicated techniques must be involved (Kachanov and Sevostianov, 2018). Herein, we assume ellipsoidal shape and get

$$\boldsymbol{B} = \left[\boldsymbol{J} + \boldsymbol{Q} : (\boldsymbol{S}_1 - \boldsymbol{S}_0)\right]^{-1} \,, \tag{7.9}$$

where $\boldsymbol{J}$ is the fourth-rank unit tensor—$\left(\delta_{ik}\delta_{j\ell}+\delta_{i\ell}\delta_{jk}\right)/2$, where δ is the Kronecker delta—and $\boldsymbol{Q}$ is the fourth-rank tensor related to Eshelby tensor, $\boldsymbol{s}$, namely,

$$\boldsymbol{Q}=\boldsymbol{C}_0:(\boldsymbol{J}-\boldsymbol{s})\,. \tag{7.10}$$

$\boldsymbol{C}_0$ is the fourth-rank elasticity tensor of the background material. Upon inserting expression (7.9) into (7.8), we obtain

$$\boldsymbol{H}=\left[\left(\boldsymbol{S}_1-\boldsymbol{S}_0\right)^{-1}+\boldsymbol{Q}\right]^{-1}\,. \tag{7.11}$$

In the next section, we refer to the above derivations to discuss the contribution of multiple, circular, and flat cavities (dry cracks) embedded in a VTI background.

7.2.3 Elastic VTI medium with circular cracks

If an embedded, single region is a flat (planar) crack, then the extra strain from equation (7.7) can be written as

$$\Delta\boldsymbol{\varepsilon}=\frac{S}{2V}\left(\boldsymbol{bn}+\boldsymbol{nb}\right)\,, \tag{7.12}$$

where $\boldsymbol{b}$ is the average—over crack surface S—displacement discontinuity vector, and $\boldsymbol{n}$ is the crack normal vector. In our notation, $\boldsymbol{bn}$ and $\boldsymbol{nb}$ are the outer products. Assuming linear displacements, we can introduce a second-rank crack compliance tensor $\boldsymbol{Z}$, namely,

$$\frac{S}{V}\boldsymbol{b}=\boldsymbol{n}\cdot\boldsymbol{\sigma}_\infty\cdot\boldsymbol{Z}\,. \tag{7.13}$$

Upon inserting expression (7.13) into (7.12) and comparing the result to the extra strain from equation (7.7), we get an equality

$$\boldsymbol{n}\boldsymbol{Z}\boldsymbol{n} = \phi_1 \boldsymbol{H} \,. \tag{7.14}$$

We see that tensor $\boldsymbol{Z}$ is akin to ”fracture system compliance tensor” shown in celebrated papers of Schoenberg and Sayers (1995) and Schoenberg and Helbig (1997). Since $\boldsymbol{Z}$ is symmetric, three principal directions of the crack compliance must exist. Therefore, we can write

$$\boldsymbol{Z} = Z_N \boldsymbol{n}\boldsymbol{n} + Z_{tt} \boldsymbol{t}\boldsymbol{t} + Z_{ss} \boldsymbol{s}\boldsymbol{s} \,, \tag{7.15}$$

where $\boldsymbol{n}$, $\boldsymbol{t}$, and $\boldsymbol{s}$ are mutually orthogonal vectors. If a crack is circular, it becomes rotationally invariant, so that $Z_{tt} = Z_{ss} =: Z_T$. Since $\boldsymbol{n}\boldsymbol{n} + \boldsymbol{t}\boldsymbol{t} + \boldsymbol{s}\boldsymbol{s} = \boldsymbol{I}$, we get

$$\boldsymbol{Z} = Z_N \boldsymbol{n}\,\boldsymbol{n} + Z_T (\boldsymbol{I} - \boldsymbol{n}\,\boldsymbol{n}) \,, \tag{7.16}$$

where $\boldsymbol{n}$ is the crack normal. Given the assumptions above, Z_N and Z_T completely determine the elastic contribution of a circular crack. To obtain them, we need to compute $\boldsymbol{H}$ that depends on crack stiffnesses and Eshelby tensor. In turn, Eshelby tensor depends on background stiffnesses and crack shape. Complicated computation of $\boldsymbol{s}$ for different symmetry classes of the background medium and shapes of inclusion is well-explained in Sevostianov et al. (2005) and Kachanov and Sevostianov (2018). Let us derive Z_N and Z_T for a VTI background. If we assume that a circular crack is dry, meaning that its elasticity parameters are zero, we get

$$Z_N = \frac{8 c_3 e}{3 c_1 \left(1 - \dfrac{c_{13}^2}{c_1^2}\right)} \geq 0 \,, \tag{7.17}$$

$$Z_T = \frac{16e}{3c_{44}\,(c_2 + c_3 - c_4)} \geq 0\,, \tag{7.18}$$

where

$$\begin{gathered} c_1 := \sqrt{c_{11}c_{33}}\,, \qquad c_2 := \sqrt{\frac{c_{66}}{c_{44}}}\,, \\ c_3 := \sqrt{\frac{(c_1 - c_{13})(c_1 + c_{13} + 2c_{44})}{c_{33}c_{44}}}\,, \qquad c_4 := \frac{2c_{44}c_3}{c_1 + c_{13} + 2c_{44}}\,. \end{gathered} \tag{7.19}$$

Throughout the paper, c_{ij} denote the stiffnesses of a background medium, expressed in Voigt's notation. Parameter

$$e = \frac{ma^3}{V}\,, \tag{7.20}$$

is the crack density with crack ratio a and number of cracks m (in this, single crack case, $m = 1$). The above results are identical to the ones of Guo et al. (2019). If the background is isotropic, then expressions (7.17) and (7.18) reduce to

$$Z_N = \frac{4c_{11}e}{3c_{44}(c_{11} - c_{44})} \geq 0\,, \tag{7.21}$$

$$Z_T = \frac{16c_{11}e}{3c_{44}(3c_{11} - 2c_{44})} \geq 0\,. \tag{7.22}$$

Expressions (7.21) and (7.22) were derived previously by numerous authors (e.g., Hudson, 1980). To satisfy stability conditions—for dry circular cracks—Z_N and Z_T must be nonnegative, no matter if the background is VTI or isotropic.

So far, we have discussed a case of a single inhomogeneity surrounded by the background medium. If there are multiple flat cracks, the strain equation (7.7) can be generalised to

$$\overline{\boldsymbol{\varepsilon}} = (\boldsymbol{S}_0 + \Delta\boldsymbol{S}) : \boldsymbol{\sigma}_\infty\,, \tag{7.23}$$

where

$$\Delta \boldsymbol{S} = \sum_{k=1}^{m} \phi_k \boldsymbol{H}_{(k)} = \sum_{k=1}^{m} \boldsymbol{n}_{(k)} \boldsymbol{Z}_{(k)} \boldsymbol{n}_{(k)} \tag{7.24}$$

with m being the total number of cracks. Tensors $\boldsymbol{Z}_{(k)}$ apart from depending on the shape and properties of cracks, they also may depend on the interactions between the inhomogeneities. In this paper, however, we assume the non-interaction approximation (NIA), so that cracks are treated as they were isolated, and $\boldsymbol{Z}_{(k)}$ can be obtained in a manner discussed above. If cracks have the same shape and orientation, Z_N and Z_T for each inhomogeneity do sum up, and the concentration of cracks is reflected in the parameter e with $m > 1$ (see expression (7.20)). The NIA is particularly useful for strongly oblate or planar cracks due to its good accuracy even for higher values of density parameter (Grechka and Kachanov, 2006). For flat cracks, the shape factors such as roughness can be ignored (Kachanov and Sevostianov, 2018). In the next section, we discuss a particular case of expression (7.24).

7.2.4 Elastic VTI medium with a single set of aligned vertical cracks

Consider one set of flat cracks having identical circular shapes that are embedded in a VTI background medium. Assume that all cracks are dry and have the same orientation. Upon combining expressions (7.16)–(7.18), we can rewrite expression (7.24) as

$$\Delta \boldsymbol{S} = \boldsymbol{n} \left[\frac{8 c_3 e}{3 c_1 \left(1 - \dfrac{c_{13}^2}{c_1^2}\right)} \boldsymbol{n}\boldsymbol{n} + \frac{16 e}{3 c_{44} \left(c_2 + c_3 - c_4\right)} \left(\boldsymbol{I} - \boldsymbol{n}\boldsymbol{n}\right) \right] \boldsymbol{n} \tag{7.25}$$

where $\boldsymbol{n}$ is a normal to the set of cracks and e describes the crack concentration with $m > 1$. Having the above expression, we can obtain the effective elasticity tensor of a homogenised medium. Since, elasticity is the inverse of the compliance tensor, we need to examine

$$\boldsymbol{C}^{\text{eff}} = (\boldsymbol{S}_0 + \Delta \boldsymbol{S})^{-1} \,. \tag{7.26}$$

If a set of cracks is vertical, then effective elasticity tensor has monoclinic or higher symmetry (Schoenberg et al., 1999). We propose to consider a simpler case, where cracks have a normal parallel to the x_1-axis. Then, the tensor exhibits at least orthotropic symmetry. In Voigt's notation, the effective elasticity tensor has the following form.

$$\boldsymbol{C}^{\text{eff}} = \begin{bmatrix} c_{11}(1-\delta_N) & c_{12}(1-\delta_N) & c_{13}(1-\delta_N) & 0 & 0 & 0 \\ c_{12}(1-\delta_N) & c_{11}\left(1-\delta_N \dfrac{c_{12}^2}{c_{11}^2}\right) & c_{13}\left(1-\delta_N \dfrac{c_{12}}{c_{11}}\right) & 0 & 0 & 0 \\ c_{13}(1-\delta_N) & c_{13}\left(1-\delta_N \dfrac{c_{12}}{c_{11}}\right) & c_{33}\left(1-\delta_N \dfrac{c_{13}}{c_{11}c_{33}}\right) & 0 & 0 & 0 \\ 0 & 0 & 0 & c_{44} & 0 & 0 \\ 0 & 0 & 0 & 0 & c_{44}\left(1-\delta_{T_1}\right) & 0 \\ 0 & 0 & 0 & 0 & 0 & c_{66}\left(1-\delta_{T_2}\right) \end{bmatrix} , \tag{7.27}$$

where $c_{12} = c_{11} - 2c_{66}$. Deltas are the combinations of crack compliances and background stiffnesses, namely,

$$\delta_N := \frac{Z_N c_{11}}{1 + Z_N c_{11}} = \frac{8 c_{11} c_3 e}{8 c_{11} c_3 e + 3 c_1 \left(1 - \dfrac{c_{13}^2}{c_1^2}\right)} \,, \tag{7.28}$$

$$\delta_{T_1} := \frac{Z_T c_{44}}{1 + Z_T c_{44}} = \frac{16 e}{16 e + 3(c_2 + c_3 - c_4)} \,, \tag{7.29}$$

$$\delta_{T_2} := \frac{Z_T c_{66}}{1 + Z_T c_{66}} = \frac{16 c_{66} e}{16 c_{66} e + 3 c_{44}(c_2 + c_3 - c_4)} \,. \tag{7.30}$$

Note that if there are no cracks, the effective tensor reduces to the background; thus, it has five independent stiffnesses, instead of nine. Dry cracks embedded in the background always increase certain compliances of the effective medium (Z_N and Z_T must be positive). Therefore, the effective elastic properties are weaker than the properties of the background. Analogously, effective stiffnesses can be derived for the isotropic background.

So far, in this section, we have discussed the limiting case of dry, circular, flat cracks. In other words, we have considered the ellipsoids with one pair of the semi-axes of equal length and the third tending to zero $(a_1 = a_2 = a,\, a_3 \to 0)$. The results of this section also can be a good approximation for strongly oblate spheroids (penny-shaped cavities). In the case of such shape, one semi-axis is much smaller than the other two $(a_3 \ll a)$. As shown by Sevostianov et al. (2005), the values of Eshelby tensor—compared to the case of $a_3 \to 0$—do not change significantly, which means that expression (7.25) is accurate enough. Note that the volume fraction ϕ_i or aspect ratio (a_3/a) of penny-shaped cavities are very small so that they are irrelevant for their characterisation (e.g., Kachanov et al., 1994). The only useful concentration parameter is the crack density, whose values are limited by the accuracy of the NIA only.

7.2.5 Vavryčuk-Pšenčík approximation

Consider a spherical coordinate system. Vavryčuk-Pšenčík approximation for the PP-wave reflection coefficient—valid for at least monoclinic halfspaces being in welded contact—is

$$
\begin{aligned}
R_{\mathrm{pp}}(\theta,\psi) = R_{\mathrm{ipp}}(\theta) &+ \frac{1}{2}\sin^2\theta \Bigg\{ \left[\Delta\left(\frac{C_{23}+2C_{44}-C_{33}}{C_{33}}\right) - 8\Delta\left(\frac{C_{44}-C_{55}}{2C_{33}}\right)\right]\sin^2\psi \\
&+ \Delta\left(\frac{C_{13}+2C_{55}-C_{33}}{C_{33}}\right)\cos^2\psi + 2\left[\Delta\left(\frac{C_{36}+2C_{45}}{C_{33}}\right) - 4\Delta\left(\frac{C_{45}}{C_{33}}\right)\right]\sin\psi\cos\psi \Bigg\} \\
&+ \frac{1}{2}\sin^2\theta\tan^2\theta \Bigg\{ \Delta\left(\frac{C_{22}-C_{33}}{2C_{33}}\right)\sin^4\psi + \Delta\left(\frac{C_{11}-C_{33}}{2C_{33}}\right)\cos^4\psi \\
&+ \Delta\left(\frac{C_{12}+2C_{66}-C_{33}}{C_{33}}\right)\sin^2\psi\cos^2\psi + \Delta\left(\frac{C_{26}}{C_{33}}\right)\sin^3\psi\cos\psi + \Delta\left(\frac{C_{16}}{C_{33}}\right)\cos^3\psi\sin\psi \Bigg\},
\end{aligned}
\tag{7.31}
$$

where θ is the incidence angle measured from the x_3-axis and ψ is the azimuthal angle measured from the x_1-axis towards the x_2-axis. Δ stands for the difference between elastic effective parameters of lower and upper halfspaces, respectively ($\Delta = w^\ell - w^u$, where w is some parameter). First term of the above approximation denotes the PP reflection coefficient between two slightly different isotropic media, proposed by Aki and Richards (1980). The rest of the terms in expression (7.31) are the correction terms due to the anisotropy of the halfspaces. The reflection coefficient of the isotropic part is

$$R_{\mathrm{ipp}}(\theta) = \frac{1}{2}\frac{\Delta\left(\rho\alpha\right)}{\overline{\rho\alpha}} + \frac{1}{2}\frac{\Delta\alpha}{\overline{\alpha}}\tan^2\theta - 2\,\frac{\Delta\left(\rho\beta^2\right)}{\overline{\rho\alpha}^2}\sin^2\theta\,, \tag{7.32}$$

where ρ is the mass density, whereas α and β are P and S wave velocities of the isotropic medium that can be chosen arbitrarily. We follow Vavryčuk and Pšenčík (1998) who have defined $\alpha = \sqrt{C_{33}/\rho}$ and $\beta = \sqrt{C_{55}/\rho}$. The bar stands for the average properties between two halfspaces, for instance, $\overline{\alpha} = (\alpha^\ell + \alpha^u)/2$.

7.3 CAVA conjecture

In this section, we analyse the effect of a single set of dry, circular cracks on azimuthal variations of amplitude. We assume that cracks are vertical with a normal parallel to the x_1-axis, the background is VTI (in some cases isotropic), and we use Vavryčuk-Pšenčík approximation. Hence, to obtain the reflection coefficient, we insert effective elasticity parameters from matrix (7.27) into expression (7.31). CAVA depends on the crack density parameter e, incidence angle, and background stiffnesses. To better understand and separate the effect of e on azimuthal variations—at the end of the section—we fix θ and the elasticity parameters. By doing so, we obtain $R_{pp}(\psi, e)$ that corresponds to various seismological situations. We present $R_{pp}(\psi, e)$ as a series of two-dimensional polar graphs that change with increasing concentration of cracks. We conjecture what the most probable patterns of such series are.

It is useful to prove that $R_{pp}(\psi)$ expressed in polar coordinates has at least two-fold rotational symmetry. In this way, one quadrant instead of entire graph may be examined, which facilitates the analysis. Throughout the paper, we focus on the quadrant, where $\psi \in [0°, 90°]$. Consider following Lemma.

Lemma 7.3.1. *The graph of PP reflection coefficient, $R_{pp}(\psi)$, computed for orthotropic medium using Vavryčuk-Pšenčík approximation has at least two-fold symmetry, where $R_{pp}(\psi)$ is expressed in polar coordinates.*

Proof. The equality,

$$R_{pp}(-\psi) = R_{ipp} + a_1 \sin^2\psi + a_2 \cos^2\psi + a_3 \sin^4\psi + a_4 \cos^4\psi + a_5 \sin^2\psi \cos^2\psi = R_{pp}(\psi)\,,$$

where a_i are constants, means that the graph is symmetric about polar x_1-axis that coincides with $\psi = 0°$. Also,

$$R_{pp}(\psi + 180°) = R_{pp}(\psi)\,;$$

the graph is symmetric with respect to the origin. The above symmetries imply the symmetry about the x_2-axis that coincides with $\psi = 90°$. Hence, the graph has at least two-fold symmetry and is represented by four identical quadrants. □

There are numerous possible shapes of azimuthal variations. In general, we can distinguish two main kinds of CAVA graphs—regular or irregular. Former one, assures that the pair of minimal and maximal value of $R_{pp}(\psi)$—where $\forall\psi \in [0°, 90°]$—is obtained for the pair of azimuths $\psi = 0°$ and $\psi = 90°$. The irregularity occurs if $\min R_{pp}(\psi)$ or $\max R_{pp}(\psi)$ is given for other azimuths. Examples of both kinds of shapes—that we discuss in the next sections—are shown in Figure 7.1.

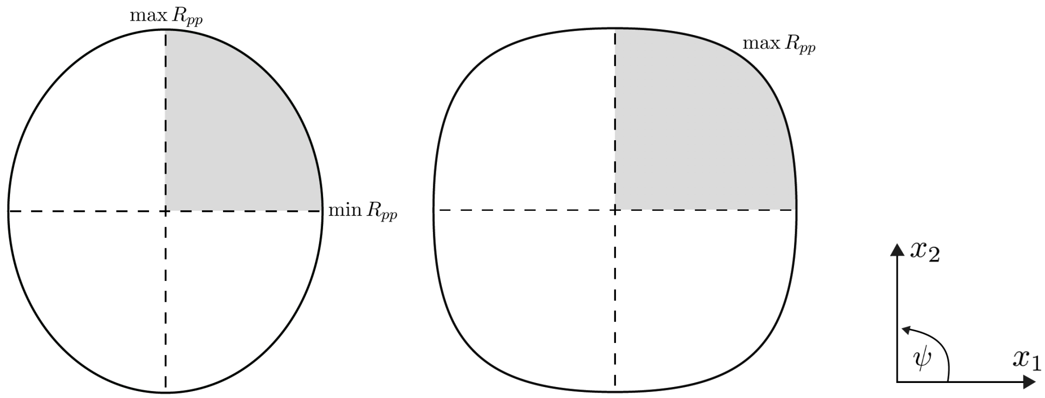

Figure 7.1: Two examples of azimuthal variations of amplitude caused by cracks (CAVA). Graphs have two-fold symmetry indicated by dashed lines. The discussed quadrants are in grey. Graph on the left illustrates a regular shape, where $\min R_{pp}$ and $\max R_{pp}$ correspond to $\psi = 0°$ and $\psi = 90°$, respectively. The graph on the right presents an irregular shape, where $\max R_{pp}$ is obtained for other azimuth (in this case $\psi = 45°$). The coordinate system used herein is the same for all figures in the paper.

7.3.1 Regular CAVA

Based on numerous works (for instance, summarised in Chopra and Castagna (2014)), we expect that cracks affect the amplitude in a most significant manner—meaning that R_{pp} reaches its extreme values—while the wave propagates perpendicular or parallel to them. Therefore, herein, we focus on the regular CAVA shape. We propose to consider

$$\Delta R_{pp} := R_{pp}(\theta, \psi_1) - R_{pp}(\theta, \psi_2)\,, \tag{7.33}$$

where the azimuthal angles are $\psi_1 = 0°$ and $\psi_2 = 90°$. We are particularly interested in the sign of ΔR_{pp} . For instance, negative ΔR_{pp} means that amplitude has a larger value for a wave propagating parallel to cracks. We want to examine how much the sign is influenced by the concentration of cracks, incidence angle, or particular stiffnesses. Upon calculation, where we use the linearity of the difference Δ (from expression (7.31)), we get

$$\Delta R_{pp}=\frac{1}{2}\sin^2\theta\left\{\Delta\left[\frac{2\left(C_{44}-C_{55}\right)+\left(C_{13}-C_{23}\right)+\frac{1}{2}\tan^2\theta\left(C_{11}-C_{22}\right)}{C_{33}}\right]\right\} \tag{7.34}$$

expressed in terms of effective elasticity parameters. Without loss of generality, we choose the single set of cracks to be embedded in the lower halfspace so that Δ can be removed. We obtain

$$\Delta R^{\ell}_{pp}=\frac{1}{2C^{\ell}_{33}}\sin^2\theta\left[2\left(C^{\ell}_{44}-C^{\ell}_{55}\right)+\left(C^{\ell}_{13}-C^{\ell}_{23}\right)+\frac{1}{2}\tan^2\theta\left(C^{\ell}_{11}-C^{\ell}_{22}\right)\right]. \tag{7.35}$$

where C^{ℓ}_{ij} are the effective stiffnesses of the lower halfspace. For small incidence angles, the third term in the numerator can be neglected. Note that if we choose the single set of cracks to be embedded in the upper halfspace $\left(\Delta R^{u}_{pp}\right)$, the minus sign appears. Hence, all the conclusions regarding the behaviour of ΔR^{ℓ}_{pp} have exactly the opposite meaning for ΔR^{u}_{pp}. Taking this into account, let us focus on ΔR^{ℓ}_{pp} only. Due to the weakening effect of embedded cracks (see expression (7.27)) and following the stability conditions, we require $C^{\ell}_{55}<C^{\ell}_{44}$, $\left|C^{\ell}_{13}\right|<\left|C^{\ell}_{23}\right|$, and $C^{\ell}_{11}<C^{\ell}_{22}$. Thus, ΔR^{ℓ}_{pp} can be either positive or negative, no matter the stiffness of the upper halfspace.

It might be important to notice that, as opposed to phase velocities, one should not expect the magnitude of R_{pp} to be larger for quasi P-waves propagating parallel to cracks. For instance, as shown by Adamus (2020), the analogous difference between squared-velocities propagating parallel and perpendicular to cracks, for small incidence angles, is

$$s^2=V_P^2(\theta,\psi_1)-V_P^2(\theta,\psi_2)\approx\frac{k}{2}\sin^2\theta\left[2\left(C_{55}-C_{44}\right)+\left(C_{13}-C_{23}\right)\right], \tag{7.36}$$

where $k>0$ is a scaling factor that depends on C_{33}. The above expression is similar to (7.35)—where the third term responsible for large angles would be neglected—however, difference $C_{44}-C_{55}$ has the opposite sign. Assuming non anomalous case of $C_{13}, C_{23} > 0$, we expect s^2 to be negative. It means that velocity should be larger for a wave propagating parallel to cracks. This is not the case for R_{pp}.

Let us express ΔR_{pp}^{ℓ} in terms of VTI background elasticities of a lower halfspace (with a certain abuse of notation, denoted same as background stiffnesses of an arbitrary halfspace) and crack compliances Z_N and Z_T. We get

$$\Delta R_{pp}^{\ell} = \sin^2\theta \left[\frac{1+Z_N c_{11}}{c_{33}+Z_N\left(c_{11}c_{33}-c_{13}^2\right)}\right] \left[\frac{c_{44}^2 Z_T}{1+Z_T c_{44}} - \frac{2c_{13}c_{66}Z_N}{1+Z_N c_{11}} - \tan^2\theta \frac{\left(c_{11}c_{66}-c_{66}^2\right)Z_N}{1+Z_N c_{11}}\right] \tag{7.37}$$

that can be reduced to

$$\Delta R_{pp}^{\ell} = k\sin^2\theta\left[\chi c_{44}^2 - 2c_{13}c_{66} - \tan^2\theta\left(c_{11}c_{66}-c_{66}^2\right)\right], \tag{7.38}$$

where

$$k := \frac{Z_N}{c_{33}+Z_N\left(c_{11}c_{33}-c_{13}^2\right)} = \frac{8c_3 e}{\left(c_1^2-c_{13}^2\right)\left(8c_3 e + 3\dfrac{c_{33}}{c_1}\right)} \geq 0 \tag{7.39}$$

and

$$\chi := \frac{Z_T\left(1+Z_N c_{11}\right)}{Z_N\left(1+Z_T c_{44}\right)} = \frac{2\left(c_1^2-c_{13}^2\right)+\frac{16}{3}c_{11}c_1c_3 e}{c_{44}c_1c_3\left(c_2+c_3-c_4+\frac{16}{3}e\right)} \geq 0\,. \tag{7.40}$$

Scaling factor k grows with increasing concentration of cracks e (assuming that stiffnesses are fixed), since $\partial_e k \geq 0$. Also, due to stability conditions, k must be positive. Since k cannot change its sign, more essential—in the context of the shape of azimuthal variations—is the content of the squared brackets in expression (7.38). Given stability conditions, each of the three terms in squared brackets must be positive. However, minus signs in front of the second and third terms make it difficult to anticipate the sign of ΔR^{ℓ}_{pp}. For instance, the effect of growing e on χ is not apparent. Function $\chi(e)$ may have extrema; only specific relations among stiffnesses assure that this function is monotonic. If

$$c_{11} c_1 c_3 \left(c_2 + c_3 - c_4\right) \geq 2 \left(c_1^2 - c_{13}^2\right) \tag{7.41}$$

then $\partial_e \chi \geq 0$. Inequality (7.41) is satisfied if $c_{11} \geq c_{33} \wedge c_{11} \geq 2c_{44}$, which is a reasonable condition, since in VTI media, horizontal velocity is usually greater than the vertical one and, in general, horizontal P/S velocity ratio is greater than $\sqrt{2}$. We have performed Monte Carlo simulations, where a million examples of VTI backgrounds satisfying stability conditions were chosen. The values of stiffnesses were distributed uniformly, and their ranges were selected based on the minimum and maximum values measured by Wang (2002). In 93.81% of cases, inequality (7.41) was satisfied. Thus, in a great majority of cases, $\partial_e \chi \geq 0$ is true. The influence of each stiffness on χ is even more complicated; again, functions may have many extrema, and lengthy inequalities must be satisfied to render them monotonic. On the other hand, the influence of stiffnesses on the second term is trivial. It grows for increasing c_{13} or c_{66}. The third term grows with increasing incidence angle and c_{11}, but dependence on c_{66} is not obvious. To remove the ambiguity associated with c_{66} and to get more insight into expression (7.38), we propose to focus on proportions between elasticity parameters, namely, $p_{11} = c_{11}/c_{66}$, $p_{33} = c_{33}/c_{66}$, $p_{13} = c_{13}/c_{66}$, and $p_{44} = c_{44}/c_{66}$. We obtain

$$\Delta R^{\ell}_{pp} = k_p \sin^2\theta \, \left[\chi p_{44}^2 - 2p_{13} - (p_{11} - 1)\tan^2\theta\right] =: k_p \sin^2\theta \, \left(a - b\tan^2\theta\right) \,, \tag{7.42}$$

where $k_p := c_{66}^2 k$ depends on p_{11}, p_{33}, p_{13}, and p_{44} solely. Also, χ can be expressed in terms of e and the aforementioned proportions only. Having this simplified form, we expect negative ΔR_{pp}^{ℓ} for smaller e and p_{44}, significant values of p_{11} and p_{13}, and larger incidence angle. On the other hand, we expect positive ΔR_{pp}^{ℓ} for larger e and p_{44}, smaller values of p_{11} and p_{13}, and smaller θ. An interesting case might happen when e and θ are neither very small nor very large, then p_{11} and p_{13} may have a deciding influence on the sign of ΔR_{pp}^{ℓ}. In such a situation, if rocks are gas-bearing—where p_{11} and p_{13} should be small—we can expect that the reflection coefficient will be bigger for a wave propagating perpendicular to cracks (positive ΔR_{pp}^{ℓ}). If there is no gas, we expect negative ΔR_{pp}^{ℓ}. To sum up, we conjecture that for

- small e and large θ: expect $\Delta R_{pp}^{\ell} < 0$ and $\Delta R_{pp}^{u} > 0$,
- moderate e and θ, and brine-saturated or dry rocks: expect $\Delta R_{pp}^{\ell} < 0$ and $\Delta R_{pp}^{u} > 0$,
- moderate e and θ, and gas-saturated rocks: expect $\Delta R_{pp}^{\ell} > 0$ and $\Delta R_{pp}^{u} < 0$,
- large e and small θ: expect $\Delta R_{pp}^{\ell} > 0$ and $\Delta R_{pp}^{u} < 0$.

As we have already discussed, the shape of azimuthal variations of a VTI medium with an embedded set of aligned cracks (with a normal parallel to the x_1-axis) essentially depends on six factors: e, θ, p_{11}, p_{33}, p_{13}, and p_{44}. Due to complicated forms of Z_N and Z_T, it is hard to grasp each factor's exact contributions to ΔR_{pp}^{ℓ}. Therefore, we propose to consider a simpler situation of an isotropic background. In such a case, the number of independent shape factors reduces to three: e, θ, and $p = c_{11}/c_{44} > 4/3$. Factor χ can be written as

$$\chi = \frac{16c_{11}^2 e + 12c_{11}c_{44} - 12c_{44}^2}{16c_{11}c_{44}e + 9c_{11}c_{44} - 6c_{44}^2} = \frac{16p^2 e + 12p - 12}{16pe + 9p - 6} > 0\,, \tag{7.43}$$

so we obtain

$$
\begin{aligned}
\Delta R^{\ell}_{pp} &= \frac{4e}{c_{44}(c_{11}-c_{44})(16e+3)}\sin^2\theta\,\left[\chi c_{44}^2 - 2c_{44}(c_{11}-2c_{44}) - \tan^2\theta\left(c_{11}c_{44}-c_{44}^2\right)\right]\\
&= \frac{4e}{(p-1)(16e+3)}\sin^2\theta\,\left[\frac{-p^2(16e+18)+p(64e+60)-36}{p(16e+9)-6} - (p-1)\tan^2\theta\right]\\
&=: k_p^{\text{iso}}\sin^2\theta\,\left[a^{\text{iso}} - b^{\text{iso}}\tan^2\theta\right]\,. \qquad (7.44)
\end{aligned}
$$

Let us discuss the influences of sole e and sole p on scaling factor k_p^{iso} and two terms in squared brackets; a^{iso} and b^{iso}. Since $\partial_e k_p^{\text{iso}} > 0$ and $\partial_e a^{\text{iso}} > 0$, we know that k_p^{iso} and a^{iso} increase with growing e. On the other hand, $\partial_p k_p^{\text{iso}} < 0$, $\partial_p a^{\text{iso}} < 0$, and $\partial_p b^{\text{iso}} > 0$; thus, k_p^{iso} and a^{iso} decrease, but b^{iso} increase with growing p. Now, let us discuss influences of sole e and sole p on ΔR^{ℓ}_{pp}. To do so, we assume a fixed incidence angle. Due to increasing e, we expect ΔR^{ℓ}_{pp} to grow (always true if $\Delta R^{\ell}_{pp} > 0$ for $\forall e$). In case p increases, we anticipate $\left|\Delta R^{\ell}_{pp}\right|$ to diminish (always true if $\Delta R^{\ell}_{pp} > 0$ for $\forall e$). The last variable that contributes to the reflection coefficient is the incidence angle. Since $\partial_\theta(b^{\text{iso}}\tan^2\theta) > 0$, growing θ renders ΔR^{ℓ}_{pp} more likely to be negative. Considering the above analysis, we expect negative ΔR^{ℓ}_{pp} for small e, large p, and large θ. On the other hand, we expect positive ΔR^{ℓ}_{pp} for large e, small p, and small θ. If the concentration of cracks and incidence angle are neither very small nor large, we anticipate a significant role of rock's saturation. Therefore, for the isotropic background, we conjecture the same bullet points as for the VTI surroundings. They appear to be more convincing for the isotropic case, where fewer unknowns are involved, and χ is simplified.

7.3.2 Irregular CAVA

In this section, we examine the irregular case of CAVA. In other words, we check if and when R_{pp} presents extreme values not only for angles normal or parallel to cracks. Mathematically, the irregularity occurs if and only if

$$
\begin{gathered}
[R_{pp}(\theta,\psi_{irr}) > R_{pp}(\theta,0^\circ) \wedge R_{pp}(\theta,\psi_{irr}) > R_{pp}(\theta,90^\circ)] \\
\vee \\
[R_{pp}(\theta,\psi_{irr}) < R_{pp}(\theta,0^\circ) \wedge R_{pp}(\theta,\psi_{irr}) < R_{pp}(\theta,90^\circ)] \ ,
\end{gathered}
\tag{7.45}
$$

where $\psi_{irr} \in (0^\circ, 90^\circ)$. The above condition is true for either lower or upper halfspace. Again, without loss of generality, we assume that cracks are embedded in the lower halfspace and consider differences between reflection coefficients. We define

$$
\Delta R_{pp\psi} := R_{pp}(\theta,0^\circ) - R_{pp}(\theta,\psi_{irr}) \tag{7.46}
$$

so that condition (7.45) can be simply formulated as

$$
\left[\Delta R^\ell_{pp\psi} < 0 \wedge \Delta R^\ell_{pp\psi} < \Delta R^\ell_{pp}\right] \vee \left[\Delta R^\ell_{pp\psi} > 0 \wedge \Delta R^\ell_{pp\psi} > \Delta R^\ell_{pp}\right] \ . \tag{7.47}
$$

Hence, to examine the irregularity, first we need to derive $\Delta R^\ell_{pp\psi}$. Upon algebraic operations, expression (7.46) can be written as

$$
\begin{aligned}
\Delta R^\ell_{pp\psi} = \frac{1}{2C^\ell_{33}} \sin^2\theta \sin^2\psi \Bigg\{ & 2C^\ell_{44} - 2C^\ell_{55} + C^\ell_{13} - C^\ell_{23} \\
& + \frac{1}{2}\tan^2\theta \left[2C^\ell_{11} - 2C^\ell_{12} - 4C^\ell_{66} + \sin^2\psi\left(2C^\ell_{12} + 4C^\ell_{66} - C^\ell_{11} - C^\ell_{22}\right)\right] \Bigg\} ,
\end{aligned}
\tag{7.48}
$$

where C^{ℓ}_{ij} are the effective stiffnesses of a lower halfspace. It has a similar form to expression (7.35). Analogously to the previous section, we express $\Delta R^{\ell}_{pp\psi}$ in terms of proportions between background elasticities, p_{ij}. We obtain

$$\begin{aligned}\Delta R^{\ell}_{pp\psi} &= k_p \sin^2\theta \sin^2\psi \Bigg\{ \chi p_{44}^2 - 2p_{13} - \tan^2\theta \\ &\qquad \left[\frac{p_{11} Z_N - Z_T - \sin^2\psi (Z_N - Z_T + Z_N Z_T c_{66}(1-p_{11}))}{Z_N(1+c_{66}Z_T)}\right] \Bigg\} \\ &=: k_p \sin^2\theta \sin^2\psi \left(a - \beta \tan^2\theta\right) \ . \end{aligned} \tag{7.49}$$

If we express Z_N and Z_T in terms of proportions p_{11} , p_{33} , p_{13} , and p_{44} , then c_{66} do cancel. Expression (7.49) is analogous to expression (7.42); similarly to ΔR^{ℓ}_{pp} , coefficient $\Delta R^{\ell}_{pp\psi}$ can be either negative or positive. The relation between $\Delta R^{\ell}_{pp\psi}$ and ΔR^{ℓ}_{pp} is not obvious. In general, $\sin^2\psi < 1$ in front of the curly brackets decreases $\left|\Delta R^{\ell}_{pp\psi}\right|$; this trigonometric function in the expression of $\left|\Delta R^{\ell}_{pp}\right|$ equals one. On the other hand, the contribution of β inside $\left|\Delta R^{\ell}_{pp\psi}\right|$ can be either smaller or larger as compared to analogous contribution of b inside $\left|\Delta R^{\ell}_{pp}\right|$; note that

$$\beta - b = \frac{(Z_N - Z_T)\left(1-\sin^2\psi\right) - Z_N Z_T c_{66}\left(1-\sin^2\psi\right)(p_{11}-1)}{Z_N\left(1+c_{66}Z_T\right)} \tag{7.50}$$

can be either positive or negative that is governed by the azimuth, crack concentration, and proportions p_{ij} . Hence, both irregular CAVA, namely, $\Delta R^{\ell}_{pp\psi} < 0 \wedge \Delta R^{\ell}_{pp\psi} < \Delta R^{\ell}_{pp}$ or $\Delta R^{\ell}_{pp\psi} > 0 \wedge \Delta R^{\ell}_{pp\psi} > \Delta R^{\ell}_{pp}$ seem to be possible. However, we can show the case where irregularity is impossible for all azimuths by introducing certain assumptions. Assume that $Z_N \le Z_T$, $p_{11} > 1$, and consider $\Delta R^{\ell}_{pp\psi} < 0$. Then, relation $\Delta R^{\ell}_{pp\psi} - \Delta R^{\ell}_{pp}$, namely,

$$k_p \sin^2\theta \left[\sin^2\psi \left(a - \beta\tan^2\theta\right) - \left(a - b\tan^2\theta\right)\right] =: k_p \sin^2\theta \left(x\sin^2\psi - y\right) \tag{7.51}$$

must be positive, since we easily obtain $\beta < b$ that leads to $x > y$, where $y < 0$. Following Grechka and Kachanov (2006), $Z_N > Z_T$ is true for isotropic rocks having negative Poisson's ratio, which is a rare case. Also, $p_{11} > 1$ is a typical situation corresponding to horizontal P-wave faster than S-wave. Hence, we can state that the irregularity is unlikely to occur for rocks with regular Poisson's ratio, where $\Delta R^{\ell}_{pp\psi} < 0$ (or $\Delta R^{u}_{pp\psi} > 0$).

Let us perform analogous analysis, assuming isotropic, not VTI, background. We obtain

$$\Delta R^{\ell}_{pp\psi} = k_p^{\mathrm{iso}} \sin^2\theta \sin^2\psi \left(a^{\mathrm{iso}} - \beta^{\mathrm{iso}} \tan^2\theta\right) , \tag{7.52}$$

where

$$\beta^{\mathrm{iso}} = \frac{12p\left(\frac{3}{4}p - 1\right) + (2-p)\left(6 - 3\sin^2\psi\right) + 16pe(p-1)\sin^2\psi}{16pe + 9p - 6} > 0 \, . \tag{7.53}$$

For isotropy, $Z_N = Z_T$ is tantamount to $p = 2$ and zero Poisson's ratio. Again, we try to compare β^{iso} with b^{iso}. We notice that $\partial_p(\beta^{\mathrm{iso}} - b^{\mathrm{iso}}) < 0$. Also, if $p = 2$, then, $\beta^{\mathrm{iso}} < b^{\mathrm{iso}}$. It means that $Z_N \leq Z_T$ is tantamount to $\beta^{\mathrm{iso}} < b^{\mathrm{iso}}$. On the other hand, if $Z_N > Z_T$, then β^{iso} can be either larger or smaller than b^{iso}. Assume that $Z_N \leq Z_T$ and consider $\Delta R^{\ell}_{pp\psi} < 0$. Then, relation $\Delta R^{\ell}_{pp\psi} - \Delta R^{\ell}_{pp}$, namely,

$$\begin{aligned} & k_p^{\mathrm{iso}} \sin^2\theta \left[\sin^2\psi \left(a^{\mathrm{iso}} - \beta^{\mathrm{iso}}\tan^2\theta\right) - \left(a^{\mathrm{iso}} - b^{\mathrm{iso}}\tan^2\theta\right)\right] \\ & \qquad = k_p^{\mathrm{iso}} \sin^2\theta \left(x^{\mathrm{iso}} \sin^2\psi - y^{\mathrm{iso}}\right) \end{aligned} \tag{7.54}$$

must be positive, since $\beta^{\mathrm{iso}} < b^{\mathrm{iso}}$ that leads to $x^{\mathrm{iso}} > y^{\mathrm{iso}}$, where $y^{\mathrm{iso}} < 0$. In other words, the irregularity cannot occur for rocks with positive Poisson's ratio, where $\Delta R^{\ell}_{pp\psi} < 0$ (or $\Delta R^{u}_{pp\psi} > 0$). We illustrate the analysis from this section in Figure 7.2, where some examples of possible irregular CAVA are discussed.

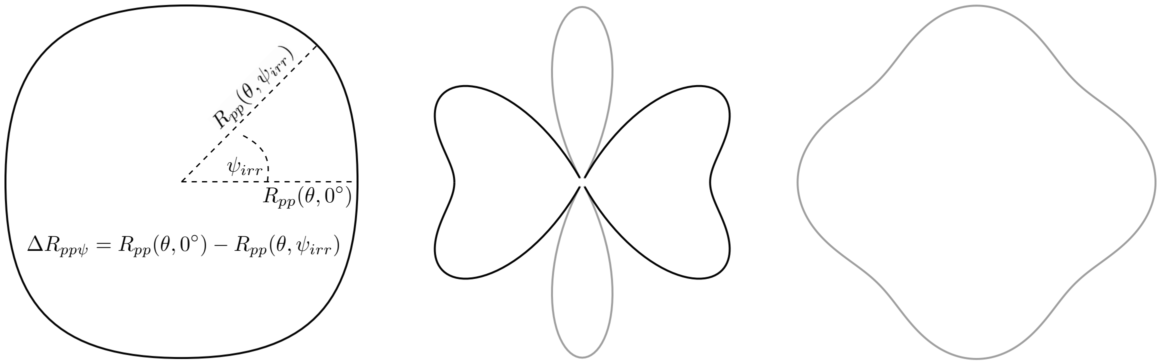

Figure 7.2: Three examples of irregular CAVA for fixed incidence are shown. Let us choose black and grey colours to represent positive and negative reflection coefficient, respectively. Despite remarkably different shapes, the irregularity of each graph corresponds to $\Delta R_{pp\psi} < 0$. Based on the analysis from Section 7.3.2, the above graphs are very unlikely to occur if cracks are embedded in a lower halfspace, since $\Delta R^{\ell}_{pp\psi} < 0$ occurs for very low Poisson's ratio only (rarely presented in seismology). Note that if we switch colours, the irregularity corresponds to $\Delta R_{pp\psi} > 0$. In such a case, the shapes are unlikely to occur if cracks are embedded in an upper—instead of lower—halfspace, since $\Delta R^{u}_{pp\psi} > 0$ happens for very low Poisson's ratio only.

7.3.3 CAVA reversing process

Previously, we have examined what parameters decide whether the reflection coefficient is larger for azimuths parallel or perpendicular to cracks (bullet points in Section 7.3.1). Also, we have discussed that extreme values of R_{pp} can correspond to other than the aforementioned directions. In such a case, we experience irregularity. Irregular CAVA is less or more likely to occur, depending on the sign of $\Delta R_{pp\psi}$ and $Z_T - Z_N$ (see Section 7.3.2). In turn, $\Delta R_{pp\psi}$ depends on the concentration of cracks, incidence angle, and stiffnesses. Due to complicated form of expression (7.51) or (7.54), it is hard to grasp what proportions of stiffnesses, or magnitudes of e and θ, lead to irregularity. In other words, we are not able to propose the analogous bullet points as it was done in Section 7.3.1. However, there is a specific case when azimuthal variations are extremely likely to be irregular. This situation occurs during "CAVA reversing process" that we discuss below.

Consider again expression (7.42) and assume certain values of stiffnesses, e, and θ for which $\Delta R^{\ell}_{pp} < 0$ (equivalently $\Delta R^{u}_{pp} > 0$). In such a case, R_{pp} is larger in parallel than in a perpendicular direction to the cracks. CAVA may be either regular or irregular. Based on the analysis from Section 7.3.1, growing e increases ΔR^{ℓ}_{pp}. Hence, if we continuously increase e (while the other parameters are fixed), we reach $\Delta R^{\ell}_{pp} = 0$ defined as a reversing point, and subsequently, $\Delta R^{\ell}_{pp} > 0$. The above process expresses CAVA reversing, illustrated in Figure 7.3. The reversing process cannot occur if $\Delta R^{\ell}_{pp} > 0$. From the seis-

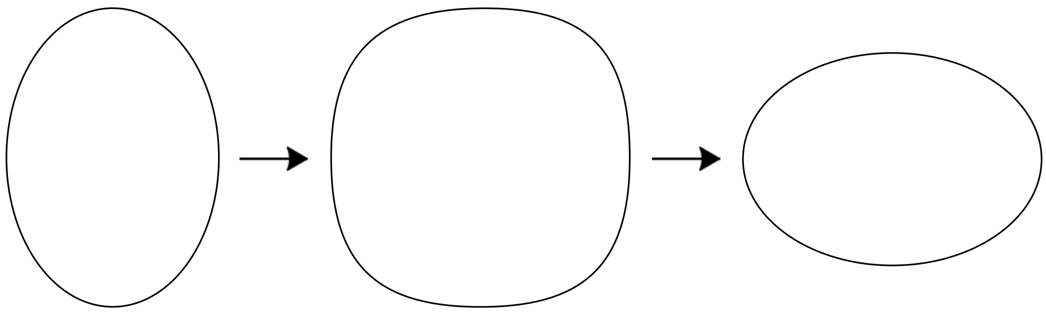

Figure 7.3: Example of CAVA reversing process for continuously growing concentration of cracks (indicated by arrows). Middle graph illustrates the reversing point, where $R_{pp}(\theta, 0°) = R_{pp}(\theta, 90°)$ equivalent to $\Delta R_{pp} = 0$. The reversing process is possible if the first graph presents either $\Delta R^{\ell}_{pp} < 0$ or $\Delta R^{u}_{pp} > 0$. Hence, the above example illustrates either positive R_{pp} calculated for a model with cracks embedded in a lower halfspace or negative R_{pp} corresponding to cracks embedded in an upper halfspace.

mological perspective, CAVA at the reversing point is very likely to be irregular, as shown in the following Lemma.

Lemma 7.3.2. *The polar graph of the PP reflection coefficient at CAVA reversing point—where $\Delta R^{\ell}_{pp} = 0$, $e > 0$, and $\theta > 0$—is either irregular or a regular circle.*

Proof. Assume that CAVA is not irregular and consider a VTI background. The graph is not irregular at reversing point if and only if $\Delta R^{\ell}_{pp\psi} = 0$ for $\forall \psi_{irr} \in (0°, 90°)$; in such a case, it represents a regular circle. □

We can show that a circle at the reversing point is unlikely in the seismological context.

To have a regular shape, we require that

$$k_p \sin^2\theta \left(x \sin^2\psi - y\right) = 0\,. \tag{7.55}$$

To satisfy stability conditions, constant k_p must be greater than zero (for $e > 0$). Expression (7.55) is true if $x\sin^2\psi = y$. Since x and y for given θ are constants, CAVA is regular if and only if $x = y = 0$, which—given definition of these constants from expression (7.51)—is true for $\beta = b$. In turn, considering expression (7.50), we see that β equals b if and only if

$$Z_N - Z_T - Z_N Z_T c_{66}(p_{11} - 1) = 0 \tag{7.56}$$

that is extremely unlikely in the seismological context—since usually $p_{11} > 1$ and $Z_T > Z_N$—but physically possible. Analogical analysis can be performed for an isotropic case.

7.3.4 Magnitude of CAVA

So far, we have thoroughly discussed the shape of azimuthal variations caused by cracks. However, we have not investigated the influence of e on the magnitude of the reflection coefficient. Due to the complexity of Vavryčuk-Pšenčík approximation, analytical analysis is challenging to perform. Even if we assume that cracks are embedded in one of the halfspaces (as we did in previous sections), we cannot get rid of Δ in expression (7.31), and stiffnesses of two halfspaces have to be considered. Therefore, we propose numerical instead of analytical analysis. We assume that both halfspaces have a VTI background, whereas cracks are embedded in the lower one. We perform three MC simulations to obtain $R^{\ell}_{pp}(\theta, \psi, e)$ for different incidence angles; $\theta = 15^\circ$, $\theta = 30^\circ$, and $\theta = 45^\circ$. Let us discuss a single simulation. MC chooses one–thousand elasticity tensors for each halfspace (again stiffnesses are distributed uniformly and their range is taken from Wang

(2002)). Then, $R^{\ell}_{pp}(\psi, e)$ is calculated for azimuths $\psi = 0^\circ$, $\psi = 45^\circ$, and $\psi = 90^\circ$. Finally, to understand the influence of cracks on the magnitude of the reflection coefficient, we compute a derivative of $R^{\ell}_{pp}(e)$ with respect to e. We check in what percentage of cases $R^{\ell}_{pp}(e)$ is a monotonic function; continuously decreases/increases for growing e. In other words, we focus on $\partial_e R^{\ell}_{pp} < 0$ or $\partial_e R^{\ell}_{pp} > 0$ for all $e \in [0, 1]$. We present our findings in Table 7.1. Based on the results from the last column, we notice that for

Table 7.1: Numbers refer to the percentages of cases, where reflection coefficient continuously decreases/increases for growing crack concentration $e \in [0, 1]$. To obtain the results, $\partial_e R^{\ell}_{pp}$ are computed for one-thousand examples of interfaces drawn three times in MC simulations (sim. I, sim. II, and sim. III). In each simulation, a different incidence angle is chosen. Percentages are presented for particular azimuthal angles (columns 2–4). The last column indicates a decrease/increase of R^{ℓ}_{pp} that must occur for all azimuths combined, namely, $\psi = 0^\circ$, $\psi = 45^\circ$, and $\psi = 90^\circ$. VTI backgrounds with cracks (with a normal parallel to the x_1-axis) embedded in the lower halfspace are assumed.

	$\psi = 0^\circ$	$\psi = 45^\circ$	$\psi = 90^\circ$	all combined
sim. I ($\theta = 15^\circ$)	73.9 / 7.3	84.3 / 4.1	91.4 / 2.3	73.9 / 2.3
sim. II ($\theta = 30^\circ$)	69.0 / 6.1	80.5 / 4.0	83.5 / 3.4	67.7 / 3.1
sim. III ($\theta = 45^\circ$)	76.7 / 3.0	84.5 / 1.9	82.4 / 2.1	72.4 / 1.3

most of the chosen models, $R^{\ell}_{pp}(e)$ decreases with the growing concentration of cracks. Such a decrease is more probable for $\theta = 15^\circ$; however, in this context, the incidence angle's influence is not significant. In general, an increase of $R^{\ell}_{pp}(e)$ seems to be very unlikely. Columns two to four—apart from giving us insight into magnitudes—provide us with interesting information on CAVA shape. We notice that the reflection coefficient is more likely to decrease in the direction parallel to cracks than the perpendicular one. Also, in some cases we can expect irregularity since there exist examples, where $R^{\ell}_{pp}(e)$ decreases for $\psi = 45^\circ$, but not for $\psi = 0^\circ$ and $\psi = 90^\circ$. Such irregularity is more likely to occur for large incidence angles.

Note that if cracks are embedded in the upper halfspace, the results are exactly the opposite.

CAVA is likely to increase but unlikely to decrease. To sum up, in at least two–third scenarios, growing e leads to a continuous decrease/increase of $R_{pp}(e)$, where the lower/upper medium is cracked, respectively. Similar results can be obtained for isotropic, instead of VTI, backgrounds.

7.3.5 CAVA patterns

In this section, we fix an incidence angle and propose patterns that consist of a series of two-dimensional polar graphs illustrating how CAVA may change with increasing crack concentration. To do so, we make use of the analysis of azimuthal shapes and magnitude, performed in the previous sections. Let us enumerate essential findings and conjectures. We assume either VTI or isotropic backgrounds and cracks embedded in the lower halfspace (conclusions are the opposite if cracks are situated in the upper halfspace). With growing crack concentration:

1. if θ is large, negative ΔR_{pp} becomes positive (reversing process),
2. if θ is small (or moderate, but rocks are saturated by gas), positive ΔR_{pp} remains positive,
3. irregularity may occur if $\Delta R_{pp\psi} > 0$ (unless Poisson's ratio is very low),
4. irregularity usually occurs during reversing process (when negative ΔR_{pp} becomes positive),
5. reflection coefficient usually decreases.

Based on the above findings, we propose patterns illustrated in Figures 7.4 and 7.5. Let us discuss Figure 7.4. The patterns shown therein, correspond to either $R_{pp} < 0$ for $e = 0$ and cracks in the lower halfspace, or $R_{pp} > 0$ for $e = 0$ and cracks in the upper halfspace.

The patterns are short since CAVA does not change the sign; negative R_{pp}^{ℓ} continuously decreases, whereas positive R_{pp}^{u} continuously increases. Figure 7.4a describes the situation, where the incidence angle is small (or moderate, but rocks are gas-bearing). On the other hand, Figure 7.4b refers to the case of a large θ. More extended patterns are shown in Figure 7.5, where CAVA changes the sign. Thus, they describe either $R_{pp} > 0$ for $e = 0$ and cracks in the lower halfspace, or $R_{pp} < 0$ for $e = 0$ and cracks in the upper halfspace. Figures 7.5a and 7.5b refer to small and large incidence, respectively.

Our CAVA patterns consist of regular, irregular, and—if a change of ΔR_{pp} sign is possible—reversed phase. However, we have introduced some simplifications to the patterns. First, the irregularity for some e_{ir} (and reversed shape for some e_{rr}) may occur at earlier stage, as indicated by two distinct pattern's branches in both Figures 7.4a and 7.4b. Such a possibility has not been shown in Figure 7.5. Therein, the irregular and reverse phases occur at the latest possible stage. Second, not in every seismological case, the irregular or reversed azimuthal variations must occur. In other words, the pattern may end earlier and not be full. The aforementioned two circumstances lead to "shortened CAVA patterns" linked to Figures 7.4 and 7.5, but not shown explicitly there. Hence, full patterns from Figures 7.4 and 7.5 should be treated as general, idealised schemes. Note that due to the change of sign, regular CAVA gains specific shapes. For instance, in Figures 7.5a and 7.5b, the third graph (counted from the upper-left corner) illustrates the last, limiting, only-convex shape (potato-like). Then, due to concave parts, CAVA becomes peanut-like. With growing e, it reaches infinity-like, knot-like, and shamrock-like shapes, respectively. Exceptionally, the information on the aforementioned shapes is not induced by the analytical analysis performed in the previous sections. We have observed the shapes upon numerous simulations, discussed in Section 7.4. Also, the irregularity may have different than oval shape, as exemplified in Figure 7.2.

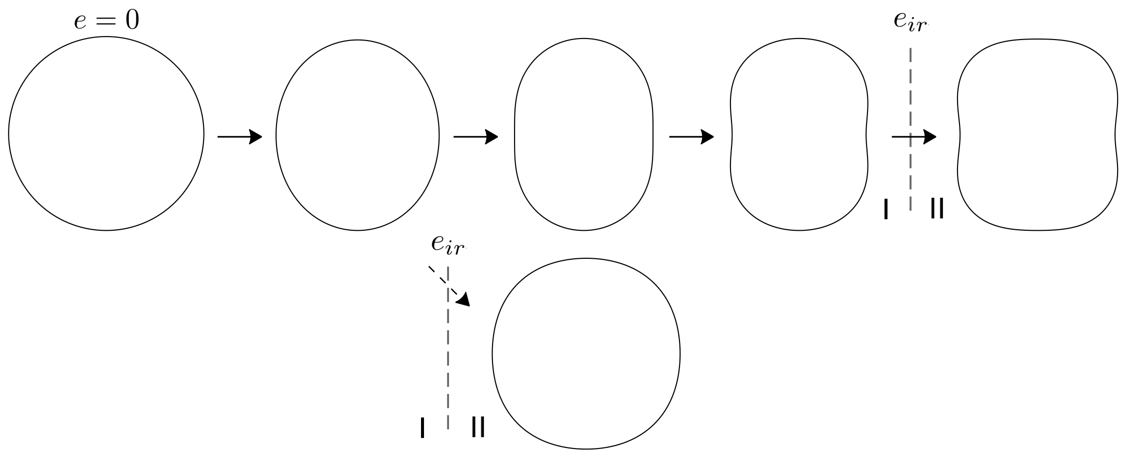

(a) smaller θ (gas saturation more likely)

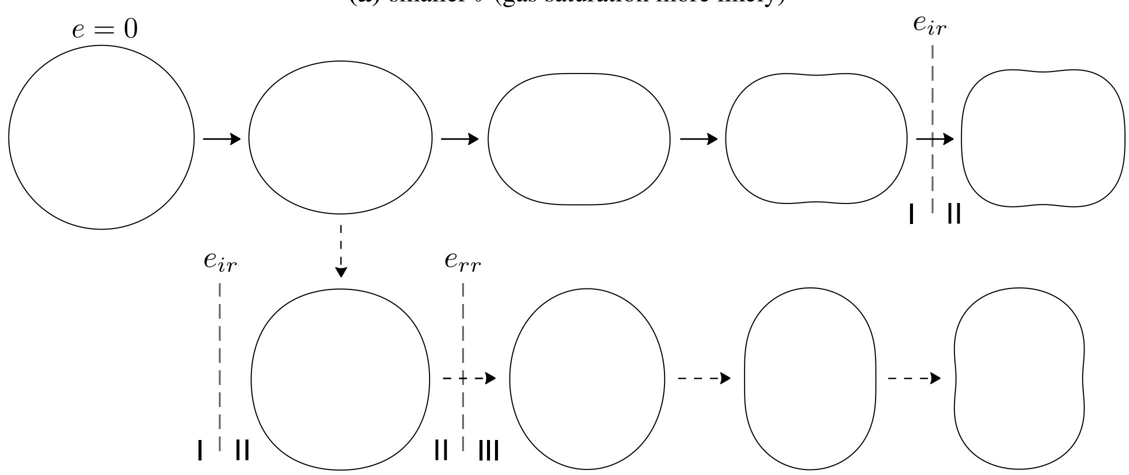

(b) larger θ (brine saturation more likely)

Figure 7.4: Short CAVA patterns illustrate changes of azimuthal variations of reflection coefficient with increasing concentration of cracks, e (indicated by arrows). Changes in shape—not in magnitude—are reflected only. Either VTI or isotropic backgrounds are assumed. Cracks are embedded either in a lower (ℓ) or upper (u) halfspace and have a normal parallel to the x_1-axis. One pattern corresponds to a small incidence angle (or moderate angle and gas-bearing rocks), whereas the second pattern refers to large θ (or moderate angle and brine-bearing rocks). Both schemes illustrate either decreasing, negative R^{ℓ}_{pp} or increasing, positive R^{u}_{pp}. Phases I, II, and III consist of regular, irregular, and reversed CAVA, respectively. Boundary between phases I and II is denoted by concentration e_{ir}. Boundary between phases II and III is described by e_{rr}. Dashed arrows indicate some possible "shortened" patterns, where the irregular phase occurs at an earlier stage. Additionally, other shortened patterns—where latter stages are absent (due to, for instance, lack of irregular and reversed phases)—are possible, but are not shown herein.

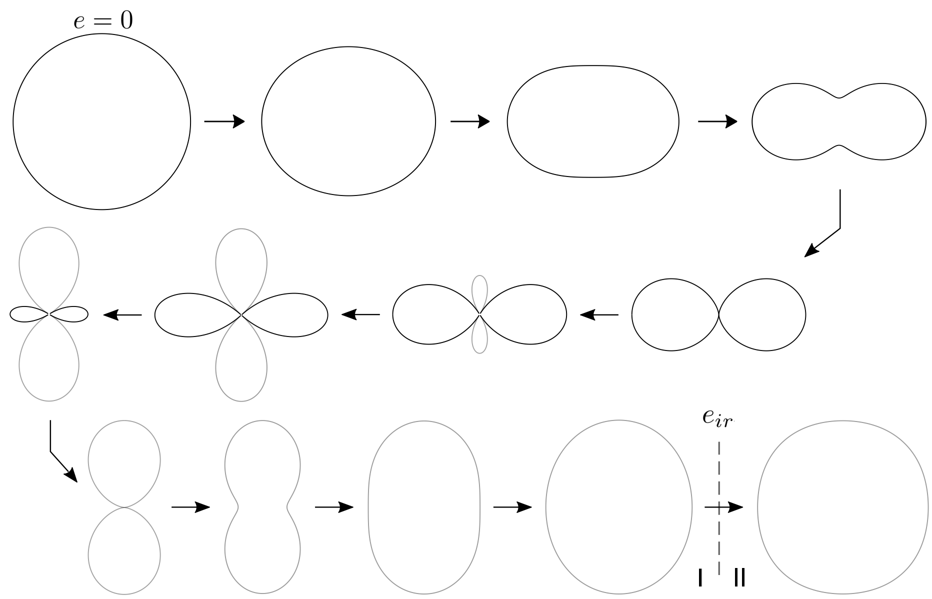

(a) smaller θ (gas saturation more likely)

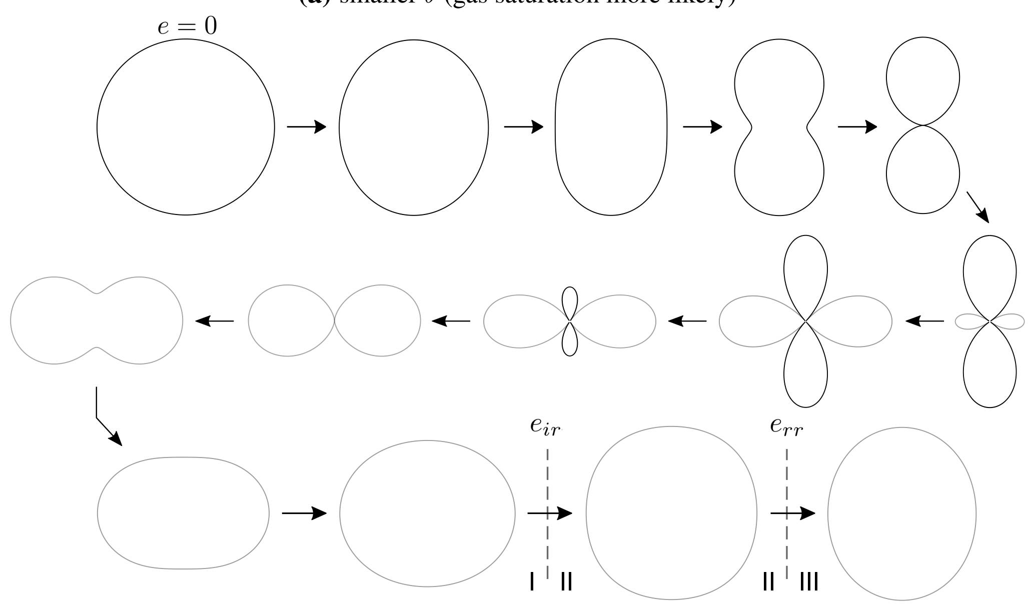

(b) larger θ (brine saturation more likely)

Figure 7.5: Long CAVA patterns illustrate changes of azimuthal variations of reflection coefficient with increasing concentration of cracks, e (indicated by arrows). Changes in shape and sign (different colours)—not in magnitude—are reflected only. Either VTI or isotropic backgrounds are assumed. Cracks are embedded either in a lower (ℓ) or upper (u) halfspace and have normal towards the x_1-axis. One pattern corresponds to a small incidence angle (or moderate angle and gas-bearing rocks), whereas the second pattern refers to large θ (or moderate angle and brine-bearing rocks). Both schemes illustrate either decreasing, initially positive R^{ℓ}_{pp} or increasing, initially negative R^{u}_{pp}. Phases I, II, and III consist of regular, irregular, and reversed CAVA, respectively. Boundary between phases I and II is denoted by concentration e_{ir}. Boundary between phases II and III is described by e_{rr}. The absence of latter stages and/or the presence of an early irregularity is possible; it leads to shortened patterns not shown herein.

Let us discuss CAVA patterns in the context of inverse problems. We notice an important but, in a way, disappointing issue. The same CAVA (shapes and signs) are present in more than one pattern. Hence, even if we know R_{pp}, cracks orientation, and the incidence angle, we cannot infer the sign of the reflection coefficient of the background medium (where $e = 0$). Also, it is hard to grasp what the magnitude of the crack concentration is, or in which halfspace the cracks are situated. Finally, perhaps most importantly, the difficulty in choosing the right pattern affects the correct inference on rock's saturation. To understand it better, consider the following example. Assume that our CAVA is negative and regular with $\Delta R_{pp} > 0$ (narrow and tall ellipse-like shape); the incidence is moderate, and cracks are embedded in the lower halfspace having a normal parallel to the x_1-axis. If our shape belonged to pattern from Figure 7.4a or 7.5a, gas-saturation would be very probable. On the other hand, if it belonged to pattern from Figure 7.4b or 7.5b, brine-saturation or no-saturation would be more probable. Unfortunately, our CAVA matches all the aforementioned figures, so the inference on rock's saturation is difficult. Nonetheless, there are examples where such inference is simple. Again consider the same location of cracks and moderate incidence. Assume positive, regular CAVA with $\Delta R_{pp} < 0$ (wide and short ellipse-like shape). Such CAVA matches Figure 7.5a only. Hence, in this example, gas-saturation is very probable. Therefore, we expect that the conjectured patterns may be useful in gas exploration despite the aforementioned difficulties.

7.4 Numerical verification

In this section, we use numerical techniques to verify and enrich our previous analysis, which led to the conjectured CAVA patterns. First, we pose the following questions to better understand the nature of azimuthal variations of amplitude for cracked media.

Are the conjectured patterns correct? How often can we expect the shortened patterns? Do patterns from Figures 7.4a and 7.5a really occur more often for small incidence angles and gas rocks? What phases (regular, irregular, or reversed) are the most common for specified crack densities and incidence angles? To answer these questions, we use twenty models of interfaces between VTI elastic backgrounds. The values of stiffnesses were measured in a laboratory by Wang (2002). In such models, we increase crack concentration in either lower or upper halfspace to obtain forty CAVA patterns for each incidence angle. We examine seven specific incidences, where $\theta \in [1^\circ, 45^\circ]$; hence, in total, we verify two hundred eighty patterns.

Results of numerical experiments obtained for $\theta = 15^\circ$ are presented in Table 7.2. Findings for the other six incidence angles are exhibited in Appendix 7.A. Additionally, a MATLAB code used to obtain the results is shown in Appendix 7.B. Herein, as an example, we analyse the aforementioned table only. Twenty models of interfaces consist of diverse geological scenarios (first column). We examine a variety of elastic backgrounds that correspond to sedimentary rocks; sands, shales, coals, limestones, and dolomites. The halfspaces may be either gas or brine saturated. Each background has a symbol assigned (second column) so that its stiffnesses can be extracted from Wang (2002) directly (we took values for the lowest overburden pressure). The third and fourth columns give us important information on R_{pp} , so we infer what CAVA pattern should be expected (fifth column). We increase crack concentration in either halfspace and obtain the actual pattern (sixth column) along with crack densities that correspond to phase boundaries (two last columns).

To gain more insight into Table 7.2, consider model number one with cracks embedded in the lower halfspace. The reflection coefficient is negative and decreases with growing crack concentration. We can expect either pattern from Figure 7.4, since the incidence is neither very small nor large. Upon continuous increase of e , CAVA reaches irregular phase at $e_{irr} = 0.16$ and reversed phase at $e_{rr} = 0.20$. Despite the occurrence of all phases, the pattern is shortened since the last two shapes indicated by dashed arrows in Figure 7.4b do not appear. This time, consider model number two with cracks again embedded in the lower halfspace having the same stiffnesses as in model one. Both examples differ by the saturation of the upper halfspace only. It occurs that the magnitude of R_{pp} at $e = 0$ is positive so that the expected pattern is different as compared to the previous example. However, crack densities e_{irr} and e_{rr} stay the same. The discussed results show that halfspace's saturation influences the magnitude of azimuthal variations, but not the shape. This phenomenon can be explained easily. The magnitude of the reflection coefficient changes since the isotropic term R_{ipp} depends on both halfspaces. On the other hand, ΔR_{pp} from expression (7.35)—responsible for CAVA shape—depends on the stiffnesses from one halfspace only (identical for both models). In Table 7.2, we present thirty distinct halfspaces; hence, we provide thirty independent measures of e_{irr} and e_{rr}.

Based on two hundred eighty examples from Table 7.2 and Appendix 7.A, we infer that our conjectured, full, and shortened CAVA patterns—in a great majority of cases—are correct. In one example only (for $\theta = 30°$), an alternative pattern is needed. It was caused by predominantly increasing (instead of decreasing) R^{ℓ}_{pp} with growing e. Our conjectured patterns are also sufficient in other examples of non-monotonic $\partial_e R_{pp}$ (see the fourth column). To answer the rest of the questions posed at the beginning of this section, we propose to condense the numerical results in Figures 7.6–7.8.

Figure 7.6 shows that in the majority of cases, CAVA patterns are shortened. Full patterns are more probable for larger incidences than small ones. Also, it illustrates that patterns from Figures 7.4a and 7.5a are less likely to occur than patterns from Figures 7.4b and 7.5b. As we have expected in the previous section, Figures 7.4a and 7.5a are typical for small θ. They do not occur for very large incidences.

Table 7.2: To verify the conjectured CAVA patterns, we propose twenty models of cracked media. Each model has embedded cracks in either upper or lower background, so that approximated critical density parameters (e_{ir} and e_{rr}) for each possibility are obtained (forty cases in total). Backgrounds are brine (b.) or gas (g.) saturated. An asterisk indicates a shortened pattern not shown explicitly in Figures 7.4 and 7.5. A small/moderate incidence angle, $\theta = 15°$, is chosen.

model nr	halfspaces (upper/lower)	R_{pp} at $e = 0$	R_{pp} monotonicity	expected pattern	actual pattern	e_{ir}	e_{rr}
1	b. sand (E5)/	negative	increasing	Fig. 7.5	Fig. 7.5a*	—	—
	b. sand (E2)		decreasing	Fig. 7.4	Fig. 7.4b*	0.16	0.20
2	g. sand (E5)/	positive	non mono.	Fig. 7.4	Fig. 7.4a*	—	—
	b. sand (E2)		decreasing	Fig. 7.5	Fig. 7.5b*	0.16	0.20
3	b. limestone (1)/	negative	increasing	Fig. 7.5	Fig. 7.5b	0.17	0.22
	b. limestone (2)		decreasing	Fig. 7.4	Fig. 7.4b*	0.12	0.15
4	g. limestone (1)/	positive	increasing	Fig. 7.4	Fig. 7.4b*	0.10	0.13
	b. limestone (2)		decreasing	Fig. 7.5	Fig. 7.5b*	0.12	0.15
5	b. shale (B1)/	positive	increasing	Fig. 7.4	Fig. 7.4b*	0.14	0.18
	b. shale (B2)		non mono.	Fig. 7.5	Fig. 7.5a*	—	—
6	b. shale (G3)/	positive	non mono.	Fig. 7.4	Fig. 7.4a*	—	—
	b. shale (G5)		non mono.	Fig. 7.5	Fig. 7.5a*	—	—
7	b. shale (E1)/	positive	increasing	Fig. 7.4	Fig. 7.4b*	0.78	> 1
	b. shale (E5)		decreasing	Fig. 7.5	Fig. 7.5b*	> 1	—
8	b. sand (E5)/	positive	non mono.	Fig. 7.4	Fig. 7.4a*	—	—
	b. shale (E5)		decreasing	Fig. 7.5	Fig. 7.5b*	> 1	—
9	g. sand (E5)/	positive	non mono.	Fig. 7.4	Fig. 7.4a*	—	—
	b. shale (E5)		decreasing	Fig. 7.5	Fig. 7.5b*	> 1	—
10	g. sand (G8)/	positive	non mono.	Fig. 7.4	Fig. 7.4a*	—	—
	b. sand (G8)		decreasing	Fig. 7.5	Fig. 7.5a*	—	—
11	g. sand (G14)/	negative	non mono.	Fig. 7.5	Fig. 7.5a*	—	—
	g. sand (G16)		non mono.	Fig. 7.4	Fig. 7.4a*	—	—
12	g. coal (G31)/	positive	non mono.	Fig. 7.4	Fig. 7.4b*	0.04	0.05
	b. coal (G31)		non mono.	Fig. 7.5	Fig. 7.5b*	0.31	0.48
13	g. limestone (9)/	positive	increasing	Fig. 7.4	Fig. 7.4a*	—	—
	g. limestone (10)		decreasing	Fig. 7.5	Fig. 7.5b*	0.10	0.13
14	b. limestone (9)/	positive	increasing	Fig. 7.4	Fig. 7.4b*	0.10	0.12
	g. limestone (10)		decreasing	Fig. 7.5	Fig. 7.5b	0.10	0.13
15	b. limestone (22)/	positive	increasing	Fig. 7.4	Fig. 7.4b*	0.20	0.26
	b. dolomite (23)		decreasing	Fig. 7.5	Fig. 7.5b*	0.10	0.13
16	g. limestone (22)/	positive	increasing	Fig. 7.4	Fig. 7.4b*	0.06	0.08
	b. dolomite (23)		decreasing	Fig. 7.5	Fig. 7.5b*	0.10	0.13
17	g. dolomite (28)/	negative	increasing	Fig. 7.5	Fig. 7.5b	0.14	0.18
	g. dolomite (29)		decreasing	Fig. 7.4	Fig. 7.4a*	—	—
18	b. dolomite (28)/	negative	increasing	Fig. 7.5	Fig. 7.5b*	0.12	0.15
	g. dolomite (29)		decreasing	Fig. 7.4	Fig. 7.4a*	—	—
19	b. dolomite (31)/	negative	increasing	Fig. 7.5	Fig. 7.5b	0.15	0.19
	b. limestone (32)		decreasing	Fig. 7.4	Fig. 7.4b*	0.35	0.49
20	g. dolomite (31)/	positive	increasing	Fig. 7.4	Fig. 7.4b*	0.09	0.11
	b. limestone (32)		decreasing	Fig. 7.5	Fig. 7.5b*	0.35	0.49

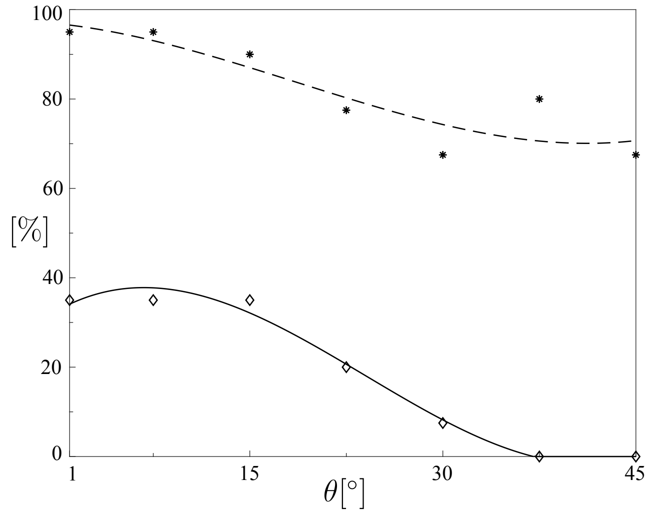

Figure 7.6: Asterisks indicate the percentage of cracked halfspaces, where CAVA follows the shortened patterns. Results are obtained for seven incidence angles, and a dashed line shows the trend for $\theta \in [1°, 45°]$. Diamonds indicate the percentage of cracked halfspaces, where CAVA follows the pattern from Figures 7.4a or 7.5a. A solid line proposes a possible trend.

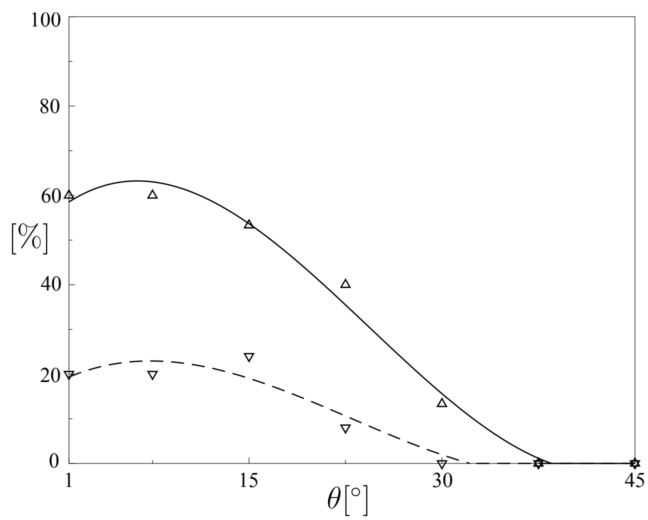

Figure 7.7: Upward pointing triangles indicate the percentage of gas-saturated cracked halfspaces, where CAVA follows the pattern from Figures 7.4a or 7.5a. Results are obtained for seven incidence angles, and a solid line shows the trend for $\theta \in [1°, 45°]$. Analogously, downward-pointing triangles correspond to brine-saturated cracked halfspaces, whereas a dashed line is the trend.

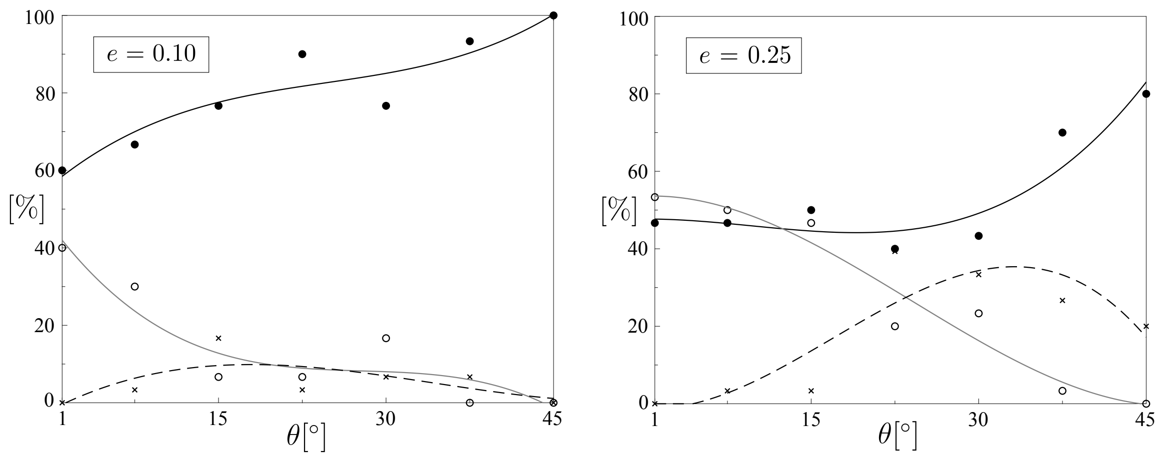

Figure 7.8: Percentage of cracked halfspaces, where CAVA is regular (filled circles), irregular (crosses), or reversed (empty circles). Either moderate concentration of cracks $e = 0.10$ (graph on the left) or large crack density $e = 0.25$ (graph on the right) is assumed. Results are obtained for seven specific incidences. Possible trends are proposed; solid black line corresponds to the regular phase, the dashed line indicates the irregularity, and the solid grey line shows the reversed phase.

Figure 7.7 illustrates that for small angles, sixty percent of gas-bearing and cracked halfspaces exhibit CAVA patterns from Figures 7.4a and 7.5a. This percentage is much smaller for brine-saturated rocks. For both saturations, the percentage decreases with increasing incidence. Knowing that cracks are embedded in a brine-saturated background, we can expect patterns from Figures 7.4b and 7.5b (for any θ). On the other hand, if we know that cracks are embedded in a gas-saturated background, for large θ we should expect Figures 7.4b and 7.5b, but for small incidence, any pattern is probable. Considering the above, if CAVA belongs to patterns from Figures 7.4a and 7.5a, we should expect that rocks are saturated by gas.

To answer the last question posed in this section, we present Figure 7.8. It shows that with growing e, irregular and reversed phases become more frequent, but the regular phase is usually predominant (except small incidence and large crack concentration). In general, the irregular phase is the most frequent for moderate angles $\theta \in [15°, 30°]$, whereas the reversed phase for very small incidences. For $e = 0.10$ irregular phase may be present up to every sixth case ($\theta = 15°$). Reversed CAVA can be demonstrated by up to forty percent interfaces ($\theta = 1°$). For $e = 0.25$ irregularity may occur in up to forty percent of cases ($\theta = 22.5°$), whereas the reversed phase in more than fifty percent of examples ($\theta = 1°$). Larger concentrations than $e = 0.25$ are not illustrated due to the dubious accuracy of the NIA in such cases.

Having verified our patterns and answered all the essential questions regarding the nature of azimuthal variations, let us summarise the key findings regarding gas exploration that interest many geophysicists dealing with cracked media. First, the saturation of cracked media changes the magnitude of variations, but not its shape. Second, knowing about the presence of gas, we cannot infer the right CAVA shape. Third, knowing CAVA that magnitude and shape is specific only for Figures 7.4a and 7.5a, with significant probability, we can expect gas saturation. Fourth, patterns from the aforementioned figures do not occur for large incidence angles.

At the end of the previous section, we have mentioned the example of CAVA attributes (sign and shape) characteristic for gas-bearing rocks only. Herein, we extract all CAVA that appear in Figures 7.4a and 7.5a, but are absent in Figures 7.4b and 7.5b. Therefore, Figure 7.9 gathers all variations characteristic for gas presence. Again, the existence of gas-bearing rocks does not assure these shapes. However, CAVA from Figure 7.9 can be treated as a gas indicator.

7.5 Conclusions

We have analysed the effect of crack concentration on the PP-wave reflection coefficient variations with azimuth. Such effect differs depending on the incidence angle and stiffnesses of the cracked medium (influenced by the rock saturation). We have assumed a

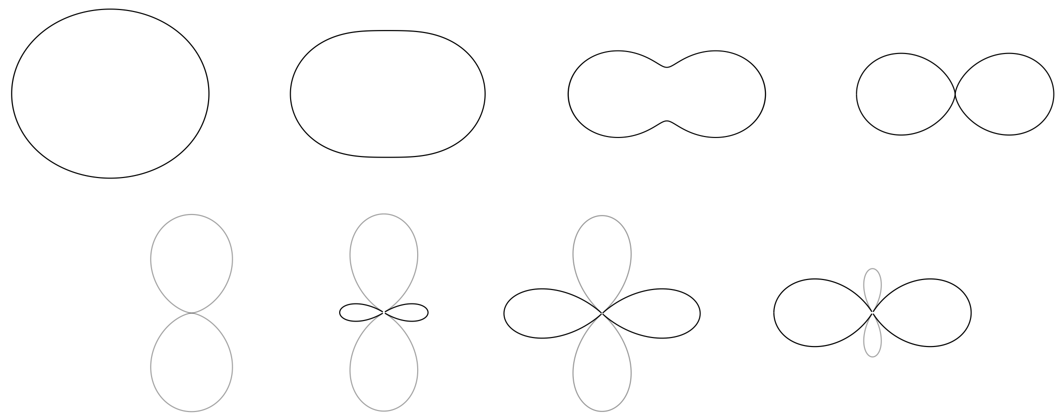

Figure 7.9: Azimuthal variations of amplitude characteristic for gas-bearing rocks. The set of cracks is vertical and normal to the x_1-axis. If cracks are embedded in the lower halfspace, then black and grey colours correspond to positive and negative reflection coefficient, respectively. If cracks are situated in the upper halfspace, the meaning of colours is the opposite.

single set of vertically aligned cracks with a normal to the x_1-axis. We have examined cracks embedded in one halfspace only, either isotropic or anisotropic (VTI), employing the effective medium theory.

We have proposed and verified patterns of two-dimensional azimuthal variations of amplitude changing with increasing crack concentration upon thorough analytical and numerical analysis. We have recognised patterns typical for small incidence and gas saturation, and schemes characteristic for large incidence and brine-bearing rocks. Certain azimuthal variations (sign and shape) are present solely in the patterns typical for gas saturation. We have indicated eight shapes characteristic for cracks situated in the gas-bearing halfspace.

We have also noticed that the reflection coefficient may have extreme absolute values in directions other than parallel or perpendicular to cracks. An irregular variation occurs in such cases, which is more frequent for moderate incidences and large crack concentration.

We are aware of the limitations imposed on our findings. Vavryčuk-Pšenčík approximation of the PP-wave reflection coefficient that we use assumes weak anisotropy and weak elastic contrasts at the interfaces. Such simplifications are needed to perform a fruitful analytical analysis. Moreover, we assume the non-interactive approximation that is inaccurate for larger concentrations of cracks. Patterns proposed by us are valid for cracks with a normal parallel to the x_1-axis only. However, analogical patterns can be obtained for other orientations of cracks, using methods from this paper. The shapes from our patterns should be rotated by the angle equal to the deviation of cracks from the x_1-axis. Further, we expect that the CAVA effect caused by several sets of cracks is a kind of superposition of patterns corresponding to each set. In the future, we aim to verify our anticipations. Also, we intend to provide real data examples to examine the findings and conjectures shown herein.

Acknowledgements

We wish to acknowledge discussions with Michael A. Slawinski. The research was done in the context of The Geomechanics Project partially supported by the Natural Sciences and Engineering Research Council of Canada, grant 202259.

7.6 References

Adamus, F. P. (2020). "Orthotropic anisotropy: on contributions of elasticity parameters to a difference in quasi-P-wave-squared velocities resulted from propagation in two orthogonal symmetry planes". *Geophysical Prospecting*, 68 (8), 2361–2378.

Aki, K. and Richards, K. G. (1980). *Quantitative Seismology: Theory and Methods*. W. H. Freeman.

Bruggeman, D. A. G. (1937). “Berechnung verschiedener physikalischer Konstanten von heterogenen Substanzen. III. Die elastischen Konstanten der quasiisotropen Mischkörper aus isotropen Substanzen”. *Annalen der Physik*, 421 (2), 160–178.

Chen, H., Zhang, G., Ji, Y., and Yin, X. (2017). “Azimuthal Seismic Amplitude Difference Inversion for Fracture Weakness”. *Pure Appl. Geophys.* 174 (1), 279–291.

Chopra, S. and Castagna, J. P. (2014). *AVO*. Investigations in Geophysics Series No. 16. Society of Exploration Geophysicists.

Eshelby, J. D. (1957). “The determination of the elastic field of an ellipsoidal inclusion, and related problems”. *Proc. R. Soc. A*, 241 (1226), 376–396.

Grechka, V. and Kachanov, M. (2006). “Seismic characterization of multiple fracture sets: Does orthotropy suffice?” *Geophysics*, 71 (3), D93–D105.

Guo, J., Han, T., Fu, L., Xu, D., and Fang, X. (2019). “Effective Elastic Properties of Rocks With Transversely Isotropic Background Permeated by Aligned Penny–Shaped Cracks”. *J. Geophys. Res. Solid Earth*, 124 (1), 400–424.

Hudson, J. A. (1980). “Overall properties of a cracked solid”. *Math. Proc. Cambridge Philos. Soc.* 88 (2), 371–384.

Ji, L. and Zong, Z. (2019). “Model parameterization and amplitude variation with angle and azimuth inversion for orthotropic parameters”. *SEG Expanded Abstracts*.

Kachanov, M. (1992). “Effective elastic properties of cracked solids: critical review of some basic concepts”. *Appl. Mech. Rev.* 45 (8), 304–335.

Kachanov, M. and Sevostianov, I. (2018). *Micromechanics of Materials, with Applications*. Springer.

Kachanov, M., Tsukrov, I., and Shafiro, B. (1994). “Effective moduli of solids with cavities of various shapes”. *Appl. Mech. Rev.* 47 (1), S151–S174.

Pšenčík, I. and Martins, J. L. (2001). “Properties of weak contrast PP reflection/transmission coefficients for weakly anisotropic elastic media”. *Studia Geophys. et Geod.* 45 (2), 176–199.

Rüger, A. (1998). “Variation of P-wave reflectivity with offset and azimuth in anisotropic media”. *Geophysics*, 63 (3), 935–947.

Rüger, A. and Gray, D. (2014). *2. Wide-azimuth amplitude-variation-with-offset analysis of anisotropic fractured reservoirs*. Encyclopedia of Exploration Geophysics. Society of Exploration Geophysicists.

Schoenberg, M. A., Dean, S., and Sayers, C. M. (1999). “Azimuth-dependent tuning of seismic waves reflected from fractured reservoirs”. *Geophysics*, 64 (4), 1160–1171.

Schoenberg, M. and Douma, J. (1988). “Elastic wave propagation in media with parallel fractures and aligned cracks”. *Geophysical Prospecting*, 36 (6), 571–590.

Schoenberg, M. and Helbig, K. (1997). “Orthorhombic media: Modeling elastic wave behavior in a vertically fractured earth”. *Geophysics*, 62 (6), 1954–1974.

Schoenberg, M. and Protazio, J. (1992). “’Zoeppritz’ rationalized and generalized to anisotropy”. *J. of Seism. Explor.* 1, 125–144.

Schoenberg, M. and Sayers, C. M. (1995). “Seismic anisotropy of fractured rock”. *Geophysics*, 60 (1), 204–211.

Sevostianov, I., Yilmaz, N., Kushch, V., and Levin, V. (2005). “Effective elastic properties of matrix composites with transversely-isotropic phases”. *Int. J. Solids Struct.* 42 (2), 455–476.

Slawinski, M. A. (2020a). *Waves and rays in elastic continua*. 4th edn. World Scientific.

Ursin, B. and Haugen, G. V. (1996). “Weak-contrast approximation of the elastic scattering matrix in anisotropic media”. *Pure Appl. Geophys.* 148 (3/4), 685–714.

Vavryčuk, V. and Pšenčík, I. (1998). “PP-wave reflection coefficients in weakly anisotropic elastic media”. *Geophysics*, 63 (6), 2129–2141.

Wang, Z. (2002). “Seismic anisotropy in sedimentary rocks, part 2: Laboratory data”. *Geophysics*, 67 (5), 1423–1440.

Xie, C., Wang, E., Zhong, T., Yan, G., He, R., and Guo, T. (2019). “Using the azimuthal derivative of the amplitude for fracture detection”. *SEG Expanded Abstracts*.

Zillmer, M., Gajewski, D., and Kashtan, B. M. (1997). “Reflection coefficients for weak anisotropic media”. *Geophys. J. Int.* 129 (2), 389–398.

Zoeppritz, K. (1919). “Über Reflexion und Durchgang seismischer Wellen durch Unstetigkeitsflächen”. *Erdbebenwellen VII B. Nachrichten von der Gesellschaft der Wissenschaften zu Göttingen, Mathematisch-Physikalische Klasse*, 57–84.

7.A Tables with numerical results

Table 7.3: To verify the conjectured CAVA patterns, we propose twenty models of cracked media. Each model has embedded cracks in either upper or lower background, so that approximated critical density parameters (e_{ir} and e_{rr}) for each possibility are obtained. Backgrounds are brine (b.) or gas (g.) saturated. An asterisk indicates a shortened pattern not shown explicitly in Figures 7.4 and 7.5. Various incidences are chosen, namely, $\theta = 1°$, $\theta = 7.5°$, $\theta = 22.5°$, $\theta = 30°$, $\theta = 37.5°$, and $\theta = 45°$.

	$\theta = 1°$					
models	R_{pp} at $e = 0$	R_{pp} monotonicity	expected pattern	actual pattern	e_{ir}	e_{rr}
b. sand (E5)/ b. sand (E2)	negative	increasing decreasing	Fig. 7.5a Fig. 7.4a	Fig. 7.5a* Fig. 7.4b*	— 0.12	— 0.12
g. sand (E5)/ b. sand (E2)	positive	increasing decreasing	Fig. 7.4a Fig. 7.5a	Fig. 7.4a* Fig. 7.5b*	— 0.12	— 0.12
b. limestone (1)/ b. limestone (2)	negative	increasing decreasing	Fig. 7.5a Fig. 7.4a	Fig. 7.5b* Fig. 7.4b*	0.01 0.08	0.01 0.08
g. limestone (1)/ b. limestone (2)	positive	increasing decreasing	Fig. 7.4a Fig. 7.5a	Fig. 7.4b* Fig. 7.5b*	0.06 0.08	0.06 0.08
b. shale (B1)/ b. shale (B2)	positive	increasing decreasing	Fig. 7.4a Fig. 7.5a	Fig. 7.4b* Fig. 7.5a*	0.09 —	0.09 —
b. shale (G3)/ b. shale (G5)	positive	increasing decreasing	Fig. 7.4a Fig. 7.5a	Fig. 7.4a* Fig. 7.5a*	— —	— —
b. shale (E1)/ b. shale (E5)	positive	increasing decreasing	Fig. 7.4a Fig. 7.5a	Fig. 7.4b* Fig. 7.5b	0.68 > 1	0.68 > 1
b. sand (E5)/ b. shale (E5)	negative	increasing decreasing	Fig. 7.5a Fig. 7.4a	Fig. 7.5a* Fig. 7.4b*	— > 1	— > 1
g. sand (E5)/ b. shale (E5)	positive	increasing decreasing	Fig. 7.4a Fig. 7.5a	Fig. 7.4a* Fig. 7.5b*	— > 1	— > 1
g. sand (G8)/ b. sand (G8)	positive	increasing decreasing	Fig. 7.4a Fig. 7.5a	Fig. 7.4a* Fig. 7.5b*	— 0.04	— 0.04
g. sand (G14)/ g. sand (G16)	negative	increasing decreasing	Fig. 7.5a Fig. 7.4a	Fig. 7.5a* Fig. 7.4a*	— —	— —
g. coal (G31)/ b. coal (G31)	positive	increasing decreasing	Fig. 7.4a Fig. 7.5a	Fig. 7.4a* Fig. 7.5b*	— 0.23	— 0.23
g. limestone (9)/ g. limestone (10)	positive	increasing decreasing	Fig. 7.4a Fig. 7.5a	Fig. 7.4a* Fig. 7.5b*	— 0.06	— 0.06
b. limestone (9)/ g. limestone (10)	positive	increasing decreasing	Fig. 7.4a Fig. 7.5a	Fig. 7.4b* Fig. 7.5b*	0.05 0.06	0.05 0.06
b. limestone (22)/ b. dolomite (23)	positive	increasing decreasing	Fig. 7.4a Fig. 7.5a	Fig. 7.4b* Fig. 7.5b*	0.15 0.06	0.15 0.06
g. limestone (22)/ b. dolomite (23)	positive	increasing decreasing	Fig. 7.4a Fig. 7.5a	Fig. 7.4b* Fig. 7.5b*	0.02 0.06	0.02 0.06
g. dolomite (28)/ g. dolomite (29)	negative	increasing decreasing	Fig. 7.5a Fig. 7.4a	Fig. 7.5b Fig. 7.4a*	0.10 —	0.10 —
b. dolomite (28)/ g. dolomite (29)	negative	increasing decreasing	Fig. 7.5a Fig. 7.4a	Fig. 7.5b* Fig. 7.4a*	0.08 —	0.08 —
b. dolomite (31)/ b. limestone (32)	negative	increasing decreasing	Fig. 7.5a Fig. 7.4a	Fig. 7.5b* Fig. 7.4b*	0.11 0.29	0.11 0.29
g. dolomite (31)/ b. limestone (32)	positive	increasing decreasing	Fig. 7.4a Fig. 7.5a	Fig. 7.4b* Fig. 7.5b*	0.05 0.29	0.05 0.29

	$\theta = 7.5°$					
models	R_{pp} at $e = 0$	R_{pp} monotonicity	expected pattern	actual pattern	e_{ir}	e_{rr}
b. sand (E5)/ b. sand (E2)	negative	increasing decreasing	Fig. 7.5a Fig. 7.4a	Fig. 7.5a* Fig. 7.4b*	— 0.12	— 0.13
g. sand (E5)/ b. sand (E2)	positive	increasing decreasing	Fig. 7.4a Fig. 7.5a	Fig. 7.4a* Fig. 7.5b*	— 0.12	— 0.13
b. limestone (1)/ b. limestone (2)	negative	increasing decreasing	Fig. 7.5a Fig. 7.4a	Fig. 7.5b* Fig. 7.4b*	0.13 0.08	0.14 0.09
g. limestone (1)/ b. limestone (2)	positive	increasing decreasing	Fig. 7.4a Fig. 7.5a	Fig. 7.4b* Fig. 7.5b*	0.07 0.08	0.08 0.09
b. shale (B1)/ b. shale (B2)	positive	increasing decreasing	Fig. 7.4a Fig. 7.5a	Fig. 7.4b* Fig. 7.5a*	0.10 —	0.11 —
b. shale (G3)/ b. shale (G5)	positive	increasing non mono.	Fig. 7.4a Fig. 7.5a	Fig. 7.4a* Fig. 7.5a*	— —	— —
b. shale (E1)/ b. shale (E5)	positive	increasing decreasing	Fig. 7.4a Fig. 7.5a	Fig. 7.4b* Fig. 7.5b	0.71 > 1	0.83 > 1
b. sand (E5)/ b. shale (E5)	negative	increasing decreasing	Fig. 7.5a Fig. 7.4a	Fig. 7.5a* Fig. 7.4b*	— > 1	— > 1
g. sand (E5)/ b. shale (E5)	positive	non mono. decreasing	Fig. 7.4a Fig. 7.5a	Fig. 7.4a* Fig. 7.5b*	— > 1	— > 1
g. sand (G8)/ b. sand (G8)	positive	increasing decreasing	Fig. 7.4a Fig. 7.5a	Fig. 7.4a* Fig. 7.5b*	— 0.05	— 0.05
g. sand (G14)/ g. sand (G16)	negative	non mono. decreasing	Fig. 7.5a Fig. 7.4a	Fig. 7.5a* Fig. 7.4a*	— —	— —
g. coal (G31)/ b. coal (G31)	positive	non mono. decreasing	Fig. 7.4a Fig. 7.5a	Fig. 7.4a* Fig. 7.5b*	— 0.25	— 0.28
g. limestone (9)/ g. limestone (10)	positive	increasing decreasing	Fig. 7.4a Fig. 7.5a	Fig. 7.4a* Fig. 7.5b*	— 0.07	— 0.07
b. limestone (9)/ g. limestone (10)	positive	increasing decreasing	Fig. 7.4a Fig. 7.5a	Fig. 7.4b* Fig. 7.5b*	0.06 0.07	0.07 0.07
b. limestone (22)/ b. dolomite (23)	positive	increasing decreasing	Fig. 7.4a Fig. 7.5a	Fig. 7.4b* Fig. 7.5b*	0.16 0.07	0.17 0.07
g. limestone (22)/ b. dolomite (23)	positive	increasing decreasing	Fig. 7.4a Fig. 7.5a	Fig. 7.4b* Fig. 7.5b*	0.03 0.07	0.03 0.07
g. dolomite (28)/ g. dolomite (29)	negative	increasing decreasing	Fig. 7.5a Fig. 7.4a	Fig. 7.5b Fig. 7.4a*	0.11 —	0.12 —
b. dolomite (28)/ g. dolomite (29)	negative	increasing decreasing	Fig. 7.5a Fig. 7.4a	Fig. 7.5b* Fig. 7.4a*	0.08 —	0.09 —
b. dolomite (31)/ b. limestone (32)	negative	increasing decreasing	Fig. 7.5a Fig. 7.4a	Fig. 7.5b* Fig. 7.4b*	0.11 0.31	0.12 0.33
g. dolomite (31)/ b. limestone (32)	positive	increasing decreasing	Fig. 7.4a Fig. 7.5a	Fig. 7.4b* Fig. 7.5b*	0.05 0.31	0.06 0.33

	$\theta = 22.5°$					
models	R_{pp} at $e = 0$	R_{pp} mono- tonicity	expected pattern	actual pattern	e_{ir}	e_{rr}
b. sand (E5)/ b. sand (E2)	positive	non mono. decreasing	Fig. 7.4 Fig. 7.5	Fig. 7.4b Fig. 7.5b	0.02 0.22	0.04 0.40
g. sand (E5)/ b. sand (E2)	positive	non mono. decreasing	Fig. 7.4 Fig. 7.5	Fig. 7.4a* Fig. 7.5b*	— 0.22	— 0.40
b. limestone (1)/ b. limestone (2)	negative	increasing decreasing	Fig. 7.5 Fig. 7.4	Fig. 7.5b Fig. 7.4b*	0.23 0.17	0.45 0.33
g. limestone (1)/ b. limestone (2)	positive	increasing decreasing	Fig. 7.4 Fig. 7.5	Fig. 7.4b* Fig. 7.5b	0.15 0.17	0.28 0.33
b. shale (B1)/ b. shale (B2)	positive	increasing non mono.	Fig. 7.4 Fig. 7.5	Fig. 7.4b* Fig. 7.5a*	0.20 —	0.38 —
b. shale (G3)/ b. shale (G5)	positive	non mono. non mono.	Fig. 7.4 Fig. 7.5	Fig. 7.4b Fig. 7.5a*	0.07 —	0.11 —
b. shale (E1)/ b. shale (E5)	positive	increasing decreasing	Fig. 7.4 Fig. 7.5	Fig. 7.4b* Fig. 7.5b*	0.92 > 1	— —
b. sand (E5)/ b. shale (E5)	positive	non mono. decreasing	Fig. 7.4 Fig. 7.5	Fig. 7.4b Fig. 7.5b*	0.02 > 1	0.04 —
g. sand (E5)/ b. shale (E5)	positive	non mono. decreasing	Fig. 7.4a Fig. 7.5a	Fig. 7.4a* Fig. 7.5b*	— > 1	— —
g. sand (G8)/ b. sand (G8)	positive	non mono. non mono.	Fig. 7.4 Fig. 7.5	Fig. 7.4a* Fig. 7.5b*	— 0.14	— 0.26
g. sand (G14)/ g. sand (G16)	negative	non mono. non mono.	Fig. 7.5 Fig. 7.4	Fig. 7.5a* Fig. 7.4a*	— —	— —
g. coal (G31)/ b. coal (G31)	positive	non mono. non mono.	Fig. 7.4 Fig. 7.5	Fig. 7.4b Fig. 7.5b*	0.13 0.41	0.31 > 1
g. limestone (9)/ g. limestone (10)	positive	non mono. decreasing	Fig. 7.4 Fig. 7.5	Fig. 7.4a* Fig. 7.5b*	— 0.16	— 0.29
b. limestone (9)/ g. limestone (10)	positive	increasing decreasing	Fig. 7.4 Fig. 7.5	Fig. 7.4b* Fig. 7.5b	0.15 0.16	0.28 0.29
b. limestone (22)/ b. dolomite (23)	positive	increasing decreasing	Fig. 7.4 Fig. 7.5	Fig. 7.4b* Fig. 7.5b*	0.26 0.16	0.54 0.29
g. limestone (22)/ b. dolomite (23)	positive	increasing decreasing	Fig. 7.4 Fig. 7.5	Fig. 7.4b* Fig. 7.5b*	0.11 0.16	0.19 0.29
g. dolomite (28)/ g. dolomite (29)	negative	increasing non mono.	Fig. 7.5 Fig. 7.4	Fig. 7.5b* Fig. 7.4b*	0.20 0.03	0.38 0.06
b. dolomite (28)/ g. dolomite (29)	negative	increasing decreasing	Fig. 7.5 Fig. 7.4	Fig. 7.5b* Fig. 7.4b*	0.18 0.03	0.32 0.06
b. dolomite (31)/ b. limestone (32)	negative	increasing decreasing	Fig. 7.5 Fig. 7.4	Fig. 7.5b Fig. 7.4b*	0.21 0.43	0.41 > 1
g. dolomite (31)/ b. limestone (32)	positive	increasing decreasing	Fig. 7.4 Fig. 7.5	Fig. 7.4b* Fig. 7.5b*	0.14 0.43	0.25 > 1

	$\theta = 30°$					
models	R_{pp} at $e = 0$	R_{pp} monotonicity	expected pattern	actual pattern	e_{ir}	e_{rr}
b. sand (E5)/ b. sand (E2)	positive	non mono. decreasing	Fig. 7.4 Fig. 7.5	Fig. 7.4b Fig. 7.5b	0.09 0.31	0.30 > 1
g. sand (E5)/ b. sand (E2)	positive	non mono. decreasing	Fig. 7.4 Fig. 7.5	Fig. 7.4a* Fig. 7.5b*	— 0.31	— > 1
b. limestone (1)/ b. limestone (2)	negative	increasing decreasing	Fig. 7.5 Fig. 7.4	Fig. 7.5b Fig. 7.4b*	0.32 0.26	> 1 > 1
g. limestone (1)/ b. limestone (2)	positive	increasing decreasing	Fig. 7.4 Fig. 7.5	Fig. 7.4b* Fig. 7.5b	0.24 0.26	> 1 > 1
b. shale (B1)/ b. shale (B2)	positive	increasing non mono.	Fig. 7.4 Fig. 7.5	Fig. 7.4b* Fig. 7.5b	0.29 0.06	> 1 0.19
b. shale (G3)/ b. shale (G5)	negative	non mono. non mono.	Fig. 7.5 Fig. 7.4	Fig. 7.5b* none	0.15 0.01	— 0.02
b. shale (E1)/ b. shale (E5)	positive	increasing decreasing	Fig. 7.4 Fig. 7.5	Fig. 7.4b* Fig. 7.5b*	> 1 > 1	— —
b. sand (E5)/ b. shale (E5)	positive	non mono. decreasing	Fig. 7.4 Fig. 7.5	Fig. 7.4b Fig. 7.5b*	0.09 > 1	0.30 —
g. sand (E5)/ b. shale (E5)	positive	non mono. decreasing	Fig. 7.4 Fig. 7.5	Fig. 7.4a* Fig. 7.5b*	— > 1	— —
g. sand (G8)/ b. sand (G8)	positive	non mono. non mono.	Fig. 7.4 Fig. 7.5	Fig. 7.4b* Fig. 7.5b	0.02 0.22	0.04 > 1
g. sand (G14)/ g. sand (G16)	negative	non mono. decreasing	Fig. 7.5 Fig. 7.4	Fig. 7.5b* Fig. 7.4b	0.03 0.01	0.06 0.03
g. coal (G31)/ b. coal (G31)	positive	non mono. non mono.	Fig. 7.4 Fig. 7.5	Fig. 7.4b Fig. 7.5b*	0.24 0.56	> 1 —
g. limestone (9)/ g. limestone (10)	positive	increasing decreasing	Fig. 7.4 Fig. 7.5	Fig. 7.4b* Fig. 7.5b*	0.02 0.24	0.07 > 1
b. limestone (9)/ g. limestone (10)	positive	increasing decreasing	Fig. 7.4 Fig. 7.5	Fig. 7.4b* Fig. 7.5b	0.24 0.24	> 1 > 1
b. limestone (22)/ b. dolomite (23)	positive	increasing decreasing	Fig. 7.4 Fig. 7.5	Fig. 7.4b* Fig. 7.5b*	0.36 0.24	> 1 > 1
g. limestone (22)/ b. dolomite (23)	positive	increasing non mono.	Fig. 7.4 Fig. 7.5	Fig. 7.4b* Fig. 7.5b*	0.19 0.24	0.76 > 1
g. dolomite (28)/ g. dolomite (29)	negative	increasing non mono.	Fig. 7.5 Fig. 7.4	Fig. 7.5b* Fig. 7.4b	0.29 0.11	> 1 0.32
b. dolomite (28)/ g. dolomite (29)	negative	non mono. decreasing	Fig. 7.5 Fig. 7.4	Fig. 7.5b* Fig. 7.4b*	0.27 0.11	> 1 0.32
b. dolomite (31)/ b. limestone (32)	negative	increasing decreasing	Fig. 7.5 Fig. 7.4	Fig. 7.5b Fig. 7.4b*	0.31 0.56	> 1 > 1
g. dolomite (31)/ b. limestone (32)	positive	increasing decreasing	Fig. 7.4 Fig. 7.5	Fig. 7.4b* Fig. 7.5b*	0.22 0.56	> 1 > 1

	$\theta = 37.5°$					
models	R_{pp} at $e = 0$	R_{pp} monotonicity	expected pattern	actual pattern	e_{ir}	e_{rr}
b. sand (E5)/ b. sand (E2)	positive	non mono. decreasing	Fig. 7.4b Fig. 7.5b	Fig. 7.4b* Fig. 7.5b*	0.19 0.45	— —
g. sand (E5)/ b. sand (E2)	positive	non mono. decreasing	Fig. 7.4b Fig. 7.5b	Fig. 7.4b Fig. 7.5b*	0.04 0.45	0.23 —
b. limestone (1)/ b. limestone (2)	negative	increasing decreasing	Fig. 7.5b Fig. 7.4b	Fig. 7.5b* Fig. 7.4b*	0.47 0.40	— —
g. limestone (1)/ b. limestone (2)	positive	increasing decreasing	Fig. 7.4b Fig. 7.5b	Fig. 7.4b* Fig. 7.5b*	0.37 0.40	— —
b. shale (B1)/ b. shale (B2)	positive	increasing non mono.	Fig. 7.4b Fig. 7.5b	Fig. 7.4b Fig. 7.5b*	0.43 0.16	— —
b. shale (G3)/ b. shale (G5)	negative	non mono. non mono.	Fig. 7.5b Fig. 7.4b	Fig. 7.5b* Fig. 7.4b	0.27 0.10	— > 1
b. shale (E1)/ b. shale (E5)	positive	increasing decreasing	Fig. 7.4b Fig. 7.5b	Fig. 7.4b Fig. 7.5b*	> 1 > 1	— —
b. sand (E5)/ b. shale (E5)	positive	non mono. decreasing	Fig. 7.4b Fig. 7.5b	Fig. 7.4b* Fig. 7.5b*	0.19 > 1	— —
g. sand (E5)/ b. shale (E5)	positive	non mono. decreasing	Fig. 7.4b Fig. 7.5b	Fig. 7.4b* Fig. 7.5b*	0.04 > 1	0.23 —
g. sand (G8)/ b. sand (G8)	positive	increasing non mono.	Fig. 7.4b Fig. 7.5b	Fig. 7.4b Fig. 7.5b*	0.11 0.35	> 1 —
g. sand (G14)/ g. sand (G16)	negative	non mono. decreasing	Fig. 7.5b Fig. 7.4b	Fig. 7.5b* Fig. 7.4b	0.12 0.11	> 1 > 1
g. coal (G31)/ b. coal (G31)	positive	non mono. non mono.	Fig. 7.4b Fig. 7.5b	Fig. 7.4b Fig. 7.5b*	0.41 0.78	— —
g. limestone (9)/ g. limestone (10)	positive	increasing decreasing	Fig. 7.4b Fig. 7.5b	Fig. 7.4b* Fig. 7.5b*	0.11 0.38	> 1 —
b. limestone (9)/ g. limestone (10)	positive	increasing decreasing	Fig. 7.4b Fig. 7.5b	Fig. 7.4b* Fig. 7.5b*	0.38 0.38	— —
b. limestone (22)/ b. dolomite (23)	positive	increasing decreasing	Fig. 7.4b Fig. 7.5b	Fig. 7.4b* Fig. 7.5b*	0.52 0.38	— —
g. limestone (22)/ b. dolomite (23)	positive	increasing decreasing	Fig. 7.4b Fig. 7.5b	Fig. 7.4b* Fig. 7.5b*	0.31 0.38	— —
g. dolomite (28)/ g. dolomite (29)	negative	increasing decreasing	Fig. 7.5b Fig. 7.4b	Fig. 7.5b* Fig. 7.4b*	0.44 0.21	— —
b. dolomite (28)/ g. dolomite (29)	negative	increasing decreasing	Fig. 7.5b Fig. 7.4b	Fig. 7.5b* Fig. 7.4b*	0.41 0.21	— —
b. dolomite (31)/ b. limestone (32)	positive	increasing decreasing	Fig. 7.4b Fig. 7.5b	Fig. 7.4b Fig. 7.5b*	0.46 0.76	— —
g. dolomite (31)/ b. limestone (32)	positive	increasing decreasing	Fig. 7.4b Fig. 7.5b	Fig. 7.4b* Fig. 7.5b*	0.35 0.76	— —

	$\theta = 45°$					
models	R_{pp} at $e = 0$	R_{pp} monotonicity	expected pattern	actual pattern	e_{ir}	e_{rr}
b. sand (E5)/ b. sand (E2)	positive	increasing decreasing	Fig. 7.4b Fig. 7.5b	Fig. 7.4b Fig. 7.5b	0.35 0.69	— > 1
g. sand (E5)/ b. sand (E2)	positive	increasing decreasing	Fig. 7.4b Fig. 7.5b	Fig. 7.4b* Fig. 7.5b*	0.21 0.69	— —
b. limestone (1)/ b. limestone (2)	negative	increasing decreasing	Fig. 7.5b Fig. 7.4b	Fig. 7.5b* Fig. 7.4b	0.71 0.62	— —
g. limestone (1)/ b. limestone (2)	positive	increasing decreasing	Fig. 7.4b Fig. 7.5b	Fig. 7.4b Fig. 7.5b*	0.58 0.62	— —
b. shale (B1)/ b. shale (B2)	negative	increasing non mono.	Fig. 7.5b Fig. 7.4b	Fig. 7.5b* Fig. 7.4b	0.66 0.32	— —
b. shale (G3)/ b. shale (G5)	negative	increasing non mono.	Fig. 7.5b Fig. 7.4b	Fig. 7.5b* Fig. 7.4b	0.46 0.24	— —
b. shale (E1)/ b. shale (E5)	positive	increasing decreasing	Fig. 7.4b Fig. 7.5b	Fig. 7.4b Fig. 7.5b*	> 1 > 1	— —
b. sand (E5)/ b. shale (E5)	positive	non mono. decreasing	Fig. 7.4b Fig. 7.5b	Fig. 7.4b* Fig. 7.5b*	0.35 > 1	— —
g. sand (E5)/ b. shale (E5)	positive	non mono. decreasing	Fig. 7.4b Fig. 7.5b	Fig. 7.4b* Fig. 7.5b*	0.15 > 1	— —
g. sand (G8)/ b. sand (G8)	positive	increasing decreasing	Fig. 7.4b Fig. 7.5b	Fig. 7.4b* Fig. 7.5b*	0.24 0.55	— —
g. sand (G14)/ g. sand (G16)	negative	non mono. decreasing	Fig. 7.5b Fig. 7.4b	Fig. 7.5b* Fig. 7.4b	0.26 0.24	— —
g. coal (G31)/ b. coal (G31)	positive	increasing decreasing	Fig. 7.4b Fig. 7.5b	Fig. 7.4b Fig. 7.5b*	0.66 > 1	— —
g. limestone (9)/ g. limestone (10)	positive	increasing decreasing	Fig. 7.4b Fig. 7.5b	Fig. 7.4b* Fig. 7.5b*	0.25 0.59	— —
b. limestone (9)/ g. limestone (10)	positive	increasing decreasing	Fig. 7.4b Fig. 7.5b	Fig. 7.4b Fig. 7.5b*	0.60 0.59	— —
b. limestone (22)/ b. dolomite (23)	positive	increasing decreasing	Fig. 7.4b Fig. 7.5b	Fig. 7.4b Fig. 7.5b*	0.78 0.60	— —
g. limestone (22)/ b. dolomite (23)	positive	increasing decreasing	Fig. 7.4b Fig. 7.5b	Fig. 7.4b* Fig. 7.5b*	0.50 0.60	— —
g. dolomite (28)/ g. dolomite (29)	negative	increasing decreasing	Fig. 7.5b Fig. 7.4b	Fig. 7.5b* Fig. 7.4b	0.68 0.39	— —
b. dolomite (28)/ g. dolomite (29)	negative	increasing decreasing	Fig. 7.5b Fig. 7.4b	Fig. 7.5b* Fig. 7.4b*	0.63 0.39	— —
b. dolomite (31)/ b. limestone (32)	positive	increasing decreasing	Fig. 7.4b Fig. 7.5b	Fig. 7.4b Fig. 7.5b*	0.71 > 1	— —
g. dolomite (31)/ b. limestone (32)	positive	increasing decreasing	Fig. 7.4b Fig. 7.5b	Fig. 7.4b* Fig. 7.5b*	0.56 > 1	— —

7.B Matlab code

```
%  This code computes azimuthaly-dependent reflection
   coefficient using Vavrycuk-Psencik approximation.
   Both VTI halfspaces may have vertical cracks aligned
   along the x1-axis. Code uses matlab functions.
%%% INPUTS %%%
% e    - crack density of an upper halfspace
% e_L  - crack density of a lower halfspace
% C##b - background stiffnesses of a VTI (or isotropic)
   upper halfspace
% L##b - background stiffnesses of a VTI (or isotropic)
   lower halfspace
% ro   - density of an upper halfspace
% ro_L - density of a lower halfspace
% x    - incidence angle
% y    - azimuthal angle
%%% OUTPUTS %%%
% C##  - effective stiffnesses of an upper halfspace
% L##  - effective stiffnesses of a lower halfspace
% Ripp - isotropic part of the PP refl. coeff.
% Rpp  - Vavrycuk-Psencik approximated PP refl. coeff.
%%% MAIN CODE %%%
[C11,C22,C33,C44,C55,C66,C12,C13,C23,L11,L22,L33,L44,L55,L66
   ,L12,L13,L23]=fun_eff(e,e_L,C11b,C33b,C44b,C66b,C13b,L11b
   ,L33b,L44b,L66b,L13b);
```

```
[Ripp,Rpp]=fun_Rpp_approx(x,y,ro,ro_L,C11,C22,C33,C44,C55,
    C66,C12,C13,C23,L11,L22,L33,L44,L55,L66,L12,L13,L23);
%%% FUNCTIONS %%%
function [C11,C22,C33,C44,C55,C66,C12,C13,C23,L11,L22,L33,
    L44,L55,L66,L12,L13,L23]=fun_eff(e,e_L,C11b,C33b,C44b,
    C66b,C13b,L11b,L33b,L44b,L66b,L13b)
% obtain effective stiffnesses of an upper halfspace
C1=sqrt(C11b*C33b);
C2=sqrt(C66b/C44b);
C3=sqrt(((C1-C13b)*(C1+C13b+2*C44b))/(C33b*C44b));
C4=2*C44b*C3/(C1+C13b+2*C44b);
ZN=8*C3*e/(3*C1*(1-((C13b^2)/(C1^2))));
ZT=16*e/(3*C44b*(C2+C3-C4));
delN=ZN*C11b/(1+ZN*C11b);
delT1=ZT*C44b/(1+ZT*C44b);
delT2=ZT*C66b/(1+ZT*C66b);
C11=C11b*(1-delN);
C22=C11b*(1-delN*(((C11b-2*C66b)^2)/(C11b^2)));
C33=C33b*(1-delN*((C13b^2)/(C11b*C33b)));
C12=(C11b-2*C66b)*(1-delN);
C13=C13b*(1-delN);
C23=C13b*(1-delN*(((C11b-2*C66b))/C11b));
C44=C44b; C55=C44b.*(1-delT1); C66=C66b.*(1-delT2);
% obtain effective stiffnesses of a lower halfspace
L1=sqrt(L11b*L33b);
```

```
L2=sqrt(L66b/L44b);
L3=sqrt(((L1-L13b)*(L1+L13b+2*L44b))/(L33b*L44b));
L4=2*L44b*L3/(L1+L13b+2*L44b);
ZN_L=8*L3*e_L/(3*L1*(1-((L13b^2)/(L1^2))));
ZT_L=16*e_L/(3*L44b.*(L2+L3-L4));
delN_L=ZN_L*L11b/(1+ZN_L*L11b);
delT1_L=ZT_L*L44b/(1+ZT_L*L44b);
delT2_L=ZT_L*L66b/(1+ZT_L*L66b);
L11=L11b*(1-delN_L);
L22=L11b*(1-delN_L*(((L11b-2*L66b)^2)/(L11b^2)));
L33=L33b*(1-delN_L*((L13b^2)/(L11b*L33b)));
L12=(L11b-2*L66b)*(1-delN_L);
L13=L13b*(1-delN_L);
L23=L13b*(1-delN_L*(((L11b-2*L66b))/L11b));
L44=L44b; L55=L44b.*(1-delT1_L); L66=L66b.*(1-delT2_L);
end
function [Ripp,Rpp]=fun_Rpp_approx(x,y,ro,ro_L,C11,C22,C33,
    C44,C55,C66,C12,C13,C23,L11,L22,L33,L44,L55,L66,L12,L13,
    L23);
% obtain the PP refl. coeff. approximation using effective
    stiffnesses
Vp=sqrt((C33)/ro); Vp_L=sqrt((L33)/ro_L);
Vs=sqrt((C55)/ro); Vs_L=sqrt((L55)/ro_L);
mVp=0.5*(Vp_L+Vp); mVs=0.5*(Vs_L+Vs); dVp=Vp_L-Vp;
Z=ro*Vp; Z_L=ro_L*Vp_L; dZ=Z_L-Z; mZ=0.5*(Z_L+Z);
```

```
G=ro*Vs^2; G_L=ro_L*Vs_L^2; dG=G_L-G; mG=0.5*(G_L+G);
for j=1:length(x)
for i=1:length(y)
Ripp(j)=0.5.*dZ./mZ+0.5.*(dVp./mVp).*tand(x(j)).^2 -2.*(dG./
    mG).*(mVs./mVp).^2.*sind(x(j)).^2;
Rapp1(i)=cosd(y(i)).^2.*(((L13+2.*L55-L33)./L33)-((C13+2.*
    C55-C33)./C33))+sind(y(i)).^2.*(((((L23+2.*L44-L33)./L33)
    -((C23+2.*C44-C33)./C33))) -8.*(((L44-L55)./(2.*L33))-((
    C44-C55)./(2.*C33))));
Rapp2(i)=cosd(y(i)).^4.*(((L11-L33)./(2.*L33))-((C11-C33)
    ./(2.*C33)))+sind(y(i)).^4.*(((L22-L33)./(2.*L33))-((C22-
    C33)./(2.*C33)))+sind(y(i)).^2.*cosd(y(i)).^2.*(((L12+2.*
    L66-L33)./L33)-((C12+2.*C66-C33)./C33));
Rpp(j,i)=Ripp(j)+0.5.*sind(x(j)).^2.*Rapp1(i)+0.5.*sind(x(j)
    ).^2.*tand(x(j)).^2.*Rapp2(i);
end; end; end
```

Chapter 8

Summary

In the thesis that consists of six research papers, we have studied the elastic anisotropy of layered or cracked materials using alternative parameterisation. Our investigation has contributed mainly to the area of seismology and micromechanics. However, particular findings can also be useful in engineering sciences or exploration geophysics.

In Chapters 2–3, we have discussed the anisotropy induced by layered media in the context of the Backus average. First, we have focused on a typical scenario of isotropic layers that result in a transversely isotropic medium. A careful numerical study of the effective anisotropy parameters has allowed us to approach the inverse problem and infer elastic information on the isotropic constituents. In turn, the knowledge of the layers' elastic properties can lead to fluid detection. According to Gassmann (1951) fluids affect Lamé coefficient λ, but not rigidity μ; hence, large variations of λ in layers can indicate the fluid's presence. We have proposed an anisotropy parameter φ that is more sensitive to λ fluctuations than the other traditional anisotropy parameters are. Specific absolute values of φ that may be estimated from macroscale seismic surveys can correspond to particular λ variations attainable from microscale well-log measurements. Therefore, if we have access to seismic—but not well-log—data, then φ can be treated as a fluid indicator. The above-mentioned conclusions on the elastic behaviour of effective media are reasonable if the Backus average provides empirically adequate results. Therefore, we have discussed the only mathematical assumption of this homogenisation tool—the product approximation. We have allowed the layers to exhibit lower symmetries that the isotropic one. It occurred that the product approximation can be mathematically incorrect in case of negative Poisson's ratio present in some layers. We have shown that such a situation is not unlikely to happen in practice. However, the aforementioned mathematical inaccuracy does not influence the results in a meaningful manner; hence, the average is physically accurate. During the analysis, we have additionally demonstrated that the averaging of cubic layers results in an effective medium with tetragonal (not cubic) symmetry. Also, we have presented concise formulations of stability conditions for low symmetry classes, such as trigonal, orthotropic, and monoclinic.

In Chapters 4–5, we have investigated cracked materials from the macro perspective. In other words, we have considered a homogenised effective medium that exhibits an orthotropic material symmetry. The elastic anisotropy has been regarded in the context of P-wave phase velocity, relations among stiffnesses, and fluid detection. We have analysed the contributions of each elasticity parameter to the difference in squared P-wave velocity propagating along mutually perpendicular planes. Such planes can correspond to the crack surfaces. It occurred that the aforementioned difference, s^2, is twice more dependent on shear moduli than on C_{13} and C_{23} stiffnesses. Anomalously high s^2 can be caused by large values of shear moduli and relatively small values of C_{33}; such a situation is typical for gas-saturated rocks. Further, contributions of each stiffness to P-wave velocity propagating in any direction can be well described by the cumulative moduli. They show the analogy to Lamé coefficients but are designed for orthotropic, not isotropic, media. In turn, cumulative moduli can be used to predict P-wave velocity for any incidence and azimuth angle, knowing less than required nine elasticity parameters. The significant discrepancy between estimated and true velocity may indicate anomalous P/S ratio characteristic of gas presence in rocks. Additionally, we have used the aforementioned moduli to propose a universal, strong anisotropy approximation of P-wave velocity for cubic media.

In Chapters 6–7, we have focused on the cracked media in the context of homogenisation techniques, azimuthal variations of amplitude, inverse problem, and fluid detection. We have proposed an alternative homogenisation method to describe better the effective properties of many parallel fractures embedded in the background material. Our approach is similar to the linear-slip method of Schoenberg and Douma (1988). We also utilise Backus average; however, we represent dense fractures by a thin layer instead of infinitesimal planes. In other words, we relax the assumptions of infinite weakness and marginal thickness of a layer so that it does not correspond to the linear-slip plane. Hence, our method is the generalisation of the Schoenberg and Douma (1988) approach; it can be used to describe a medium with any number of parallel cracks. The advantage of our generalised method becomes apparent if cracks occupy more than one per cent of the medium's space. Also, we have discussed the effect of crack concentration on the PP-wave reflection coefficient. The azimuthal variations of amplitude occur not to change in the same manner for the increasing crack density. The change depends on the cracks orientation, incidence angle, and elasticity parameters of the cracked material (influenced by the fluid saturation). To obtain meaningful results, we have assumed a single set of vertical cracks parallel to the x_1-axis embedded in either isotropic or anisotropic background. We have recognised changes (caused by the growing crack concentration) typical for small incidence and gas saturation, and schemes characteristic for large incidence and brine-bearing materials. Certain azimuthal variations (sign and shape) are present solely in the patterns typical for gas saturation. We have separated eight shapes characteristic for cracks situated in the gas-bearing halfspace. Unfortunately, specific shapes are identical for various combinations of crack concentration, stiffnesses, and incidence angles; therefore, the inverse problem is complicated to solve, even if we know the orientation of fractures.

To conclude, this thesis provides fresh insight into the elastic description of layered or cracked materials and their response to seismic waves. Readers that are interested in viewing such materials in the context of exploration geophysics or fluid detection can find a number of novelties regarding these topics. The following approaches are worth considering: the φ method (Chapter 2), verification of s^2 values (Chapter 4), comparison of true and estimated P-wave velocities using cumulative module υ (Chapter 5), or identification of the azimuthal shapes characteristic for gas-bearing rocks (Chapter 7). Researchers who are involved into homogenisation techniques may be interested in: the relationship between inhomogeneity and anisotropy in Backus average (Chapter 2 and Appendix A), the discussion of the Backus averaging procedure and the related problematic cases (Chapter 3), or the generalised Schoenberg-Douma method (Chapter 6). Readers who look at inverse problems from an alternative, non-Bayesian, perspective should appreciate methods presented in Chapter 2 and Chapter 7. Furthermore, material engineers may find useful a part of Chapter 3, devoted to auxetic materials and stability conditions for low symmetry classes.

There is still plenty of work to do in the future. All methods and findings from this document have a theoretical background and are supported by the numerical experiments, but it might be beneficial—especially for the approaches related to fluid detection—to test them also in the real-data cases. Moreover, the methods proposed in Chapters 4–5 can be expanded to S-waves and ray velocities. Further, analysis from Chapter 7 may be augmented to the other (than PP-wave) reflection or transmission coefficients. Also, different orientations of cracks can be examined.

In this document, we have approached only a few aspects related to layered or cracked media. We have tried to propose new, alternative methods rather than follow and improve the old ones. We are aware of the vastness of the elastic anisotropy field. We do not expect this thesis to be a milestone in the area mentioned above. Nevertheless, we hope that findings presented in the discussed research papers will contribute to the better understanding of elastic anisotropy, in general, and layered or cracked media, in particular.

Appendix A

On effects of inhomogeneity on anisotropy in Backus average*

Abstract

In general, the Backus average of an inhomogeneous stack of isotropic layers is a transversely isotropic medium. Herein, we examine a relation between this inhomogeneity and the strength of resulting anisotropy, and show that, in general, they are proportional to one another. There is an important case, however, in which the Backus average of isotropic layers results in an isotropic—as opposed to a transversely isotropic—medium. We show that it is a consequence of the same rigidity of layers, regardless of their compressibility. Thus, in general, the strength of anisotropy of the Backus average increases with the degree of inhomogeneity among layers, except for the case in which all layers exhibit the same rigidity.

*This appendix consists of the original research paper and the post-publication comments. Herein, we invoke the following paper: Adamus, F. P., Slawinski, M. A., and Stanoev, T. (2018). "On effects of inhomogeneity on anisotropy in Backus average". *arXiv*, 1802.04075v3 [physics.geo-ph].

A.1 Introduction

A.1.1 Backus average

In this paper, we discuss the Backus (1962) average of isotropic layers as a measure of inhomogeneity of these layers. Herein, the Backus (1962) average results in a homogeneous transversely isotropic medium. Each isotropic layer is defined by the density-scaled elasticity parameters, c_{1111} and c_{2323}. The corresponding five parameters of the transversely isotropic medium are

$$c_{1111}^{\overline{\mathrm{TI}}} = \overline{\left(\frac{c_{1111} - 2c_{2323}}{c_{1111}}\right)}^{2}\ \overline{\left(\frac{1}{c_{1111}}\right)}^{-1} + \overline{\left(\frac{4(c_{1111} - c_{2323})c_{2323}}{c_{1111}}\right)}, \tag{A.1}$$

$$c_{1133}^{\overline{\mathrm{TI}}} = \overline{\left(\frac{c_{1111} - 2c_{2323}}{c_{1111}}\right)}\ \overline{\left(\frac{1}{c_{1111}}\right)}^{-1}, \tag{A.2}$$

$$c_{1212}^{\overline{\mathrm{TI}}} = \overline{c_{2323}}\,, \tag{A.3}$$

$$c_{2323}^{\overline{\mathrm{TI}}} = \overline{\left(\frac{1}{c_{2323}}\right)}^{-1}, \tag{A.4}$$

$$c_{3333}^{\overline{\mathrm{TI}}} = \overline{\left(\frac{1}{c_{1111}}\right)}^{-1}. \tag{A.5}$$

Herein, the bar indicates an average, which is defined by Backus (1962) as

$$\overline{f}(x_3) = \int_{-\infty}^{\infty} w(\xi - x_3) f(\xi)\,\mathrm{d}\xi\,, \tag{A.6}$$

where the weight, $w(x_3)$, allows us the use of many functions, since the conditions imposed on it are not restrictive. w is required to be a continuous nonnegative function tending to zero at infinities and to exhibit the following properties:

$$\int_{-\infty}^{\infty} w(x_3)\,\mathrm{d}x_3 = 1\,,$$

$$\int_{-\infty}^{\infty} x_3\,w(x_3)\,\mathrm{d}x_3 = 0 \qquad \text{and} \qquad \int_{-\infty}^{\infty} x_3^2\,w(x_3)\,\mathrm{d}x_3 = \ell'^{\,2}\,,$$

where ℓ' denotes the width of the stack of parallel layers. Readers interested in further details of the Backus (1962) average might refer to Bos et al. (2017, 2018).

A.1.2 Thomsen parameters

To examine the strength of anisotropy of a transversely isotropic homogeneous medium, we invoke Thomsen (1986) parameters,

$$\gamma := \frac{c_{1212}^{\overline{\mathrm{TI}}} - c_{2323}^{\overline{\mathrm{TI}}}}{2\,c_{2323}^{\overline{\mathrm{TI}}}}\,, \tag{A.7}$$

$$\delta := \frac{\left(c_{1133}^{\overline{\mathrm{TI}}} + c_{2323}^{\overline{\mathrm{TI}}}\right)^2 - \left(c_{3333}^{\overline{\mathrm{TI}}} - c_{2323}^{\overline{\mathrm{TI}}}\right)^2}{2\,c_{3333}^{\overline{\mathrm{TI}}}\left(c_{3333}^{\overline{\mathrm{TI}}} - c_{2323}^{\overline{\mathrm{TI}}}\right)}\,, \tag{A.8}$$

$$\epsilon := \frac{c_{1111}^{\overline{\mathrm{TI}}} - c_{3333}^{\overline{\mathrm{TI}}}}{2\,c_{3333}^{\overline{\mathrm{TI}}}}\,. \tag{A.9}$$

A quantitative measure on the strength of anisotropy is given by the absolute values of these parameters. In the case of isotropy, they are zero.

A.2 Effects of inhomogeneity on anisotropy

A.2.1 Alternating layers: Anisotropic medium

In the context of the Backus (1962) average, Thomsen (1986) parameters can be also used to infer the effects of inhomogeneity between layers. In general, as the inhomogeneity within a stack of layers increases, so does the anisotropy of the medium.

To exemplify this increase, let us consider a stack of identical isotropic layers. To introduce inhomogeneity, we multiply the two elasticity parameters of every second layer by a; we obtain c_{1111}, c_{2323} and $a\,c_{1111}$, $a\,c_{2323}$, for the adjacent layers. Using, for such a model, expressions (A.1)–(A.5), we obtain the parameters of a transversely isotropic medium, $c^{\overline{\rm TI}}_{ijk\ell}$, which, in turn, we use in expressions (A.7)–(A.9) to obtain

$$\gamma = \frac{(a-1)^2}{8\,a}\,, \tag{A.10}$$

$$\delta = 0\,,$$

$$\epsilon = \frac{(a-1)^2\,(c_{1111}-c_{2323})\,c_{2323}}{2\,a\,c_{1111}^2}\,. \tag{A.11}$$

In contrast to parameters (A.7) and (A.9), in general, their counterparts (A.10) and (A.11), for this model, can be only nonnegative. Also, $\delta=0$ is a consequence of alternating layers whose both parameters are scaled by the same value of a; it is not a general property for alternating isotropic layers in the context of the Backus (1962) average.

If $a=1$, which means that all layers are the same, then also $\gamma=\epsilon=0$; hence, in such a case, the averaged medium is isotropic, as expected. If $a\to 0$ or $a\to\infty$, which is tantamount to increasing inhomogeneity between layers, then γ and ϵ tend to infinity; in such a case, the averaged medium is extremely anisotropic.

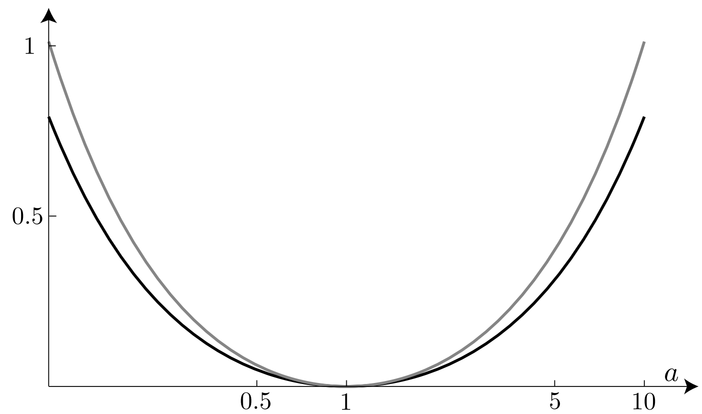

Figure A.1: Anisotropy of the Backus (1962) average as a function of layer inhomogeneity: Thomsen (1986) parameters, γ and ϵ, plotted as grey and black lines, respectively, against logarithmic values of $a \in \left(10^{-1}, 10^{1}\right)$.

To illustrate the relationship between inhomogeneity and anisotropy, let us consider a numerical example. We use $c_{1111} = 12.15$ and $c_{2323} = 3.24$, which are density-scaled elasticity parameters that correspond to sandstone. Their SI units are $\mathrm{km}^2/\mathrm{s}^2$, and their square roots are P-wave and S-wave speeds, respectively. Figure A.1 illustrates a monotonic increase in anisotropy of the averaged medium with an increase of inhomogeneity between layers. At $a = 1$, which means that all layers are the same, $\gamma = \epsilon = 0$. As a tends to zero or to infinity, γ and ϵ tend to infinity. For $a \in (10^{-1}, 10^{0})$, the values of the elasticity parameters of the alternating layer are progressively diminished by up to one order of magnitude; for $a \in (10^{0}, 10^{1})$, they are progressively increased by up to one order.

For the SH and qP waves, respectively, γ and ϵ are measures of difference between propagation speeds along, and perpendicular to, the layers,

$$\frac{v_{\parallel}^2 - v_{\perp}^2}{2\, v_{\perp}^2}\,.$$

Parameter δ, whose definition does not have such a geometrical interpretation, remains equal to zero. If, however, the elasticity parameters of the alternate layers are $a\, c_{1111}$ and

$\sqrt{a}\, c_{2323}$, δ asymptotically approaches a finite value, as a tends to infinity; γ and ϵ still tend to infinity and, as such, they are symptomatic of inhomogeneity among layers.

As illustrated in Figure A.1, for a stack of isotropic layers, the strength of anisotropy of the resulting transversely isotropic medium is solely a function of inhomogeneity of that stack. In other words, herein, the strength of anisotropy is a measure of inhomogeneity.

A rather slow increase of values of γ and ϵ as functions of a supports the adequacy of weakly anisotropic models in many quantitative studies in seismology. Herein, according to the Backus (1962) average, even moderately inhomogeneous alternating layers result only in a weakly anisotropic medium.

A.2.2 Isotropic layers: Isotropic medium

Even though, in general, isotropic layers result—by the Backus (1962) average—in a transversely isotropic medium, there exists a case for which inhomogeneity of the stack of isotropic layers results in an isotropic medium. In such a case, the inhomogeneity among layers is expressed only by differences in c_{1111} ; c_{2323} remains constant. Backus (1962, Section 6) states that

> if a layered isotropic medium has constant μ , the STILWE medium is isotropic.[†]
>
> This much was proved by Postma (1955) for periodic two-layered media.

Let us examine such a case. Following expressions (A.1)–(A.5), and using a symbolic-calculation software—without any assumption of periodicity (Postma, 1955, p. 788)—we

[†] In this quote, $\mu \equiv c_{2323}$ and STILWE stands for smoothed, transversely isotropic, long-wave equivalent.

obtain,

$$c_{1111}^{\overline{\mathrm{TI}}} = \overline{\left(\frac{1}{c_{1111}}\right)}^{-1}, \tag{A.12}$$

$$c_{1133}^{\overline{\mathrm{TI}}} = \overline{\left(\frac{1}{c_{1111}}\right)}^{-1} - 2c_{2323}\,, \tag{A.13}$$

$$c_{1212}^{\overline{\mathrm{TI}}} = c_{2323}\,, \tag{A.14}$$

$$c_{2323}^{\overline{\mathrm{TI}}} = c_{2323}\,, \tag{A.15}$$

$$c_{3333}^{\overline{\mathrm{TI}}} = \overline{\left(\frac{1}{c_{1111}}\right)}^{-1}, \tag{A.16}$$

respectively. Since $c_{1111}^{\overline{\mathrm{TI}}} = c_{3333}^{\overline{\mathrm{TI}}}$, $c_{1212}^{\overline{\mathrm{TI}}} = c_{2323}^{\overline{\mathrm{TI}}}$ and $c_{1133}^{\overline{\mathrm{TI}}} = c_{1111}^{\overline{\mathrm{TI}}} - 2\,c_{2323}^{\overline{\mathrm{TI}}}$, the medium is isotropic.

In view of the mechanical interpretation of c_{1111} and c_{2323} (e.g., Slawinski, 2015, Section 5.12.4), expressed in terms of the Lamé parameters, this result shows that the anisotropy of the Backus (1962) average is not a consequence of inhomogeneity, in general, but of the difference in the rigidity among the layers. The difference in compressibility alone does not result in an anisotropic medium.

In terms of wave propagation, the speed of a shear wave, $v_S^2 = c_{2323}^{\overline{\mathrm{TI}}} = c_{2323}$, depends on rigidity, which is constant, and the speed of a pressure wave, $v_P^2 = c_{1111}^{\overline{\mathrm{TI}}}$, on the average compressibility. Since, as shown by Rochester (2010), in the context of the necessary and sufficient conditions, the shear wave is due to an equivoluminal deformation, $\nabla\times u$, and the pressure wave is due to dilatation, $\nabla\cdot u$, where u stands for displacement, it is reasonable to expect anisotropy to originate in a vectorial, not a scalar, quantity.

A.2.3 Transversely isotropic layers: Isotropic medium

Even though, in general, transversely isotropic layers result, by the Backus (1962) average, in a transversely isotropic medium, there exists a case for which inhomogeneity of the stack of transversely isotropic layers results in an isotropic medium. Let us examine such a case.

Lemma A.2.1. *A transversely isotropic tensor with* $c_{1111} = c_{3333}$, $c_{1133} = c_{1111} - 2c_{2323}$, $c_{1212} \neq c_{2323}$ *and* c_{2323} *being constant is transversely isotropic.*

Proof. Consider

$$C = \begin{bmatrix} c_{1111} & c_{1111}-2c_{1212} & c_{1111}-2c_{2323} & 0 & 0 & 0 \\ c_{1111}-2c_{1212} & c_{1111} & c_{1111}-2c_{2323} & 0 & 0 & 0 \\ c_{1111}-2c_{2323} & c_{1111}-2c_{2323} & c_{1111} & 0 & 0 & 0 \\ 0 & 0 & 0 & 2c_{2323} & 0 & 0 \\ 0 & 0 & 0 & 0 & 2c_{2323} & 0 \\ 0 & 0 & 0 & 0 & 0 & 2c_{1212} \end{bmatrix}.$$

Its eigenvalues are

$$\lambda_1 = \tfrac{3}{2}c_{1111} - c_{1212} - \frac{\sqrt{9c_{1111}^2 - 32c_{1111}c_{2323} - 4c_{1111}c_{1212} + 32c_{2323}^2 + 4c_{1212}^2}}{2},$$

$$\lambda_2 = \tfrac{3}{2}c_{1111} - c_{1212} + \frac{\sqrt{9c_{1111}^2 - 32c_{1111}c_{2323} - 4c_{1111}c_{1212} + 32c_{2323}^2 + 4c_{1212}^2}}{2},$$

$$\lambda_3 = \lambda_4 = 2c_{2323},$$

$$\lambda_5 = \lambda_6 = 2c_{1212},$$

which—due to the eigenvalue multiplicities—implies that C is a transversely isotropic tensor (Bóna et al., 2007), as required. □

Proposition A.2.1. *The Backus (1962) average of a stack of transversely isotropic layers with $c_{1111} = c_{3333}$, $c_{1133} = c_{1111} - 2c_{2323}$, $c_{1212} \neq c_{2323}$ and c_{2323} being constant (Lemma A.2.1), can result—depending on the values of parameters—in an isotropic medium.*

Proof. In general, the Backus (1962) average of transversely isotropic layers is (e.g., Slawinski, 2016, Section 4.2.3)

$$c_{1111}^{\overline{\mathrm{TI}}} = \overline{\left(c_{1111} - \frac{c_{1133}^2}{c_{3333}}\right)} + \overline{\left(\frac{c_{1133}}{c_{3333}}\right)}^2 \, \overline{\left(\frac{1}{c_{3333}}\right)}^{-1}, \tag{A.17}$$

$$c_{1133}^{\overline{\mathrm{TI}}} = \overline{\left(\frac{c_{1133}}{c_{3333}}\right)} \, \overline{\left(\frac{1}{c_{3333}}\right)}^{-1}, \tag{A.18}$$

$$c_{1212}^{\overline{\mathrm{TI}}} = \overline{c_{1212}}\,, \tag{A.19}$$

$$c_{2323}^{\overline{\mathrm{TI}}} = \overline{\left(\frac{1}{c_{2323}}\right)}^{-1}, \tag{A.20}$$

$$c_{3333}^{\overline{\mathrm{TI}}} = \overline{\left(\frac{1}{c_{3333}}\right)}^{-1}. \tag{A.21}$$

Isotropy of the average requires

$$c_{1212}^{\overline{\mathrm{TI}}} = c_{2323}^{\overline{\mathrm{TI}}}\,, \tag{A.22}$$

$$c_{1111}^{\overline{\mathrm{TI}}} = c_{3333}^{\overline{\mathrm{TI}}}\,, \tag{A.23}$$

$$c_{1133}^{\overline{\mathrm{TI}}} = c_{1111}^{\overline{\mathrm{TI}}} - 2c_{2323}^{\overline{\mathrm{TI}}}\,. \tag{A.24}$$

To satisfy condition (A.22), we equate relations (A.19) and (A.20). Since c_{2323} is constant,

$$c_{2323}^{\overline{\mathrm{TI}}} = \overline{\left(\frac{1}{c_{2323}}\right)}^{-1} = \overline{c_{2323}} = c_{2323} = \overline{c_{1212}} = c_{1212}^{\overline{\mathrm{TI}}}\,.$$

To satisfy condition (A.23), we equate relations (A.17) and (A.21). Since $c_{1111} = c_{3333}$,

$c_{1133} = c_{1111} - 2c_{2323}$,

$$
\begin{aligned}
c_{1111}^{\overline{\mathrm{TI}}} &= \overline{\left(c_{1111} - \frac{c_{1133}^2}{c_{3333}}\right)} + \overline{\left(\frac{c_{1133}}{c_{3333}}\right)}^2 \; \overline{\left(\frac{1}{c_{3333}}\right)}^{-1} \\
&= \overline{\left(\frac{c_{1111} - 2c_{2323}}{c_{1111}}\right)}^2 \; \overline{\left(\frac{1}{c_{1111}}\right)}^{-1} + \overline{\left(\frac{4(c_{1111} - c_{2323})c_{2323}}{c_{1111}}\right)} \\
&= \overline{\left(\frac{1}{c_{1111}}\right)}^{-1} = \overline{\left(\frac{1}{c_{3333}}\right)}^{-1} = c_{3333}^{\overline{\mathrm{TI}}}\,,
\end{aligned}
$$

as required. To satisfy condition (A.24), we equate relations (A.17), (A.18), (A.20). Since $c_{1111} = c_{3333}$, $c_{1133} = c_{1111} - 2c_{2323}$ and c_{2323} is constant,

$$
\begin{aligned}
c_{1133}^{\overline{\mathrm{TI}}} &= \overline{\left(\frac{c_{1133}}{c_{3333}}\right)} \; \overline{\left(\frac{1}{c_{3333}}\right)}^{-1} = \overline{\left(\frac{c_{1111} - 2c_{2323}}{c_{1111}}\right)} \; \overline{\left(\frac{1}{c_{1111}}\right)}^{-1} \\
&= \overline{\left(\frac{1}{c_{1111}}\right)}^{-1} - 2c_{2323} = c_{1111}^{\overline{\mathrm{TI}}} - 2c_{2323}^{\overline{\mathrm{TI}}}\,,
\end{aligned}
$$

as required, which completes the proof. □

A.3 Conclusions

For a stack of isotropic layers, the strength of anisotropy—resulting from the Backus (1962) average—is solely a measure of inhomogeneity. However, if c_{2323} is constant, then that inhomogeneity of c_{1111} alone does not result in anisotropy. In other words, the anisotropy of the Backus (1962) average is a consequence of the difference in rigidity among layers, not in compressibility.

A physical counterpart of such a mathematical model might be a porous rock of constant rigidity, whose compressibility varies depending on the amount of liquid within its pores. Following such a physical interpretation, and according to the Backus (1962) average, the level of saturation alone has no effect on the isotropy of the medium, even though it has an effect on the value of $c^{\overline{\mathrm{TI}}}_{1111}$, whose value determines the P-wave propagation speed.

It is impossible to distinguish—from the Backus (1962) average—if the stack of isotropic layers is homogeneous in both elasticity parameters or homogeneous in c_{2323} only. Let us consider a numerical example.

If $c_{1111} = 10$ and $c_{2323} = 2$, then—regardless of the number of layers—$c^{\overline{\mathrm{TI}}}_{1111} = 10$, $c^{\overline{\mathrm{TI}}}_{1133} = 6$, $c^{\overline{\mathrm{TI}}}_{1212} = 2$, $c^{\overline{\mathrm{TI}}}_{2323} = 2$, $c^{\overline{\mathrm{TI}}}_{3333} = 10$; the average is isotropic. For a case discussed in Section A.2.2, we let c_{1111}: 20, 10, 20, 5, 20, 20, 5, 5, 20, 20, and we let $c_{2323} = 2$, for all layers. The Backus (1962) average is the same as for $c_{1111} = 10$ and $c_{2323} = 2$.

Furthermore, as illustrated in Appendix A.A, the Backus (1962) average of transversely isotropic layers can again result in the same values of the isotropic elasticity parameters. Thus, from the Backus (1962) average that results in an isotropic medium, it is possible to infer neither the material symmetry of layers nor the constancy of c_{1111}.

Acknowledgments

We wish to acknowledge the graphic support of Elena Patarini and computer support of Izabela Kudela. This research was performed in the context of The Geomechanics Project supported by Husky Energy. Also, this research was partially supported by the Natural Sciences and Engineering Research Council of Canada, grant 238416-2013.

A.4 References

Backus, G. E. (1962). “Long-Wave Elastic Anisotropy Produced by Horizontal Layering”. *J. Geophys. Res.* 67 (11), 4427–4440.

Bóna, A., Bucataru, I., and Slawinski, M. A. (2007). “Coordinate-free characterization of the symmetry classes of elasticity tensors”. *Journal of Elasticity*, 87 (2), 109–132.

Bos, L., Dalton, D. R., Slawinski, M. A., and Stanoev, T. (2017). “On Backus average for generally anisotropic layers”. *Journal of Elasticity*, 127 (2), 179–196.

Bos, L., Danek, T., Slawinski, M. A., and Stanoev, T. (2018). “Statistical and numerical considerations of Backus-average product approximation”. *Journal of Elasticity*, 132 (1), 141–159.

Postma, G. W. (1955). “Wave Propagation in a Stratified Medium”. *Geophysics*, 20 (4), 780–806.

Rochester, M. G. (2010). “Note on the necessary conditions for P and S wave propagation in a homogeneous isotropic elastic solid”. *Journal of Elasticity*, 98 (1), 111–114.

Slawinski, M. A. (2015). *Waves and rays in elastic continua*. 3rd edn. World Scientific.

— (2016). *Waves and rays in seismology: Answers to unasked questions*. World Scientific.

Thomsen, L. (1986). “Weak elastic anisotropy”. *Geophysics*, 51 (10), 1954–1966.

A.A Transversely isotropic layers: special case

For the values in Table A.1, the Backus (1962) average is

$$c^{\overline{\mathrm{TI}}}_{1111} = 10\,, \quad c^{\overline{\mathrm{TI}}}_{1133} = 6\,, \quad c^{\overline{\mathrm{TI}}}_{1212} = 2\,, \quad c^{\overline{\mathrm{TI}}}_{2323} = 2\,, \quad c^{\overline{\mathrm{TI}}}_{3333} = 10\,.$$

Table A.1: Elasticity parameters of ten transversely isotropic layers

c_{1111}	c_{1133}	c_{1212}	c_{2323}	c_{3333}
20	16	3	2	20
5	1	1	2	5
20	16	3	2	20
20	16	1	2	20
20	16	2.5	2	20
20	16	1.5	2	20
5	1	1	2	5
10	6	1	2	10
5	1	3	2	5
20	16	3	2	20

Post-publication comments

In contrast to the main part of the thesis, in this paper, we do not use Voigt's notation of the elasticity tensor. Instead, we utilise Kelvin's notation (Section 3.2.4.4, Slawinski, 2020b), indispensable for proving Lemma A.2.1 using method of Bóna et al. (2007). Throughout the paper, for the computational purposes, we assume equal thicknesses of the layers, where the thickness weights the average. Also, we assume that the stack of layers stands for the interval of the average; therefore, we use an arithmetic average (see Slawinski, 2020b, Exercise 4.9).

To verify the symmetry of the tensor in the proof of Lemma A.2.1, we check the multiplicities of the eigenvalues. However, following the method of Bóna et al. (2007), to complete the proof, we need to examine the eigenvectors as well. A six dimensional eigenvector can be expressed—in Kelvin's notation—as a 3×3 eigentensor, namely,

$$\varepsilon = \begin{bmatrix} \varepsilon_1 & \frac{\sqrt{2}}{2}\varepsilon_6 & \frac{\sqrt{2}}{2}\varepsilon_5 \\ \frac{\sqrt{2}}{2}\varepsilon_6 & \varepsilon_2 & \frac{\sqrt{2}}{2}\varepsilon_4 \\ \frac{\sqrt{2}}{2}\varepsilon_5 & \frac{\sqrt{2}}{2}\varepsilon_4 & \varepsilon_3 \end{bmatrix} . \tag{A.25}$$

Tensor from Lemma A.2.1, represented by matrix C, has four distinct eigenvalues λ_1, λ_2, λ_3, and λ_5. Therefore, there are four corresponding spaces of eigentensors expressed as,

$$\begin{aligned} \Sigma_{\lambda_1} &= \{a_1(\varepsilon_1 + \varepsilon_2 + \gamma_1\, \varepsilon_3)\,;\, a_1 \in \mathbb{R}\}\,, \\ \Sigma_{\lambda_2} &= \{a_2(\gamma_1(\varepsilon_1 + \varepsilon_2) - 2\varepsilon_3)\,;\, a_2 \in \mathbb{R}\}\,, \\ \Sigma_{\lambda_3} &= \{a_3\, \varepsilon_4 + a_4\, \varepsilon_5\,;\, a_4, a_5 \in \mathbb{R}\}\,, \\ \Sigma_{\lambda_5} &= \{a_5(\varepsilon_1 - \varepsilon_2) + a_6 \varepsilon_6\,;\, a_5\,, a_6 \in \mathbb{R}\}\,, \end{aligned} \tag{A.26}$$

where

$$\gamma_1 = \frac{\lambda_1 - 2c_{1111} + 2c_{1212}}{c_{1111} - 2c_{2323}} . \tag{A.27}$$

All ε in Σ_{λ_1} and Σ_{λ_2} have two distinct eigenvalues and have a common one-dimensional eigenspace. Also, all ε in Σ_{λ_5} have a common zero eigenvalue and the corresponding eigenspace is common with the common one-dimensional eigenspace of ε in Σ_{λ_1} and Σ_{λ_2}. The above statements regarding the spaces of eigentensors are in agreement with Bóna et al. (Theorem 4.3, 2007), which completes the proof of Lemma A.2.1.

Perhaps, an explanatory comment is needed for the proof of Proposition A.2.1. Therein, we show that the average of particular transversely isotropic layers represented by tensors from Lemma A.2.1 may result in an isotropic medium. Two out of three isotropic conditions (A.23) and (A.24) are obeyed. However, we emphasise that the remaining condition (A.22) is satisfied only if $c_{2323} = \overline{c_{1212}}$. Thus, it is obeyed for specific values only.

Overall Bibliography

Adamus, F. P. (2020). "Orthotropic anisotropy: on contributions of elasticity parameters to a difference in quasi-P-wave-squared velocities resulted from propagation in two orthogonal symmetry planes". *Geophysical Prospecting*, 68 (8), 2361–2378.

Adamus, F. P., Slawinski, M. A., and Stanoev, T. (2018). "On effects of inhomogeneity on anisotropy in Backus average". *arXiv*, 1802.04075 [physics.geo-ph].

Aki, K. and Richards, K. G. (1980). *Quantitative Seismology: Theory and Methods*. W. H. Freeman.

Backus, G. E. (1962). "Long-Wave Elastic Anisotropy Produced by Horizontal Layering". *J. Geophys. Res.* 67 (11), 4427–4440.

Bakulin, A., Grechka, V., and Tsvankin, I. (2000). "Estimation of fracture parameters from reflection seismic data–Part II: Fractured models with orthorhombic symmetry". *Geophysics*, 65 (6), 1803–1817.

Baughman, R. H., Stafstrom, S., Cui, C., and Dantas, S. O. (1998). "Materials with Negative Compressibilities in One or More Dimensions". *Science*, 279 (5356), 1522–1524.

Beljankin, D. S. and Petrov, V. P. (1938). "Occurrence of Cristobalite in A Sedimentary Rock". *American Mineralogist*, 23 (3), 153–155.

Berryman, J. G. (1979). "Long-wave elastic anisotropy in transversely isotropic media". *Geophysics*, 44 (5), 896–917.

Berryman, J. G., Grechka, V. Y., and Berge, P. A. (1999). "Analysis of Thomsen parameters for finely layered VTI media". *Geophysical Prospecting*, 47 (6), 959–978.

Bóna, A., Bucataru, I., and Slawinski, M. A. (2007). "Coordinate-free characterization of the symmetry classes of elasticity tensors". *Journal of Elasticity*, 87 (2), 109–132.

Bos, L., Dalton, D. R., Slawinski, M. A., and Stanoev, T. (2017). "On Backus average for generally anisotropic layers". *Journal of Elasticity*, 127 (2), 179–196.

Bos, L., Danek, T., Slawinski, M. A., and Stanoev, T. (2018). "Statistical and numerical considerations of Backus-average product approximation". *Journal of Elasticity*, 132 (1), 141–159.

Bruggeman, D. A. G. (1937). "Berechnung verschiedener physikalischer Konstanten von heterogenen Substanzen. III. Die elastischen Konstanten der quasiisotropen Mischkörper aus isotropen Substanzen". *Annalen der Physik*, 421 (2), 160–178.

Budiansky, B. and O'Connell, R. J. (1976). "Elastic moduli of a cracked solid". *Int. J. Solids Struct.* 12 (2), 81–97.

Bunge, M. (1967). *Foundations of Physics*. Springer.

Calvert, S. E., Burns, R. G., Smith, J. V., and Kempe, D. R. C. (1977). "Mineralogy of Silica Phases in Deep-Sea Cherts and Porcelanites [and Discussion]". *Phil. Trans. Roy. Soc. Lond. Math. Phys. Sci.,* 286 (1336), 239–252.

Carcione, J. M., Kosloff, D., and Behle, A. (1991). "Long-wave anisotropy in stratified media: A numerical test". *Geophysics*, 56 (2), 245–254.

Castagna, J. P. and Smith, S. W. (1994). "Comparison of AVO indicators: A modeling study". *Geophysics*, 59 (12), 1849–1855.

Cheadle, S. P., Brown, R. J., and Lawton, Don C. (1991). "Orthorhombic anisotropy: A physical seismic modeling study". *Geophysics*, 56 (10), 1603–1613.

Chen, H., Zhang, G., Ji, Y., and Yin, X. (2017). "Azimuthal Seismic Amplitude Difference Inversion for Fracture Weakness". *Pure Appl. Geophys.* 174 (1), 279–291.

Chichinina, T. and Obolentseva, I. (2009). “Generalization of Schoenberg’s linear slip model to attenuative media: Physical modeling versus theory”. *SEG Expanded Abstracts*, 3451–3457.

Chopra, S. and Castagna, J. P. (2014). *AVO*. Investigations in Geophysics Series No. 16. Society of Exploration Geophysicists.

Clausius, R. (1879). *Die mechanische Behandlung der Elektricität*. Vieweg.

Coleman, B. D. and Noll, W. (1963). “The thermodynamics of elastic materials with heat conduction and viscosity”. *Arch. Ration. Mech. Anal.* 13 (1), 167–178.

Cowin, S. C. and Mehrabadi, M. M. (1987). “On the Identification of Material Symmetry for Anisotropic Elastic Materials”. *Q. J. Mech. Appl. Math.* 40 (4), 451–476.

Coyner, K. B. (1984). “Effects of stress, pore pressure, and pore fluids on bulk strain, velocity, and permeability in rocks”. PhD thesis. Massachusetts Institute of Technology.

Cui, X., Lines, L., Krebes, E. S., and Peng, S. (2017). *Seismic Forward Modeling of Fractures and Fractured Medium Inversion*. Springer.

Damby, D. E., Llewellin, E. W., Horwell, C. J., Williamson, B. J., Najorka, J., Cressey, G., and Carpenter, M. (2014). “The α—β phase transition in volcanic cristobalite”. *J. Appl. Crystallogr.* 47 (4), 1205–1215.

Dewangan, P. and Grechka, V. (2003). “Inversion of multicomponent, multiazimuth, walkaway VSP data for the stiffness tensor”. *Geophysics*, 68 (3), 1022–1031.

Dvorkin, J., Moos, D., Packwood, J. L., and Nur, A. M. (1999). “Identifying patchy saturation from well logs”. *Geophysics*, 64 (6), 1756–1759.

Dziewoński, A. M. and Anderson, D. L. (1981). “Preliminary reference Earth model”. *Phys. Earth Planet. Inter.* 25 (4), 297–356.

Einstein, A. (1906). “A new determination of molecular dimensions.” *Annalen der Physik*, 19 (4), 289–306.

Emery, D. J. and Stewart, R. R. (2006). "Using VP/VS to explore for sandstone reservoirs: well log and synthetic seismograms from the Jeanne d'Arc basin, offshore Newfoundland". *CREWES Research Report*, 18 (1), 1–20.

Eshelby, J. D. (1957). "The determination of the elastic field of an ellipsoidal inclusion, and related problems". *Proc. R. Soc. A*, 241 (1226), 376–396.

Fay, M., Larter, S., Bennett, B., Snowdon, L., and Fowler, M. (2012). "Petroleum Systems and Quantitative Oil Chemometric Models for Heavy Oils in Alberta and Saskatchewan to Characterize Oil-Source Correlations". *GeoConvention 2012:Vision*.

Fomel, S., Sava, P., Vlad, I., .Liu, Y, and Bashkardin, V. (2013). "Madagascar: Open-source software project for multidimensional data analysis and reproducible computational experiments". *J. Open Res. Softw.* 1 (1), e8.

Freund, D. (1992). "Ultrasonic compressional and shear velocities in dry clastic rocks as a function of porosity, clay content, and confining pressure". *Geophys. J. Int.* 108 (1), 125–135.

Garbin, H. D. and Knopoff, L. (1973). "The compressional modulus of a material permeated by a random distribution of circular cracks". *Q. Appl. Math.* 30 (4), 454–464.

Gassmann, F. (1951). "Über die Elastizität poröser Medien". *Vierteljahrsschrift der Naturforschenden Gesellschafy in Zurich*, 96 (1), 1–23.

Goodway, B. (2001). "AVO and Lamé constants for rock parameterization and fluid detection". *CSEG Recorder*, 26 (6), 39–60.

Grechka, V. and Kachanov, M. (2006). "Seismic characterization of multiple fracture sets: Does orthotropy suffice?" *Geophysics*, 71 (3), D93–D105.

Grechka, V., Vasconcelos, I., and Kachanov, M. (2006). "The influence of crack shape on the effective elasticity of fractured rocks". *Geophysics*, 71 (5), D153–D160.

Gregory, A. R. (1976). "Fluid saturation effect on dynamic elastic properties of sedimentary rocks". *Geophysics*, 41 (5), 895–921.

Grima, J. N., Gatt, R., Zammit, V., Williams, J. J., Evans, K. E., Alderson, A., and Walton, R. I. (2007). “Natrolite: a zeolite with negative Poisson’s ratios”. *J. Appl. Phys.* 101 (8), 086102.

Grima, J. N., Jackson, R., Alderson, A., and Evans, K. E. (2000). “Do Zeolites Have Negative Poisson’s Ratios?” *Advanced Materials*, 12 (24), 1912–1918.

Guo, J., Han, T., Fu, L., Xu, D., and Fang, X. (2019). “Effective Elastic Properties of Rocks With Transversely Isotropic Background Permeated by Aligned Penny–Shaped Cracks”. *J. Geophys. Res. Solid Earth*, 124 (1), 400–424.

Han, D.-H. (1986). “Effects of porosity and clay content on acoustic properties of sandstones and unconsolidated sediments:” PhD thesis. Stanford University.

Hay, R. L. (1986). “Geologic Occurrence of Zeolites and Some Associated Minerals”. *Stud. Surf. Sci. Catal.* 28 (1), 35–40.

Hayes, B. J. R., Christopher, J. R., Rosenthal, L., Los, G., McKercher, B., Minken, D., Tremblay, Y. M., and Fennel, J. (1994). “Cretaceous Mannville Group of the Western Canada Sedimentary Basin; in Geological Atlas of the Western Canada Sedimentary Basin”. *Canadian Society of Petroleum Geologists and Alberta Research Council*, 19 (URL: https://ags.aer.ca/publications/chapter-19-cretaceous-mannville-group.htm).

Helbig, K. (1984). “Anisotropy and dispersion in periodically layered media”. *Geophysics*, 49 (4), 364–373.

— (1994). *Foundations of anisotropy for exploration seismics*. Pergamon Press.

Helbig, K. and Schoenberg, M. (1987). “Anomalous polarization of elastic waves in transversely isotropic media”. *J. Acoust. Soc. Am.* 81 (5), 1235–1245.

Hommand-Etienne, F. and Houpert, R. (1989). “Thermally Induced Microcracking in Granites: Characterization and Analysis”. *Int. J. Rock Mech. Min. Sci. Geomech. Abstr.* 26 (2), 125–134.

Hudson, J. A. (1980). “Overall properties of a cracked solid”. *Math. Proc. Cambridge Philos. Soc.* 88 (2), 371–384.

— (1994). “Overall properties of a material with inclusions or cavities”. *Geophys. J. Int.* 117 (2), 555–561.

— (1981). “Wave speeds and attenuation of elastic waves in material containing cracks”. *Geophys. J. R. Astron. Soc.* 64 (1), 133–150.

Hudson, J. A. and Liu, E. (1999). “Effective elastic properties of heavily faulted structures”. *Geophysics*, 64 (2), 479–485.

Hudson, J. A., Liu, E., and Crampin, S. (1996). “Transmission properties of a plane fault”. *Geophys. J. Int.* 125 (2), 559–566.

Ji, L. and Zong, Z. (2019). “Model parameterization and amplitude variation with angle and azimuth inversion for orthotropic parameters”. *SEG Expanded Abstracts*.

Ji, S., Li, L., Motra, H. B., Wuttke, F., Sun, S., Michibayashi, K., and Salisbury, M. H. (2018). “Poisson’s Ratio and Auxetic Properties of Natural Rocks”. *J. Geophys. Res. Solid Earth*, 123 (2), 1161–1185.

Ji, S., Sun, S., Wang, Q., and Marcotte, D. (2010). “Lamé parameters of common rocks in the Earth’s crust and upper mantle”. *J. Geophys. Res.* 115(B6), 1–15.

Ji, S., Wang, Q., and Li, L. (2019). “Seismic velocities, Poisson’s ratios and potential auxetic behavior of volcanic rocks”. *Tectonophysics*, 766 (1), 270–282.

Jizba, D. (1991). “Mechanical and acoustical properties of sandstones and shales”. PhD thesis. Stanford University.

Kachanov, M. (1992). “Effective elastic properties of cracked solids: critical review of some basic concepts”. *Appl. Mech. Rev.* 45 (8), 304–335.

Kachanov, M. and Sevostianov, I. (2018). *Micromechanics of Materials, with Applications*. Springer.

Kachanov, M., Tsukrov, I., and Shafiro, B. (1994). “Effective moduli of solids with cavities of various shapes”. *Appl. Mech. Rev.* 47 (1), S151–S174.

Keller, J. B. (1960). *Wave Propagation in Random Media*. Tech. rep. EM–164. New York University, Institute of Mathematical Sciences Division of Electromagnetic Research.

Koren, Z. and Ravve, I. (2017). “Fourth-order normal moveout velocity in elastic layered orthorhombic media – Part 2: Offset-azimuth domain”. *Geophysics*, 82 (3), C113–C132.

Kudela, I. and Stanoev, T. (2018). “On possibile issues of Backus average”. *arXiv*, 1804.01917 [physics.geo-ph].

Kumar, D. (2013). “Applying Backus averaging for deriving seismic anisotropy of a long-wavelength equivalent medium from well-log data”. *J. Geophys. Eng.* 10 (5), 1–15.

Lakes, R. S. (2017). “Negative-Poisson’s-Ratio Materials: Axetic Solids”. *Annu. Rev. Mater. Res.* 47 (1), 63–81.

Liner, C. and Fei, T. (2007). “The Backus number”. *Lead. Edge*, 26 (4), 420–426.

Lynn, H. (2014). “Field data evidence of orthorhombic media: changes in the P-P bright azimuth with angle of incidence”. *SEG Expanded Abstracts*.

Mahmoudian, F., Margrave, G., Daley, P. F., and Wong, J. (2012). “Estimation of stiffness coefficients of an orthorhombic physical model from group velocity measurements”. *CREWES Research Report*, 24 (1), 1–16.

Malvern, L. E. (1969). *Introduction to the mechanics of a continuous medium*. Prentice-Hall Inc.

Mase, G. E. (1970). *Theory and problems of continuum mechanics*. McGraw-Hill Book Company.

Maugin, G. A. (2017). *Non-Classical Continuum Mechanics*. Springer.

Mavko, G. and Jizba, D. (1994). “The relation between seismic P- and S-wave velocity dispersion in saturated rocks”. *Geophysics*, 59 (1), 87–92.

Mavko, G., Mukerji, T., and Dvorkin, J. (2009). *The rock physics handbook: Tools for seismic analysis of porous media*. 2nd edn. Cambridge University Press.

McKnight, R. E. A., Moxon, T., Buckley, A., Taylor, P. A., Darling, T. W., and Carpenter, M. A. (2008). “Grain size dependence of elastic anomalies accompanying the α–β phase transition in polycrystalline quartz”. *J. Phys. Condens. Matter*, 20 (7), 075229.

Mensch, T. and Rasolofosaon, P. (1997). “Elastic-wave velocities in anisotropic media of arbitrary symmetry–generalization of Thomsen’s parameters ϵ, δ and γ”. *Geophys. J. Int.* 128 (1), 43–64.

Mizota, C., Toh, N., and Matsuhisa, Y. (1987). “Origin of cristobalite in soils derived from volcanic ash in temperate and tropical regions”. *Geoderma*, 39 (4), 323–330.

Mossotti, O. F. (1836). *Sur les forces qui regissent la constitution interieur des corps apercu pour server a la determination de la cause et des lois de l’action moleculaire*. Societe Italienne des Sciences.

Mouchat, F. and Coudert, F. X. (2014). “Necessary and Sufficient Elastic Stability Conditions in Various Crystal Systems”. *Phys. Rev. B*, 90 (22), 1–4.

Nishizawa, O. (1982). “Seismic velocity anisotropy in a medium containing oriented cracks—transversely isotropic case”. *Journal of Physics of the Earth*, 30 (4), 331–347.

Nur, A. and Simmons, G. (1969). “The effect of saturation on velocity in low porosity rocks”. *Earth Planet. Sci. Lett.* 7 (2), 183–193.

O’Connell, R. J. and Budiansky, B. (1977). “Viscoelastic properties of fluid-saturated cracked solids”. *J. Geophys. Res.* 82 (36), 5719–5736.

Osinowo, O. O., Chapman, M., Bell, R., and Lynn, H. B. (2017). “Modelling Orthorhombic Anisotropic Effects for Reservoir Fracture Characterization of a Naturally Fractured Tight Carbonate Reservoir, Onshore Texas, USA”. *Pure Appl. Geophys.* 174 (11), 4137–4152.

Poisson, S. D. (1824). *Memoire sur la theorie du magnetisme*. Académie des sciences de l'Institute de France.

Postma, G. W. (1955). "Wave Propagation in a Stratified Medium". *Geophysics*, 20 (4), 780–806.

Pšenčík, I. and Martins, J. L. (2001). "Properties of weak contrast PP reflection/transmission coefficients for weakly anisotropic elastic media". *Studia Geophys. et Geod.* 45 (2), 176–199.

Rochester, M. G. (2010). "Note on the necessary conditions for P and S wave propagation in a homogeneous isotropic elastic solid". *Journal of Elasticity*, 98 (1), 111–114.

Rubino, J. G., Castromán, G. A., Müller, T. M., Monachesi, L. B., Zyserman, F. I., and Holliger, K. (2015). "Including poroelastic effects in the linear slip theory". *Geophysics*, 80 (2), 1–6.

Rüger, A. (1998). "Variation of P-wave reflectivity with offset and azimuth in anisotropic media". *Geophysics*, 63 (3), 935–947.

Rüger, A. and Gray, D. (2014). *2. Wide-azimuth amplitude-variation-with-offset analysis of anisotropic fractured reservoirs*. Encyclopedia of Exploration Geophysics. Society of Exploration Geophysicists.

Saenger, E. H., Kruger, O. S., and Shapiro, S. (2006). "Effective Elastic Properties of Fractured Rocks: Dynamic vs. Static Considerations". *Int. J. Fract.* 139 (3), 569–576.

Sanchez-Valle, C., Lethbridge, Z. A. D., Sinogeikin, S. V., Williams, J. J., Walton, R. I., Evans, K. E., and Bass, J. D. (2008). "Negative Poisson's ratios in siliceous zeolite MFI-silicalite". *J. Chem. Phys.* 128 (18), 184503.

Sayers, C. and Kachanov, M. (1991). "A simple technique for finding effective elastic constants of cracked solids for arbitrary crack orientation statistics". *Int. J. Solids Struct.* 7 (6), 671–680.

Schoenberg, M. (1980). “Elastic wave behavior across linear slip interfaces”. *J. Acoust. Soc. Am.* 68 (5), 1516–1521.

Schoenberg, M. A., Dean, S., and Sayers, C. M. (1999). “Azimuth-dependent tuning of seismic waves reflected from fractured reservoirs”. *Geophysics*, 64 (4), 1160–1171.

Schoenberg, M. and Douma, J. (1988). “Elastic wave propagation in media with parallel fractures and aligned cracks”. *Geophysical Prospecting*, 36 (6), 571–590.

Schoenberg, M. and Helbig, K. (1997). “Orthorhombic media: Modeling elastic wave behavior in a vertically fractured earth”. *Geophysics*, 62 (6), 1954–1974.

Schoenberg, M. and Muir, F. (1989). “A calculus for finely layered anisotropic media”. *Geophysics*, 54 (5), 581–589.

Schoenberg, M. and Protazio, J. (1992). “’Zoeppritz’ rationalized and generalized to anisotropy”. *J. of Seism. Explor.* 1, 125–144.

Schoenberg, M. and Sayers, C. M. (1995). “Seismic anisotropy of fractured rock”. *Geophysics*, 60 (1), 204–211.

Sevostianov, I., Yilmaz, N., Kushch, V., and Levin, V. (2005). “Effective elastic properties of matrix composites with transversely-isotropic phases”. *Int. J. Solids Struct.* 42 (2), 455–476.

Slawinski, M. A. (2015). *Waves and rays in elastic continua*. 3rd edn. World Scientific.

— (2020a). *Waves and rays in elastic continua*. 4th edn. World Scientific.

— (2016). *Waves and rays in seismology: Answers to unasked questions*. World Scientific.

— (2018). *Waves and rays in seismology: Answers to unasked questions*. 2nd edn. World Scientific.

— (2020b). *Waves and rays in seismology: Answers to unasked questions*. 3rd edn. World Scientific.

Svitek, T., Vavryčuk, V., Lokajíček, T., and Petružálek, M (2014). “Determination of elastic anisotropy of rocks from P- and S-wave velocities: numerical modelling and lab measurements”. *Geophys. J. Int.* 199 (3), 1682–1697.

Takanashi, M., Nishizawa, O., Kanagawa, K., and Yasunaga, K. (2001). “Laboratory measurements of elastic anisotropy parameters for the exposed crustal rocks from the Hidaka Metamorphic Belt, Central Hokkaido, Japan”. *Geophys. J. Int.* 145 (1), 33–47.

Thomsen, L. (1995). “Elastic anisotropy due to aligned cracks in porous rock”. *Geophysical Prospecting*, 43 (6), 805–829.

— (1986). “Weak elastic anisotropy”. *Geophysics*, 51 (10), 1954–1966.

Ting, T. C. T. and Chen, T. (2005). “Poisson’s ratio for anisotropic elastic materials can have no bounds”. *Q. J. Mech. Appl. Math.* 58 (1), 73–82.

Tsvankin, I. (1997). “Anisotropic parameters and P-wave velocity for orthorhombic media”. *Geophysics*, 62 (4), 1292–1309.

Ursin, B. and Haugen, G. V. (1996). “Weak-contrast approximation of the elastic scattering matrix in anisotropic media”. *Pure Appl. Geophys.* 148 (3/4), 685–714.

Vavryčuk, V. and Pšenčík, I. (1998). “PP-wave reflection coefficients in weakly anisotropic elastic media”. *Geophysics*, 63 (6), 2129–2141.

Wang, Z. (2002). “Seismic anisotropy in sedimentary rocks, part 2: Laboratory data”. *Geophysics*, 67 (5), 1423–1440.

Wanniarachichi, W. A. M., Ranjith, P. G., Perera, M. S. A., Rathnaweera, T. D., Lyu, Q., and Mahanta, B. (2017). “Assessment of dynamic material properties of intact rocks using seismic wave attenuation: an experimental study”. *R. Soc. Open Sci.* 4 (10), 170896.

Xie, C., Wang, E., Zhong, T., Yan, G., He, R., and Guo, T. (2019). “Using the azimuthal derivative of the amplitude for fracture detection”. *SEG Expanded Abstracts*.

Yeganeh-Haeri, A, Weidner, D. J., and Parise, J. B. (1992). “Elasticity of α-Cristobalite: A Silicon Dioxide with a Negative Poisson’s Ratio”. *Science*, 257 (5070), 650–652.

Zaitsev, V. Y., Radostin, A. V., Pasternak, E., and Dyskin, A. (2017). “Extracting real-crack properties from non-linear elastic behaviour of rocks: abundance of cracks with dominating normal compliance and rocks with negative Poisson ratios”. *Nonlinear Process. Geophys.* 24 (3), 543–551.

Zillmer, M., Gajewski, D., and Kashtan, B. M. (1997). “Reflection coefficients for weak anisotropic media”. *Geophys. J. Int.* 129 (2), 389–398.

Zoeppritz, K. (1919). “Über Reflexion und Durchgang seismischer Wellen durch Unstetigkeitsflächen”. *Erdbebenwellen VII B. Nachrichten von der Gesellschaft der Wissenschaften zu Göttingen, Mathematisch-Physikalische Klasse*, 57–84.